Low Temperature Thermal History and Denudation along the Liquiñe-Ofqui Fault Zone in the Southern Chilean Andes, 41-42°S

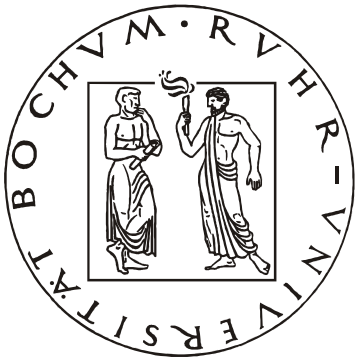

Dissertation

Zur Erlagerung des Grades eines
Doktors der Naturwissenschaften
der Fakultät für Geowissenschaften
an der Ruhr-Universität Bochum

vorgelegt von

Alberto Adriasola Muñoz

aus Santiago de Chile

Bochum,Oktober 2003

Referent: Prof. Dr. B. Stöckhert

Die vorliegende Dissertation wurde in dieser oder ähnlicher Form bei keiner anderen Fakultät oder Hochschule eingereicht. Ich versichere diese Arbeit selbständig angefertigt sowie keine anderen als die angegebenen Hilfsmittel und Quellen verwendet zu haben.

Abstract

Fission track (FT) thermochronology of zircon and apatite, combined with structural observations and microfabric analyses on deformed rocks, were applied to investigate the history of cooling and denudation of the Southern Andes in relation to the late Cenozoic activity of the Liquiñe-Ofqui Fault Zone (LOFZ) and the northward migration of the Chile Triple Junction (CTJ), within the Los Lagos and Chiloé Regions of Chile (41-42ºS).

Three different areas of the study region were examined: (a) Chiloé Island at the fore-arc (73°30'-74°W, 41°50'-43°S), (b) Reloncaví, and (c) Hornopirén areas at the Main Cordillera (72°-72°45'W, 41°-42°15'S). On Chiloé Island, 5 zircon and 7 apatite FT ages were obtained in rocks of a late Paleozoic to early Mesozoic accretionary wedge complex. These range between Late Jurassic and Early Eocene. Late Cretaceous partially reset zircon FT ages point out the presence of shallow-level intrusions in the central and southern part of the island. Late Eocene extrusion ages were obtained from volcanic rocks on the central part of the island.

56 zircon and 51 apatite FT ages, plus 37 apatite track-length distributions were obtained from plutonic rocks of the North Patagonian Batholith (NPB) and contact metamorphic rocks in the Reloncaví and Hornopirén areas of the Main Range. The apatite FT ages and track length distributions indicate rapid cooling histories occurred between ~3-5 Ma along the LOFZ, whereas away from the fault zone tend to older Miocene ages with normal-to-rapid cooling histories. The zircon FT ages range between Cretaceous and Pliocene, with marked differences across the LOFZ in the Reloncaví area.

The FT data from the NPB and contact metamorphic rocks of the Main Range were assembled together with available thermochronologic data to produce cooling paths based on closure temperatures. Three different types of intrusions were characterized by their cooling histories: (a) Cretaceous upper-crustal intrusions, with initial rapid cooling after Cretaceous emplacement followed by slow cooling and rapid exhumation in the late Miocene-Pliocene, (b) Cretaceous to Early Miocene deep intrusions, with steady cooling rates during the Miocene followed rapid exhumation in the Late Miocene-Pliocene, and (c) Miocene shallow intrusions. The regional distribution of the type-(a) and type-(b) cooling paths indicates west-side block uplift along the LOFZ in the Reloncaví area. Type (c) curves are distributed over the batholith, and tend to younger ages towards the fault zone.

The structural and microstructural data from the exhumed plutons along the LOFZ point out an episodic history of intrusion and deformation since Cretaceous times. Different styles of deformation in the plutons are related to their cooling histories and to variable vertical components along the fault zone. At Reloncaví, weak deformation at low temperatures was generally observed in plutons with type-(a) and -(b) cooling histories, with some exceptions of older deformation at higher temperatures. At Hornopirén, uplift of the eastern block is indicated by the different grades of deformation observed across the LOFZ, by shear sense indicators in a deformed tonalite, geobarometry and contact metamorphic phase assemblages.

If the episode of denudation in the region is controlled by vertical displacement components along the LOFZ, then this activity can be dated as Late Miocene-Pliocene (6-3Ma). The non-uniform denudation pattern across the LOFZ is most probably caused by transpression, supporting tectonic reconstructions of the contemporaneous arrival of the Chile rise beneath the Taitao Peninsula. The results of this study point out a coupling between late Cenozoic tectonics and magmatism along the Southern Andes. Additionally, they emphasize tectonically-driven differential uplift and erosion processes dominating the lanscape development of the region during pre-Pliocene times.

Contents

Index of Figures

Chapter 1

Chapter 2

Chapter 3

Chapter 4

Chapter 5

Chapter 6

Index of Tables

Chapter 3

Chapter 4

1 Introduction

1.1 Motivation and Objectives of the Study

Deformation, magmatism, and metamorphism in the Earth's continental crust often occur along convergent plate boundaries. Crustal deformation at active continental margins is complex and typically heterogeneous in intensity and distribution. It depends on several factors, some of which are the angle of plate convergence, the nature and thermal structure of the overriding plate, and the properties of the subducted oceanic plate.

The thermal structure of the overriding plate is strongly influenced by the interaction between the continental margin and a colder, subducted oceanic crust, which drags the geotherms down. The elevation of the heat flow in the volcanic arc reflects the advective heat transport by rising magma. Forced flow of the asthenosphere in the mantle wedge above the subducting plate may enhance heat flow. Within the upper crust, changes in the thermal structure are likely to occur related to magmatism, fluid circulation, and in particular situations, advection of heat during denudation. The landscape of magmatic arcs formed above subduction zones is mainly dominated by volcanic landforms that evolve by uplift and erosion until most of these features are erased to expose deeper igneous intrusions.

Denudation processes at the Earth's surface are sensible to the influence of tectonic forcing, topography, orography, and climate changes. The combined application of low-temperature thermochronometry and structural analysis allows insight into these processes, which are important for understanding the development of orogens. Timing and kinematics of deformation can be constrained. Furthermore, information on the erosional history can reveal the character and the dynamics of the mountain building process.

The Southern Chilean Andes provide an ideal natural laboratory for testing these methods, as they constitute an orogen at the western margin of South America where an active oceanic ridge is currently being subducted, with a triple junction (the Chile Triple Junction, CTJ) between the active continental margin and the diverging plate boundary (figure 1). The tectonic signature in the overriding plate is represented by the long-lived intra-arc Liquine-Ofqui Fault Zone (LOFZ), which extends ca. 1000 km northward from the CTJ along the Main Andean Range. As an effect of ridge ridge subduction and northward migration of the CTJ, a tectonic discontinuity in the overriding plate is suggested at the latitude of the triple junction, with different structural domains characterizing strain partitioning along the Southern Andes.

The long-lived history of the LOFZ is closely related to the episodic evolution of an old magmatic arc, which has remained stationary in its position relative to the subduction front since early Cenozoic times, and suggests a coupling between magmatism and tectonic activity in the region. In addition, a strong influence of climate on the landscape evolution of the Southern Andes is implied by the widespread distribution of glacial landforms in the region. The effect of glaciation on

the landscape evolution of the region can be addressed with low-temperature thermochronology.

The main objective of this study is to determine the low temperature history of the basement rocks of the Southern Andes within the Los-Lagos and Chiloé Regions in relation to the late Cenozoic activity of the Liquiñe-Ofqui Fault Zone (LOFZ).

Important problems to be solved or addressed in this study are:

a) Emplacement and cooling histories of the plutons of the North Patagonian Batholith (NPB), and their regional distribution.

b) Relations between the cooling histories of the plutons of the NPB and the activity of the LOFZ.

c) Deformation in the exhumed plutons along the LOFZ, and relationships with their cooling histories.

d) Timing of denudation along the LOFZ in relation to the position of the CTJ.

e) Paleo-geotherm and denudation rates in the region.

f) Effects of displacement along the LOFZ on the denudation history and landscape evolution of the Southern Andes.

1.2 Tectonic Setting and Location of the Study Area

The Southern Andes represent a segment of the orogenic belt at the western South American margin where an actively spreading ocean ridge is currently being subducted (figure 1). The present site of subduction of the Chile rise, the Nazca, and the Antarctic oceanic plates, forms the Chile Triple Junction (CTJ), that is situated at ~46°30'S along the Peru-Chile trench.

North of the CTJ deformation is evident along the long-lived intra-arc Liquiñe-Ofqui fault zone (LOFZ, Cembrano et al., 1996, 2000), whose main lineaments extend up to ca. 1000 km northward from the Golfo de Penas basin. The actual volcanic arc related to subduction of the Nazca plate beneath the South American plate is situated along its main traces, at a varying distance from the Peru-Chile Trench of between 150 km near the CTJ, and 220 km to the north.

Plate tectonic reconstructions indicate that since ca. 25 Ma convergence between the Nazca and South American plates in the southern part of South America has retained a largely constant east-northeast trend, with an angle of oblique convergence with respect to the Peru-Chile trench normal of between 10° and 30° (Pardo-Casas and Molnar, 1987; Somoza, 1998). Initial subduction of the Chile ridge first occurred at the southernmost tip of South America at ca. 14-10 Ma (Cande and Leslie, 1986). The general NW-SE trend of the Chile ridge and its oblique NE movement relative to the

NS-trending margin of the South American plate caused the CTJ to migrate northward along the Peru-Chile trench. Available fault plane solutions indicate present-day trench orthogonal shortening at the active margin, with a small component of trench-parallel dextral strike-slip motion north of the CTJ (Cifuentes, 1989; Dewey and Lamb, 1992; Murdie et al., 1993).

The study area is located in the northern part of Patagonia, between 41° and 43°S. It was chosen mainly because of the recently improved knowledge of the regional geology, based on mapping and an extensive geochronological database (Duhart et al., 2000; SERNAGEOMIN-BRGM, 1995). A major problem is the difficult field access due to the extreme weather conditions and the thick vegetation characteristic for the region. Abundant outcrops of granites from the Main Andean Range nevertheless provide excellent samples for fission track studies. Three different sectors within the study area are analysed and discussed separately in the following chapters (outlined in red boxes in figure 1): the Chiloé Island representing the Coastal Range, and the Reloncavi and Hornopirén areas at the Main Range.

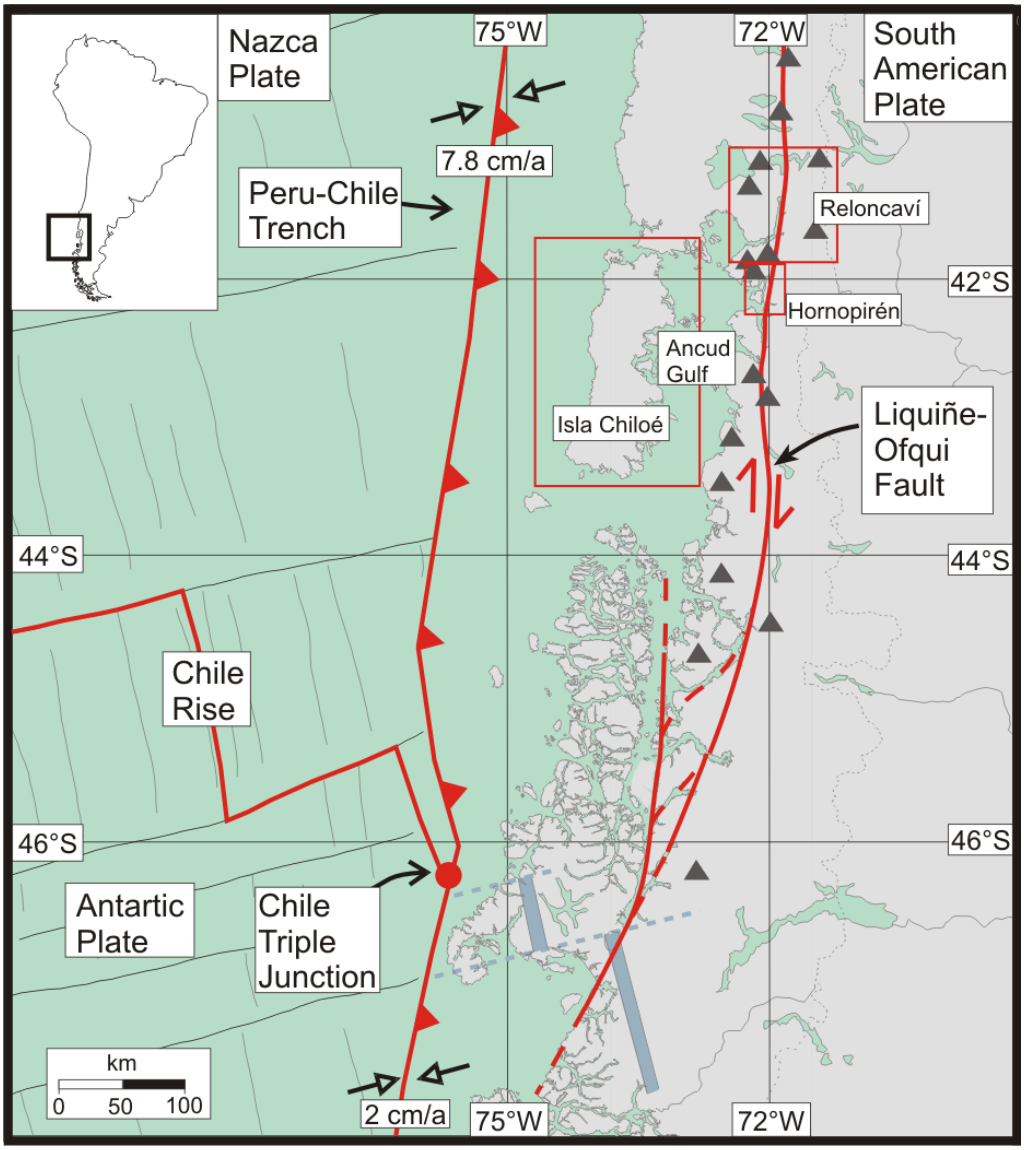

Figure 1: Tectonic Setting and Location of the Study Area (from Thomson et al., 2001)

1.3 Geomorphology and Climate

Climate has a strong effect on the landscape of the Southern Andes (e.g. Thomson et al. 2002; Montgomery et al., 2001). The study region comprises three main geomorphologic units: the Coastal Ranges, the Central Valley (here represented by the Ancud Gulf), and the Main Andean Range.

The Coastal Ranges extend continuously between ~36°S and ~47°S. They are characterized by low topographies that descend gradually southwards to reach below sea level at Taitao Peninsula. The Main Range is defined along the axis of the Andes, with its highest areas built up by recent volcanoes and denuded granites. Steep relief and low topographies characterize their landscapes. A dissected Quaternary ice-capped volcano, Monte Tronador (41°09'S, 3470 meters above sea level), represents the highest elevation of the region. The mean elevation is ca. 800 meters above sea level, and decreases southwards by about 40 m per degree of latitude (Montgomery et al., 2001). The elevation of the modern perennial snowline in the region varies between 1500 and 2000 meters above sea level. The presence of glacial cirques becomes ubiquitous towards the south of Paso Cochamó (41°30'S). South of ~42°S, the continental divide is located on the eastern side of the Main Range.

The present-day climate in the Los Lagos and Chiloé regions is temperate, with a permanent precipitation regime during the whole year, and typical average rates of 2000-3000 mm/yr. The vegetation in the Los Lagos and Chilóe regions is dominated by a rainy temperate forest and an impenetrable, thick rainforest (Selva Valdiviana).

1.4 Outline of the Study

Samples for fission track (FT) analysis of apatite and zircon have been collected during two field campaigns within the areas of Reloncaví and Hornopirén of the Main Range, and at Chiloé Island in the fore-arc (figure 1). The samples were taken from granitoids of the North Patagonian Batholith (NPB), overlying dacitic volcanic rocks, and metamorphic basement rocks. Additional samples for FT thermochronology were provided by the SERNAGEOMIN office in Puerto Varas, Chile. Samples for petrography and microfabric analyses were collected along the main traces of the LOFZ. Where possible, field relationships are described with map sketches and supported with photographs.

A review of the regional geology of the Southern Andes and its tectonic evolution was compiled from published articles and theses, and is presented here in chapter 2. A compilation of published geochronologic and geobarometric data from the studied region is also included in the chapter, and the interpretation of these dates is discussed further in chapters 5 and 6.

Chapter 3 explains in detail the FT - analysis technique and some applications important for this study. The analytical results from this investigation are presented in

chapter 4, together with preliminary discussions on their geological context for each of the three sampling areas.

Chapter 5 presents a structural analysis of the areas of Reloncaví and Hornopirén at the Main Range, based on independent field observations, microfabric analyses on deformed rocks, geochronologic data, Al-in-hornblende geobarometry, and contact metamorphic phase assemblages. Relationships between the deformation of the exposed plutons along the LOFZ and their cooling histories are explored and discussed.

Chapter 6 discusses the histories of cooling and denudation of the plutons of the NPB in relation to the activity of the LOFZ. Thermal constraints for the interpretation of magmatic cooling are briefly introduced. Time-Temperature (t-T) paths for the plutons of the NPB are constructed, based on the correlation of the obtained FT ages with compiled K-Ar, Ar-Ar, and intrusion ages from similar outcrops. A classification of the t-T histories for the plutons with different emplacement depths and exhumation histories along the LOFZ is established and displayed together with their regional distribution.

The timing of the major denudation episode along the LOFZ within the Chiloé Region is discussed and related to the migrating position of the CTJ. Constraints for the denudation rates in the region are finally established, together with some important implications for the denudational history of the Southern Andes. The conclusions are summarized in Chapter 7.

2. Geology of the Southern Chilean Andes

This chapter comprises a review of the tectonic evolution and geological history of the Southern Andes, followed by a description of the main geological units outcropping today in the Chiloé-Los Lagos regions.

2.1 Tectonic Evolution of the South American Margin

Regional tectonic reconstructions for the evolution of the southeast Pacific have been developed through paleomagnetic studies (Duncan and Hargraves, 1984; Cande and Leslie, 1986; Pardo-Casas and Molnar, 1987; Forsythe, 1982; Forsythe et al., 1985; Jaillard et al., 1990; Tebbens and Cande, 1997; Somoza, 1998). These are summarized in figures 2.1a-d.

At least until Mesozoic times, the history of subduction at the western coast of South America is not well constrained. In the Late Jurassic, the separation of North America and South America/Africa was seemingly associated with spreading along a NE/SW trending ridge in the proto-Pacific ocean and a consequent southeast motion of the Farallon-Phoenix plates toward the South American continent (figures 2.1a-b; Duncan and Hargraves, 1984; Jaillard et al., 1990).

The opening of the Southern Atlantic Ocean during the late Early Cretaceous (100-120 Ma) led to rapid orthogonal convergence between the Phoenix and the South America plates. When spreading stopped on the Farallon-Phoenix ridge, the now enlarged Farallon plate continued to move north-

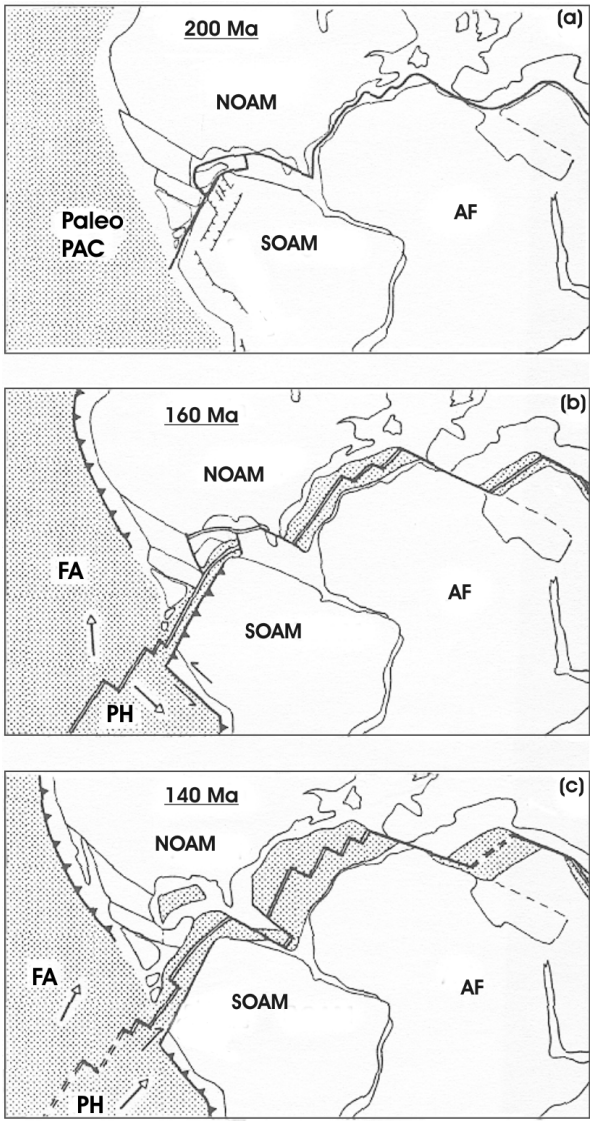

Figure 2.1a: Geodynamic model for the Central Andes related to the early to middle Mesozoic Tethyan evolution (Jaillard et al., 1990). Abbreviations in captions: NOAM North America, SOAM South America, AF Africa, PAC Pacific, FA Farallon, PH Phoenix plates.

eastwards, returning to oblique motion with respect to South America, a situation that persisted into Tertiary times (Duncan and Hargraves, 1984; figure 2.1b).

According to Pardo-Casas and Molnar (1987), a major change back to orthogonal convergence occurred at ca. 49 Ma (anomaly 21), probably connected to the splitting of the Farallon into the Cocos and Nazca plates (figure 2.1c; Pankhurst et al., 1999). From this time onwards, the motion between the latter and South America continued to be orthogonal or slightly oblique, with variable spreading rates due to changes in the position and direction of the Chile Ridge (Tebbens and Cande, 1997). A reassessment of the relative motions between the Nazca and South American plates in the light of new data (Somoza, 1998; figure 2.1c) confirms a marked increase in convergence rate and

orthogonality in late Oligocene times (28-26Ma), followed by a slight decrease during the late Miocene (from ca. 11 Ma).

Initial subduction of the Chile ridge first occurred at the southernmost tip of South America between 14 and 10 Ma (figure 2.1d; Ramos and Kay, 1992; Gorring et al., 1997). The general NW-SE trend of the Chile ridge and its oblique NE movement relative to the NS-trending margin of the South American plate caused the CTJ to migrate northward along the Peru-Chile

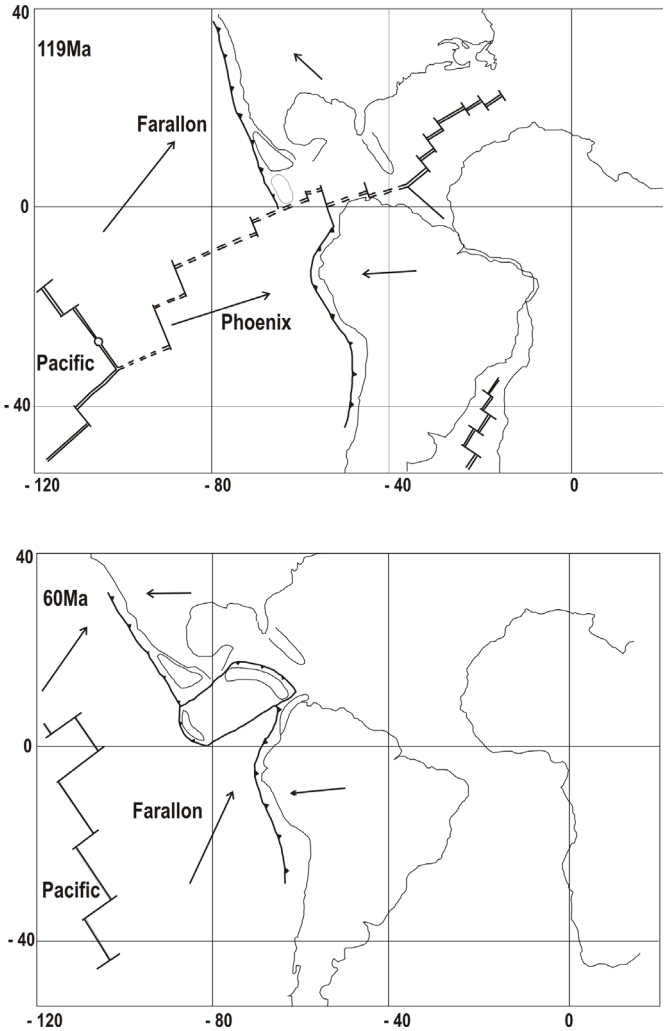

Figure 2.1b: Inferred evolution of the Phoenix and Farallon plates during the Cretaceous and Early Paleocene (simplified from Duncan and Hargraves, 1984).

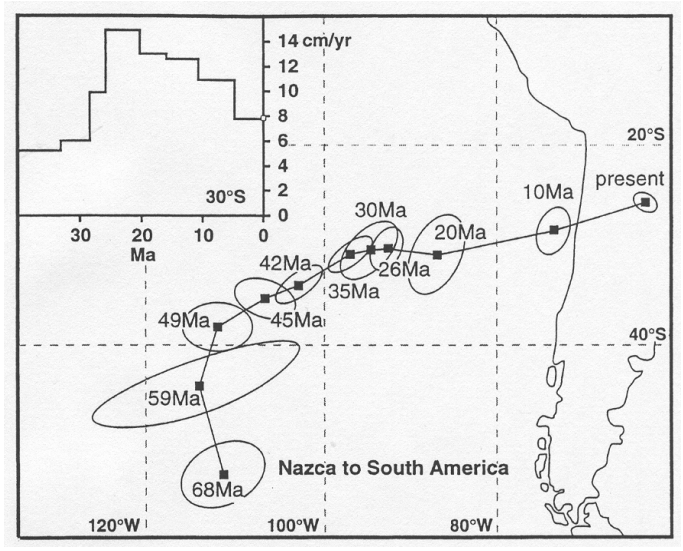

Figure 2.1c: Motion of the Nazca plate since Early Cenozoic times (Pardo-Casas and Molnar, 1987). Insert shows Nazca/ South America plate convergence rates determined by Somoza (1998) as a funtion of time.

trench. The similar trend of the Chile Rise and the Peru-Chile trench between 54°S and 48°S meant that the initial stages of subduction of the spreading center must have occurred along this 700 km section of the South American active continental margin within a few million years.

At present, the configuration shows that the overriding plate is strongly influenced by subduction of the Chile Rise (figure 2.1d). North of the CTJ, the most important feature is the long-lived intra-arc Liquiñe Ofqui fault zone, which extends continuously ca. 1000 km northwards from the Golfo de Penas. During the Pliocene, the subduction of several closely spaced oceanic fracture zones seems to have resulted in the obduction of the Taitao ophiolite at the leading edge of the forearc (Forsythe et al., 1986). The passage of subducted spreading center segments beneath the active margin is interpreted to have created a migrating lithospheric window into the asthenosphere, correlated with pauses in arc volcanism and the eruption of large areas of late Cenozoic backarc plateau basaltic lavas (Gorring et al., 1997).

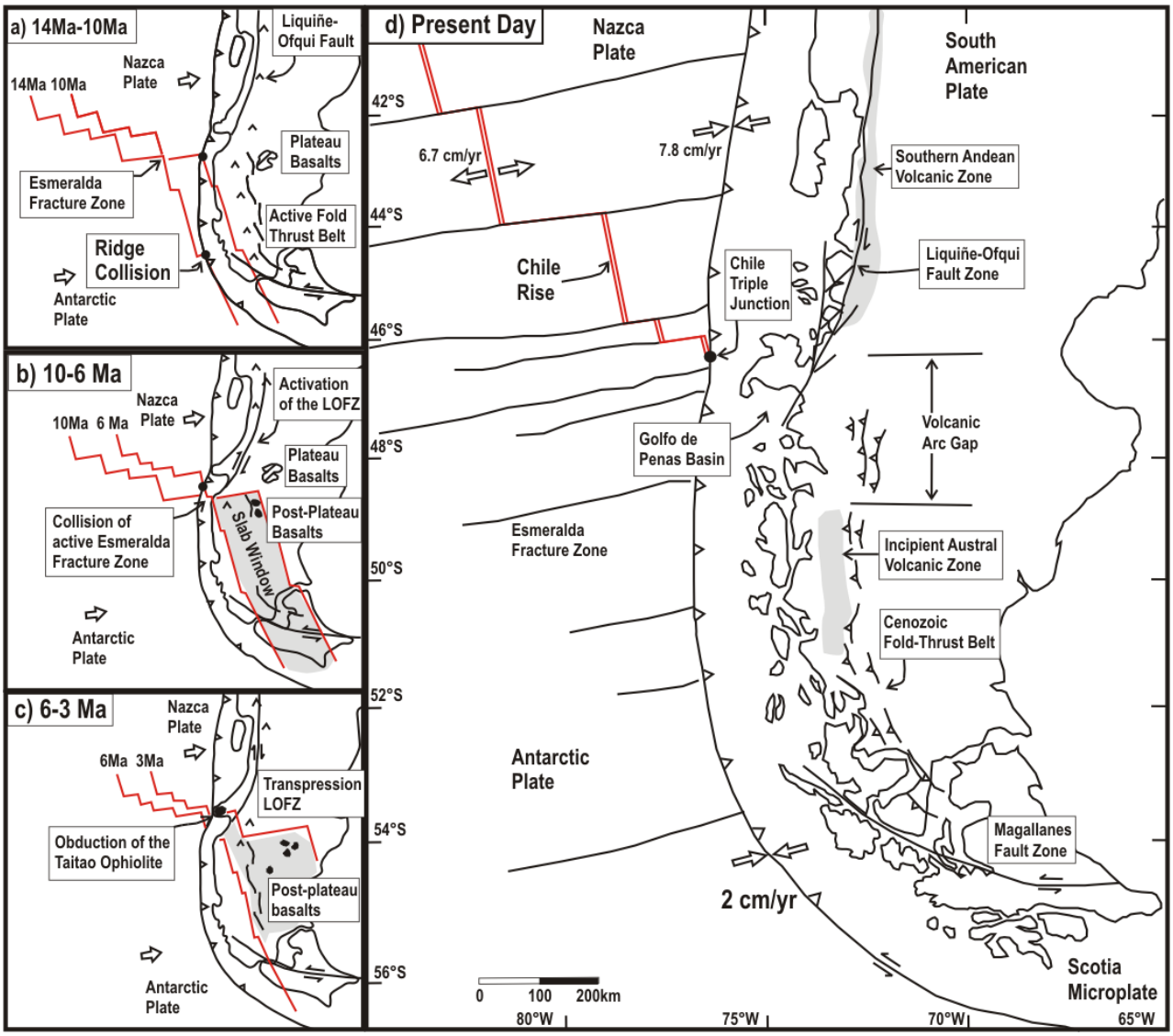

Figure 2.1d: (after Thomson 2002) Actual plate configuration and position of the Chile Triple Junction. On the left, sketch showing the reconstruction of the Chile ridge collision and indention beneath South America during the past 14 Ma (Ramos and Kay, 1992, Gorring et al. 1997).

Another apparent effect of the subduction of the Chile Rise is a tectonic discontinuity in the overriding plate at the latitude of the Golfo de Penas. North of 46°30'S, deformation is most evident along the LOFZ (Cembrano et al. 1996, 2000, 2002). South of the CTJ, an extensive Cenozoic fold-and-thrust belt affects back-arc and foreland basin sequences of the Patagonian Andes (Ramos, 1989).

2.2 Geological History of the Southern Andes

The geological history of the Southern Andes is represented by episodes of accretion, magmatism, faulting, and sedimentation that have occurred within an active continental margin since Paleozoic times.

A simplified map of the geology of the Southern Andes is shown in figure 2.2. The oldest geological units are Late Paleozoic-Early Mesozoic metamorphic accretionary complexes, that, west of the main Andean divide, were formerly part of the ancestral Pacific margin of Gondwana: the Bahía Mansa Metamorphic Complex (BMMC) and the Chonos Metamorphic Complex (CMC) to north of the Gulf of Penas, the Denaro, the Duque de York, the Tarlton Limestone and the Diego de Almagro complexes to the south (out of figure 2.2, Aguirre et al., 1972; Forsythe, 1982; Forsythe and Mpodozis, 1983; Hervé, 1988; Hervé et al., 1999, 2000, Pankhurst et al., 1998; Martin et al., 1999; Duhart et al., 2000). Their discontinuous preservation and patchy record of ages are interpreted to result from discrete events of accretion and tectonic erosion along the active margin of South America (Hervé et al., 2000, 2001).

To the east of the main Andean divide, late Devonian to early Carboniferous low grade metamorphic turbidites, with intercalations of massive limestone bodies, which crop out at Lago General Carrera, are ascribed to the Eastern Andean Metamorphic Complex (EAMC, Hervé, 1993). This complex was deposited within a passive margin setting (Hevé, 1998; Augustsson and Bahlburg, 2003), the massive limestones indicating a platform environment (Hagesawa et al., 1971).

A major event in the evolution of the southern Andean region is the mid-Jurassic silicic volcanism of the Ibañez Formation, probably related to the break up of Gondwana (Pankhurst et al., 1998, 1999). This voluminous and widespread unit is related to the Chon-Aike Formation of similar age and lithology, which covers most of the extra-Andean Patagonia, all the way to the Atlantic coast. Subsequently shallow marine sedimentary units with subaereal volcanic intercalations of the Aysén basin were deposited in Tithonian to Barremian times (De la Cruz et al., 1996; Suárez and De la Cruz, 2000).

The climax of mid-Cretaceous plutonic activity is represented by the Patagonian Batholith, which intrudes both the metamorphic basement rocks and the earlier Mesozoic volcanic and sedimentary sequences. The exposed parts of this extensive batholith developed episodically on the leading edge of the South American plate, from Late Jurassic to Pliocene times, in a response to sequentially eastward subduction of the Phoenix, Farallon, and Nazca plates (Pankhurst el al., 1999). After voluminous Cretaceous plutonism, sparse magmatic activity occurred until Early Miocene times, when another intense outburst took place, which (northwards from the

Golfo de Penas) is probably active until the present. Miocene plutonic activity was focused along the branches of the Liquiñe-Ofqui fault zone, where the actual volcanic arc is localized. Towards the south of the Gulf of Penas, the position of the batholith is in the fore-arc, where some minor Neogene plutonism is presently exposed at the surface (Weaver et al., 1990; Bruce et al., 1991; Thomson, 2002).

Tertiary volcanic activity was concentrated along the Coastal Ranges, between 36° and 43° on Chiloé Island. The activity of this coastal magmatic belt is interpreted to be in conjunction with an episode of regional extension, which thinned the crust below the Central Valley (Muñoz et al., 2000).

Between the late Cretaceous and early Miocene times, several basins developed within the main lineaments of the LOFZ, best represented by the volcano-sedimentary Traiguén Formation around the Moraleda canal (~45°S; Hervé et al., 1995). The sequence sits uncomformably on Cretaceous parts of the NPB and over metamorphic basement rocks, and is intruded by Miocene plutons. The basin is interpreted to be formed in a dextral releasing offset of the LOFZ, during a period of oblique convergence between the Nazca and South American plates. Other basins structurally related to the LOFZ are found at the Golfo de Penas (Forythe and Nelson, 1985; Murdie et al., 1993) and at Buill (ca.~42°, Ayacara Formation, Hervé et al., 1979).

Starting from the Late Miocene, expansive glaciations covered the Patagonian Andes, of which the present day ice fields are remnants. Glaciers extended to the Pacific coast until ca. 20000 years ago, and eastwards far into the extra-Andean Patagonia, where well-developed moraine systems still occur (Mercer and Sutter, 1982, Rabassa and Clapperton, 1990; Heusser et al., 1990).

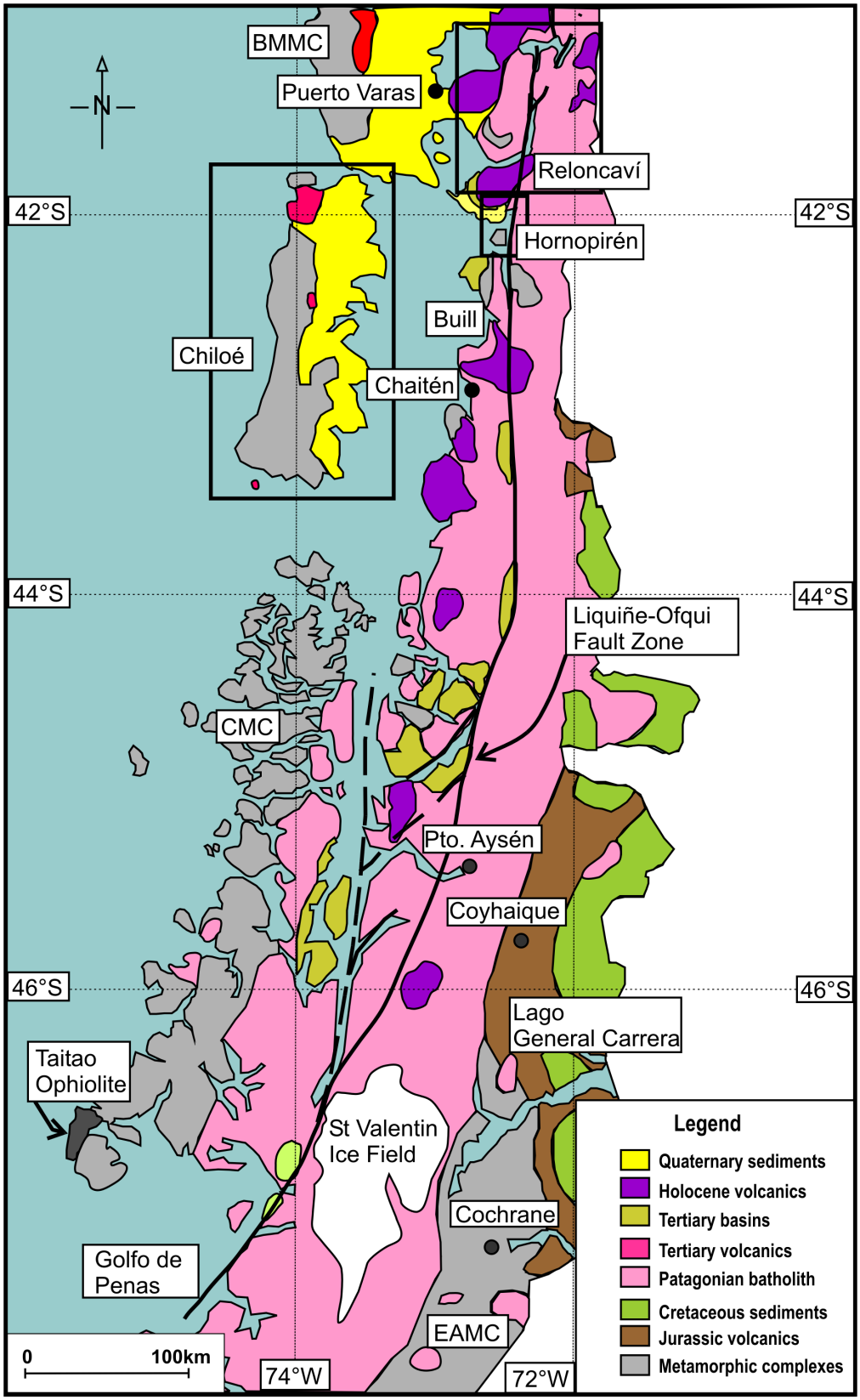

Figure 2.2 Geology of the Southern Chilean Andes (simplified after SERNGAGEOMIN, 1980; Hervé et al., 2000) The boxes enclose the studied areas.

2.3 Geology of the Chiloé-Los Lagos Regions

This section describes the geology of the study area in more detail. The distribution of the geologic units in the study area is displayed together with a compilation of thermochronologic and geobarometric data in figures 2.3a-b-c.

2.3.1 The Metamorphic Basement

The oldest rocks forming the basement in the study area correspond to a series of Paleozoic-Early Mesozoic accretionary wedge complexes that crop out along the Coastal Ranges between ~34°S and the Taitao Peninsula (figures 2.2-2.3a).

The Bahía Mansa Metamorphic Complex (BMMC, or Western Metamorphic Series, Martin et al., 1999; Duhart et al., 2001) has been defined along the Coastal Ranges between 39°S and 42°S at the northern border of Chiloé Island. It consists of a heterogeneous group of metamorphic rocks, mainly pelitic to semi-pelitic schists, meta-graywackes, metabasites, some mafic to ultramafic intrusives, and, more scarcely, metacherts. Some of these rocks are mylonitic.

The whole unit is characterized by pervasive greenschist facies metamorphism associated with a regional foliation striking in NW-SE direction, and dipping with moderate angles towards the NE or SW. This foliation is very pronounced in the metasediments and is defined by mica layers alternating with granoblastic quartz. In the mafic schists it is defined by the preferred orientation of amphiboles and in places of epidote. Open symmetric folding of the foliation on all length scales is characteristic for the whole unit, although tight to isoclinal folds and crenulation cleavage have also been reported in outcrops of the northern border of Chiloé Island (Duhart et al., 2001). Near Ancud (figure 2.3a), isoclinal folds in quartz veins and albite porphyroblasts with graphite inclusion trails in the metapelitic rocks show the presenence of an older schistosity (S_1). This means that the dominant foliation is to be regarded as a second schistosity (S_2), at least in the metapelites.

Typical mineral assemblages in the metasediments are quartz, albite, white mica, chlorite, graphite, sphene, and occasionally garnet and biotite. In the mafic schists the common assemblage is amphibole, epidote, sphene, chlorite, albite, quartz, and stilpnomelane. The sporadic occurrence of garnet and biotite in the metapelites suggests higher temperatures within the greenschist facies (biotite grade), possibly reaching amphibolite facies in places. These assemblages were later affected by a partial retrograde metamorphism.

For the main metamorphism at Bahía Mansa, Kato and Godoy (1995) reported temperature and pressure conditions of 300°C to 400°C and 3 to 4 kbar. Nevertheless, abundant indicators of high-pressure metamorphism in the unit have been reported at other localities within the Coastal Ranges. Kato (1985) and Kato and Godoy (1995) have described glaucophane. Zussmanite has been reported by Massone et al. (1998), cymrite by Muñoz and Hervé (2000), and widespread phengite with Si-rich core by Massone et al. (1996).

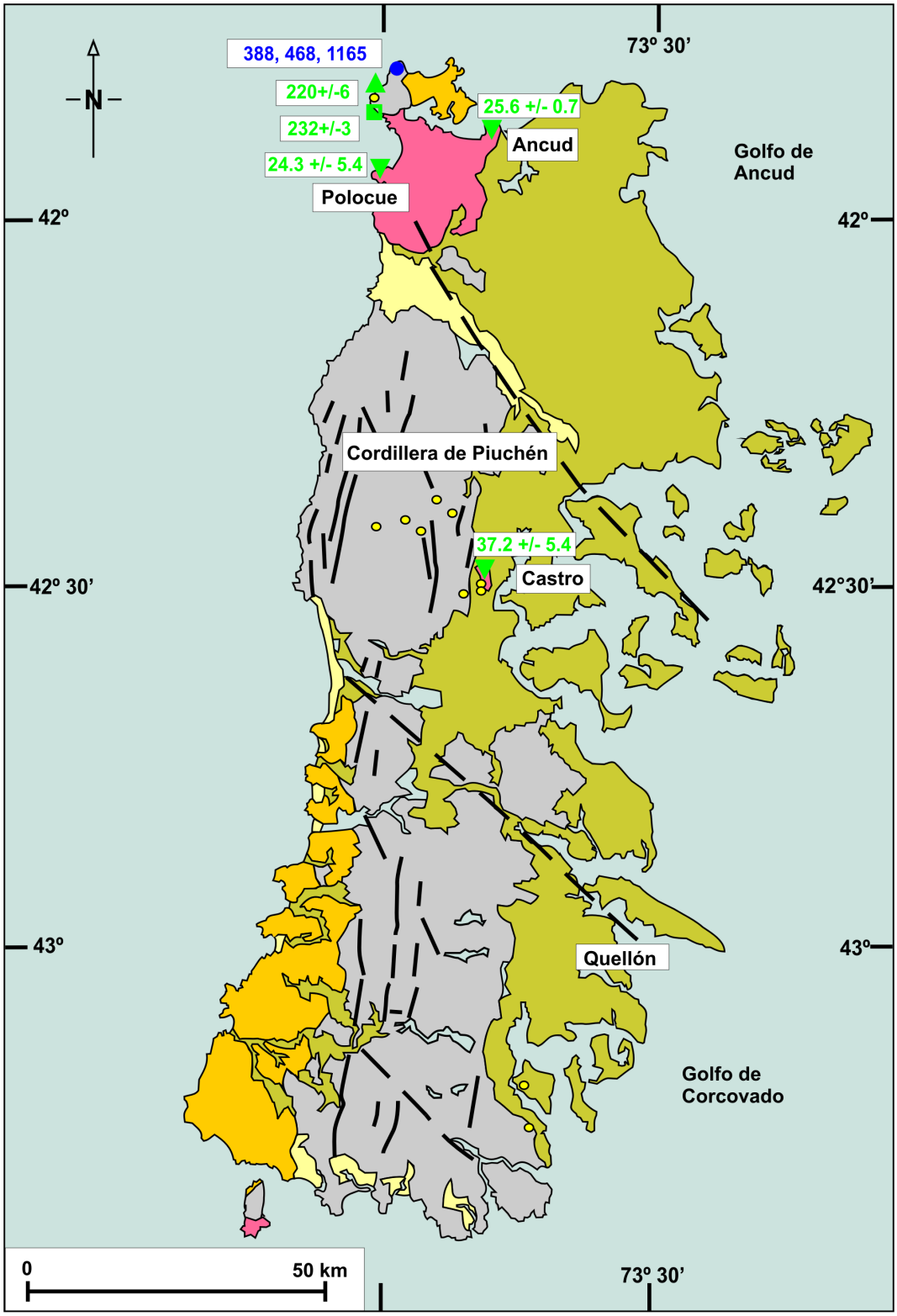

Figure 2.3a: Geology of the Chiloé Island (after SERNAGEOMIN,1980; Muñoz et al., 2000)

- Quaternary beach, estuarine and fluvial sediments
- Quaternary glacial sediments
- Tertiary marine sediments
- Tertiary volcanic Rocks
- Late Paleozoic-Triassic metamorphic rocks
- Lineaments, Faults

Radiometric ages
(after Muñoz et al., 2000; Duhart et al., 1999; Stern and Vergara,1992)

- U-Pb in detrital zircon
- K-Ar in biotite
- Ar-Ar in muscovite
- K-Ar in whole-rock
- Samples for FT dating (present study)

Lenses of spessartine-quartzites intercalated within mafic greenschists at Tril-Tril beach have been recently analysed by Willner et al. (2001). The calculated peak conditions of the metamorphism reached 270°-370°C and 6 to 8 kbar. These were followed by a retrograde P-T evolution through decompression to 2 kbar during cooling below 300°C, with the influx of fluids, and crystallisation of retrograde phases of actinolite around Na-Ca amphibole, low-Si rims on white mica, and high Fe-rims on epidote.

Few details are known from the metamorphic conditions of the basement rocks at Chiloé Island. Saliot (1969) and Aguirre (1972) have reported the sporadic but widespread occurrence of Na-amphibole and lawsonite as relic minerals within greenschists on the Island. These metamorphic assemblages were reported to have formed during an early event of deformation (D_1).

The chemical composition of the metapelitic rocks of the BMMC indicates a detrital origin (with erosion of a continental crust), while for the metavolcanics a basaltic composition of tholeiitic and alkaline affinity (Diaz et al., 1988; Crignola, 1997). Southwards of Guabún, Chiloé Island, outcrops of metavolcanics display tholeiitic and calcalkaline affinities instead (Huffman and Massone, 2000). Duhart et al. (2001) suggest that these differences correspond to the accretion of crustal fragments from different tectonic environments along the southwestern margin of Gondwana.

A detailed compilation of K-Ar, Ar-Ar and U-Pb radiometric ages for rocks of the BMMC has been published in Duhart et al (2001). The Ar-Ar and K-Ar cooling ages constrain the main deformation event (D_2) of the BMMC to the Permian and Triassic, between 260-220 Ma, with a Late Carboniferous age (320-300 Ma) for the previous high P/T stage. U-Pb ages of detrital zircons indicate maximum depositional ages between Middle Devonian and Early Permian for some components of the BMMC. Devonian Trilobites have been reported within the metamorphic rocks at Buill, southeast of the study area (Pankhurst et al., 1992).

The Chonos Metamorphic Complex (CMC) is defined as the basement unit of the Coastal Ranges that includes the Chonos Archipelago and Chiloé Island (Davidson et al., 1987; Hervé, 1988; Martin et al., 1999; Hervé and Fanning, 2001, Thomson and Hervé, 2002). Recent fossil descriptions (Fang et al., 1998) and U-Pb SHRIMP detrital zircon ages (Hervé and Fanning, 2001) show that sedimentation in the eastern part of the CMC occurred during the Late Triassic. Thomson and Hervé (2002), combining these U-Pb zircon detrital ages with fission track cooling ages concluded that the metamorphism in the CMC took place between Late Triassic and Early Jurassic times. Willner et al. (2000) have shown that the metamorphism within the eastern part of the CMC took place under peak P-T conditions of 5.5 kbar and 250° to 280°C, and within the western part at 8 to 10 kbar and 380° to 500°C.

2.3.2 The North Patagonian Batholith

The Mesozoic-Cenozoic Patagonian batholith extends between the latitudes 40°S and 53°S, and is one of the world's largest cordilleran plutonic complexes related to subduction processes at a continental margin. The North Patagonian Batholith (NPB), north of the Gulf of Penas, extends at least 500 km north of Aysén. It crops out as a quasi-continuous igneous body ca. 200 km wide, encompassing the main Andean Range and the eastern portion of the Coastal Ranges.

Pankhurst et al. (1992, 1999) have described the NPB in detail. It comprises a calcalkaline series of rocks, in which hornblende-biotite tonalite and granodiorite predominate. The age distribution of the batholith displays a complex episodic pattern, which is mainly defined by Early Cretaceous intrusion ages along its margins and Early Miocene (Eocene) to Pliocene towards its axis. The discrete episodes of magmatic emplacement were found to correspond to increasing rates of subduction and decreasing obliquity with respect to the Peru-Chile trench (Pankhurst et al., 1999).

Hervé et al. (1996) carried out Al-in hornblende geobarometry for the plutons of the NPB along the Aysén and Chiloé regions. These studies have been extended more recently further north along the Los Lagos region (Seifert et al., 2003). Crystallization depths of ~13 km were derived from samples on the eastern margin of the batholith, and up to ~20 km on its western margin. Low average denudation rates (~0.2 mm/a) for the early Cretaceous components of the NPB are thus implied, which is consistent with low-pressure contact metamorphic aureoles reported at the batholith's margins (Pankhurst et al., 1999). Samples of Miocene plutons located within the central parts of the NPB yielded crystallization depths ranging between ~8 km and ~17 km, implying average denudation rates of between ~0.7 and ~3.1 mm/yr. The higher denudation rates were obtained along the LOFZ (Hervé et al. 1996).

Late Miocene-Pliocene intrusion ages have been reported in plutons sporadically emplaced along the traces of LOFZ, and interpreted as syntectonic (Hervé et al., 1993; Pankhurst et al., 1992; Pankhurst et al., 1999). Near Puerto Cisnes (44°S), small bodies of peraluminous muscovite-garnet granites bear synmagmatic foliation, and have been related to dextral movements of the LOFZ. Outcrops of plutons displaying both magmatic and tectonic foliation have been described at Pitipalena (~44°S), Fiordo Quitralco (~46°S), and in the Hornopirén area of the study region (Hervé et al., 1979; Cembrano et al., 1996, 2000; Pankhurst et al., 1999). Within the central portion of the NPB, along the LOFZ, centimetre- to meter-sized mylonitic bands are common. According to Ar-Ar dating by Cembrano et al. (2000, 2002), many of these mylonites have been formed in Pliocene times.

Miocene shallow-level intrusions have been described as well on the eastern side of the NPB, at Paso de las Llaves (~46°S; Vargas and Hervé, 1995). These consist in isolated bodies displaying a variety of rock types from gabbro to granitic pegmatite with miarolitic cavities.

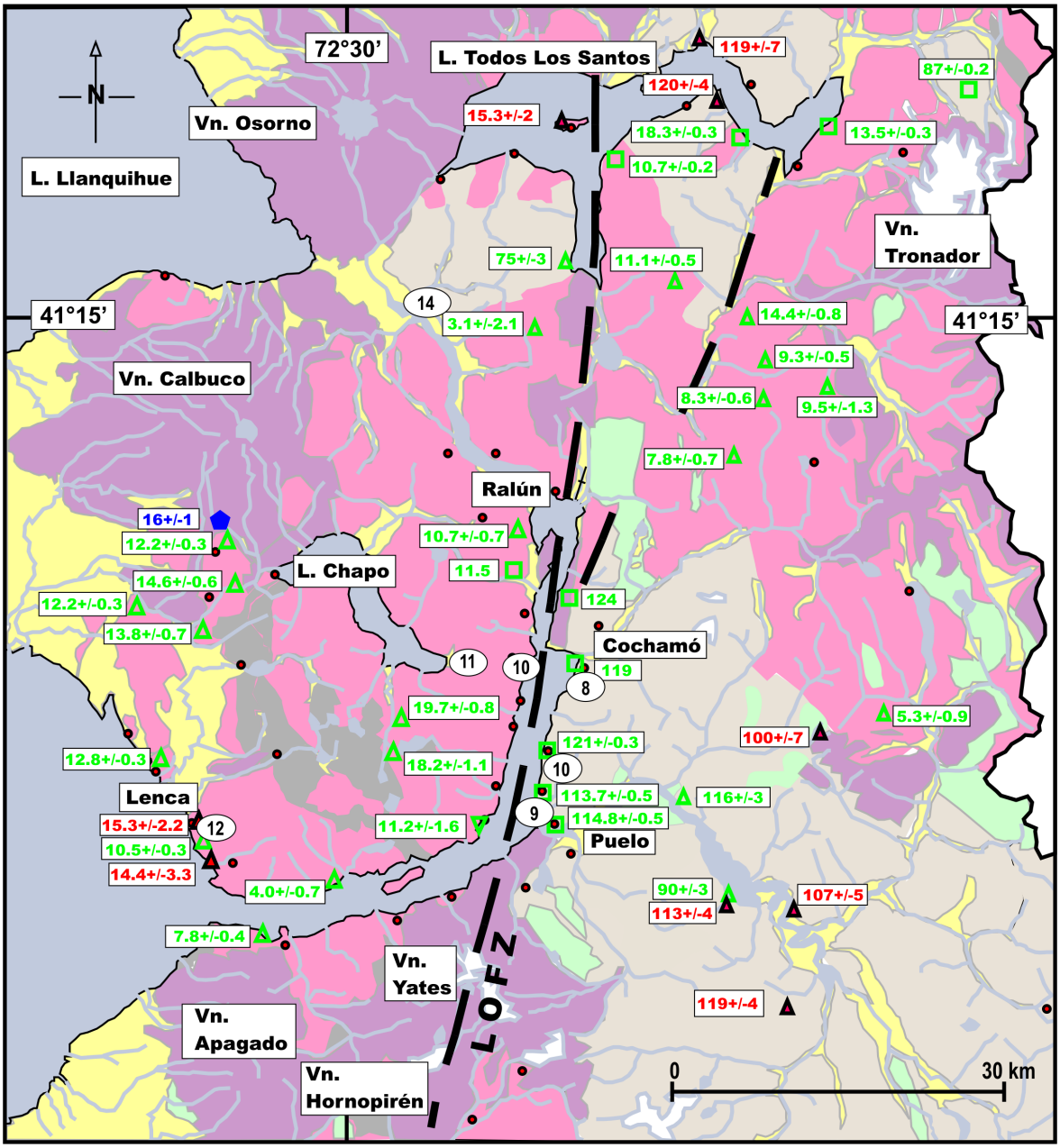

Figure 2.3b: Geology of the Reloncaví Area (after Duhart et al., 2000)
Compiled radiometric ages after SERNAGEOMIN (1995), Carrasco (1995) and Munizaga et al. (1988)

- Quaternary glacial, fluviatile and marine sediments
- Quaternary lavas, cinder cones, piroclastic deposits, lahars and avalanches
- Miocene plutonic rocks
- Cretaceous plutonic rocks
- Jurassic-Cretaceous volcanic and sedimentary rocks
- Late Paleozoic metamorphic rocks
- Liquiñe-Ofqui Fault Zone (LOFZ)

- Ar-Ar biotite age
- K-Ar biotite age
- K-Ar whole-rock age
- K-Ar hornblende age
- Rb-Sr whole rock age
- 11 Al in Hb cristallization depth [km] (Seifert et al., 2003)
- Samples for FT dating (this study)

All of the rocks from the NPB show similar major and trace element geochemical patterns, regardless of age (e.g. Hervé, 1984; Pankhurst et al., 1992, 1999; Parada et al., 1987; Munizaga et al., 1988). However, variations exist in their isotopic compositions at the time of emplacement (Pankhurst et al., 1999). The early Cretaceous plutons have relatively high initial $^{87}Sr/^{86}Sr$ ratios (0.7045-0.7050) and significantly negative $\varepsilon_{Nd(T)}$ values, indicating the involvement of relatively mature crust. The Tertiary plutons have lower initial $^{87}Sr/^{86}Sr$ ratios (down to 0.7038) and less negative $\varepsilon_{Nd(T)}$ values, similar to those exhibited by the Miocene to recent volcanic rocks of the Southern Andes. Pankhurst et al. (1999) propose that the Sr/Nd trends are consistent with lower or mid-crustal involvement rather than contamination in the upper crustal magmatic processes. They propose remelting of underplated mafic rocks in the lower crust as the main petrogenetic process, with the Tertiary magmas being derived by more rapid remelting of juvenile mafic rocks very soon after underplating.

The distribution of the plutonic units of the NPB in the study region is shown in more detail in figures 2.3b and 2.3c. In the Reloncaví area (figure 2.3b) Miocene and Cretaceous plutons are in sharp contact along the main trace of the LOFZ. Two Rb-Sr whole-rock ages of 16±1 and 26±16 Ma (Munizaga et al., 1988) are the only available time constraints for the emplacement of the plutons west of the LOFZ. The orographic distribution of the outlined plutonic units in figure 2.3b is based principally on K-Ar, and Ar-Ar hornblende and biotite dates (Carrasco, 1994; SERNAGEOMIN-BRGM, 1995). Their interpretation as intrusion ages needs to be regarded with caution, as the latter dating methods yield the time of cooling after emplacement of the intrusions and depend on the cooling history of the sampled pluton. The Miocene plutonic rocks west of the LOFZ intrude into high-grade metamorphic rocks of unknown age (Sotomó-Chaiquenes Complex; Thiele et al., 1986). Low-pressure contact metamorphic associations have been reported within these intruded basement rocks (Parada et al., 1987), suggesting rapid cooling after emplacement at the near surface. Small patches of low-grade contact metamorphosed sandstones found near Lenca have been proposed to correlate with inferior members of the Tertiary Ayacara formation (Thiele et al., 1986).

In the Hornopirén area, Late Miocene and Pliocene plutons intrude into Cretaceous parts of the NPB, pelitic schists and amphibolites from the metamorphic basement, and dacitic tuffs from the Tertiary Ayacara Formation (Hervé et al., 1979; Cembrano et al., 1996, 2000; Pankhurst et al., 1992; Duhart et al., 2000). A complex history of intrusion, deformation, and post-tectonic magmatic overprinting is evidenced within the fault zone. The structural context is revised in more detail in chapter 5.

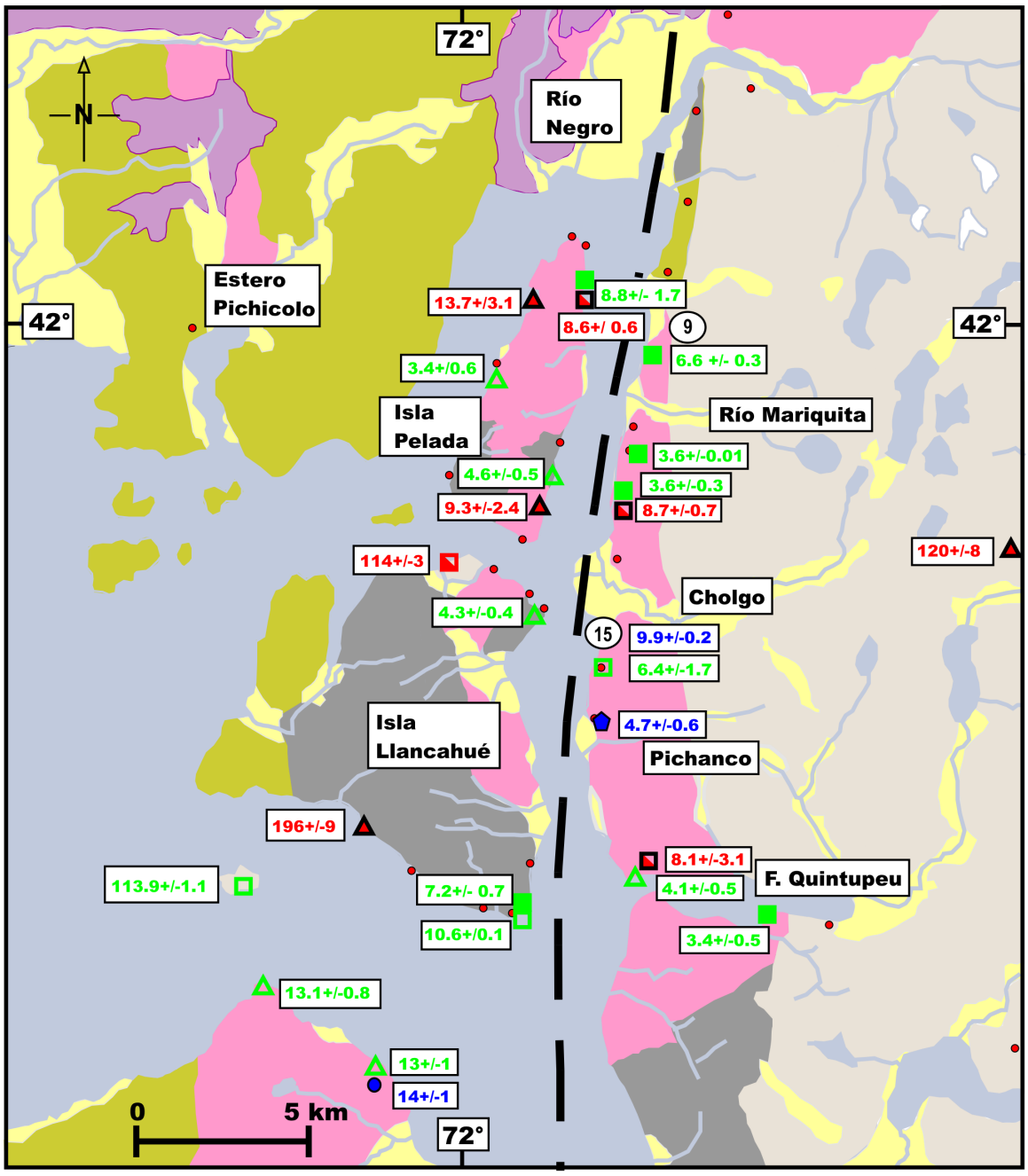

Figure 2.3c: Geology of the Hornopirén Area (after Cembrano et al. (2000) and Duhart et al. (2000)).
Compiled radiometric ages from Cembrano et al. (2000), Pankhurst et al. (1992), and SERNAGEOMIN-BRGM (1995)

- Quaternary sediments
- Quaternary volcanic rocks
- Miocene plutonic rocks
- Tertiary volcanic rocks
- Cretaceous plutonic rocks
- Late Paleozoic metamorphic rocks
- Liquiñe-Ofqui Fault Zone (LOFZ)

- Ar-Ar muscovite age
- Ar-Ar biotite age
- Ar-Ar hornblende age
- K-Ar biotite age
- Rb-Sr whole rock age
- U-Pb zircon age
- (9) Al in Hb crystallization depth [km] (Seifert et al., 2003)
- Samples for FT dating and microfabric analysis

2.3.3 The Meso-Cenozoic Volcanic and Sedimentary Sequences

The Mesozoic volcanic and sedimentary units have a scarce distribution within the study area, but are well exposed in the back-arc region near Aysén (figures 2.2 and 2.3b). Within the Chiloé region, the rocks intruded by the NPB to the east belong to the Futaleufú Group (Thiele et al., 1978; Ulloa, 1980), constituting mainly Jurassic silicic volcanic rocks, and to the Palena Group (Hein, 1979; Romero, 1983), defined by Neocomian marine sedimentary rocks. These are unconformably covered by the La Cascada Eocene marine sequence near the town of Futaleufú (Castillo, 1983).

Towards the eastern margin of the Central Valley, Late Eocene to Early Miocene marine volcano-sedimentary sequences represented by the Traiguén (Hervé et al., 1995) and Ayacara Formations (Rojas et al., 1994) are found close to the Liquiñe Ofqui fault. The Traiguén Formation is deposited uncomformably over metamorphic rocks and at its western border over Cretaceous components of the North-Patagonian Batholith, enclosed within the main branches of the LOFZ. It is intruded by Miocene components of the Batholith at Magdalena Island, and hosts a basic dyke swarm of early Miocene age. Hervé et al. (1995) propose that the rocks of the Traiguén Formation were deposited in pull-apart basins formed in a transtensional setting. Pankhurst et al. (1999) point out that the older parts of the batholith must have been denuded and exposed during its sedimentation in the Eocene to Early Miocene, reburied before intrusion by plutons at ~10 km depth during the Late Miocene, and finally re-exposed following a second phase of denudation that continues to the present day. The maximum depth of burial of the basin sequence is constrained by amphibolite-facies contact metamorphism as being <5 kbar or 17 km (Hervé et al., 1995). Further north, between the Hornopirén area and Buill (~42°-43°S), the Ayacara Formation represents another structurally constrained Miocene fore-arc basin (Hervé et al., 1979; Levi et al., 1966; Fuenzalida, 1979). It has been originally defined by an inferior member including conglomerates and silicic volcanic sandstones, and a superior member that includes dacitic tuffs and mudstones. The lithologic features, syn-sedimentary structures, and microfossils within the sequence indicate an unstable marine basin. Until the present study, no geochronologic date has been reported for the Ayacara Formation within the Hornopiren area (chapter 4.5).

Another important sequence of Tertiary volcanic rocks crops out continuously along the Chilean Coastal Ranges between 36°S and 43°S (figure 2.3a). This Tertiary Coastal Magmatic Belt is interpreted to originate from regional extension in response to the subsidence of a thinned crust below the Central Valley (Vergara and Munizaga, 1974; Muñoz et al., 2000). North of Puerto Varas, the volcanics are interbedded with late Oligocene to Miocene continental and marine sediments grading towards the Central Valley. On the northern part of Chiloé Island, these consist mainly in well-preserved basaltic to andesitic lava flows with subvertical columnar joints, while minor outcrops of rhyolitic pyroclastic flow deposits occur near Ancud. Isolated outcrops of dacites have also been reported near Castro, and at the southernmost part of the island. Published whole-rock K-Ar ages of these volcanic rocks on the Chiloé island concentrate between Late Eocene and Early Miocene (figure 2.3a; Vergara and Munizaga, 1974; Stern and Vergara, 1992; Muñoz et al., 2000). Muñoz et al. (2000) suggest that the older K-Ar ages may correspond to deeper levels of the exposed volcanic edifices.

2.3.4 The Pliocene-Holocene Volcanic Arc

The present-day volcanic arc in the Southern Andes is defined by large stratovolcanoes and small monogenetic cones emplaced along the Main Andean Range. Their spatial distribution differs to the north and south of the Chile Triple Junction. Approximately three stratovolcanoes per degree of latitude occur to the north of the CTJ, instead only four postglacial volcanoes in a distance of ~900 km are known southwards (Hervé et al., 2000).

The composition of the stratovolcanoes is typically basaltic to andesitic, and all of them have calc-alkaline affinities (Lopez-Escobar et al., 1995). The Holocene stratovolcanoes in the study region are (from north to south, figures 2.3b-c): Puntiagudo, Osorno, Calbuco, Yates, and Hornopirén. The Calbuco and Osorno register historical activity. The Calbuco is an andesitic composite stratovolcano that has a truncated cone shape and consists mainly of blocky and AA-type lava flows interbedded with pyroclastic rocks (Moreno and Varela, 1985; Lopez-Escobar et al., 1995). The youngest "dome-cone" and associated lava flows developed during the eruptions of 1893-94, 1917, and 1961. These eruptions have been more violent than those related to the Osorno volcano. The Osorno is a composite stratovolcano comparable in size and and age to the Calbuco; it is predominantly basaltic in composition except for two dacitic domes within the most recent unit (Moreno and Varela, 1985; Lopez-Escobar et al., 1992).

Small monogenic cones are widely distributed in the Patagonian Andes. They are often emplaced on the flanks or in the neighbourhood of the stratovolcanoes, but are also frequent within the main strands of the LOFZ. In the Reloncaví area, well-preserved post-glacial monogenetic cones are distributed between the southern border of the Todos los Santos Lake and Cochamó (Moreno and Varela, 1985; Carrasco, 1995). These minor eruptive centers consist of maars, scoria cones, and lava flows of basaltic to andesitic composition (figure 2.3b).

Pleistocene volcanic rocks form the base of both the Osorno and Calbuco (Moreno and Varela, 1985; Lopez-Escobar, 1992; Lara et al., 1992). These consist mainly in volcaniclastic material interbedded with porhyritic basaltic lavas. Late Pliocene-Pleistocene volcanic outcrops are also found at the northern border of the todos Los Santos Lake, along the Reloncaví sound, and also further east at the main Andean divide (Lara et al., 2001; figure 2.3b). They correspond to a wide suite of eroded basaltic and andesitic volcanic centres distributed between 39°S and 42°S. K-Ar geochronology and geochemical analyses carried out by Lara et al. (2001) show that many of these eroded centres are contemporary and similar in affinity to other centers located in the back-arc region of the Southern Andes. They propose that the wide distribution of the Late Pliocene-Pleistocene volcanism has been controlled primarily by subduction. A decrease in subduction rates from Pleistocene to Holocene times could have resulted in the restricted location of the present-day volcanic activity along the LOFZ (e.g. Lavenu and Cembrano, 1999).

2.3.5 The Pliocene to Holocene Glacial Sediments

The oldest glaciation event in Patagonia has been reported from till deposits intercalated within laval flows, dated at 7.0 and 4.6 Ma (Mercer and Sutter, 1982). Since then as many as 40 further glaciations have been reported until the Last Glacial Maximum, between 25000 and 14000 years ago (Heusser, 1990; Llitboutry, 1999). The greatest advance of the Patagonian glaciation, dated at ~1.2-1 Ma, covered most of the Main Range and extended to the east as far as Lago Argentino in the Río Santa Cruz valley (Mercer, 1976).

The Chilotan piedmont glacier (Heusser, 1990) is representative of the Last Glacial Maximum in the study area. It covered the Central Valley in the Lake District and occupied most of Chiloé Island. A thickness of up to 1 km has been reported near Puerto Montt (Heusser, 1990; Hervé and Ota, 1993).

Pleistocene glaciation along southern Chile seems to have significantly contributed to the infill and accretion of sediments into the Peru-Chile trench both to the north and south of the Chile Triple Junction (Bangs and Cande, 1997). At the CTJ only a shallow trench with almost no sediment infill is actually being developed, implying important localized erosion. Bangs and Cande (1997) suggest furthermore that erosion along the South American Pacific margin is increasing by the fact that present day glaciation is retreating.

In mountain belts that intersect the snowline, glacial erosion processes are most effective above the mean glacial-equilibrium line altitude (ELA, e.g. Brozovic et al., 1997). The present day ELA of the North Patagonian ice field at ~47° varies between 1200 m and 1350 m on the eastern side (Lliboutry, 1999). Patagonian ice fields are reported to be temperate (Lliboutry, 1999). During the Last Glacial Maximum, Hulton (1994) estimated that the ELA was 560 m lower at 40°S than at present day, whereas at ~50°S, it has been elevated ca.~160m. Hallet et al. (1996) estimated that basin-wide long-term average glacier erosion rates can approach 10-100 mm/yr for fast-moving, high flux, temperate glacier landscapes in Alaska, comparable to those of Patagonia (e.g. Thomson, 2002). These rates are more than enough to counteract high uplift/erosion rates from any active orogen, such as the Himalayas (e.g. Brozovic et al., 1997).

^{14}C age determinations of Holocene shell material from elevated beaches in the Chiloé Region (42°S) were carried out by Hervé and Ota (1993). Based on the correlation of shoreline profiles across the Ancud Gulf, they estimated a differential uplift of 10 mm/yr in the area. They considered uncertainties related to the paleo-sea level at which the organisms lived, and compared the east-west distribution of these rates with the expected values from glacial rebound isostacy after the last glacial retreat, estimated at ~10,000 a B.P. They determined that the expected rates derived from glacial rebound isostacy were insufficient to compensate the high rates obtained in their profiles, and concluded that the uplift rates are most probably related to coseismic deformation associated to the 1960 earthquake.

2.4 The Liquiñe Ofqui Fault Zone

The Liquiñe Ofqui Fault Zone (LOFZ) is a long lived intra-arc fault zone, about 1000 km long, that lies parallel to and about 300 km E of the Nazca-South American plate boundary, and curves at its southern extremity towards the west. Its south-central part has been described as having two main branches, connected by NE trending structures. The whole configuration is interpreted as an active dextral transpressional flower structure (Cembrano et al., 2002; Thomson, 2002).

The LOFZ reveals different displacements in time. Pre-Late Cretaceous sinistral motion has been reported in its northern part, at Liquiñe (Cembrano et al., 1996; Hervé, 1976). Tertiary dextral extensional pull-apart basins have been described within its central and southern segments (Herrvé et al., 1993, 1995). Late-Miocene and Pliocene evidences for dextral transpression have been reported along its central and southern parts (Cembrano et al., 2000, 2002; Lavenu and Cembrano, 1999; Thomson et al., 2001; Thomson, 2002). Seismic data suggests that between 39°S and 46°S the Chilean forearc is undergoing trench-orthogonal shortening wheras the arc is absorbing a small trench-parallel component (Chinn and Isacks, 1983; Cifuentes, 1989; Barrientos and Acevedo, 1992; Dewey and Lamb, 1992). East of the LOFZ, no regional fold and thrust belt is developed in the back arc of this part of the Andean range (Ramos, 1989; Ramos and Kay, 1992).

Northwards-oblique subduction has been considered as the driving mechanism of the LOFZ activity (Hervé, 1976; Cembrano et al., 1996, 2000, 2002), but the indenter effect of ridge subduction has also been raised as a possible mechanism (Forsythe and Nelson, 1985; Nelson and Forsythe, 1994; Murdie et al., 1993). Cembrano et al. (2002) propose that the differences of deformation styles along the strike of the fault are a result of partitioning of the bulk transpressional deformation, and that a short-term deformation was controlled by the indention of the Chile ridge.

Paleomagnetic studies within the vicinity of the LOFZ have been carried out by Rojas et al. (1994) and Beck et al. (1993, 2000). They point out a pattern of counterclockwise rotation in the fore-arc and clockwise rotation in the back arc, with the magnitude of rotation increasing from both sides towards the fault zone. Nevertheless, no meridional displacements beyond the error limits of the paleomagnetic method have been established. This has been formerly interpreted as a buttressing manifestation of the northwards translation of the fore-arc region (Beck et al., 1993). More recently, Beck et al. (2000) interpret the block rotations as related to a general state of subcrustal ductile shearing localized along the LOFZ. They propose that the small amounts of rotations result from the curved nature of its fault strands. No meridional displacement of the Batholith has been identified since its formation with respect to its actual position in the South American Continent.

Cembrano et al. (1996, 2000, 2002) have studied the LOFZ along several transects between Liquiñe (39°S) and Aysén (46°S). They describe different patterns of deformation and timing along strike. The microstructures and mineral assemblages from the deformed rocks at the fault zone show ductile fabrics in the plutons formed at greenschist facies conditions. Ar-Ar dating of biotites from deformed plutons and

muscovites from pelitic schists, with overall dextral and oblique inverse kinematics, yield ages between 6 Ma and 3 Ma.

No conclusive evidence has been reported for the amount of lateral displacement occurred along the LOFZ. This problem may be principally due to the difficult field access and hard weather conditions in the Southern Andes. Additionally, episodic magmatic activity along its traces may easily overprint its kinematics (e.g. Hervé, 1984, Pankhurst et al. 1992; Cembrano et al., 2000).

An extensive database of zircon and apatite FT thermochronology from the Southern Andes between ~43° and 46° S has been recently reported in Thomson et al. (2001) and Thomson (2002). The data indicates that the LOFZ was the focus of enhanced cooling and denudation starting from ~16 Ma. Thomson (2002) interpreted the LOFZ as a flower structure, in which several uplifted fault blocks can be inferred from their different cooling histories (figure 2.4). The estimated cooling rates for the western and central blocks of the LOFZ vary between 20°C/Myr and >25°C/Myr, which, assuming a constant upper-crustal geotherm resembling a present day value of ~34°±11°C (Hamza and Muñoz, 1996), should correspond to denudation rates of between 0.4 and 1.3 mm/yr (figure 2.4). Less than 1°C/Myr was obtained for the easternmost block, implying ~0.02-0.04 mm/yr.

Very fast cooling rates occurred between ca. 7 and 2 Ma were obtained near the traces of the LOFZ, coeval with plate reconstructions of the indention of the Chile Rise beneath the Taitao Peninsula. Anomalously young apatite FT dates found along the fault zone were attributed to the presence of late Miocene to recent magmatism and numerous hot springs in the area.

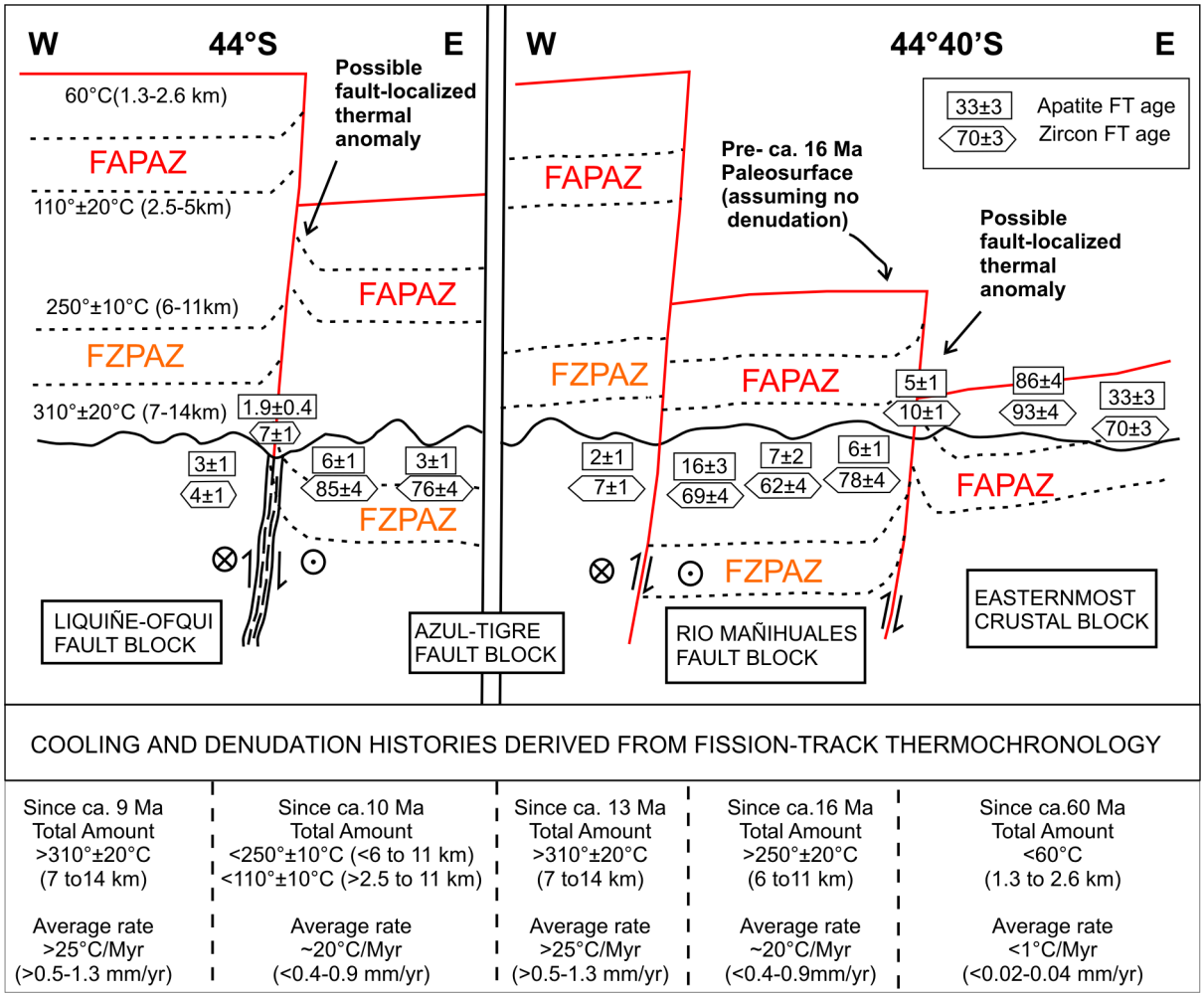

Figure 2.4: (from Thomson, 2002) East-west profiles across the Azul-Tigre and Mañihuales faults at ~44°30' and across the LOFZ at ~44°S. The interpretation of block uplift is based on the assumption of a constant upper-crustal geotherm of 34° ±11°C/km. Uplifted isotherms are reconstructed based on pre- 16 Ma denuded fossil apatite and zircon partial annealing zones (FAPAZ and FZPAZ respectively). The relative vertical offsets and total amounts of denudation are constrained by assuming that cooling below ~300°C results solely from denudation, and avoiding the presence of shallow-level intrusions along the fault zone. The estimated cooling and denudation rates for each of the fault blocks are summarized at the bottom of the figure.

3. A Short Review on Fission Track Analysis and its Practical Applications

3.1 What are Fission Tracks?

Fission tracks are trails of damage in an insulating solid produced by the linear path of a nuclear fission fragment. Nuclear fission is possible either spontaneously or by induced bombardment of a heavy nuclide with neutrons, protons or other particles, as well as by gamma irradiation. The reaction is accompanied by emission of α–particles, neutrons, and other particles along with a large amount of energy (typically 210 MeV). Fission tracks were first reported by Silk and Barnes (1959), inducing fission of ^{235}U in irradiated micas and detecting them using transmitted electron microscopy. A short time later Price and Walker (1962) discovered that the tracks could be enlarged enough to be made visible with an optical microscope by chemical etching of the solid with a suitable reagent.

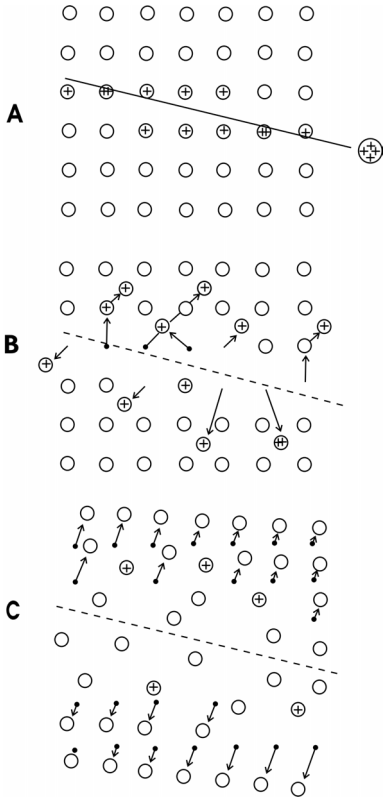

Figure 3.1 The ion spike explosion model for the formation of fission tracks in a mineral (Fleischer et al., 1965c). A) Ionisation of the atoms by a moving charged particle. B) Due to Coulomb repulsion, ions are displaced from the lattice sites into interstitial positions, at the same time a number of vacant lattice sites is created. C) The stressed region of the track relaxes, elastically straining the surrounding undamaged lattice.

The atomic interactions that generate the disrupted zones are complex and incompletely understood (Fleischer et al., 1975; Chadderton, 1988). The most widely accepted hypothesis to explain the process of formation of fission tracks in natural solids (e.g. glass, minerals) is the ion explosion spike mechanism (Fleischer et al., 1965c), explained in figure 3.1.

Spontaneous fission occurs only for very heavy nuclides of atomic number ≥ 90 and atomic mass ≥ 230 belonging to the actinide series (Th, Pa, U, Np, Pu, etc.). Most of these isotopes disintegrate by other processes, like α-decay. Only ^{232}Th, ^{238}U, and ^{235}U occur in measurable concentrations as primary constituents in natural substances (see table 3.1).

Within natural terrestrial materials almost all fission reactions, and hence all spontaneous fission tracks result from the decay of ^{238}U. Natural fission tracks from other sources can be expected in only extreme cases, for example from ^{232}Th in very lead-rich samples and from ^{235}U induced by the spontaneous fission of ^{238}U in uranium-rich ores (e.g. Oklo U deposit in Gabon; Bodu et al., 1972; Petrov, 1977). Cosmic and lunar materials may have had other possible sources for fission track formation. The fission of ^{244}Pu could have been induced by cosmic rays in the early life of the solar system (Fleischer et al., 1965b).

Table 3.1: Abundances and half-lives of major naturally occurring nuclides suffering spontaneous fission (after Wagner and Van den haute, 1992)

Nuclide	Relative abundance (compared to ^{238}U)	Total half-life (years)	Spontaneous fission half-life (years)
^{232}Th	4 [d]	$1.4 \cdot 10^{10}$ [a]	$1.0 \cdot 10^{21}$ [c]
^{234}U	$5.44 \cdot 10^{-5}$	$2.46 \cdot 10^{5}$ [b]	$1.5 \cdot 10^{16}$ [b]
^{235}U	$7.25 \cdot 10^{-3}$	$7.04 \cdot 10^{8}$ [a]	$1.0 \cdot 10^{19}$ [b]
^{238}U	1	$4.47 \cdot 10^{9}$ [a]	$8.2 \cdot 10^{15}$ [b]

[a]Steiger and Jäger (1977), [b]Holden (1989), [c]Baard et al. (1989), [d]Geochemical average.

3.2 Stability of Fission Tracks and Principles of Fission Track Dating

Fission tracks are metastable features in non-conducting solids, such as silicates, whereas in semi-conducting and conducting materials the lattice structure reforms immediately, leaving no record of the fission event (e.g. Fleischer et al. 1965a). The number of spontaneous tracks within the material is dependent on the time of residence of the tracks, the concentration of ^{238}U, the rate of spontaneous fission of ^{238}U, and the degree of thermally activated track removal. Together with the discovery of the etching technique, this allows the dating of materials using fission tracks.

The main factors controlling fission track stability are temperature, time, chemical composition, and atomic structure of the material (section 3.5). Other factors, such as fluids and weathering, were found to have little or no effect (Gleadow and Lovering, 1974; Fleischer et al., 1975; Naeser, 1979). The direct parameter used to measure fission track stability in apatites is the track length distribution, which has allowed to determine a partial annealing zone (PAZ) and to model thermal histories (sections 3.3.4 and 3.5.1). Zircons have usually higher uranium contents, and are steadily exposed to a background level of ionizing radiation and bulk damage, which complicates the determination of a PAZ (section 3.5.2).

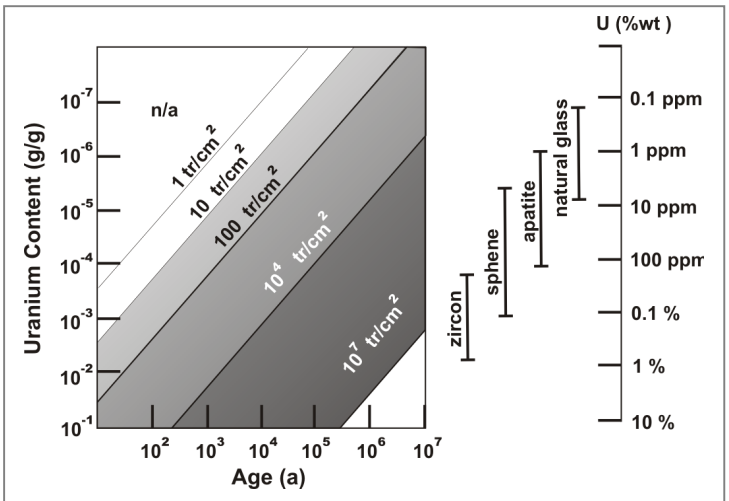

Figure 3.2: Scheme of the relationship between sample age, uranium content and fission track density (after Wagner & Van den haute, 1992).

Spontaneous fission of ^{238}U occurs at a constant rate of 10^{-16} fission events per year (table 3.1, Flerov and Pterjak, 1940). Hence, if the ratio of spontaneous track density to uranium content of a material is known, then its age can be calculated. This is possible by subjecting a sample to a known dose of thermal neutrons, or neutron fluence (ϕ), in a nuclear reactor. These induce fission in ^{235}U. Since the isotopic ratio $^{235}U/^{238}U$ is known to be constant in nature, the concentration of ^{238}U can be obtained. The neutron fluence can be determined by including a standard dosimeter glass, with a uniformly distributed

and known amount of uranium, alongside the sample. Induced fission tracks from ^{235}U are then produced, which can be etched and counted as an estimate of ϕ.

The fission track dating technique is used for dating a variety of minerals, the suitability of them being shown in figure 3.2. The most common minerals for fission track analysis are apatite, zircon and sphene, together with natural glass. Other minerals such as muscovite, biotite, epidote, and garnet may also be used, but usually contain too low uranium concentration for a general use.

3.3 Methodology

In very simple terms, a fission track age is determined from the density ratio of the spontaneous fission tracks (ρ_s) to the induced tracks (ρ_i) produced during irradiation. To do this, several factors need to be taken into consideration, such as the geometry of the etched surfaces, radiation damage, anisotropic etching and inhomogeneous uranium distribution within a mineral. Different methods for handling samples are cited in Gleadow (1981). This study applies the external detector method, which avoids assumptions of uniform uranium distribution in the population of grains analyzed, as well as the uncertainties inherent in the thermal flux and fission decay constants (e.g. Green and Hurford, 1984). Fluence determinations have been carried out using the ζ –calibration with age standards against uranium dosimeters, following the recommendations of the International Union of Geological Sciences Working Group (Hurford 1990a,b).

3.3.1 Sample Preparation

The methods of mounting different mineral grains have been discussed in detail by Naeser (1967) and Gleadow et al. (1976). Apatite grains are mounted in epoxy resin on a glass microscope slide, whereas zircons are mounted in FEP-Teflon. Afterwards they are mechanically polished, finishing with 0.25 μm grade diamond abrasive, until 25 μm is removed off from their external surface. An internal surface for counting is required to avoid the possibility of any external contamination from groundwater, or by uranium fission from adjacent mineral phases. Practical details applied in this study are included in appendix 1.

3.3.2 Etching of Tracks

In order to reveal the fission tracks intersecting a mineral surface, chemical etching is required. Both the concentration and temperature of the reagent, as well as the etching time, place an important control on the shape and length of the revealed fission tracks. Appropriate etching conditions for fission track revelation has been determined on an empirical basis and vary considerably for different minerals, as shown in table 3.3.2.

Table 3.3.2: Etching Conditions for Different Minerals (from Thomson, 1992)

Mineral	Etching Solution	Temperature °C	Duration	Reference
Apatite	Conc. HNO_3*	25	20-25 sec.	1
	5% HNO_3	20	45 sec.	2
Zircon	11.5g KOH: 8g NaOH eutectic*	220	3-100 hr	3
	HF(48%):H_2SO_4(98%) (1:1)	165	1-10 hr	4
Muscovite	HF (48%)*	20	45 min	5

* applied in this study.

References:

1. Naeser (1967)
2. Wagner and Reimer (1972)
3. Gleadow et al. (1976)
4. Krishnaswami et al. (1974)
5. Gleadow and Lovering (1974)

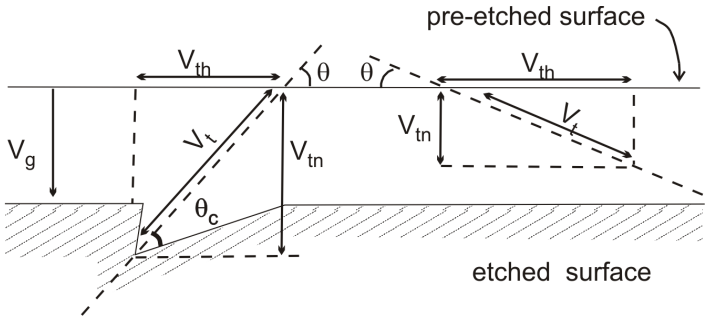

Figure 3.3.2. Principles of Fission Track Etching (after Fleischer and Price, 1964). In order to be revealed by the etching process, the normal component V_{tn} of the track-etching rate V_t must exceed the bulk-etching rate of the material V_g. Taking into account that $V_{tn}=V_g\sin(\theta)$, this implies that the critical angle of incidence θ_c of the track must exceed $\arcsin(V_g/V_t)$. The track at the right does not meet this criterion and is not revealed by etching. The difference between the etching rates determines the shape of each etch pit. In glass and metamict minerals, where V_t is usually only slightly larger than V_g, the etch pit is broad and shallow. Etch pits in most minerals are instead typically long and narrow. The fraction of tracks crossing a surface that are revealed by etching is termed etching efficiency of that surface. This is high for most minerals, but for glass it is low (<0.5).

The principles of etching are described in figure 3.3.2. Most minerals show anisotropic etch rates, depending on the orientation of the track relative to the crystal lattice. The appearance of a track may thus vary according to its orientation in the plane of the etched surface. In zircon and apatite, the etching efficiency (η) can vary from 100% on sections parallel to the c-axis to close to 0% on sections perpendicular to the c-axis (Naeser et al., 1980). Hence, when dating minerals, the grain surfaces to be used are those parallel to the c-axis. This avoids any possible undercounting problems associated with underetched tracks. These surfaces can be recognized by the parallelism between the orientation of the c-axis and the surface etch pits of the fission tracks. Additionally, such sections can be distinguished in the apatite grains by the presence of sharp polishing scratches on their etched surfaces (refer to figure 3.3.3). In some cases, particularly within zircon grains, it may be possible to observe damaged glass-like areas along their etched surfaces. These are caused by α-recoil associated with the more common α-decay of uranium and thorium. This is a process in which the energy released after the emission of an α-particle causes a recoil in the product nucleus, which in turn destroys the surrounding crystal lattice. This damage may be very severe causing the crystal to become metamict and leading to isotropic etching properties.

3.3.3 Counting of Track Density

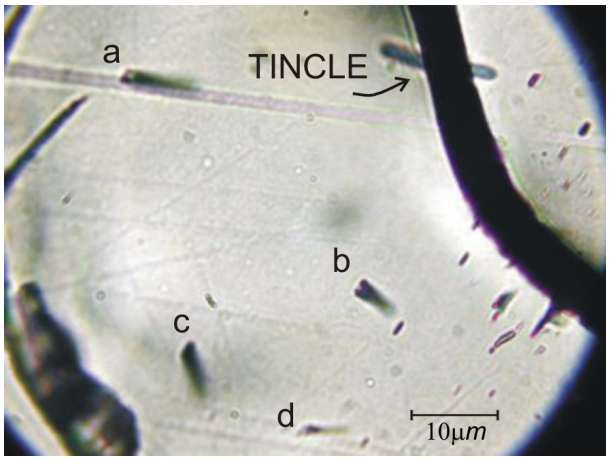

Figure 3.3.3. Photomicrograph of a polished and etched prismatic section through an apatite crystal from this study, showing etched surface-intersecting tracks (a-d) and one horizontal confined track (TINCLE). The acid etchant reached the confined track through a large fracture.

Track counting under the microscope is carried out by a human observer who uses a square grid mounted in one of the oculars. This grid serves as a unit-counting area and is calibrated against a stage micrometer. When dating a sample using the external detector method (chap. 3.3.6), it is of major importance to count the induced tracks in an area of the detector image, which exactly matches the area of the grain that was scanned for spontaneous tracks. A motorized microscope stage helps to accomplish this task efficiently in a rapid and accurate way. Spontaneous and induced tracks of the same sample or grain are counted consecutively. Both very low ($<10^3$ tr/cm^2) and very high ($>10^7$ tr/cm^2) track densities are difficult to determine precisely (see figure 3.2). At high densities, tracks overlap each other and, in addition, care should be taken not to count confined tracks (especially TINTS, figure 3.3.4). Confined tracks do not crop out in surface (figure 3.3.4). At high track densities, the visibility of a surface etch pit from a single fission track may be obliterated by the presence of tracks in the vicinity, thus inducing overcounting errors. The use of reflected light shows the surface outcrop of the tracks, and can be helpful here.

3.3.4 Fission Track Length Measurements

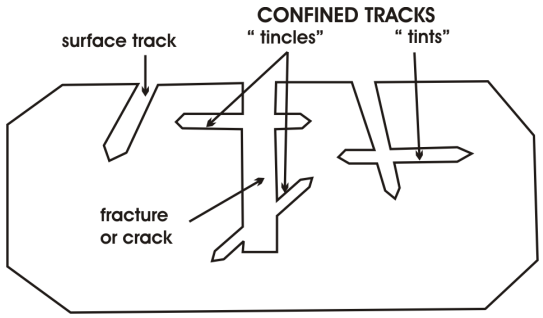

Figure 3.3.4a: Schematic section through an apatite crystal illustrating different types of confined tracks (after Gleadow et al., 1983)

Fission track lengths are measured on horizontal confined tracks. Confined tracks are those entirely below the surface (e.g. Bhandari et al., 1971; Laslett et al., 1982). The etchant reaches these tracks through some conduit, such as cracks or cleavage (TINCLES; McDougall et al., 1971)) or intersection of other tracks (TINTS, Lal et al., 1968). Confined tracks are readily identified as they show a strong backscattered image in reflected light and tend to be more or less simultaneously in focus along the total length (see figure 3.3.4). Tracks lengths are typically measured using a digitalizing tablet, with a cursor equipped with a high-intensity light-emitting diode (LED). The image of the LED can be seen in the microscope via a drawing tube attachment. By calibrating the

digitalizing tablet against a stage micrometer, it is straightforward to measure the length of individual tracks observed under the microscope.
In addition to measuring the length, it is becoming common practice to measure the angle of the track with respect to the crystallographic c-axis (Laslett el al., 1982; Green et al., 1986; Gleadow et al., 1986; Donelick et al., 1990). This is because both the etching and the track shortening processes can be anisotropic with respect to the crystallographic axes (see chapter 3.4). Typically, 50-100 individual track length measurements are made, with a precision of up to 0.2 μm (Green et al., 1986). These data are usually reported in terms of a representative track length distribution with its mean standard deviation, accompanied graphically by a histogram binned at 1μm intervals.

3.3.5 Irradiation

Irradiation of the samples should be carried out in a well-thermalised reactor facility, in order to avoid epithermal-neutron induced fission of ^{232}Th and ^{238}U, producing tracks indistinguishable from thermal-neutron induced ^{235}U. Since the U/Th ratio of samples is highly variable, large errors may be produced in induced track densities by using a poorly thermalised flux.

The cadmium ratio (CR) is defined as the ratio of the activity of a base monitor to that of a monitor enclosed in cadmium, when irradiated in identical conditions. Knowledge of the CR (which can be experimentally measured) allows the observed activity to be broken down into that of epithermal and thermal neutrons (Green and Hurford, 1984). No exact assessment of thermalisation has been agreed on, but Green and Hurford (1984) propose a minimum permissible CR of 3 for Au monitors, 48 for Cu and 24 for Co, and that cadmium ratios for the reactor facility should be reported.

Fluence monitors, typically made from specially manufactured glass, should be used in each radiation, to safeguard against changes in thermal neutron flux in the irradiation facility. The importance of spatial flux gradients should be assessed, and the final arrangement of samples for irradiation arranged so that either the fluence monitors and the samples are irradiated precisely with the same fluence, or a fluence gradient can be obtained for each sample by interpolation within the known form of the variation. The former is much preferred. It is advantageous to include at least two different fluence monitors in each irradation, so that the consistency of the chosen fluence calibration can be monitored continuously over many irradiations.

The choice of which glass to use during the irradiation is largely determined by the uranium content of the mineral being used to provide a countable track density. High U minerals, such as zircon, require a low neutron fluence dose to induce fission of ^{235}U. Thus, a high U concentration glass is used to register the induced tracks. For materials with lower uranium concentration, such as apatite, the required neutron fluence dose is higher and a glass with a low U concentration is used. Suitable high-uranium glasses include CN-1 (39 ppm natural U), and CN-2 (36 ppm natural U), prepared by Dr. Schreurs at the Corning Institute. Suitable low concentration glasses include CN-5 (11 ppm natural U).

3.3.6 The External Detector Method

This dating method is based on counting spontaneous tracks at an internal surface of an etched mineral and induced tracks at an external detector (usually a low-uranium muscovite mica), which is placed next to the mineral surface during the neutron irradiation (see figure 3.3.6). The external detector registers all ^{235}U fission events induced within an identical area corresponding to the adjacent mineral. The mica is subsequently etched and both spontaneous and induced tracks counted and recorded as data pairs.

The main advantage of this procedure is that it accounts for any inhomogeneous uranium distribution within an individual crystal. It also allows a better selection of individual crystals, so that any badly etched, poorly orientated, and inclusion- or dislocation-rich crystals can be excluded from the analysis.

The main disadvantage is related to geometrical differences in the contact zone between an internal mineral surface and the external detector (Gleadow and Lovering, 1977; Green and Durrani, 1978). A fission track intersecting an internal surface of a crystal could have been produced within a sphere of influence with a radius of half its length (4π geometry). However, a track induced in the external surface must be the product of fission decay from the adjacent crystal, in effect from anywhere within a hemisphere (2π geometry). It has been thus assumed that a geometry factor of 0.5 in the age equation will correct this difference (chap. 3.3.7). Experimental results have demonstrated that this is valid only for mineral surfaces with low bulk etch rates (Naeser et al., 1980). Such crystals possess a high etching efficiency, closely resembling the etching efficiency of the muscovite detector, which approximates 100% (chap. 3.3.2).

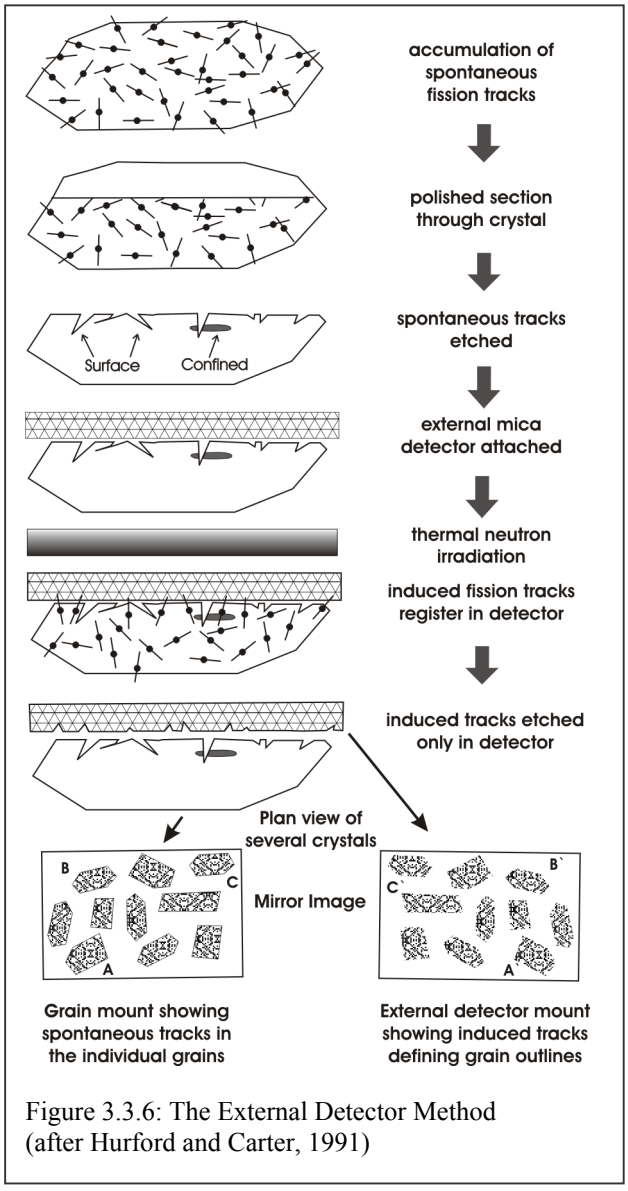

Figure 3.3.6: The External Detector Method (after Hurford and Carter, 1991)

3.3.7 The Fission Track Age Equation

Like any other radioisotopic system, the fission track age equation is based on the law of radioactive decay: the rate of decay of an unstable radioactive nuclide is proportional to the number of atoms of that nuclide, N_t, which remain after a time interval t,

$$dN_t/dt = -\lambda N_t , \qquad (3.3.1)$$

where λ is the decay constant (expressed in a^{-1}), representing the probability that the nuclide will decay after a given period of time t. Integration of this equation while taking into account that $(N_t)_0$ is the original number of atoms at the time t = 0 yields

$$N_t = (N_t)_0 \, e^{-\lambda t} , \qquad (3.3.2)$$

which is the general formula for describing the number of radioactive nuclei remaining after time t. The number of decay events (D_t) which have occurred after time t is given by:

$$D_t = (N_t)_0 - N_t \qquad (3.3.3)$$

Thus, eq. (3.3.2) can be arranged more conveniently in the form:

$$D_t = N_t(e^{\lambda t} - 1) \qquad (3.3.4)$$

The radioactive nuclide ^{238}U decays both by α-emission, eventually forming ^{206}Pb, and spontaneous fission. Each process has a specific decay constant that can be summed up to give λ_D, the total decay constant for ^{238}U. Because λ_f (fission decay constant) is known to be six orders of magnitude smaller than the λ_α (α-decay constant), it is assumed that $\lambda_D \approx \lambda_\alpha$ (Thiel and Herr 1976). Thus, for the total decay of ^{238}U, eq. (3.3.4) reads:

$$D_t = N_t(e^{\lambda_D t} - 1) , \qquad (3.3.5)$$

and the small fraction of events due to spontaneous fission, D_s, is given by:

$$D_s = (\lambda_f/\lambda_D)N_t(e^{\lambda_D t} - 1) \qquad (3.3.6)$$

Eq. (3.3.6) gives the number of fission events that have taken place over time t in a material containing N_t atoms of ^{238}U. Provided the material contained no fission tracks at the beginning of time t and that it has lost no fission tracks through annealing, it will now contain D_s spontaneous fission tracks and t will be its fission track age.

The number of fission tracks per unit volume, D, can be measured from the area density of etched fission tracks, ρ, on a detector surface of the uranium-bearing material (figure 3.3.7). Only a fraction of the fission events within one fission track

range of the surface will actually intersect it to give an etchable track. This fraction can be expressed in terms of an effective distance from the etched surface, R, within which every fission event is registered as an etchable track.

The number of fission tracks per unit volume, D, situated within a layer of unit area and elementary thickness dz, is given by $D \cdot dz$. When this layer is situated at a distance z ($\leq R$) from the detector surface, only the tracks that make a dip angle $\theta \geq \arcsin(z/R)$ will cut the surface (figure 3.3.7). The probability P(z) of a track for intersecting this surface is therefore given by:

$$P(z)=2\pi Rh/2\pi R^2=R(R-\sin\theta)/R^2=1-\sin\theta \qquad (3.3.7)$$

The fraction number of tracks that cut the detector surface is thus given by $D \cdot (1-\sin\theta)dz$ and the areal track density, ρ, is obtained from

$$\rho = \int_0^R D(1-\sin\theta)dz = \int_0^R D(1-z/R)dz = D \cdot R/2 \qquad (3.3.8)$$

In the case when the investigated surface is situated within the volume of the insulating sample, tracks can originate from nuclei at both sides of the surface, and the density will be given by

$$\rho = D \cdot R \qquad (3.3.9)$$

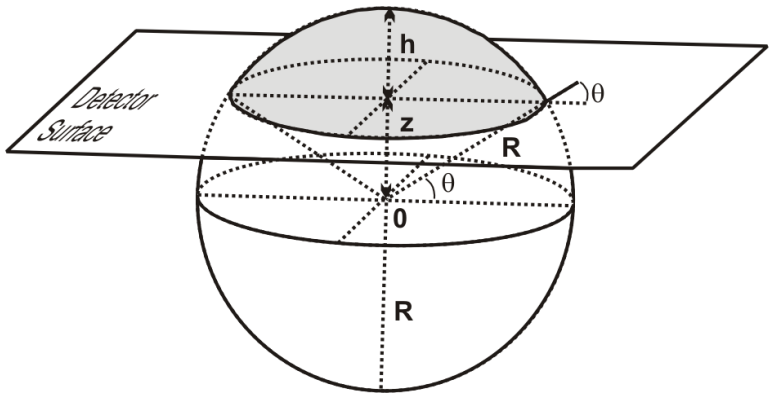

Figure 3.3.7 Spatial and Areal Density of Fission Tracks (from Wagner and Van den haute, 1992) When an atom situated at point 0 and depth z beneath the detector surface fissions, only a track whose upper end falls in the hatched zone of the sphere with radius R will cut the surface (R is the length of one fission fragment). The probability of a track cutting the detector surface is defined as the area of the sphere zone/ the area of the semi-sphere representing all possible orientations, i.e. $P(z) = 2\pi Rh/2\pi R^2$.

Thus, both of the above equations can be combined into

$$\rho = g \cdot D \cdot R\,, \qquad (3.3.10)$$

in that g represents the geometry factor and, depending upon whether the observed surface is internal or external, g =1 (so-called 4π geometry) or g =0.5 (2π geometry).The track density, ρ, is also influenced by the etching efficiency, η, i.e. the fraction of tracks crossing the surface revealed by etching. Thus the etched fission density on any surface can be rewritten as:

$$\rho = D \cdot R \cdot \eta \cdot g \tag{3.3.11}$$

For the ^{238}U spontaneous fission track density, ρ_s, equations (3.3.6) and (3.3.10) can be combined to give:

$$\rho_s = (\lambda_f/\lambda_D)^{238}c(e^{\lambda_D t}-1)R \cdot \eta \cdot g_s \tag{3.3.12}$$

where N_t has been replaced by ^{238}c, the number of atoms of ^{238}U per unit volume of the uranium-bearing material. It is possible to determine t from eq. (3.3.12) only if ^{238}c (or ^{238}U) can be evaluated. This is achieved by irradiating the sample in a nuclear reactor with a well-controlled thermal neutron fluence, which induces only fission of ^{235}U (section 3.3.5). The number of thermal neutron induced ^{235}U fissions per unit volume, D_i, can be expressed as:

$$D_i = {}^{235}c \cdot \sigma \cdot \Phi \tag{3.3.13}$$

where ^{235}c is the number of ^{235}U atoms per unit volume, σ is the nuclear cross section of ^{235}U fission induced by thermal neutrons, and Φ the neutron fluence, or time-integrated dose received by the sample, and expressed in neutrons/cm^2. These induced tracks can be etched on an external surface from a detector attached to the sample (figure 3.3.6). Substituting D_i for D in eq. (3.3.11) gives the induced track density, ρ_i, observed on an external surface:

$$\rho_i = {}^{235}c \cdot \sigma \cdot R \cdot \Phi \cdot \eta \cdot g_i \tag{3.3.14}$$

based on the reasonable assumption that R and η are essentially identical for ^{238}U and ^{235}U fission tracks. By taking the ratio of the two track densities from equations (3.3.12) and (3.3.14), the range and etching efficiency terms cancel and we have:

$$\frac{\rho_s}{\rho_i} = \frac{\lambda_f \, {}^{238}c \cdot (e^{\lambda_D t}-1) \cdot g_s}{\lambda_D \, {}^{235}c \cdot \sigma \cdot \Phi \cdot g_i} \tag{3.3.15}$$

Assuming the atomic ratio $^{235}c/^{238}c$ for uranium to be constant in nature (represented by I, table 3.1), and that the spontaneous and induced track densities are measured on internal and external surfaces representing the same etching efficiencies (sections 3.3.2-3.3.6), eq. (3.3.15) can be solved for t to give the general form of the fission track age equation (Naeser, 1967):

$$t = \frac{1}{\lambda_D} \ln\left(1 + \frac{\lambda_D \sigma I \Phi \rho_s}{2\lambda_f \rho_i}\right) \tag{3.3.16}$$

For fission track ages younger than 600 Ma eq. (3.3.16) can be simplified, using the approximation: ln (x+1) ≈ x, when x □ 1:

$$t=\frac{\sigma I \Phi \rho_s}{2\lambda_f \rho_i} \qquad (3.3.17)$$

The fission track age equation follows four fundamental assumptions:

a) The spontaneous fission decay constant ^{238}U is invariant with time and unaffected by chemical and physical conditions. This is substantiated by the similarity of ages obtained by other methods.

b) The material being dated has remained a closed system with respect to fission tracks and uranium since formation and the only change in the ratio of ^{238}U to fission tracks has resulted from radioactive decay. This means first that the fission tracks once formed must be stable over the lifetime of the material recording them. This depends strongly upon the geological history of the sample. Second, there must be no migration of uranium in or out of the track recording material, for example by interaction with hydrothermal fluids.

c) The isotopic abundance ratio of $^{235}U/^{238}U$ is constant in nature. This assumption is probably valid for normal geological materials, with very few exceptions being known (section 3.1).

d) All spontaneous and induced tracks result exclusively from the spontaneous fission of ^{238}U and the induced fission of ^{235}U respectively (see discussion in section. 3.1).

The values of λ_D ($1.55125\ 10^{-10}$ a^{-1}; Jaffey et al., 1971) and I ($7.2527\ 10^{-3}$; Cowan and Adler, 1976) are accepted and recommended by the IUGS Subcommision on Geochronology (Hurford, 1990). No general agreement has been reached yet over the values of λ_f and Φ (Hurford, 1986). These are briefly discussed in the following sections.

3.3.8 The Problem of the Decay Constant of ^{238}U Spontaneous Fission, λ_f

Since the discovery of the spontaneous fission of ^{238}U, numerous determinations of the decay constant λ_f have been carried out. Two different types of procedures have been followed: direct measurements with ionisation chambers or rotating bubble chambers, and radiochemical methods including the accumulation of natural fission tracks in micas or other detectors, followed by analyses of samples of a known age. Clusters of values for λ_f ranging around $7\cdot10^{-17}$ a^{-1} have been reported by track accumulation experiments (e.g. Thiel and Herr, 1976). In contrast, direct measurements yield values around $8.5\cdot10^{-17}a^{-1}$ (e.g. Segre, 1952; Galliker et al., 1970; Bigazzi, 1981). This difference between the two measured values of λ_f has created in the past scepticism to the reliability of the fission-track method as an absolute geochronometer. Hurford and Green (1982) have also noted that most λ_f determinations using track accumulation experiments and the fission track dating of

material of known age have employed thermal neutron irradiation procedures to determine the uranium content of the fission source. Thus, the method and accuracy of the neutron dosimetry set limits in addition to those related to the uncertainty of the physical decay constant.

3.3.9 The Problem of the Absolute Measurement of the Neutron Fluence (ϕ)

Two methods are available for fluence measurement. Firstly, the neutron-induced γ activity in a metal activation foil of gold, copper or cobalt may be counted electronically after the irradiation. Precise knowledge of the activation cross-section, the mass of the activation foil, and the efficiency of the detection system enables the system to be calibrated (Green and Hurford, 1984). Secondly, a fission track technique can be employed, using a uranium-bearing glass, with the neutron-induced ^{235}U fission events being recorded in an adjacent mica or plastic detector. Since the detection efficiency of such fission track systems is poorly known, they must be calibrated prior to their use on a routine basis.

Hurford and Green (1982) demonstrated that an absolute, unique neutron fluence value is exceedingly difficult to define, even if the flux is extremely well thermalised. The 20% disparity in measured λ_f decay constants cannot be isolated from neutron fluence measurement. This problem has given rise to the use of the ζ calibration factor in the fission track age equation, as discussed below.

3.3.10 The ζ Calibration in Fission Track Analysis

In the 1970's, in order to overcome the dispute about the value of λ_f, a dating system was proposed in which the age of a sample was determined from a comparative analysis with one or more age standards (Fleischer and Hart, 1972; Fleischer et al., 1975). Later, because of the doubt that was cast on the accuracy of absolute neutron fluence determinations, this approach was elaborated and has become strongly advocated by several fission track geochronologists (Hurford and Green, 1982, 1983).

Age standards are materials whose geological age is known or can be confidently inferred, and which satisfy specific requirements for reliability, unambiguity, and homogeneity (Hurford and Green, 1981). These criteria are best met by rapidly cooled volcanic rocks showing no post-depositional alteration. Recommended standards for apatite and zircon are cited in Hurford (1990a, 1990b). A list of the age standards used for this study is shown in table 3.3.9.

The procedure is divided into two stages. In the first step, age standards are repeatedly irradiated and analyzed together with an uranium-bearing glass monitor to establish a personal calibration factor ζ. The track density in the glass monitor ρ_m is proportional to the fluence Φ:

$$\Phi = B \cdot \rho_m \qquad (3.3.18)$$

B being the proportionality factor, expressed in (neutrons/track). The B factor is obtained from track counting in the glass monitor (or the adjacent mica). It may vary by differences in track revelation and observation, and it depends as well on the response of the glass monitor to the neutron fluence.

The fission decay constant λ_f, the $^{235}U/^{238}U$ ratio I and the ^{235}U nuclear cross-section σ, can be replaced in the FT age equation by the calibration factor ζ:

$$\zeta = (\sigma I B)/ \lambda_f \,, \qquad (3.3.19)$$

expressed in $(a \cdot cm^{-2})$

By substituting ζ into the fission track age equation 3.3.16 (evaluated for t_{St}), we obtain:

$$\zeta = \frac{e^{\lambda_D t_{St}} - 1}{2\lambda_D \, (\rho_s/\rho_i)_{St} \, \rho_m} = \frac{I\sigma B}{\lambda_f} \qquad (3.3.20)$$

Once the ζ-factor has been evaluated, ages of unknown samples can be determined after co-irradiation with the corresponding glass monitor, from the equation:

$$t = \frac{1}{\lambda_D} \ln\left(1 + \frac{\lambda_D}{2} \zeta \left(\frac{\rho_s}{\rho_i}\right) \rho_m\right) \qquad (3.3.21)$$

For each dosimeter glass a range of ζ values for individual minerals are determined using different age standards from several irradiations. Such values vary between individuals and should be used only by the individual analyst concerned. A specification of the age determination and data reporting has been the subject of a report to the International Union of Geological Sciences Subcomission on Geochronology (Hurford 1990a, 1990b).

Table 3.3.10 Age Standards Applied for Fission Track Dating in the Present Study
(from Wagner and Van den haute, 1992)

Reference Material	Geologic specification (Region, Country)	Age (Ma)	Reference
Apatite Zircon	Fish Canyon Tuff (San Juan Mts., Colorado)	Tst=27.8 ± 0.2 [Tst=27.9 ± 0.7]	Hurford and Hammerschmidt (1985) [Steven et al. (1967)]
Apatite Zircon	Mt. Dromeday Bananite (NSW, Australia)	Tst=98.7 ± 0.6	Williams et al. (1982) Green (1985)
Apatite	Durango Iron Deposit (Co. de Mercado, Mexico)	Tst= 31.4 ± 0.5	McDowell and Keizer (1977)
Zircon	Buluk Member Volc. Tuff (N. Kenya)	Tst= 16.4 ± 0.2	McDougal and Watkins (1985)
Zircon	Tardee Rhyolite (Northern Ireland)	Tst= 58.7 ± 1.1	Hurford et al. (unpubl.)

3.4 Statistical Analysis of Fission Track Data Sets for the External Detector Method.

In the external detector method, counts of the spontaneous and induced tracks are obtained in pairs, the induced tracks being counted in an area that exactly matches the area used for the spontaneous track counting. As a consequence, each grain yields an individual ρ_s/ρ_i ratio, and hence its individual fission track age. The precision of a single grain age is calculated using conventional Poisson statistics. For an individual rock sample, the fission track age is reported as some kind of average estimate of 20 to 40 single grains. There are three kinds of age estimates in common use: the "mean", "pooled", and "central" ages. The pooled age is simply the sum of the spontaneous counts divided by the sum of induced counts, while the mean age is the arithmetic mean of the individual ratios of spontaneous to induced counts. The latter has been used when the distribution of counts are inconsistent with purely Poissonian variation. The central age is a more recent development, which essentially consists in the geometric mean of the population grain age. Overall, the central age is the preferred age estimate, as it is more robust to geologic outliers and non-Poissonian variations. These topics are extended in the following sections.

3.4.1 Precision of the Fission Track Age

The precision of a fission track age is determined by the precision of the track density ratio R ($=\rho_s/\rho_i$) of spontaneous to induced tracks and the determination of the neutron fluence Φ. The conventional relative error on t is given by (Green, 1981a):

$$\sigma(t)/t = K\sqrt{(\sigma(R)/R)^2 + (\sigma(\Phi)/\Phi)^2} \qquad (3.4.1)$$

where $\sigma(R)/R$ and $\sigma(\Phi)/\Phi$ are the relative errors on R and Φ, respectively, and K represents a correction coefficient which allows for the decay of uranium during time t (after Johnson et al., 1979):

$$K=\lambda_d/t(1-e^{-t/\lambda_D}) \qquad (3.4.2)$$

$K \approx 1$ for samples with a fission track age younger than 600 Ma. The relative error on R is calculated with the use of conventional Poisson statistics, given by:

$$\sigma(R)/R = \sqrt{(1/N_s) + (1/N_i)} \qquad (3.4.3)$$

where N_s and N_i are the spontaneous and induced tracks counted in a surface of equal area A. The error on Φ is generally smaller than the error on R and includes all uncertanties related to system calibration. In the case where the ζ–age standard approach is used, $\sigma(\Phi)$ refers mainly to the error on the track density ρ_m of the monitor glass irradiated together with the sample. This also follows a Poisson distribution, so that $\sigma(\rho_m)=\sqrt{N_m/A_m}$, where N_m is the sum of tracks and A_m the total area counted in a dosimeter glass or its detector. The error on ζ is less important, since after calibration with several standards, it can be evaluated with a precision of 1.5%

(1σ). For practical purposes, where N >20, and t < 600 Ma eq. (3.4.1) can be simplified to:

$$\sigma(t) = t\sqrt{(1/N_s) + (1/N_i) + (1/N_m)} \tag{3.4.3}$$

which represents the form of error assessment used by most fission track chronologists.

3.4.2 The Chi-Square Test and the Mean Age Estimate

When calculating a FT age using the external detector method, the uranium variation between grains should bear no influence on the individual ρ_s/ρ_i ratios. Thus, no variation of these ratios should be expected apart from the random variation governed by the Poisson statistics. However, experimental data and sample problems often show that this is not the case (e.g. Green, 1981a; Burchart, 1981). To allow a detection of this variation, a χ^2 test has been developed (Galbraith, 1981a,b; Green, 1981a). The calculation (with n-1 degrees of freedom) uses the formula:

$$\chi^2 = \sum_{j=1}^{n} \frac{(N_{sj} - \hat{N}_{sj})^2}{\hat{N}_{sj}} + \sum_{j=1}^{n} \frac{(N_{ij} - \hat{N}_{ij})^2}{\hat{N}_{ij}} \tag{3.4.4}$$

where N_{sj} and N_{ij} are, respectively, the number of spontaneous and induced tracks in the jth grain, and where:

$$\hat{N}_{sj} = \frac{N_s}{N_s + N_i}(N_{sj} + N_{ij}), \quad \hat{N}_{ij} = \frac{N_i}{N_s + N_i}(N_{sj} + N_{ij}), \tag{3.4.5}$$

When an analysis fails the χ^2 test at the 5% level, a method of assessment is required which makes allowance for this extra-Poissonian source of error. Green (1981a) suggested to calculate t using the mean of each individual crystal ratio (ρ_s/ρ_I), given by:

$$\text{Mean}\left(\rho_s/\rho_i\right) = \sum_{j=1}^{n} \frac{(\rho_s/\rho_i)_j}{n} \tag{3.4.6}$$

with its own standard deviation $\sigma(\rho_s/\rho_I)$:

$$\sigma(\rho_s/\rho_i) = \frac{1}{n(n-1)} \sqrt{\left\{ \sum_{j=1}^{n} (\rho_s/\rho_i)_j^2 - \left[\sum_{j=1}^{n} (\rho_s/\rho_i)_j^2 \right]^2 \right\}} \tag{3.4.7}$$

This yields the sample mean age, an estimate similar to the conventional analysis, but with a larger corresponding error, as a result of additional uncertainty in the data set.

To apply the χ^2 test in an appropriate way, a large number of counted grains is required, which may often not be available in FT analysis. As well, its algorithm requires the data to be binned into intervals that may not be representative of the sample's information. Skézely (2002) has recently proposed an alternative technique,

based on the Kolmogorov-Smirnov test, which is still not common in the field of FT analysis. This technique can be applicable having less data, and is simpler, since it does not need any binned data.

3.4.3 The Central Age and Age Dispersion

Because fission track density depends on the mean track length, a spread in ages within a sample is often caused by thermal annealing when there is compositional variation between the grains (chap. 3.5; Green et al., 1986, 1989). Considering this problem, a random effects model (Galbraith and Laslett, 1993) has been designed; whose parameters describe the location and spread of the grain ages within a sample grain population.

In the random effects model, it is assumed that for the sample grains the values of $\ln(\rho_s/\rho_i)$ follow a Normal distribution with mean μ and standard deviation σ; and that for each value of $\ln(\rho_s/\rho_i)$, the corresponding N_s has a binomial distribution with index N_s+N_i and parameter $\rho_s/(\rho_s+\rho_i)$. The parameters σ and μ correspond to the standard deviation and mean of $\ln(\rho_s/\rho_i)$ for the whole grain population. σ is defined as the age dispersion, and the age t that corresponds to μ the central age, i.e. the age t corresponding to e^{μ} in the age equation (3.3.16). Because ρ_s/ρ_i is, to a close approximation, proportional to t (eq. 3.3.17), the age dispersion is the relative standard deviation of the population ages (expressed as a percentage) and the central age is the population geometric mean age. Thus, the central age and age dispersion describe together the distribution of the population ages.

The random effects model specifies a probability for any observed sample of counts, so it is possible to estimate the unknown parameters of σ and μ and their precisions by maximum likelihood. The formula of the likelihood function and its calculation (which is simplified in an iterative algorithm) are described in Galbraith and Laslett, (1993).

An age dispersion with a value of above 20% is taken as indicating that the sample has a mixed age. For small values of σ the central age estimate resembles the pooled age, but with a slightly larger standard error. The advantage of this model is that it indicates spreads in the individual crystal ages, often not obvious using the conventional approach. It sometimes happens, particularly when there is a small number of tracks per grain, that data "pass" the χ^2 test even when there is over-dispersion. However, as with any model, it will not always be appropriate, and its parameters will not always be meaningful. In particular, if some grains in the sample have been completely annealed (what can happen to fluorapatites), while others have not, then it is of more interest to estimate the age of these rather than the central age. In the next section a generalized model is dealt with to account for this problem. The central age approach is the actual recommended standard for the statistical calculation of fission track ages, and therefore applied in this study.

3.4.4 Models for Mixed Ages

When a sample consists of crystals with mixed ages, termed a finite mixture, the use of a single mean and error is meaningless. It is more useful to make an estimate of the component ages within the finite mixture. Mixed distributions are expected from samples that have "detrital" FT ages, such as sandstone with unreset zircon FT ages. In this case, the grain ages preserve the information about cooling history of the source region from which zircons were eroded, assuming that the sandstone has remained cool enough after deposition to preserve these ages. Discordant FT age distributions are also encountered in reset samples. In some cases, discordance is taken as evidence for partial resetting, but more often the cause is differential resetting of grains with different annealing properties (refer to chapter 3.5).

Various methods are available for estimating components in a grain-age distribution (Seward and Rhoades, 1986; Galbraith and Green, 1990; Brandon, 1992; Galbraith and Laslett, 1993; Sambridge and Compston, 1994; Brandon, 1996). Galbraith and Laslett (1993) introduced the minimum age concept, which informally represents the pooled age of the largest concordant fraction of young ages in the fission track grain age distribution. For reset rocks, the minimum age represents the time of closure for that fraction of grains with the lowest retention for fission tracks, such as fluorapatites in apatite FT dating (e.g. Brandon et al., 1998) and radiation-damaged zircons in zircon FT dating (e.g. Brandon and Vance, 1992).

Component ages within a sample can also be easily discerned by using graphical methods. One way to plot the age estimates is on a weighted histogram of age vs. frequency, taking into account the differing standard errors (e.g. Hurford et al., 1984; figure 3.4.3a). Another form is on a radial plot (Galbraith, 1988, 1990; figure 3.4.3b), which allows discriminating between the uncertainty of individual crystal ages and the variation between the ages of individual crystals.

A program for estimating components in a mixed distribution of fission track ages, BINOMFIT (Brandon, 2002), is used in this study. Its algorithm is based on the binomial peak-fitting method of Galbraith and Green (1990). In general lines this consists in searching the best fit solution by directly comparing the distribution of the grain data to a predicted mixed binomial distribution, estimated by maximum likelihood. The best-fit peaks are reported by age, uncertainty, and size. The uncertainty of the individual peaks is given at 68% and 95% confidence intervals. The size of the individual peaks is reported as a fraction (in percent) and as a count (number of grains).

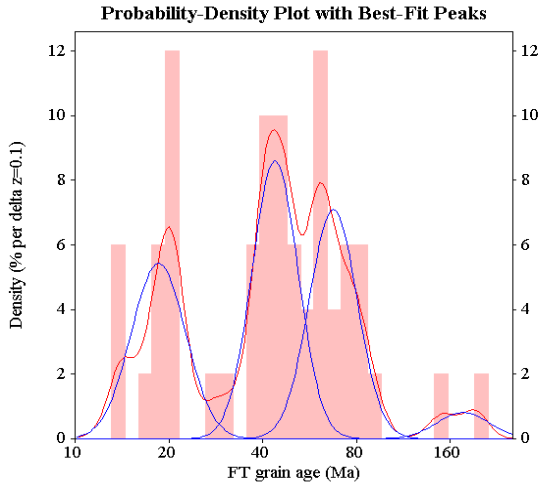

Figure 3.4.3a: Example of a combined histogram and probability density plots (red line), with best-fit peaks (blue line), obtained with the program BINOMFIT (Brandon, 2002). 3 peak solutions are shown for the age components of the mixed detrital zircon FT sample from Mount Tom in the Olympics Mountains (Brandon and Vance, 1992). The histogram in the background is scaled to the same density as the density plot. Histogram bars have an approximate width of 10% of their age, explaining the constant width on the logarithmic scale (i.e., $\Delta z = 0.1$; see Brandon 1996 for details).

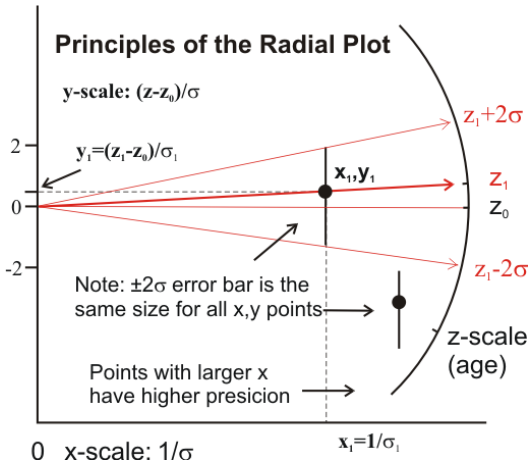

Figure 3.4.3b: The Radial Plot (Galbraith 1988, 1990) Each point or age has a unit standard error that can be read off the y-scale and a precision (increasing to the right) represented on the x-scale. The formula used to plot the (x,y) data points allows the age of each point to be represented on a z-scale, whereby the age is simply read through extrapolating a line from (0,0) or 0 on the y-scale through (x,y) and on to the circular z-scale. The central FT age of the sample (z_0) plots as a horizontal line.

3.5 Fission Track Annealing and Cooling Histories

From the very beginning of fission track studies (Fleischer et al., 1965a) it has been known that tracks shorten irreversibly, or anneal, when the host material is at an elevated temperature, as a consequence of a thermally activated diffusion process that is still poorly understood. It is believed that heat input into the damaged mineral lattice causes diffusion of atoms back to their more stable positions. This process seems to progress from the end of the track towards its middle, thus causing a shortening of the track and a decrease of the track density (e.g. Green et al., 1986; Carlson, 1990). As a consequence, thermal annealing induces a reduction in the fission track age, although the relationship between track shortening and track density is complex (e.g. Duddy et al., 1988; Carlson, 1990; Carlson et al. 1999).

The temperature range over which annealing occurs is generally referred to as the partial annealing zone (PAZ, e.g. Naeser, 1981). It varies greatly between minerals and also depends on the cooling rate. The rate of annealing depends on temperature, time, and track length through a strong non-linear relationship, and it is likely that the dominant process changes as annealing progresses (Laslett et al., 1987; Crowley et al., 1991; Laslett and Galbraith, 1996). Annealing characteristics are best known for apatites, although recent research on zircons has improved knowledge of annealing in this mineral (e.g. Tagami et al., 1998; Yamada et al., 1995).

The interpretation of thermochronometric data is usually based on the concept of closure temperature (Dodson, 1973). This refers to the temperature of the system at the time given by its apparent age, and is a function of the cooling rate as well as the mineral composition or its damage structure (e.g. Harrison et al., 1985; Stöckhert et al., 1999). For the fission track system, because of its annealing properties, this statement may result in an oversimplification. Fission track ages should be better understood as a protracted cooling age, since the track length distribution of the studied sample can give additional information about its thermal history within the PAZ. The annealing characteristics for apatite and zircon are extended in the following sections.

3.5.1 Annealing Characteristics of Apatite

In addition to temperature, other factors affecting annealing rates for apatite are the chemical composition, the track's orientation with respect to the crystal lattice, and structural defects within the lattice. The dependence of these factors has been the subject of extensive experimental research and modelling in the past 25 years (e.g. Green et al., 1986, 1989; Laslett et al., 1987; Carlson, 1990; Crowley et al., 1991; Carlson et al., 1999). The basic outcome is a quantitative, although empirical, predictive model of fission track annealing, expressed in terms of the reduction in track length over a particular time interval. The formulation is a fanning-Arrhenius type model, dependent on inverse absolute temperature and log of time.

Extrapolation of the Laslett et al. (1987) Durango apatite model to geological time scales (10^6-10^8 years) predicts a partial annealing temperature range (PAZ) from 60°C to 110°C, with an uncertainty of about 10°C (figure 3.5.1a). This temperature range is consistent with studies of geological samples at their maximum present-day temperatures from deep boreholes (e.g. Gleadow et al., 1983). The 60°C temperature for apatite annealing is a minimum limit for its PAZ, since it is well known that induced tracks in apatite are 1-1.5 μm longer than spontaneous tracks measured since their formation (Green, 1988). Donelick et al. (1990) demonstrated that some annealing of induced tracks in apatite occurs at room temperatures over time-scales of minutes to a few weeks, although the track lengths seem to stabilize after this.

The relative proportions of Cl, F, and OH within the apatite composition ($Ca_5(PO_4)_3(F,Cl,OH)$) also places control on the annealing rates, although there is still debate remaining on how much each of these influence. Cl-apatite has been observed to be more resistant to annealing than F-apatite (Gleadow and Duddy, 1981; Green et al., 1986; Donelick, 1991; O'Sullivan and Parrish, 1995), although Crowley et al. (1991) obtained slightly different results based on annealing experiments on F-apatite. More recently, Laslett and Galbraith (1996) used a slightly different model parametrization than Crowley et al. (1991), which is consistent with the previous observations that F-apatite anneals more easily than the Durango apatite (~0.45 wt% Cl). Contents of OH seem to correlate with Cl, but it is unclear how to generalize resistance to annealing in terms of OH concentration (Ravenhurst et al., 1992; Bergmann and Corrigan, 1996; Ketcham and Donelick, 2000). Recently, Burtner et al. (1994) have presented data relating the degree of annealing to Cl composition and the etching characteristics of apatite (termed "Dpar", quantified in terms of the mean size of the etch pits parallel to the c-axis for each apatite grain).

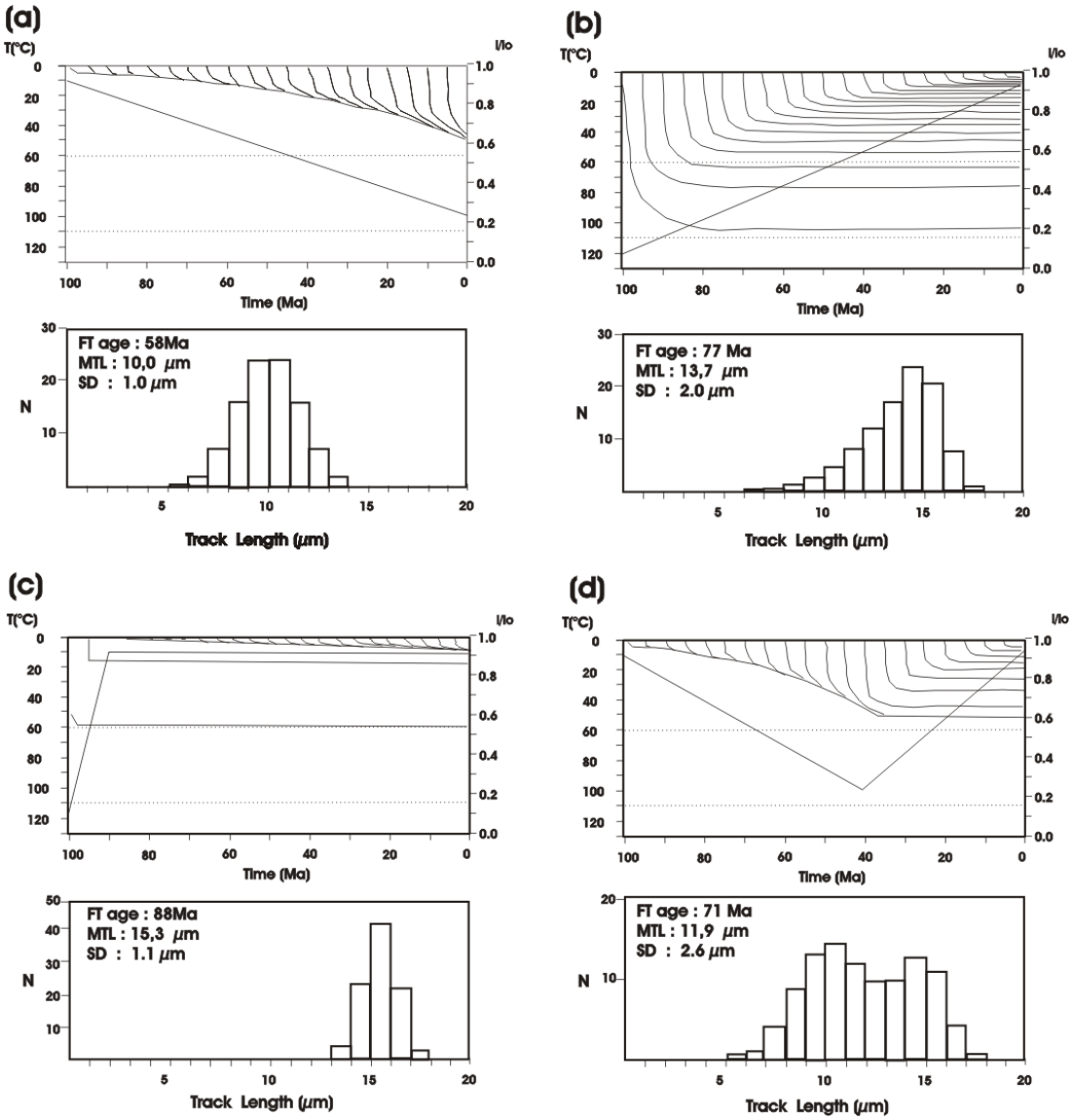

Figure 3.5.1a: Some simple thermal annealing histories (heavy lines in upper panels) and the predicted length parameters (lower panels) for Durango apatite, using the model of Laslett et al. (1987). Calculation procedures are detailed in Duddy et al. (1988), Green et al. (1989), Corrigan (1991), and Crowley (1993). The model simulations consider 20 tracks formed at equal time increments over the total duration of the thermal history. The evolving reduced track lengths are represented as the ratio to the initial track length (l/l_0), shown in the upper right axis of the panel. The two horizontal lines at 60° and 110°C are the typical range of the apatite partial annealing zone (APAZ). a) Linear heating. The track length distribution is unimodal, symmetrical, has a short mean length, and a small standard deviation. b) Linear cooling. Each track experiences a different maximum paleotemperature as cooling progresses, and is reflected in the negatively skewed length distribution. The age does not relate to any discrete event. c) Rapid Cooling. As nearly all tracks are formed after the cooling episode, they all are relatively long. In this case the fission track age is indicative of the timing of the cooling. d) Heating/cooling. The tracks formed during the heating period have similar lengths, while those formed after reflect the progressive cooling. The track length distribution is typically bimodal and the fission track age does not relate directly to the timing of the cooling or the timing of maximum paleotemperature.

A further consideration is the structural properties of the crystal lattice. It has been readily shown that fission tracks parallel to the c-axis shorten more slowly than do tracks perpendicular to it (e.g. Green and Durrani, 1977; Green, 1988). Effects of this anisotropy can be understood in terms of varying activation energy with varying crystallographic orientations. Carlson (1990) developed kinetic equations derived from a physical model of the atomic-scale processes involved in apatite FT-annealing. He proposes that the fundamental controls on annealing are the initial axial and radial distribution of the crystalline damages, and the rate at which these are eliminated. More recently, Barbarand et al. (1996) using cathodoluminiscence spectroscopy, have identified an apparent control in terms of crystal structure, rather than F/Cl composition. They argue that there are controls in addition to the composition effects, such as crystallographic imperfections, and these are reflected in the etch pit geometries.

The most recent development corresponds to a multi-compositional kinetic model for apatites (Carlson et al., 1999; Ketcham et al., 1999), based on the integration of old and new laboratory apatite annealing data with a range of F-Cl compositions, crystallographic orientation effects on annealing, and on new geologic observations from exploration wells. An incorporated software that enables to discriminate thermal histories for different kinetic annealing populations is used in this study and an example shown in figure 3.5.1b (Aftsolve 1.1.3©, Ketcham and Donelick, 2000).

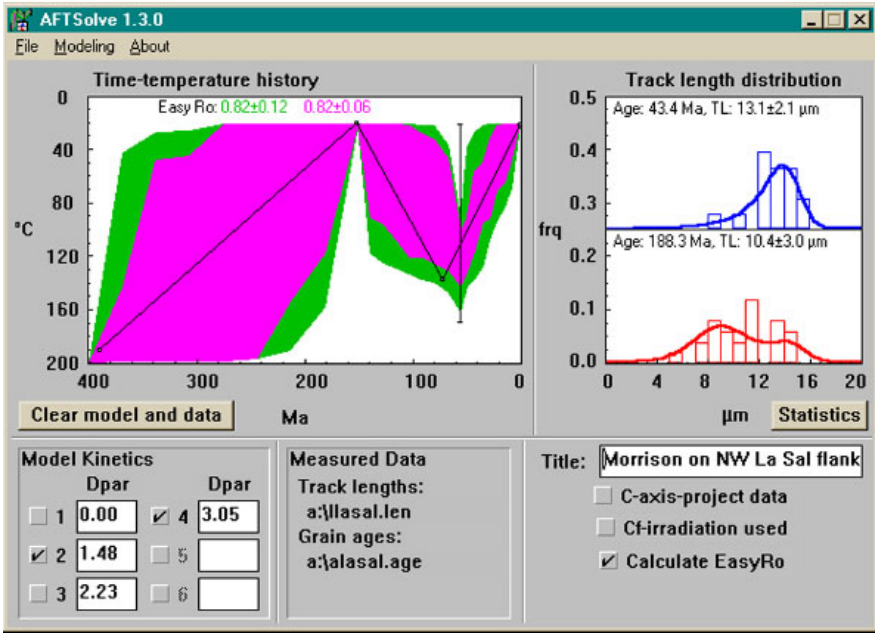

Figure 3.5.1b: Example of inverse modelling from the software Aftsolve© v.1.1.3 (Ketcham and Donelick, 2000). The sample corresponds to a Jurassic formation from the Sal Mountains in Utah. The data fitting dialog box is superimposed after an inverse model has been completed. The time-Temperature history area is located on the upper left box. The resulting coloured regions are envelopes that encompass all fits of their respective types. "Acceptable" fits are green coloured, and "good" fits are magenta. Model kinetics box is located below, indicating 4 different options for the kinematic parameter Dpar, two of them selected for the modelling. The track length distribution data is on the right box. Normalized frequencies (up to 1.0) are in the y-axis. The data is split into two kinetic populations defined by the Dpar variable. Model 1 corresponds to a 54.3 Ma oldest component that survived annealing, model 2 to a 362 Ma age of the oldest FT to survive annealing. The measured lengths are displayed in bars, and curves represent those estimated by forward modelling.

3.5.2 Annealing characteristics of Zircon

Estimating the temperature limits for the zircon partial annealing zone (ZPAZ) is complicated by the effects of radiation damage on the annealing process (e.g. Brandon et al., 1998). Nevertheless, in rocks where zircons are rapidly cooled from high temperatures, little accumulated radiation damage may be expected (Rahn et al., 2000). Tagami et al. (1998), based on experimental work on pristine zircon, developed fanning and parallel kinetic-annealing models, whose Arrhenius-type temperature estimates of the ZPAZ for different heating durations are described in figure 3.5.2.

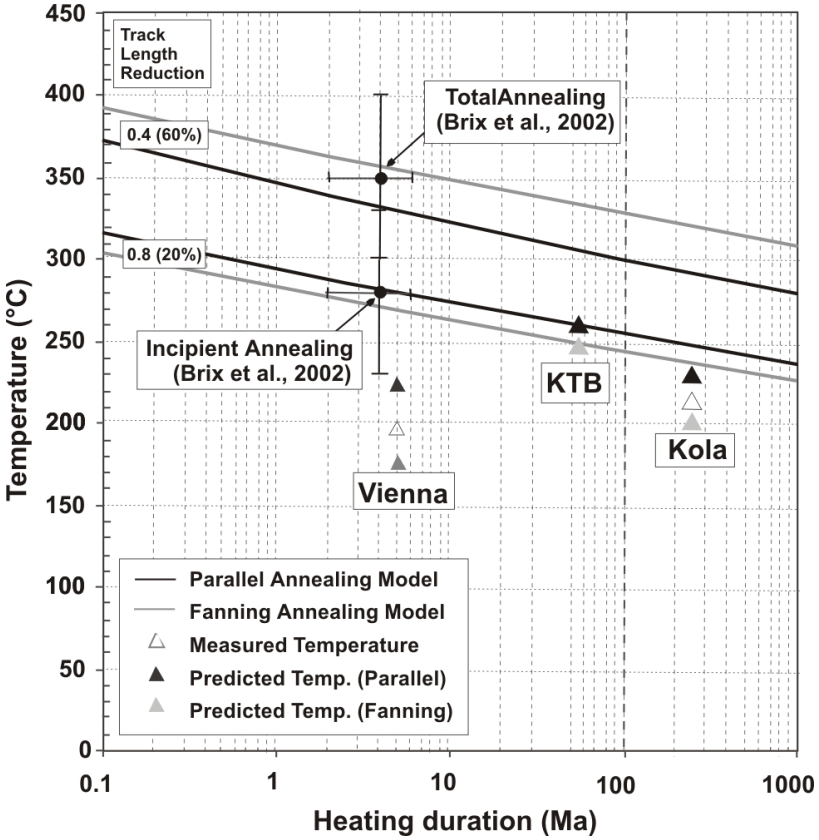

Figure 3.5.2: (after Thomson, 2002) Arrhenius type plot of the temperature limits of the zircon FT partial annealing zone (ZPAZ) against the heating duration, defined by 20% and 60% track-length reduction (Tagami and Shimada, 1996), calculated for both the fanning (grey) and parallel (black) kinetic annealing models of Tagami et al. (1998). Open triangles are the measured temperature and estimated heating duration values from several ultra deep boreholes (KTB, Kola, and Vienna, see text). The grey and black solid triangles are the temperatures predicted by the fanning and parallel kinetic-annealing models respectively, based on the measured track length and estimated heating duration for each borehole. The temperature estimates of the ZPAZ based on fission track results from high-pressure/low temperature metamorphic rocks of Crete (Brix et al., 2002) are shown for comparison.

The ZPAZ is defined by the 20% and 60% track-length reduction isopleths implied by the reduction in FT age across a contact metamorphic aureole (Tagami and Shimada, 1996). Despite the fact that these models have been derived from experiments on zircons with low radiation damage, they are in general agreement to observed track-length data from several ultra-deep boreholes (Coyle & Wagner, 1996; Green et al., 1996; Tagami et al., 1996, Wagner et al., 1997), where temperature and heating

duration are well constrained. Also, independent estimates of the ZPAZ from natural zircons in high pressure/ low temperature metamorphic rocks from Crete (Brix et al., 2002) are consistent with the Tagami et al. (1998) models. For the batholithic rocks of the Southern Andes, Thomson (2002) proposes a ZPAZ within the limits of 250 ± 10 °C to 310 ± 20° C. This is based on the assumption that following intrusion during Cretaceous times, rocks should have maintained relatively stable temperatures for as long as ~50 Ma prior to Cenozoic denudation.

3.5.3 Application of Apatite Annealing Models to Geologic Time Scales

Accepting the basic limitations on chemistry and crystallography of the apatites in the extrapolation of laboratory measurements to geologic timescales, time-Temperature (t-T) histories below ~120°C on time scales of 1 Ma to ~100 Ma can be readily registered by the apatite FT data. Predictive annealing models for apatite allow quantitative reconstruction of thermal histories in the upper 3-5 km of the upper crust of the Earth. These reconstructions can be generalized by forward modelling (e.g. Duddy et al., 1998; Willet, 1992, Crowley, 1993) or, preferably, by some optimization procedure using the observed data as constraints (e.g. Gallagher, 1995; Ketcham and Donelick, 2000).

The important attribute of the fission track system is that it records information over a protracted temperature range, rather than just an estimate of the timing of a closure temperature. In addition, because tracks are being formed continuously, each track records a different proportion of the total thermal history.

3.5.4 Integrating Zircon and Apatite FT Cooling Histories with Different Thermochronologic Methods.

Cooling histories obtained using different radiometric techniques on cogenetic minerals from a single sample often include zircon and apatite fission track ages as low-temperature bounds to a temperature interval of several hundred degrees (e.g. Wagner et al., 1972; Harrison et al., 1979, Zeitler et al., 1982; Hurford, 1986; Hunziker et al., 1992; Hurford et al., 1991a, Stöckhert et al., 1999). An example of this is shown in figure 3.5.4.

Relating a fission track age to a closure temperature is only plausible when it can be demonstrated that no annealing has occurred at post-closure time. This requires monotonic cooling (e.g. Dokka et al., 1986), which should be reflected in the track length distribution (e.g. figure 3.5.4). Even in the absence of a reliable quantitative annealing model, zircon and apatite fission track data allow for qualitative assessment of the validity of inferred cooling rates. The temperature range for the whole integrated cooling system provides valuable information on the time when cooling commenced and the rate at which cooling proceeds.

In synthesis, fission track analysis provides a powerful means of evaluating thermal histories of rocks beyond the conventional geochronologic application. The main parameters of evaluation are the central age and age dispersions, mean track length,

and track length distribution. These data allow to define if the sample has recorded a high or low heat flux, the timing of this event, and the magnitude of its effects. The low-temperature sensibility of the FT data allows its application to a variety of geological problems, including tephrachronology, sedimentary provenance studies, thermal evolution of sedimentary basins, structural evolution of mountain belts, and long-term landscape modelling in anorogenic settings (see Gallagher et al., 1998).

Nevertheless, FT analysis requires systematic sampling directed towards the solution of the specific problem and complementary information from the geology of the area. Well-designed detailed sampling strategies supplied with critical structural information can provide important insight into the evolution of fault systems.

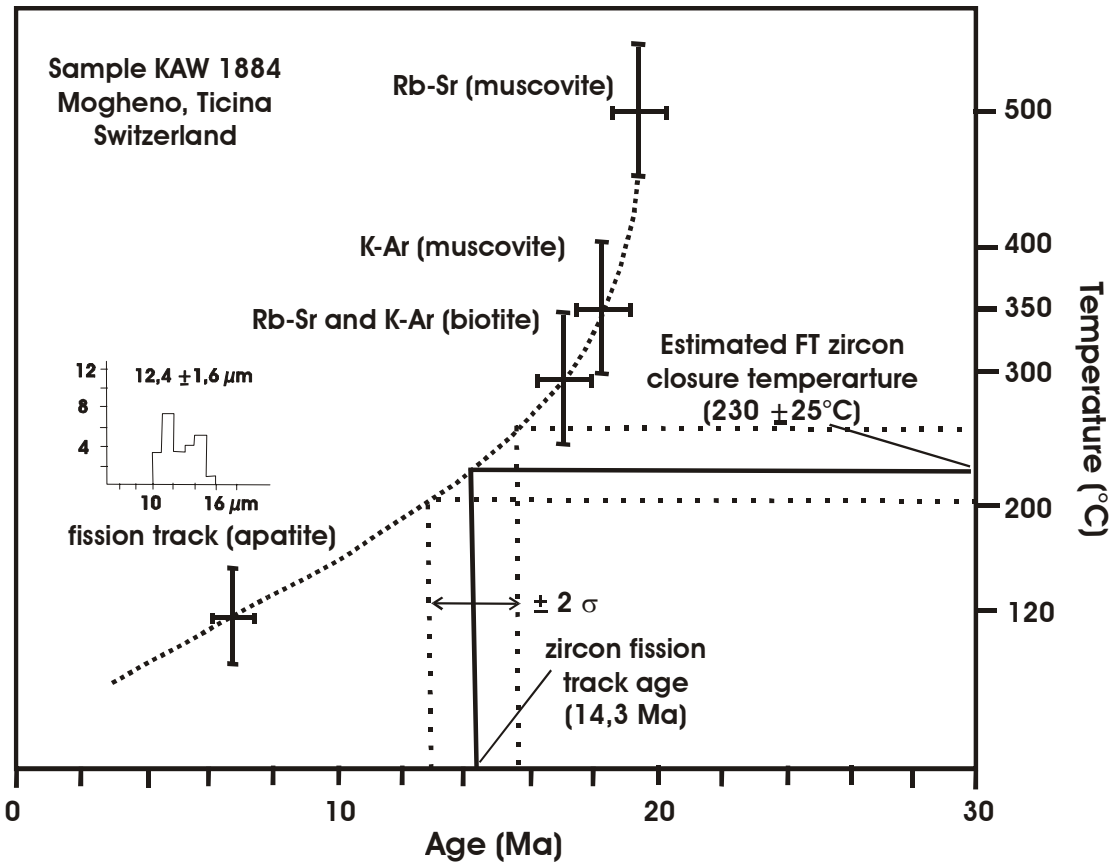

Figure 3.5.4: A cooling curve based on a variety of thermochronometers with different closure temperatures (Hurford, 1986). The confined track length distribution of the apatite indicates that this sample experienced a complex cooling history, which makes the adoption for a closure temperature of 120°C inappropriate.

4 Apatite and Zircon Fission Track Results

4.1 Sample Preparation and Dating Procedure

50 samples from granitoids, dacites, and schists were collected during two excursions to the Chiloé Island, the southern Chilean Coastal Ranges, and in the Reloncaví and Hornopirén sectors of the Main Andean Range. 20 additional samples were provided by the SERNAGEOMIN office in Puerto Varas, Chile. Finally, three additional samples collected and analyzed independently by Manfred Brix have also been included in this study. The field descriptions of the sampled outcrops are included in appendix 2.

Apatite and zircon crystals were separated, mounted, polished, and etched according to the techniques outlined by Hurford et al. (1991). These are discussed in chapter 3.3 and more practical details applied in this study are included in appendix 1.

Fission track samples were analyzed using the external detector method (chap. 3.3.7) and irradiated in the Risø reactor of the National Laboratory at Roskilde, Denmark, and at the Oregon State University TRIGA Reactor, in Corvallis, USA. The neutron fluence was monitored using uranium-dosed Corning glasses CN5 for apatite and CN2 for zircon. Zircon packages (RU21, RU22, and RU24) were irradiated with a total neutron fluence of 1.0×10^{15} n cm^{-2}. Apatite packages (RUA20 and RUA21) were irradiated each with a total neutron fluence of 1.2×10^{16} n cm^{-2}. Fission track densities were counted using a Zeiss Axioplan microscope at 1250 times magnification. Apatite fission track lengths were measured following the recommendations of Laslett et al (1982), using an attached drawing tube and digitizing tablet calibrated against a stage micrometer.

Central ages (Galbraith and Laslett, 1993) were calculated using the International Union of Geological Sciences (IUGS) recommended ζ-calibration approach of Hurford and Green (1983). ζ–calibration factors (chap. 3.3.8) were obtained with the Fish Canyon (apatite and zircon), Durango (apatite), Mount Dromedary (apatite and zircon), Buluk (zircon), and Tardree (zircon) age standards (Hurford, 1990). The values used for the age equations are included in table 4.2, and their calculation details are extended in appendix 3.

4.2 Analytical Results

A total of 63 zircon and 60 apatite fission track ages and 38 apatite length measurements are presented in table 4.2, following the IUGS standard format (Hurford, 1990).

Many of the fission track ages showed some degree of discordance in their single grain age distributions. 10 zircon samples and 7 apatite samples even indicated age dispersions above 20%. These can be regarded as mixed or partially reset ages (chap 3.4.4), since counting errors are expected to follow a symmetrical distribution within the sample, and are usually lower than the variations of the Poissonian distribution of fission decay.

Zircon samples with high age dispersions occur probably because of partial resetting of single grain ages with different annealing properties (e.g. Brandon et al., 1998; chapter 3.5.2). Most of the partially reset zircon FT ages were found along the main trace of the LOFZ, and display evidence for localized heat advection along the fault zone. This may be due to the presence of hot springs, active volcanism, and localized late Miocene to Pliocene plutonic activity within the fault zone. Another possible mechanism of heat advection could be due to rapid denudation along the fault zone, although this would require high rates of erosion (e.g. Mancktelow and Grasemann, 1997).

Apatite samples that display high age dispersions are commonly caused by different annealing characteristics within single grains or by their low uranium contents. Some samples may even show big spread in ages without any clear age components. These result mainly from a chemistry effect, in which grains with a high Cl/F ratio are more resistant to annealing (ref. chap. 3.5.1). Apatites with low uranium contents may not necessarily indicate great spread in their FT ages, but instead display larger errors.
The distribution of the fission track ages and their interpretation in the local geologic context is described separately for each sampled region in the following sections.

Table 4.2 Fission Track Data from the Los Lagos and Chiloé Regions (41°S-43°S)

Sample Number	Location GPS coordinates (South American Provisory Datum, 1956)	Rock Type	Mineral	Number of Crystals	Track Density ($\times 10^6 tr \cdot cm^{-2}$) ρ_s (N_S)	ρ_i (N_i)	ρ_d (N_d)	Age Dispersion ($P(\chi^2)$)	Central Age, Ma ($\pm 1\sigma$)	Apatite Mean Track Length ($\mu m \pm 1\sigma$)	No.of Conf. Tracks	Std. Dev. (μm)
AA1	Lago Llanquihue 41°12'58''S; 72°40'13''W	Granodiorite	Apatite* Zircon*	20 20	0.074 (32) 2.295 (970)	0.762 (328) 2.754 (1164)	1.508 (10415) 0.3906 (5395)	0% (98%) 0% (83%)	24.9 ± 4.7 21.2 ± 1.0	-	-	-
AA2	Ralun 41°22'55''S; 72°18'11''W	Tonalite	Apatite* Zircon*	20 20	0.1665 (69) 1.412 (1026)	9.853 (4082) 2.949 (2142)	1.516 (10467) 0.390 (5386)	0% (99%) 0% (65%)	4.4 ± 0.5 12.2 ± 0.5	13.7 ± 0.21	76	1.79
AA3	E. Reloncaví 41°32'10''S; 72°20'06''W	Tonalite	Apatite* Zircon*	20 20	0.029 (8) 2.958 (3117)	1.342 (367) 5.233 (5514)	1.523 (10519) 0.3903 (5390)	0%(100%) 12%(0%)	5.6 ± 2.0 14.1 ± 0.6	14.81 ± 0.22	26	1.08
AA4	E. Reloncaví 41°36'24''S; 72°23'08''W	Tonalite	Apatite* Zircon*	18 20	0.116 (20) 0.7636 (522)	8.094 (1386) 2.402 (1642)	1.531 (10572) 0.3916 (5408)	0% (97%) 19% (6%)	3.8 ± 0.9 8.0 ± 0.6	-	-	-
AA5	E. Reloncaví 41°36'06''S; 72°21'42''W	Tonalite	Apatite* Zircon*	8 20	0.408 (8) 0.9401(653)	1.489 (292) 2.606 (1810)	1.538 (10624) 0.3791 (5236)	0% (82%) 11%(26%)	7.2 ± 2.6 9.0±0.5	-	-	-
AA6	E. Reloncaví 41°34'14''S; 72°20'45''W	Tonalite	Apatite* Zircon*	20 20	0.054 (18) 0.719(1267)	3.513 (1247) 1.733 (3054)	1.546 (10677) 0.3894 (5678)	14% (53%) 22%(0%)	3.8 ± 0.9 10.5 ± 0.7	14.1 ± 0.29	15	1.08
AA8	E. Reloncaví 41°36'59''S; 72°18'40''W	Granodiorite	Apatite*	20	0.0519 (33)	4.149 (2636)	1.554 (10729)	1% (77%)	3.3 ± 0.6	14.45 ± 0.29	24	1.39
AA9	E. Reloncavi 41°34'02''S; 72°18'32''W	Granite	Apatite* Zircon*	20 20	0.054 (21) 2.238 (5399)	4.162 (1592) 0.6151(1418)	1.561 (10781) 0.3882 (5361)	0% (98%) 1% (60%)	3.5 ± 0.7 91.6 ± 3.3	14.76 ± 0.5	12	1.65
AA10	Cochamo 41°30'33''S; 72°16'35''W	Granite	Zircon*	20	3.973 (5701)	1.329 (1907)	0.3831 (5290)	4% (22%)	74.2 ± 2.6			
AA11	E. Reloncaví 41°26'55''S; 72°19'57''W	Granodiorite	Apatite* Zircon*	20 20	0.0128 (8) 0.6652(1016)	1.052 (655) 2.101 (3209)	1.569 (10834) 0.3875 (5352)	0% (94%) 17% (0%)	3.3 ± 1.2 8.0 ± 0.5	14.18 ± 0.35	21	1.56
AA12	Canutillar 41°30'16''S; 72°20'35''W	Tonalite	Apatite* Zircon*	14 20	0.0658 (10) 0.808 (849)	4.391 (667) 2.045 (1971)	1.576 (10886) 0.3869 (5344)	0% (90%) 4% (48%)	4.0 ± 1.3 10.9 ± 0.5	14.77 ± 0.64	6	1.43
AA13	L.Chapo 41°30'00''S;72°22'39''W	Tonalite	Apatite* Zircon*	16 7	0.2179 (34) 2.359 (303)	12.16 (1897) 0.5069 (651)	1.584 (10938) 0.3863 (5355)	0% (99%) 5% (35%)	4.8 ± 0.8 11.7 ± 0.9	-	-	-
AA14	Chiloe Guabun 41°47'45''S; 74°02'14"W	Micaschist	Apatite** Zircon*	16 14	0.6426 (134) 13.52 (2633)	3.040 (634) 2.188 (426)	1.591 (10991) 0.3890 (5335)	43% (0%) 11% (14%)	67.0 ± 10.7 155.6 ± 10.1	-	-	-
AA17	Chiloe Gamboa Alto	Dacite	Apatite**	20	0.1563 (64)	1.599 (852)	1.599 (11043)	14% (51%)	33.9 ± 3.6	13.66 ± 0.28	30	1.53

	42°51’51”S; 73°51’51”W		Zircon*	20	6.4114 (5464)	4.345 (3864)	0.3923 (5417)	7% (4%)	36.0 ± 12			
AA18	Chiloe Gamboa Bajo 42°27’21”S; 73°50’30”W	Dacitic porphiry	Apatite* Zircon*	20 20	0.1766 (69) 4.901 (4758)	1.331 (520) 3.778 (3668)	1.607 (11095) 0.3785 (5227)	1%(82%) 3% (46%)	36.1 ± 4.7 35.4 ± 1.1	-	-	-
AA19	Chiloe Gamboa alto 42°27’33“S; 73°53’45“W	Micaschist	Zircon*	20	10.36 (5637)	2.218 (1207)	0.3864 (5336)	13%(2%)	117.9 ± 5.9			
AA20	Correntoso 41°27’42”S; 72°37’40”W	Granodiorite	Apatite* Zircon*	16 20	0.0648 (42) 2.824 (2211)	1.604 (1037) 4.698 (3679)	1.614 (11148) 0.3837 (5299)	1%(71%) 2%(50%)	11.1 ± 1.8 15.1 ± 0.5	-	-	-
AA21	L. Chapo 41°25’41”S; 72°37’20”W	Granodiorite	Apatite* Zircon*	20 20	0.0949 (62) 2.236 (2436)	2.283 (1491) 4.527 (4933)	1.621 (11200) 0.3857 (5326)	1% (60%) 14% (0%)	11.4 ± 1.5 12.4 ± 0.6	13.14 ± 0.85	7	2.08
AA22	L. Chapo 41°26’41”S; 72°33’49”W	Granodiorite	Apatite* Zircon*	20 20	0.1536 (105) 2.612 (2211)	3.887 (2657) 5.026 (4255)	1.629 (11252) 0.3857(5327)	6% (57%) 10% (2%)	10.9 ± 1.1 12.9 ± 0.5	-	-	-
AA23	L. Chaiquenes 41°30’38”S; 72°35’44”W	Gneiss	Apatite* Zircon*	20 20	0.1432 (72) 1.267 (560)	4.947 (2487) 3.799 (1679)	1.637 (11305) 0.3851 (5318)	9% (90%) 13% (14%)	8.0 ± 1.0 8.3 ± 0.5	14.29 ± 0.13	100	1.32
AA24	Punta Metri 41°35’20”S; 72°40’32”W	Granodiorite	Apatite* Zircon*	20 20	0.0244 (24) 0.839 (2717)	2.754 (715) 1.494 (3590)	1.644(11357) 0.3758 (5190)	0% (99%) 11% (1%)	9.4 ± 2.0 13.7 ± 0.6	14.54 ± 0.2	85	1.79
AA25	Punta Metri 41°33’33”S; 72°42’27”W	Tonalite	Apatite* Zircon*	20 20	0.0961 (65) 0.829 (913)	2.155 (1458) 1.883 (2072)	1.652 (11410) 0.387 (5345)	0% (92%) 3% (32%)	12.5 ± 1.6 11.1 ± 0.5	14.72 ± 0.14	77	1.26
AA26	Caleta Larenas 41°37’38”S; 72°38’38”W	Tonalite	Apatite* Zircon*	20 19	0.2246 (76) 1.232 (854)	8.134 (2752) 2.992 (2074)	1.66 (11462) 0.385 (5317)	0% (77%) 9% (22%)	7.8 ± 0.9	13.63 ± 0.19	80	1.65
AA27	Caleta Larenas 41°39’24”S; 72°36’23”W	Tonalite	Apatite* Zircon*	20 19	0.2682 (140) 0.688 (978)	8.118 (4238) 1.584 (2251)	1.667 (11514) 0.3826 (5284)	0% (95%) 8% (25%)	9.3 ± 0.8 10.8 ± 0.5	13.77 ± 0.21	100	2.05
AA29	Rio Cochamo 41°28’44”S; 72°15’38”W	Granite	Apatite* Zircon*	20 20	0.0935 (43) 4.924 (6297)	4.849 (2230) 1.848 (2363)	1.675 (11567) 0.3811 (5263)	1% (73%) 6% (10%)	5.5 ± 0.9 65.9 ± 2.3	15.03 ± 0.28	15	1.16
AA30	Balseo 41°37’38”S; 72°18’11”W	Tonalite	Apatite* Zircon*	20 20	0.0274 (19) 5.427 (5614)	1.963 (1361) 1.543 (1596)	1.682 (11619) 0.3839 (5301)	2% (52%) 31%(0%)	4.0 ± 0.9 85.9 ± 6.8	14.38 ± 0.28	30	1.49
AA31	Puelo Chico 41°39’02”S; 72°17’14”W	Granite	Apatite* Zircon*	20 20	0.0312 (19) 5.311 (4973)	2.233 (1360) 1.793 (1679)	1.690 (11671) 0.391 (5399)	1% (86%) 20% (0%)	4.0 ± 0.9 73.0 ± 4.2	-	-	-
AA32	Puelo 42°40’23”S; 72°19’47”W	Granite	Apatite* Zircon*	20 20	0.0245 (9) 7.377 (4592)	2.093 (766) 2.961 (1123)	1.697 (11724) 0.3778 (5217)	1% (97%) 17%(0%)	3.4 ± 1.4 62.0 ± 3.0	-	-	-
AA33	Volcan Yates 41°41’57”S; 72°27’08”W	Granodiorite	Apatite* Zircon*	30 20	0.1499 (125) 0.4692 (600)	7.022 (5857) 2.368 (2857)	1.552 (11004) 0.3884 (5308)	0% (80%) 2% (44%)	5.5 ± 0.5 5.3 ± 0.3	15.03 ± 0.19	40	1.21
AA34	Volcan Yates 41°40’41”S; 72°23’56”W	Tonalite	Apatite* Zircon*	20 20	0.1227 (72) 0.4308(1040)	7.647 (4488) 1.642 (3963)	1.559 (11196) 0.3832 (5293)	0% (97%) 9% (12%)	4.2 ± 0.5 6.6 ± 0.3	14.11 ± 0.14	52	1.03
AA35	Termas de Ralún 41°21’06”S; 72°21’32”W	Tonalite	Apatite* Zircon*	20 20	0.1858 (58) 0.6055 (541)	8.017 (2502) 1.268 (1133)	1.566 (11387) 0.3804 (5254)	2% (64%) 0% (73%)	6.2 ± 0.8 11.9 ± 0.7	14.84 ± 0.3	16	1.17

AA36	Parque Alerce Andino 41°34'34"S; 72°33'08"W	Gneiss	Apatite* Zircon*	20 20	0.2114 (40) 1.518 (870)	6.866 (1299) 4.821 (2763)	1.573 (11579) 0.3896 (5381)	0% (96%) 11% (10%)	8.2 ± 1.3 8.0 ± 0.4	13.85 ± 0.45	17	1.79
AA37	Chaparrano 41°43'43"S; 72°33'21"W	Tonalite	Apatite* Zircon*	20 20	0.05895 (53) 0.6225(1017)	2.315 (2081) 1.928 (3150)	1.580 (11771) 0.3877 (5354)	5% (62%) 18% (1%)	6.8 ± 1.0 8.2 ± 0.5	13.77 ± 0.16	88	1.48
AA39	Rio Mariquita 42°01'20"S; 72°26'47"W	Tonalite, foliated	Apatite* Zircon*	20 20	0.0342 (9) 0.1762 (319)	1.582 (426) 0.7324(1326)	1.587 (11963) 0.3765 (5199)	0% (97%) 16% (17%)	5.7 ± 1.9 6.1 ± 0.5	-	-	-
AA40	Pichanco 42°06'46"S; 72°27'37"W	Granodiorite	Apatite* Zircon*	20 20	0.0975 (33) 0.3413 (632)	6.106 (2066) 2.103 (3895)	1.594 (12155) 0.3820 (5276)	0% (98%) 19% (2%)	4.3 ± 0.7 3.8 ± 0.3	14.87 ± 0.20	49	1.37
AA42	Rio Negro 41°50'51"S; 72°22'39"W	Tonalite	Apatite* Zircon*	18 20	0.0441 (13) 0.8605 (776)	1.254 (369) 4.236 (3820)	1.601 (12347) 0.3814 (5267)	146% (78%) 33% (0%)	4.2 ± 2.7 4.8 ± 0.4	13.4 ± 0.46	9	1.30
AA43	Pichicolo 41°59'36"S; 72°36'20"W	Dacite	Apatite* Zircon*	20 20	0.04180 (37) 0.4196(1049)	0.7230 (640) 1.874 (1795)	1.607 (12539) 0.3818 (5272)	0% (97%) 0% (89%)	15.5 ± 2.7 14.6 ± 0.6	14.71 ± 0.22	35	1.30
AA44	F. Quintupeu 42°09'40"S; 72°27'30"W	Tonalite	Apatite* Zircon*	20 20	0.0695 (62) 0.7418(1049)	5.851 (5220) 4.174 (5903)	1.614 (12730) 0.3771 (5208)	31% (15%) 12% (2%)	3.3 ± 0.5 4.4 ± 0.2	13.67 ± 0.20	52	1.40
AA45	I. Llancahué 42°04'17"S; 72°28'40"W	Micaschist	Apatite* Zircon*	18 20	0.06896 (14) 0.2522 (659)	4.369 (887) 1.943 (5076)	1.621 (12922) 0.3824 (5281)	0% (82%) 27% (0%)	4.3 ± 1.2 3.2 ± 0.5	14.11 ± 0.44	8	1.17
AA46	I. Llancahué 42°03'53"S; 72°29'50"W	Tonalite	Zircon*	20	0.3929 (656)	2.129 (3555)	0.3802 (5250)	20% (0%)	4.5 ± 0.3			
AA102	Petrohué 41°08'38"S; 72°24'44"W	Tonalite	Apatite** Zircon**	20 20	0.02566 (9)) 0.6744 (393)	1.015 (356) 3.863 (2251)	1.504 (10380) 0.3990 (5510)	0% (97%) 0% (94%)	6.3 ± 2.2 4.5 ± 0.3	-	-	-
AA106	Isla Pelada 42°00'59"S; 72°27'18"W	Tonalite	Apatite** Zircon**	12 20	0.0692 (10) 0.4269 (385)	3.709 (589) 3.034 (2736)	1.496 (10330) 0.4019 (5550)	39% (34%) 28% (0%)	4.3 ± 1.5 3.4 ± 0.3	-	-	-
AA111	Isla Pelada 42°01'50"S; 72°29'43"W	Aplite	Apatite** Zircon**	15 20	0.08378 (14) 0.5088 (456)	4.734 (791) 3.534 (3167)	1.489 (10280) 0.4161 (5747)	0% (70%) 21% (0%)	4.4 ± 1.2 3.9 ± 0.3	-	-	-
AA119	I. Llancahué 42°10'15"S; 72°29'16"W	Tonalite	Apatite**	16	0.0118 (8)	0.5982 (404)	1.474 (10179)	1% (64%)	4.9 ± 1.7	-	-	-
AA125	Rio Blanco 41°56'55"S; 72°23'05"W	Granite	Apatite**	20	0.1253 (32)	4.814 (1230)	1.460 (10078)	16% (7%)	6.5 ± 1.2	14.83 ± 0.15	100	1.53
AA128	Lago Todos Los Santos 41°07'44"S; 72°20'25"W	Granite	Zircon**	10	5.538 (2394)	2.133 (922)	0.4004 (5530)	11% (3%)	67.0 ± 3.8			
AA129	Lago Todos Los Santos 41°06'44"S; 72°17'14"W	Granite	Apatite** Zircon**	20 20	0.0692 (56) 0.4883 (412)	3.883 (3142) 3.417 (2883)	1.445 (9978) 0.4133 (5707)	19% (57%) 7% (23%)	4.4 ± 0.6 3.8 ± 0.2	14.38 ± 0.21	39	1.28
AA130	Lago Todos Los Santos 41°04'34"S; 72°07'10"W	Granite	Apatite** Zircon**	20 20	1.324 (68) 1.591 (1433)	5.217 (2680) 2.357 (2122)	1.438 (9928) 0.4176 (5767)	0% (96%) 23% (0%)	6.1 ± 0.8 17.7 ± 1.1	14.56 ± 0.13	99	1.29
AA131	Lago Todos Los Santos	Tonalite	Apatite**	20	0.0531 (31)	1.849 (1080)	1.431 (9877)	0% (85%)	6.9 ± 1.3	14.41 ± 0.28	36	1.63

	41°08’16”S; 72°04’18”W		Zircon**	20	1.395 (1040)	2.726 (2033)	0.409 (5648)	16% (1%)	13.8 ± 0.8			
AA132	Lago Todos Los Santos 41°05’30”S; 72°10’51”W	Tonalite	Apatite** Zircon**	20 10	0.0455 (19) 6.411 (3152)	1.650 (688) 1.886 (927)	1.511 (10430) 0.419 (5786)	38% (12%) 19% (2%)	7.2 ± 1.8 93.3 ± 6.9	1.88 ± 0.39	12	1.29
XK610	Castro Chiloe 42°32’17”S; 73°52’56”W	Micaschist	Apatite**	20	0.0773 (14)	0.2322 (42)	1.628 (13144)	4% (79%)	91.5 ± 28.3	-	-	-
XK611	Castro Chiloe 42°21’46“S; 73°55’17“W	Micaschist	Apatite** Zircon**	12 20	0.0827 (8) 10.84 (6390)	0.2896 (28) 2.015 (1188)	1.635 (13306) 0.3798 (5245)	0% (95%) 5% (16%)	78.8 ± 31.7 131.8 ± 5.2	-	-	-
XK614	Castro Chiloe 42°19’25”S; 73°50’28”W	Micaschist	Apatite**	13	0.2334 (39)	0.9455 (158)	1.642 (13498)	41% (15%)	77.0 ± 18.6	-	-	-
XK617	Castro Chiloe 42°20’8”S; 73°48’23”W	Micaschist	Apatite**	20	0.0877 (12)	0.4901 (67)	1.649 (13690)	0% (97%)	49.9 ± 15.7	-	-	-
XK619	Castro Chiloe 42°29’41”S; 73°48’35”W	Micaschist	Apatite** Zircon**	15 30	0.1998 (32) 9.450 (8378)	0.7928 (127) 2.616 (2319)	1.656 (13881) 0.3883 (5363)	21% (72%) 15%(0%)	75.0 ± 16.1 90.9±3.9	-	-	-
XK621	C. Piuchén Chiloe 42°22’50”S; 73°59’20”W	Micaschist	Apatite**	19	0.1303 (18)	0.490 (62)	1.670 (14265)	1% (96%)	81.7 ± 21.9	-	-	-
XK705	Isla San Pedro, Chiloé 43°17’44“S; 73°39’54“W	Micaschist	Zircon**	10	8.405 (2542)	2.020 (611)	0.4247 (5865)	34% (0%)	103.0 ± 12.4			
AL106	Monte Tronador 41°09’48”S; 71°58’12”W	Granite	Zircon**	4	0.9974 (73)	3.019 (221)	0.4061 (18)	1% (24%)	8.7 ± 1.2			
AL112	Volcan Casablanca 40°05’20”S; 72°00’28”W	Tonalite	Apatite** Zircon**	21 20	0.0228 (77) 0.5361 (362)	5.330 (1796) 1.459 (985)	1.482 (10229) 0.4076 (5628)	0% (53%) 8% (34%)	10.6 ± 1.3 9.8 ± 0.7	14.4 ± 0.16	100	1.54
AL122	Rio Cochamo 41°21’21”S; 72°03’30”W	Tonalite	Apatite**	20	0.0438 (19)	1.630 (698)	1.467 (10129)	4% (44%)	6.7 ± 1.6	14.32 ± 0.28	26	1.42
AL130	Cochamo 41°23’54”S; 72°22’20”W	Granite	Zircon**	20	0.4128 (354)	0.8069 (692)	0.4033 (5569)	0% (90%)	13.4 ± 0.9			
AL137	Puelo 41°34’18”S; 72°25’12”W	Granodiorite	Apatite** Zircon**	20 20	0.1493 (31) 0.7374 (553)	1.448 (878) 1.168 (876)	1.658 (11445) 0.4118 (5688)	18% (64%) 10% (63%)	9.8 ± 1.9 16.8 ± 1.1	14.44 ± 0.18	76	1.57
AL143	Rio Traidor 41°48’48”S; 72°20’06”W	Tonalite	Zircon**	20	7.028 (2174)	2.189 (677)	0.4204 (5806)	0% (99%)	87.6 ± 4.2			
AL152	Llanada Grande 41°50’06”S; 72°50’26”W	Tonalite	Apatite** Zircon**	20 20	0.0397 (17) 6.046 (3181)	1.600 (685) 1.492 (785)	1.624 (10280) 0.4233 (5865)	4% (44%) 18% (0%)	6.7 ± 1.7 110.6 ± 8.11	13.75 ± 0.60	6	1.60
AL169	Arroyo Ventisquero 42°46’02”S; 72°05’06”W	Granite	Apatite** Zircon**	20 20	0.0780 (43) 6.446 (4184)	1.793 (988) 2.126 (1380)	1.613 (11136) 0.4047 (5589)	0% (70%) 0% (90%)	11.7 ± 1.9 79.3 ± 2.9	14.58 ± 0.22	33	1.27
AL181	Cholgo 42°12’06”S; 72°16’12”W	Tonalite	Apatite** Zircon**	20 20	0.189 (34) 0.3555 (464)	9.690 (2770) 1.297 (1693)	1.602 (11059) 0.3976 (5490)	0% (90%) 15% (9%)	3.3 ± 0.6 7.1 ± 0.5	14.46 ± 0.29	37	1.73

AH378	Cochamo 41°20'48"S; 72°23'30"W	Granite	Apatite** Zircon**	20 20	0.2092 (76) 1.372 (1652)	8.615 (3129) 2.662 (3206)	1.591 (10904) 0.4104 (5668)	8% (50%) 10% (7%)	6.4 ± 0.8 13.5 ± 0.6	13.87 ± 0.83	6	1.85
AL539	Lago Vidal Gormaz 41°27'12"S; 71°58'05"W	Ganodiorite	Apatite**	12 20	0.0637 (12) 0.6319 (233)	3.040 (382) 4.488 (1255)	1.579 (10904) 0.4147 (5767)	0%(88.5%) 12% (55%)	5.5±2.0 3.8±0.3	-	-	-
BR409	Pte Las Trancas (Ralún) 41°25'04"S; 72°26'57"W	Granitic bands	Zircon (***)	5	0.5493 (22)	4.120 (165)	0.4284 (5916)	0% (0%)	3.4 ± 0.8			
BR410	Laguna Patas, Ralún 41°17'17"S; 72°26'57"W	Diorite	Zircon (***)	20	3.155 (1050)	3.663 (1219)	0.4284 (5916)	9% (21%)	22.4 ± 1.1			
BR411	L. Llanquihue-Ensenada 41°13'00"S; 72°40'30"W	Granite	Zircon (***)	7	11.85 (491)	13.81 (572)	0.4284 (5916)	10% (9%)	21.8 ± 1.6			

* Samples calculated with Zeta calibration factors of 129.9 ± 1.64 (1σ) for CN2 (zircon) or 333.9±7.3 for CN5 (apatite)

** Samples calculated with Zeta calibration factors of 130.7 ± 1.9 (1σ) for CN2 (zircon) or 333.3±8.2 for CN5 (apatite)

*** Samples calculated by M.B. with a CN1 zircon zeta value of 119.00±5.0 (1σ)

Note: samples with considerable (>10%) and high age dispersions (>20%) and are outlined grey tones and discussed in sections 4.3, 4.4, and 4.5.

4.3 Fission Track Results from Chiloé Island

7 zircon and 9 apatite fission track ages were obtained from 10 samples on Chiloé Island. Figure 4.3 shows the distribution of the fission track ages on the island.

For the rocks of the metamorphic basement, the zircon samples yield ages ranging between Late Jurassic (155.6 ±10.1 Ma) and Late Cretaceous (90.4 ± 4.7 Ma). The youngest ages were obtained from samples XK619 and XK705, located at the central part and southernmost tip of the island. These have higher age dispersions (figure 4.3b), with single component FT ages which tend towards ~60-80 Ma.
Apatites samples from the metamorphic complex yielded FT ages ranging between Early Cretaceous (117.9±5.8 Ma) and Eocene (49.9±15.7 Ma). Most of these had low U contents, thus their fission track ages are accompanied with large errors. No statistically representative track length measurement could be obtained from them either, thus making a well-constrained interpretation from the data is difficult.

Comparison of the zircon and apatite FT ages from sample AA14 with the available K-Ar biotite and ^{40}Ar-^{39}Ar muscovite ages from the basement rocks at the northern border of the island (Duhart et. al., 2001, figure 2.3a), suggest very slow cooling rates and hence little erosion occurred at the fore-arc since pre-late Triassic metamorphism (up to ~5°C/Myr between 220 Ma and 60Ma). Nevertheless, the correlated apatite central age carries high age dispersion and no information from its tracks-length distribution, thus this estimate is very preliminary. More thermochronologic data from Chiloé Island is also necessary to establish better constraints.

The youngest zircon and apatite FT ages from the central and southern part of the island have high age dispersions and could reflect thermal overprinting by intrusives at the near surface (figure 4.3a-b), or due to a more widespread distribution of Eocene volcanism on the Island. Two mixed post-metamorphic zircon FT single grain ages and one late Cretaceous rapidly cooled apatite sample have been reported recently in the area near Castro by Thomson and Hervé (2002). They interpret these results as an effect of nearby intrusions, supported on reports of isolate outcrops of upper Cretaceous members of the NPB found within the Coastal Ranges to the north and south of the island (e.g. Munizaga et al., 1988; Pankhurst et al., 1999).

At Gamboa, a few kilometers SW of Castro, an outcrop of porphyric dacites with subvertical columnar joints has intruded into metamorphic basement rocks. These rocks have been previously mapped by Valdivia and Valenzuela (1988) and reinterpreted as a sill by Muñoz et al. (2000). One K-Ar whole rock date of 37.2±1.2 Ma for this outcrop has been reported by Muñoz et al. (2000).

Two samples from this outcrop were dated in this study (AA17 and AA18, figure 4.2a). The zircon and apatite FT ages yielded values between 36.0±1.2 Ma and 33.9±3.6 Ma. These are compatible with a fast cooling event by ca. 36 Ma. One of the apatite FT age is slightly younger, possibly because the sample has undergone some annealing at the surface in time, which is reflected by the rather short mean track length (13.7±0.8 μm) and relatively high age dispersion (14%) found in the sample.

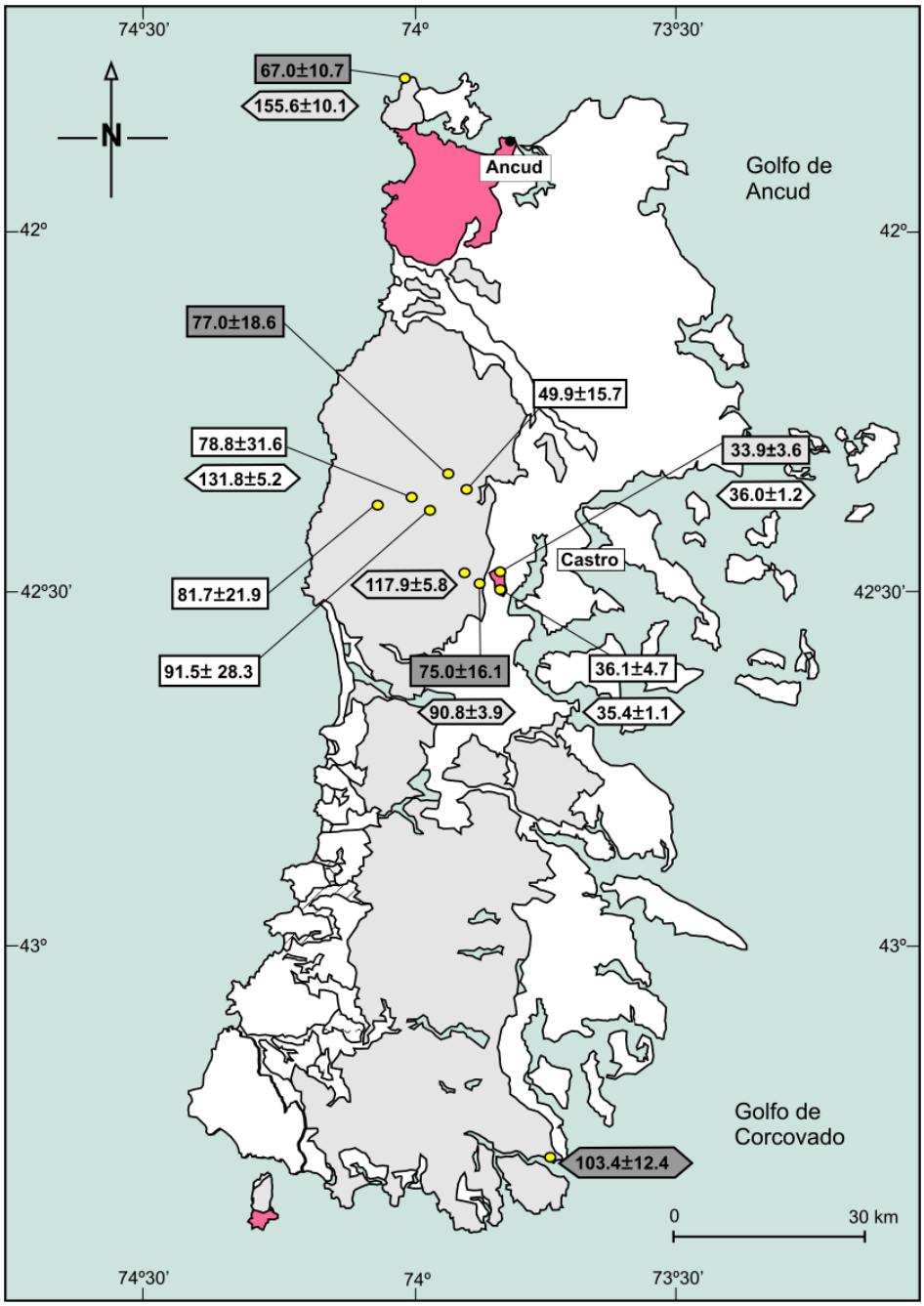

Figure 4.3a: Apatite and zircon FT ages on Chiloé Island

Geology

- Tertiary and Quaternary sediments
- Tertiary volcanic rocks
- Late Paleozoic-Triassic metamorphic rocks

Apatite FT Central Ages (Ma)

- Central ages with age dispersion <10%
- Central ages with age dispersion >10%
- Central ages with age dispersion >20%

Zircon FT Central Ages (Ma)

- Central ages with age dispersion <10%
- Central ages with age dispersion >10%
- Central ages with age dispersion >20%

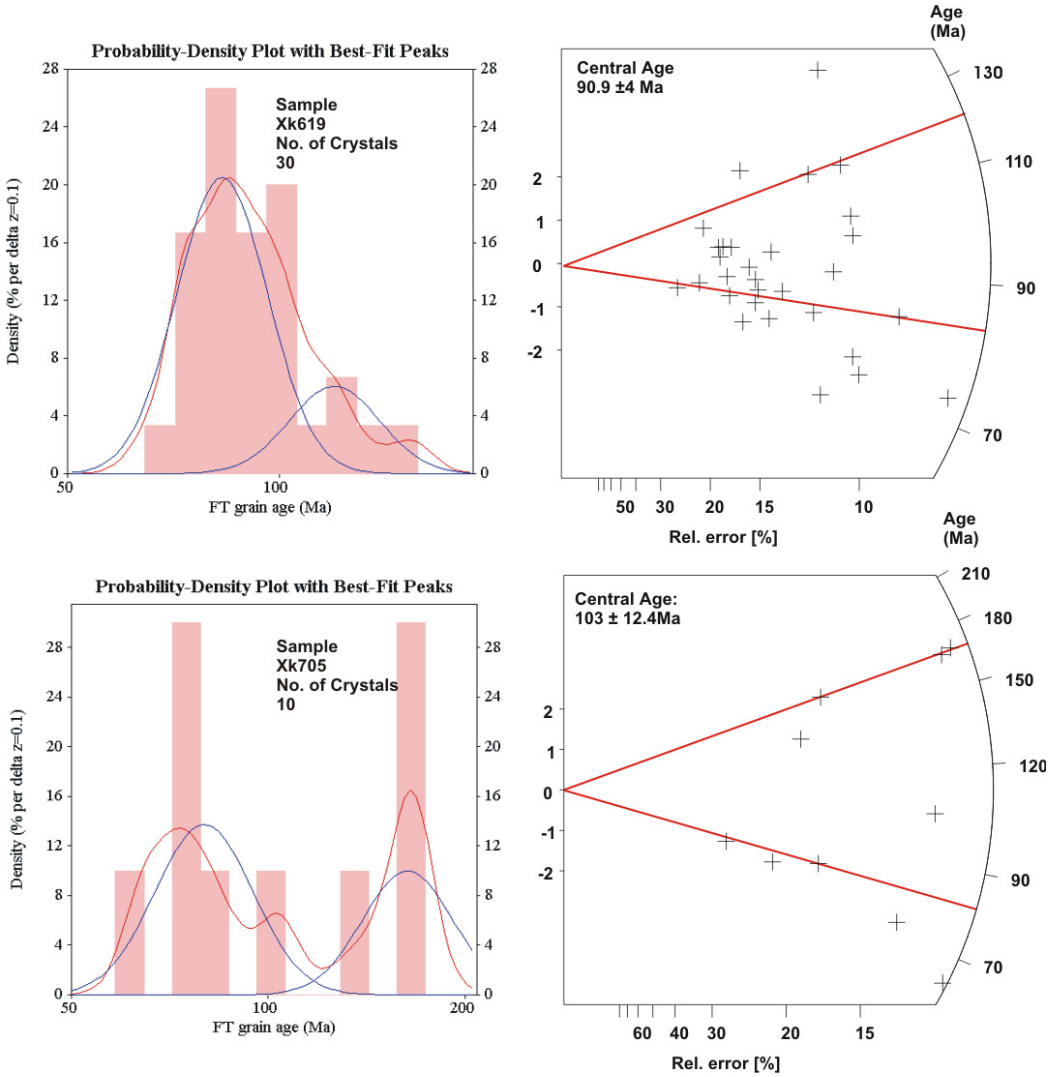

Figure 4.3b: Combined histograms and radial plots for zircon samples of the basement rocks at Chiloé Island. The probability-density plots (using BINOMFIT; Brandon, 2002) for the population distribution of FT zircon single-grain ages are from samples XK619 and XK705, located on the central and southern parts of the Island. The determined peak ages are projected with red lines in the radial plots (Galbraith, 1990), for comparison on the relative distribution and precision of the component ages (plotted with Trackey© 4.1, Dunkl, 2002). The younger age components in these samples tend towards Late Cretaceous times, and could represent thermal resetting from granitoids at the near surface. Refer to chapter 3.4.4 for details on the plots.

4.4 Fission Track results from the Reloncaví Area

41 apatite and 46 zircon FT ages, plus 22 apatite track length distributions have been obtained in the Reloncaví area, mainly from plutonic rocks of the NPB. Two samples correspond to metamorphic rocks of unknown age, strongly affected by contact metamorphism.

Figure 4.4a shows the apatite fission track ages and track length distributions in the Reloncaví area. Apatite FT ages are as young as 3.3±1.2 Ma within the LOFZ, whereas towards the west older Miocene ages are obtained. Late Miocene apatite FT ages are also obtained to the east of the fault zone. Apatite FT length distribution patterns are typically characterised by negatively-skewed histograms, with long mean track lengths (between 13.77±0.16 μm and 14.4±0.16 μm) and relatively large standard deviations (1.26 μm and 2.05 μm), thus indicating a trend between normal and fast cooling. The inferred cooling rates tend to increase towards the main traces of the LOFZ. Very rapid cooling along the LOFZ is implied by the pattern of young ages and long apatite mean track lengths with unimodal distribution (generally between 14μm and 15μm, with the only exception of sample AA2).

Figure 4.4b shows the location of the zircon and apatite FT ages within the Reloncaví area. The distribution of the zircon FT ages is, in contrast to that of the apatites, remarkably influenced by the geology of the area. On the western side of the LOFZ the ages are Miocene and tend to be younger at the border of the Reloncaví estuary. At the eastern margin of the LOFZ, the ages are Late Cretaceous. Similar zircon FT ages were also obtained from samples located on the eastern side of the study area, and further north at the Todos Los Santos Lake.

In several cases the zircon FT ages display high age dispersions, as shown by the radial plots and histograms in figure 4.4c. Many are located near the LOFZ, and suggest thermal resetting by fluids and magmatism. The Cretaceous partially reset zircon FT ages could reflect thermal overprinting after being denuded in pre-Miocene times. The discordant age distributions plotted in the figures may correspond as well to variations in radiation damage or trace element chemistry of the components of the sample grain population. Advection of heat during rapid denudation is also possible, although significant amounts of denudation in a short time should be required to reset the apatite FT system. A discussion on the effects of heat advection over denudation in the region is given in chapter 6.

Samples from Miocene plutons and contact metamorphic rocks located away from the fault zone could reflect thermal overprinting from shallow-level intrusions. Apatite samples with high age dispersions do not necessarily imply partial resetting, but could reflect internal variations in the chemistry of the sample grain population.

Nevertheless, The differences in ages displayed between the zircon and apatite FT data across the fault zone clearly indicate an important tectonic event registered under low temperature conditions, below the zircon FT “closure” temperature. The correlation of these with the available intrusion ages and other thermochronologic data will be discussed in chapter 6.

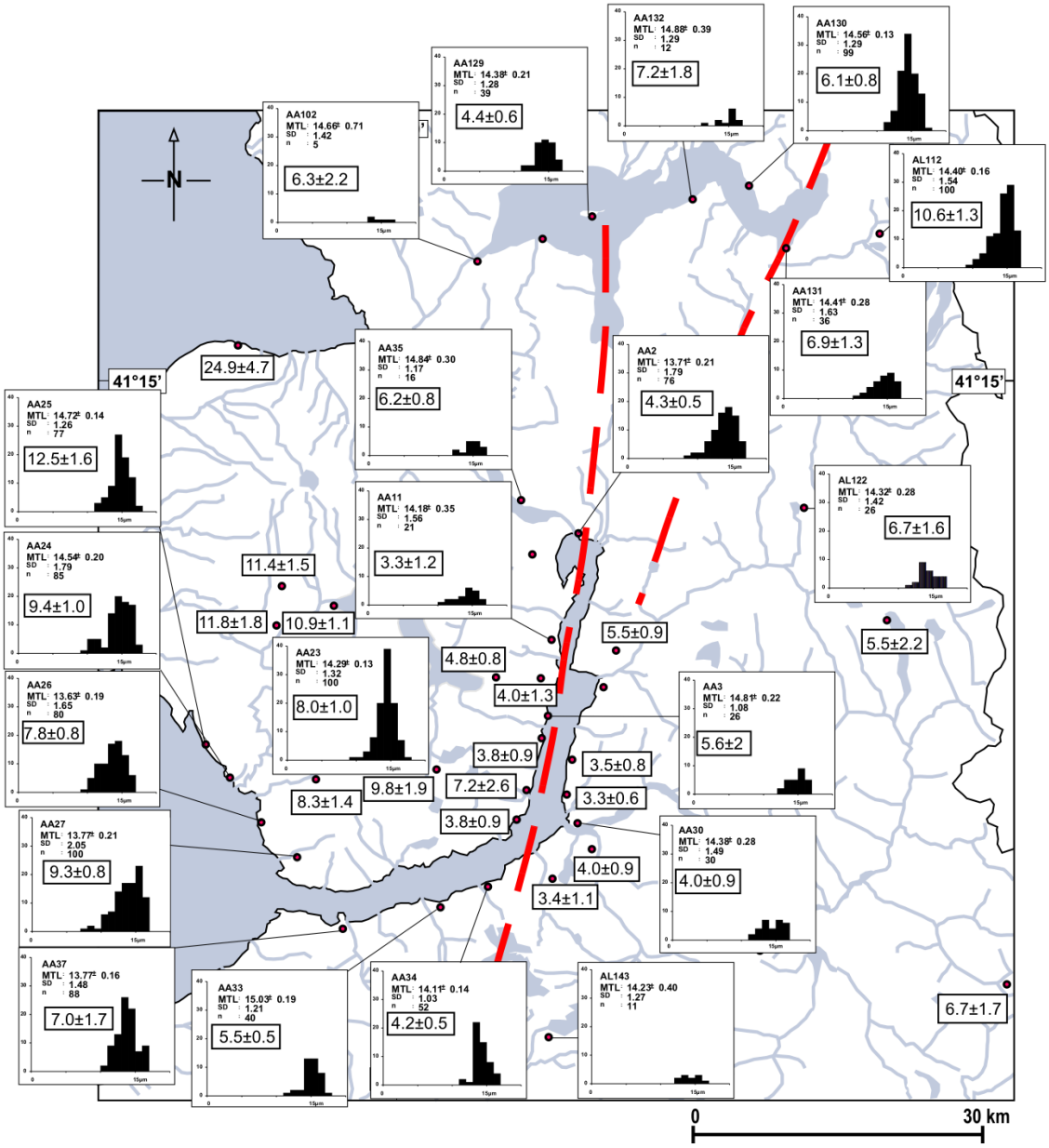

Figure 4.4a
Apatite FT ages and track length distributions in the Reloncaví Area

Location of Samples for FT Dating

Apatite ages in Ma.

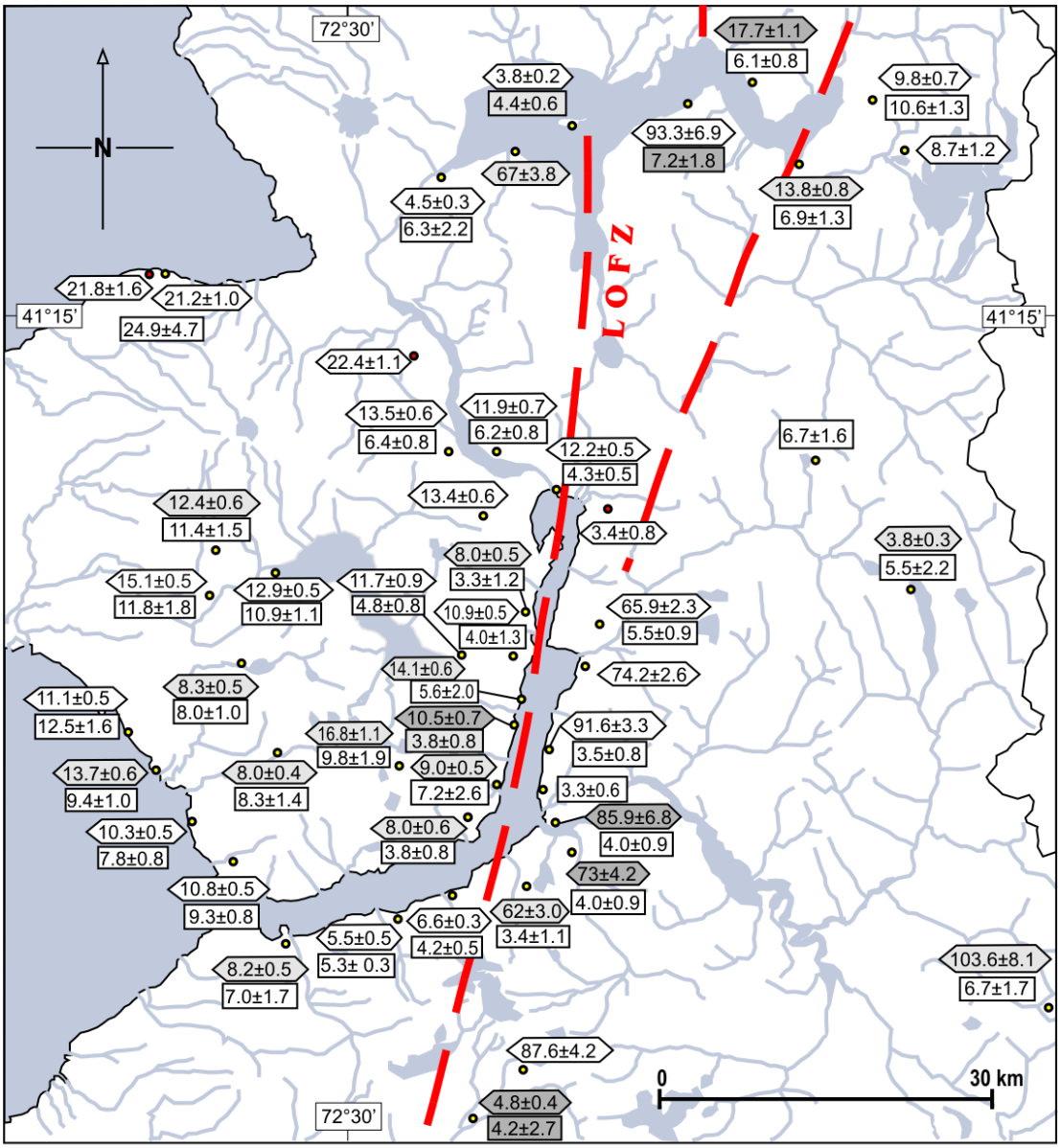

Figure 4.4b: Apatite and zircon FT ages in the Reloncaví Area

Apatite FT Central Ages (Ma)

- Central ages with age dispersion <10%
- Central ages with age dispersion >10%
- Central ages with age dispersion >20%

Zircon FT Central Ages (Ma)

- Central ages with age dispersion <10%
- Central ages with age dispersion >10%
- Central ages with age dispersion >20%

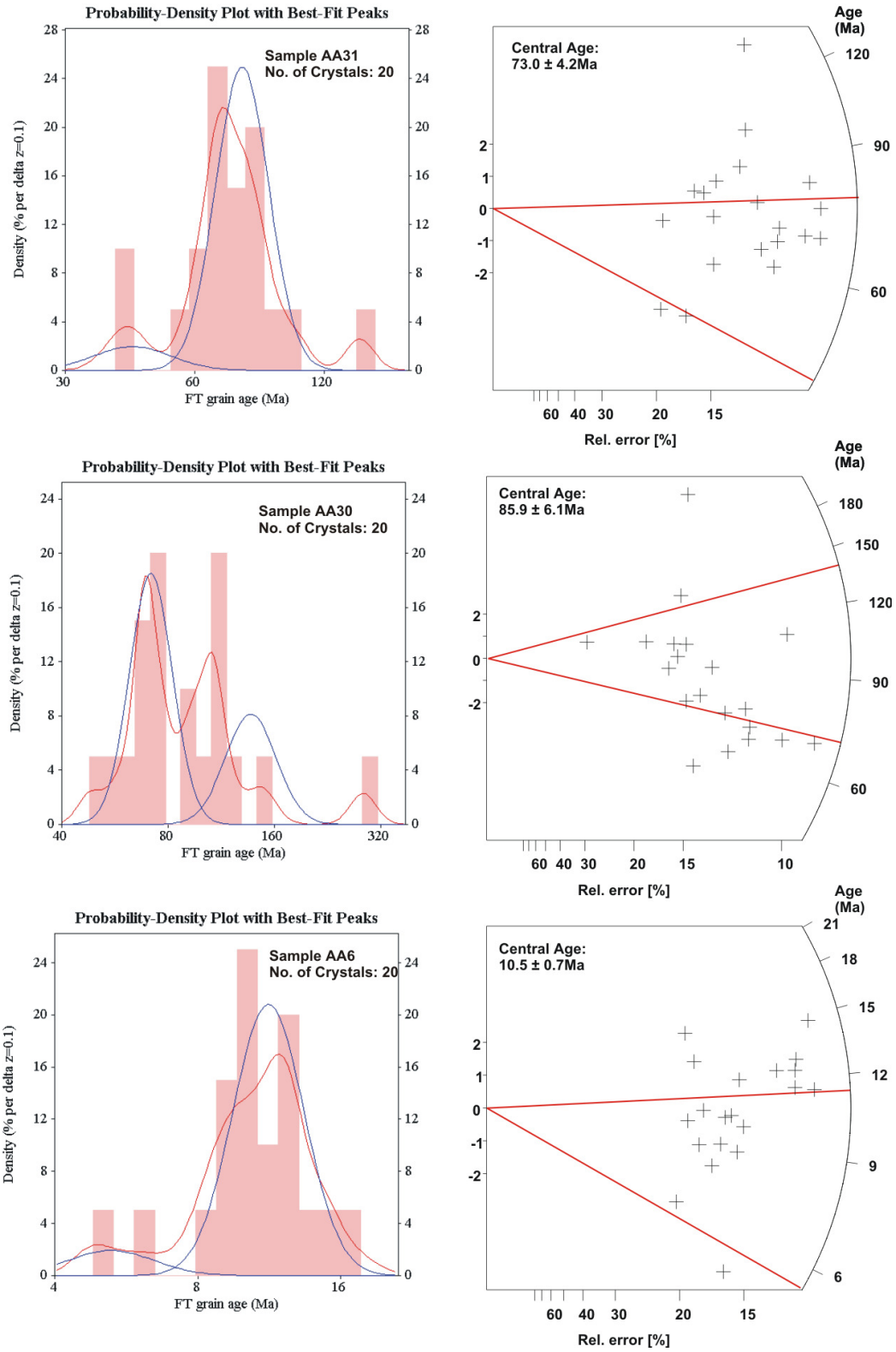

Figure 4.4c: Combined histograms and radial plots for individual zircon FT grain ages with high age dispersions along the LOFZ in the Reloncaví area. The peak ages determined from the probability density distribution plots are projected in red on the radial plots. These suggest partial resetting from fluids, magmatic activity or denudation. Refer to discussion in text and chapter 3.4.4 for more details over the plots.

4.5 Fission Track results from the Hornopirén Area

9 zircon and 10 apatite fission track ages, plus 7 apatite length measurements have been obtained in the Hornopirén Area (figure 4.5a). These correspond mainly to the plutonic rocks of the NPB and contact metamorphic rocks of the basement on Llancahué Island.

Along both sides of the LOFZ, apatite fission track ages are Late Miocene to Pliocene (between 4.3 ± 1.5 Ma and 6.5 ± 1.2 Ma). The obtained confined track length distributions display large mean track lengths (between 14μm and 15μm) with negatively skewed to uniform patterns characterized by small standard deviations (between 1.53 μm and 1.3 μm), thus indicating fast cooling histories.

Large errors and age dispersions of the apatite FT ages were obtained in samples AA42, AA44 and AA125. This was caused by their low track density and small countable areas of spontaneous tracks due to the presence of inclusion trails or etched fractures. Another problem to account for was the ubiquitous presence of grains within the grain population with no spontaneous tracks on their surfaces.

Across the both sides of the LOFZ, zircon fission track ages overlap the apatite ages within 1 sigma error, between 6.1±0.5 Ma and 3.2±0.3 Ma. The similarity of both apatite and zircon FT ages, with their different closure temperatures, implies a very rapid cooling history of the sampled intrusives. This is probably due to the near presence of shallow-level plutons in the area, which is discussed in more detail in chapters 5 and 6.

High age dispersions were obtained as well from the zircon FT ages near the LOFZ. Some examples are shown in figure 4.5b. The big spread in ages suggests partial resetting following thermal perturbations along the fault zone within the area, in a similar manner to those described in the previous section.

Sample AA43 was obtained from an outcrop of dacitic volcanic rocks of the Ayacara Formation (Hervé et al., 1979), interpreted as one of the mid-Tertiary basins that developed in conjunction to dextral movements of the LOFZ. No age for this sequence has been previously published. Overlapping zircon and apatite FT ages of 14.6±0.6 Ma and 15.5±2.7 Ma, respectively, were obtained from this sample, indicating rapid cooling at the surface. This yield probably represents an age for the upper member of the basin sequence. The larger error obtained from the apatite sample is caused by its low uranium contents.

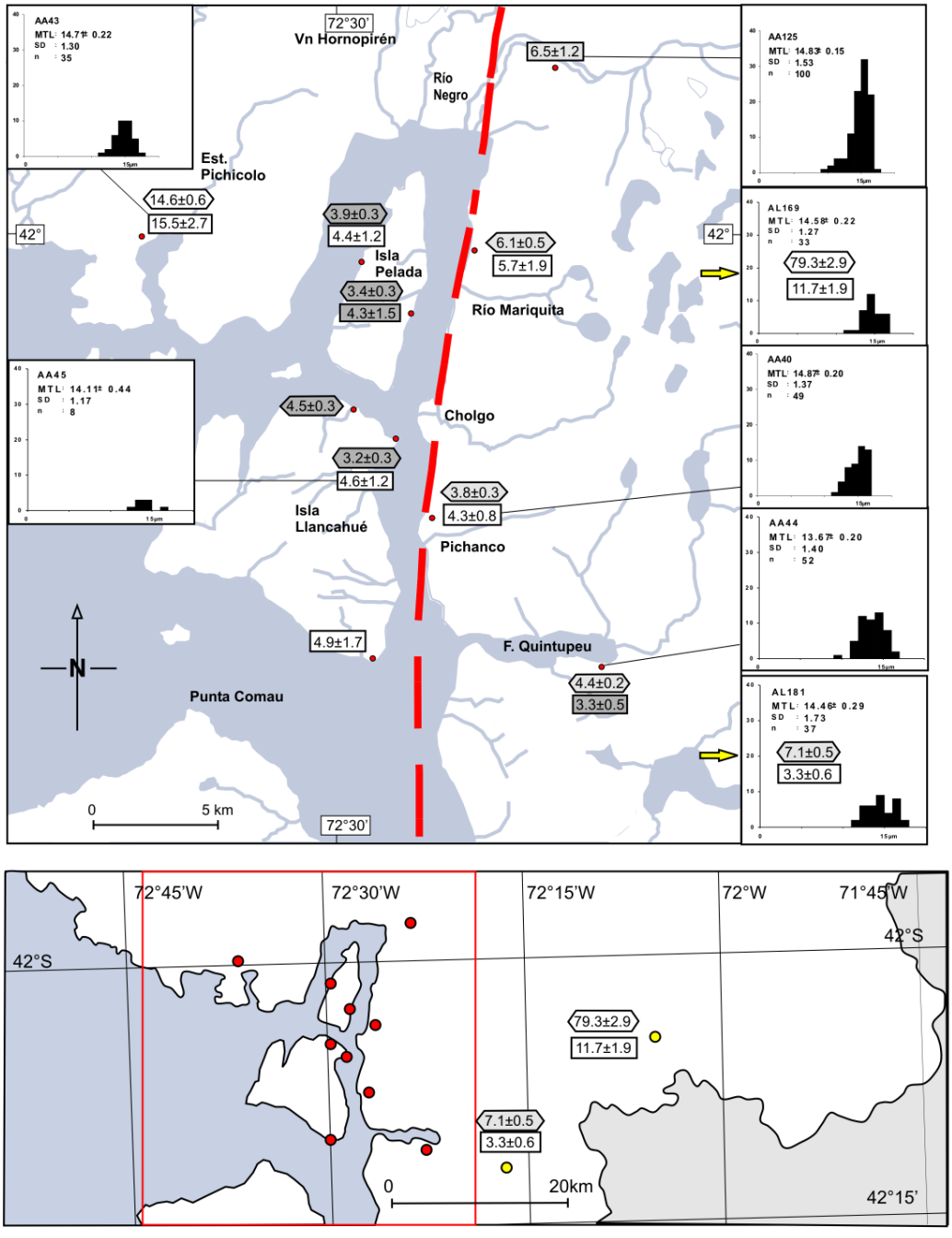

Figure 4.5a: Zircon and Apatite FT ages and track length distributions in the Hornopirén Area

Apatite FT Central Ages

- Central ages with age dispersion <10%
- Central ages with age dispersion >10%
- Central ages with age dispersion >20%

Zircon FT Central Ages

- Central ages with age dispersion <10%
- Central ages with age dispersion >10%
- Central ages with age dispersion >20%

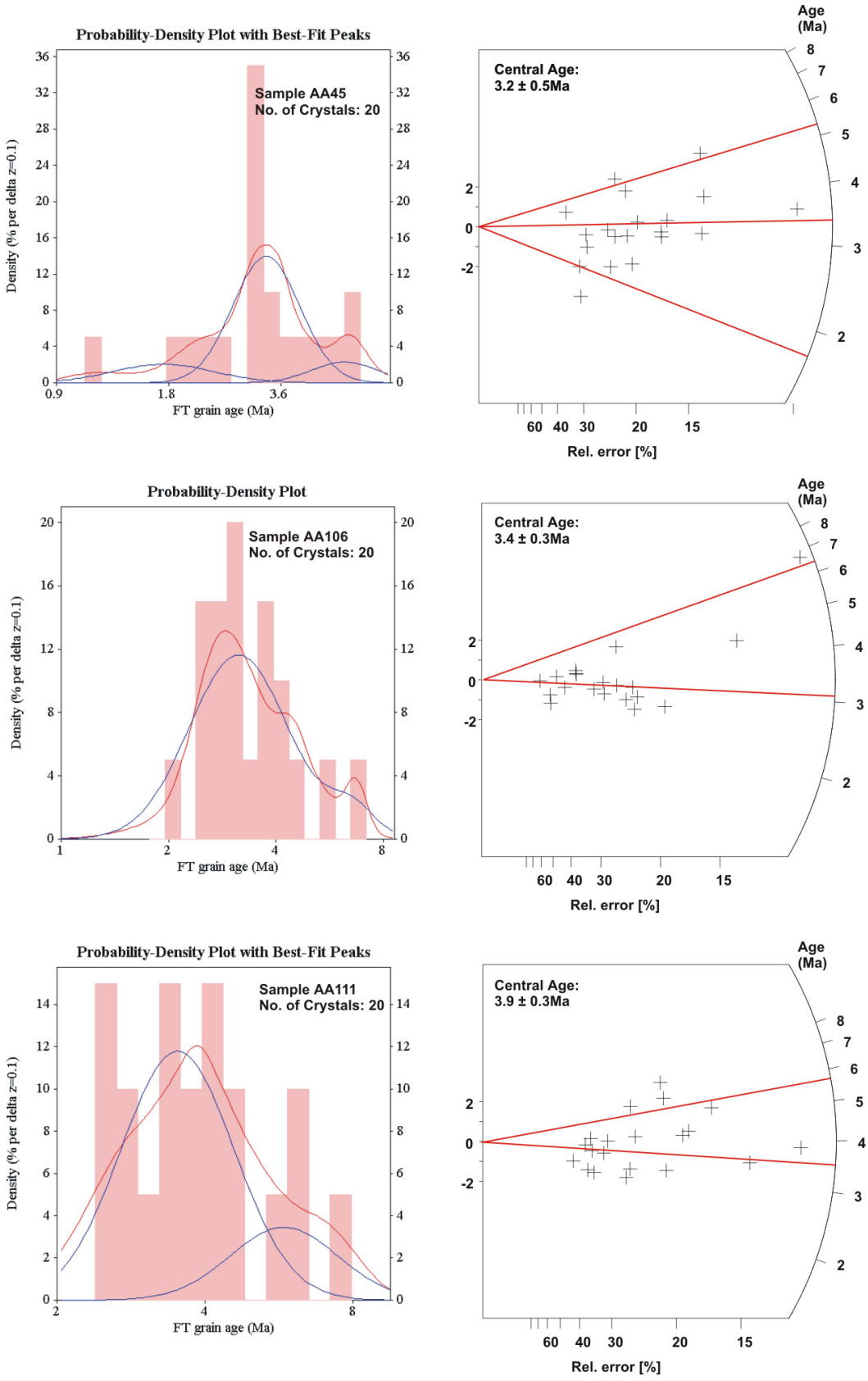

Figure 4.5b: Combined histograms and radial plots for individual zircon FT grain ages with high age dispersions along the LOFZ in the Hornopirén area. The best-fit peaks determined from the probability density distribution are projected in the radial plots. The samples belong to the western side of the LOFZ within the Hornopirén Area. The spread in single ages suggest thermal overprinting leading to reduced mean ages. Refer to discussion in text.

5. Structural and Petrologic Observations

The microstructures and phase assemblages were examined in 36 samples from the areas of Reloncaví and Hornopirén, to obtain information on the formation and deformation of the rocks exposed along the LOFZ, and to explore relationships with their cooling histories determined by FT analysis. This part of the study is based on independent fieldwork and samples collected during two field trips. The results are therefore biased to own observations. Sampling was focussed on isolated high strain zones along the fault zone within the NPB and its host rocks, which range in scale from centimeter- to meter- wide. Indicators of different deformation conditions were obtained in the areas of Reloncaví and Hornopirén. These are extended in the following sections.

5.1 Structural Observations in the Reloncaví Area

The structure in the Reloncaví area is defined by two N-NNE diverging fault segments of the LOFZ, that juxtapose Miocene and Cretaceous plutons with sharp contacts along the Reloncaví estuary and the Todos Los Santos lake (figure 5.1a, images I-III). The main segment is approximately NS trending, arcuate and concave to the west, and follows the general trend of the fault zone. The second is oblique to the main segment and limited in extension, suggesting an origin as a megascale dextral Riedel shear.

The contact relations between plutons are based on regional mapping and geochronology carried out by Duhart et al. (2000), Carrasco (1995), Munizaga et al. (1988), and SERNAGEOMIN-BRGM (1995). Assuming that the Cretaceous parts of the NPB along both sides of the LOFZ were emplaced simultaneously, a total dextral displacement of ca. 30 km along the fault zone can be inferred. Although a rough estimate, this amount of displacement compares to the extension of Eocene-Miocene pull-apart basins developed within the fault zone south of the study area (chapter 2, figure 2.2).

5.1.1 Field Observations in the Reloncaví Area and Geobarometry

A huge sector of the study area is densely covered by vegetation, which restricted field access. Observations were made towards the west and to a limited extent in the northern part of the study area. Outcrops of plutonic rocks along the LOFZ consist mainly of coarse-grained granodiorites and tonalites with minor diorites, monzonites and granites. Abundant synplutonic mafic and granodioritic dikes were found within Miocene plutons west of the Reloncaví estuary. Along the fault zone, the rocks were observed weakly deformed and not foliated, whereas the landscape surrounding the Reloncaví sound is deeply carved by glacial erosion. (image IV, fig.5.1a). Magmatic foliation and compositional layering were recognized within plutons near Ralún and at the Isla Las Cabras (image V, fig.5.1a). Little evidence of faulting was observed, except for discrete steeply-dipping surfaces of NNE and ENE orientation cutting through the intrusives along the eastern border of the Reloncaví sound, between Ralún and Puelo.

Al-in hornblende geobarometry from selected locations of the NPB indicate depths of crystallization ranging between 8 km and 14 km, with some variation across the LOFZ (Seifert et al., 2003). Cretaceous plutons at the eastern border of the Reloncaví estuary yield depths between 8km and 10km, whereas slightly deeper levels (10km to 12km) were obtained from Miocene plutons located at the western border. An emplacement depth of 14 km was obtained from a Cretaceous pluton on the northwestern side of the study area, suggesting an exposure of deeper levels of an older unit of the batholith.

Westwards of the estuary and away from the fault zone, outcrops of andalusite-K feldspar-sillimanite gneisses of the metamorphic basement have been reported by Parada et al. (1987) (fig. 5.1a, image VII). Based on the intersection of the *andalusite = sillimanite* equilibrium curve of Holdaway (1971) and the *muscovite + quartz = andalusite + K-feldspar+* H_2O isograd (Spear and Cheney, 1991; St. Onge, 1984), the coexistence of these contact metamorphic associations indicates low pressure conditions (~2 kbar) and thus shallow depths for the intruding plutons. This is in good agreement with the very rapid cooling histories obtained by the integrated thermochronologic data in those locations (refer to chapter 6).

5.1.2 Microstructures from the Reloncaví Area

Figure 5.1b shows microstructures of samples collected along both sides of the LOFZ. Some differences in deformation grade are pointed out considering the cooling histories of the plutons, detailed in chapter 6.

Samples from Miocene plutons at the western of the Reloncaví sound, with moderate cooling rates, evidence mechanical twinning and microcracking in plagioclase, undulatory extinction in quartz, and bent or slightly kinked biotites (e.g. samples AA2, AA11, AA4, BR409). The microfractures in feldspar are infilled with fine-grained sheet-silicates, epidote and (in places) calcite, suggesting solution transfer at low temperature conditions (e.g. Chester and Logan, 1987; Evans, 1988). In general, the observed microstructures are consistent with deformation at very low grade conditions (below ~300°C; e.g. Stöckhert et al., 1999).

Samples from Cretaceous plutons located on the eastern side of the estuary indicate scarce evidence of deformation, with the exception of sample AA29. Bent plagioclase grains were observed together with variable quartz fabrics, ranging from undulatory extinction to subgrain boundaries.

The microstructures of quartz indicate recovery during deformation by dislocation creep (e.g. Yund and Tullis, 1991; FitzGerald and Stünitz, 1993). The deformation could have taken place related to the LOFZ in the Cretaceous plutons at their emplacement levels, or due to internal stresses originating during cooling of the intrusion. A systematic survey of the small scale shear zones including identification of shear sense indicators would be required to solve this question.

Another important exception was found in sample AA128, from the western side of the Todos Los Santos Lake. A marked deformation is recorded in the quartz fabrics, with undulatory extinction and migration recrystallization. Rotated feldspar

porphyroclasts within the quartz matrix were also observed. Biotites are kinked and fractured, and often recrystallized into fine-grained aggregates. Based on the microstructures of quartz and feldspar, this deformation was probably taken place at temperatures of ~ 300-350°C (e.g. Simpson, 1985; Stöckhert et al., 1999). A ~67 Ma zircon FT age from this sample provides a lower age bound to the timing of this deformation. It must be pre-late Cretaceous.

Comparing the cooling histories of the plutons on both sides of the fault zone, an enhanced uplift of the western block in the late Miocene is indicated (chap. 6). Nevertheless, no significant difference could be established in the microstructural record of deformation across the LOFZ. This can be explained by the fact that the exhumed level corresponds to temperatures below the onset of quartz plasticity (e.g. Stöckhert et al., 1999; Cembrano et al., 2000). Likewise, the wide time-span available for the cooling of the plutons along both sides of the LOFZ allow older ductile deformation at depth to be preserved in the rocks, not related to the late history covered by the fission track results.

Samples AA42 and AA4, from rapidly cooled Miocene plutons at the southern part of the Reloncaví Estuary show little deformation, but a marked oscilatory zoning in plagioclase grains. These probably reflect cyclic changes in the intensive parameters throughout the magma chamber (e.g. Johnson et al., 1994). Similar textures have been reported from samples of shallow-level plutons at the coastal magmatic arc of northern Chile (Grocott et al., 1994).

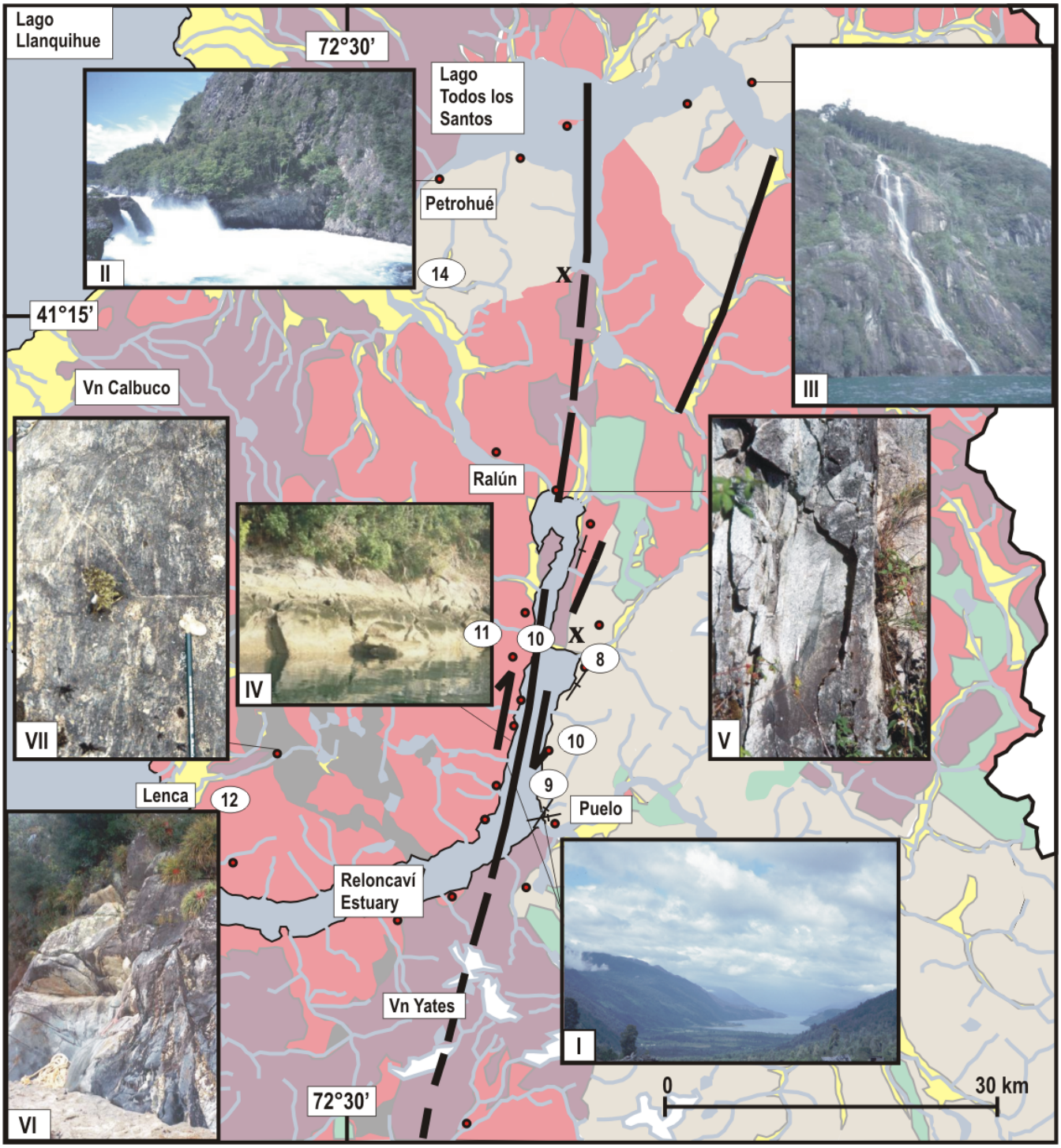

Figure 5.1a: Mesoscopic structures in the Reloncaví Area. Refer to discussion in section 5.1.1.

Geological map after Duhart et al.(2000)

- Quaternary sediments
- Quaternary volcanic rocks
- Miocene plutonic rocks
- Jurassic-Cretaceous volcanic rocks
- Cretaceous plutonic rocks
- Metamorphic basement rocks

- Main lineaments of the LOFZ
- (9) Al-in Hb Crystallization depths (Seifert et al., 2003)
- x Inferred offset marker (see text for discussion)
- Sample for microstructure analysis and/or FT dating

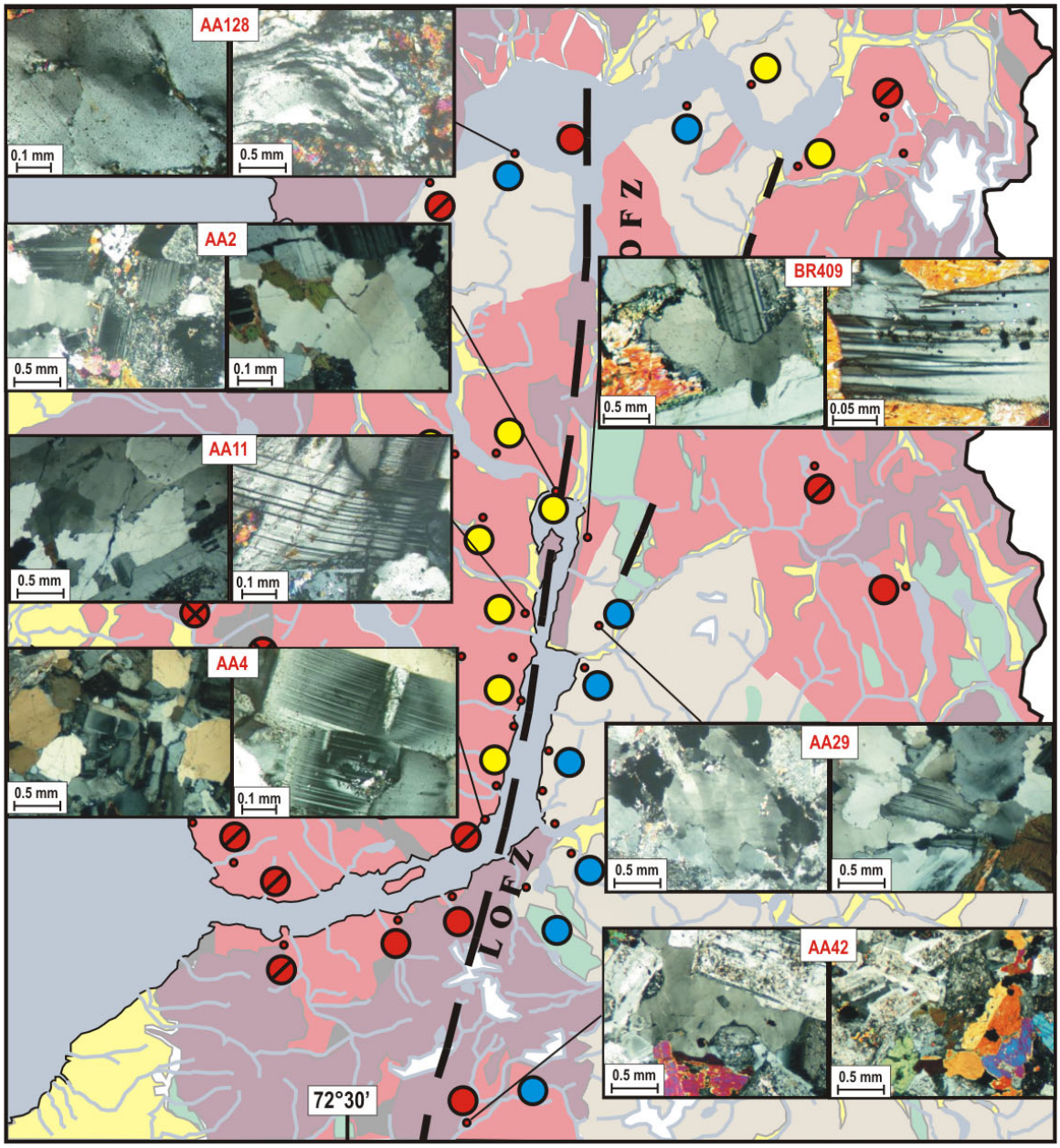

Figure 5.1b: Characteristic microstructures in samples from the Reloncaví Area. The microstructures of the samples are cited and discussed in section 5.1.2.

Geological Map after Duhart et al. (2000)

- Quaternary sediments
- Quaternary volcanic rocks
- Miocene plutonic rocks
- Cretaceous plutonic rocks
- Jurassic-Cretaceous volcanic rocks
- Late Paleozoic metamorphic rocks
- Sample for Microstructure Analysis and/or FT Dating

Thermal History (see chapter 6)

~5Ma ~10Ma ~15Ma — Shallow intrusion and rapid cooling in the upper crust (<5km)

Slow denudation with moderate cooling rates (exhumation from >10km)

Cretaceous intrusions in the upper crust, exhumation from 3-7 km in the Late Miocene- Pliocene

5.2 Structural Observations in the Hornopirén Area

The structure of the Hornopirén area is defined by one NS-trending, arcuate, concave to-the-east fault strand of the LOFZ along the eastern border of the Cholgo channel (figure 5.2a). Along both sides of the fault zone a small plutonic complex of Late Miocene to Pliocene age has intruded into Cretaceous and Miocene parts of the NPB and its metamorphic wallrocks. Contact relations between plutons are based on geological maps from Cembrano et al. (1996, 2000) and Duhart et al. (2000), together with compiled thermochronologic data from Pankhurst et al. (1992), Cembrano et al. (2000) and SERNAGEOMIN-BRGM (1995). A pattern of sequential intrusion and deformation along the LOFZ is outlined in the following sections.

5.2.1 Field observations in the eastern block at Hornopirén

Tonalites of Miocene age located at the eastern border of the LOFZ display zones with pronounced fault-related foliation overprinting a previous magmatic foliation (figure 5.2a, images IV-VI). The magmatic foliation is evident by the alignment of euhedral feldspar and quartz grains, with deflections around large microgranitoid enclaves. Synplutonic mafic dikes cutting through the foliation and zones with lensoid compositional heterogeneity were observed within the tonalites (figure 5.2c), indicating magmatic flow for the origin of the foliation of the rocks (Paterson et al., 1989).

The tectonic foliation in these rocks is defined by zones with regular alignment of flattened quartz and feldspar aggregates. It is roughly oriented in NNW direction, and in general dips steeply to the E. Its extension to the north was observed beyond the outcrops of the plutons, affecting metamorphic and pyroclastic wallrocks (compare image IV in figure 5.2a, samples AA43-AA113 in figure 5.2b) near Río Negro on the eastern border of the LOFZ. The obliquity of the foliation with respect to the orientation of the main trace of the LOFZ may indicate a dextral shear sense. Towards the south, the foliation within the plutonic units disappears near Pichanco, where outcrops of undeformed coarse-grained tonalites and granodiorites suggest a post-tectonic emplacement. This interpretation is supported by the U-Pb intrusion age of ca. 10 Ma for the deformed rocks near Cholgo, reported by Cembrano et al. (2000), and the Rb-Sr whole-rock isochron of ca. 5 Ma for a coarse grained tonalite and associated finer grained diorites and aplites near Pichanco, reported by Pankhurst et al. (1992).

5.2.2 Microfabrics in samples from the eastern block at Hornopirén

Microfabrics of the foliated tonalites reveal solid-state deformation overprinting a previous magmatic foliation (figure 5.2b, 5.2d). The magmatic fabric is evident from the alignement of the feldspar crystals, surrounded by aggregates of quartz, biotite, and amphibole (e.g. Paterson et al. 1989). The quartz domains display variable fabrics, ranging from undulatory extinction and deformation lamellae to subgrains and grain boundary migration (Sample AA53, figures 5.2b-d). Plagioclase grains display deformation twins, are often kinked and fragmented, and in places the fractures are sealed with quartz and biotite.

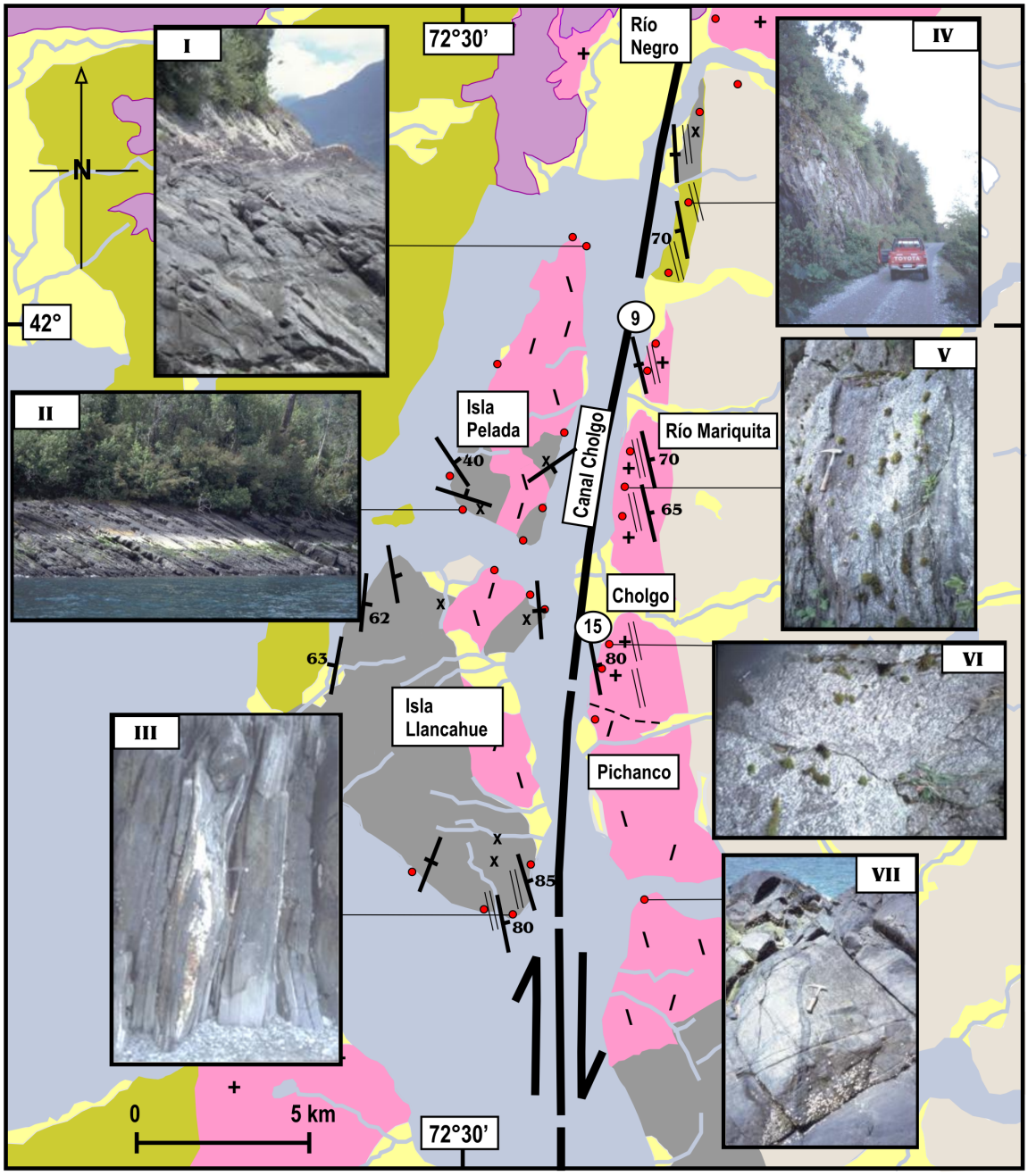

Figure 5.2a: Mesoscopic structures in the Hornopirén Area. Refer to discussions in sections 5.2.1 and 5.2.3.

Geological map after Cembrano et al.(2000) and Duhart et al. (2000)

- Quaternary sediments
- Quaternary volcanic rocks
- Undifferentiated Miocene and Pliocene plutonic rocks
- Miocene plutonic rocks
- Mid-Tertiary volcanic rocks
- Cretaceous plutonic rocks
- Metamorphic Basement rocks

- Sample for Microstructure Analysis and/or FT Dating
- Areas with strongly foliated rocks
- x Areas with contact metamorphism
- 50 Strike/dip of foliation
- (9) Al in Hb crystallization depth [km] (Seifert et al., 2003)

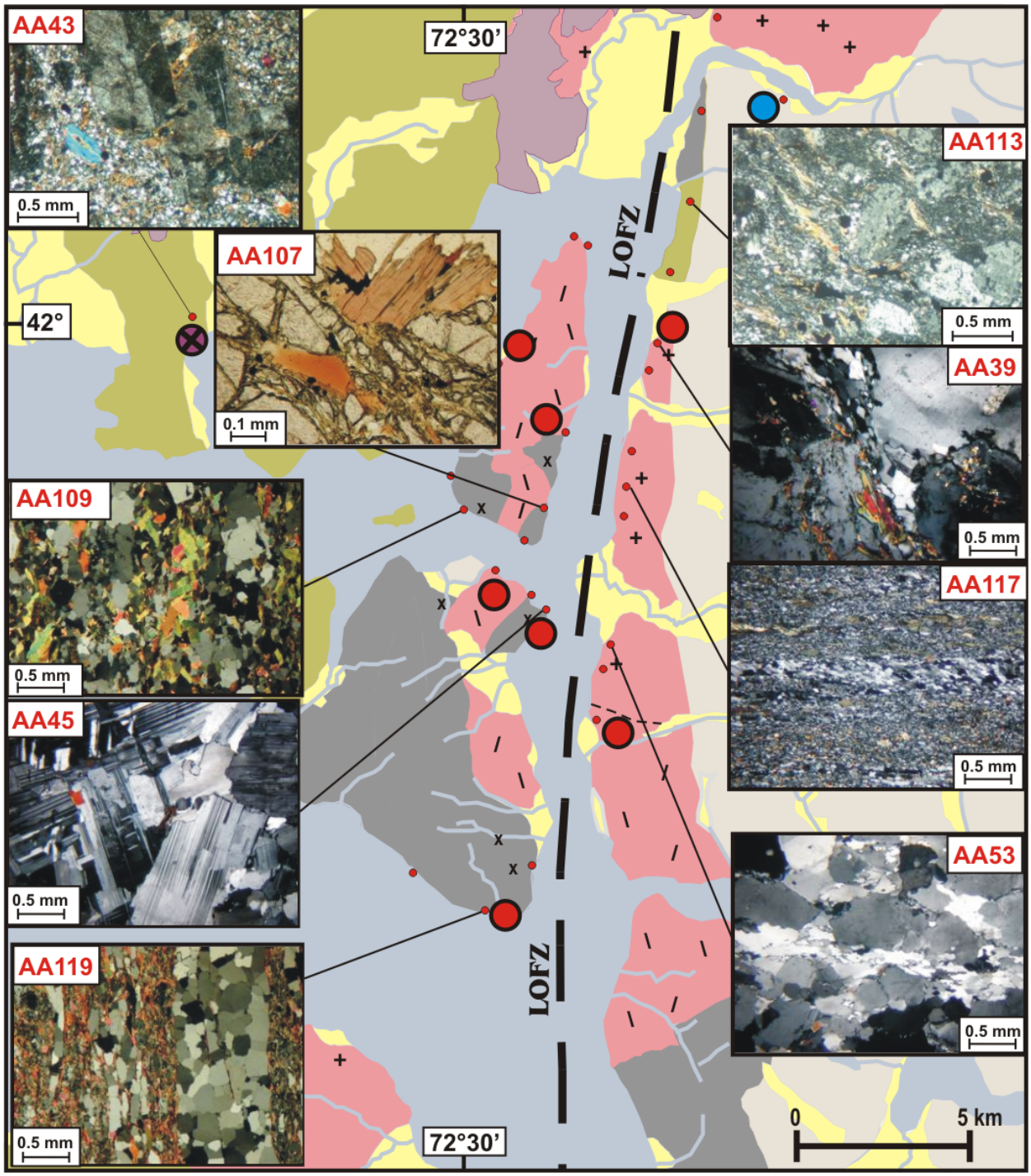

Figure 5.2b: Characteristic microstructures in samples from the Hornopirén Area. Refer to descriptions in sections 5.2.2 and 5.2.4.

Geology

- Quaternary sediments
- Quaternary volcanic rocks
- Undifferentiated Miocene and Pliocene plutonic rocks
- Miocene plutonic rocks
- Mid-Tertiary volcanic rocks
- Cretaceous plutonic rocks
- Metamorphic Basement rocks
- Sample for Microstructure Analysis and/or FT dating

Thermal History (see chapter 6)

- Shallow intrusion and rapid cooling in the upper crust (<5km)
- ~5Ma
- rapid cooling after volcanic extrusion (~ 14 Ma)
- Cretaceous intrusions in the upper crust, exhumation from 3-7 km in the Late Miocene-Pliocene

The magmatic biotite and amphibole crystals are often kinked and fractured, locally replaced by new fine-grained aggregates (sample AA126, figure 5.2d). In general these microstructures indicate deformation in the greenschist facies by ca. 300°-400°C (regime 1 from Hirth and Tullis, 1992; Simpson, 1985; Stöckhert et al., 1999).

Well developed S-C fabrics (Lister and Snoke, 1984; Dell'Angelo and Tullis, 1989) at the microscopic scale were observed in samples AA117 and AA126, located within dark-coloured shear zones near río Mariquita (figures 5.2b-e). The s-planes are defined by the preferred orientation of the long axes of homogeneously flattened quartz grains (with sizes of ~10μm) oblique to shear bands (c-planes). In some cases, the shear bands tend to anostomose around feldspar porphyroclasts (e.g. AA126 in figure 5.2d). For the available samples, the S-C fabrics indicates a dip-slip displacement with the relative upward displacement of the eastern block.

S-C fabrics are characteristic of deformation by dislocation creep at green schist facies to lower amphibolite facies conditions, and may be related to a transition from magmatic flow to solid-state flow during the cooling of the plutons (e.g. Paterson et al., 1989). Nevertheless, little evidence for solid-state deformation at high temperatures was found in the samples from this area. Paterson et al. (1989) point out that tectonic foliations in granitites tend to be heterogeneous in intensity of development. Once strain increases in discrete zones, fluid activity and associated strain-softening processes will promote continued deformation there, rather than initiating deformation in non-foliated domains (Paterson et al., 1989). This could explain as well the restricted distribution of the mylonites within the study region.

5.2.3 Field observations in the western block at Hornopirén

Plutons located at the western side of the LOFZ are predominantly dioritic to tonalitic in composition, and often display compositional layering with aplitic segregations. These were observed in unfoliated and weakly deformed rocks (figures 5.2a-f).

Outcrops of quartz-mica schists at the southeastern shore of the Llancahué island display a very regular NNW-trending and steeply dipping foliation, following the general tectonic grain (image III in figure 5.2a). The metamorphic basement rocks on other parts of the island display an irregular foliation, following the regional schistosity or disrupted by contact aureoles (figure 5.2f). On the eastern side of the island, intercalations of basic volcanic rocks are present within the metasediments, some of which preserve pillow structures. The mafic rocks are considered to constitute remnants of an ophiolite of unknown age, which probably intruded into the accretionary complex during its formation (Pankhurst et al., 1992).

Contact metamorphic associations of andalusite, cordierite, and sillimanite, formed in pelitic schists and gneisses of the basement rocks on Llancahué Island have been reported by Pankhurst et al. (1992). The phase assemblages indicate low pressure conditions (~2 kbar), constrained by intersection of the *andalusite =sillimanite* equilibrium curve of Holdaway (1971) and the breakdown reaction curve *muscovite + cordierite = andalusite + biotite+ Kfeld + H_2O* (Spear and Cheney, 1989). This is consistent with shallow level of emplacement for the intruding rocks in the island.

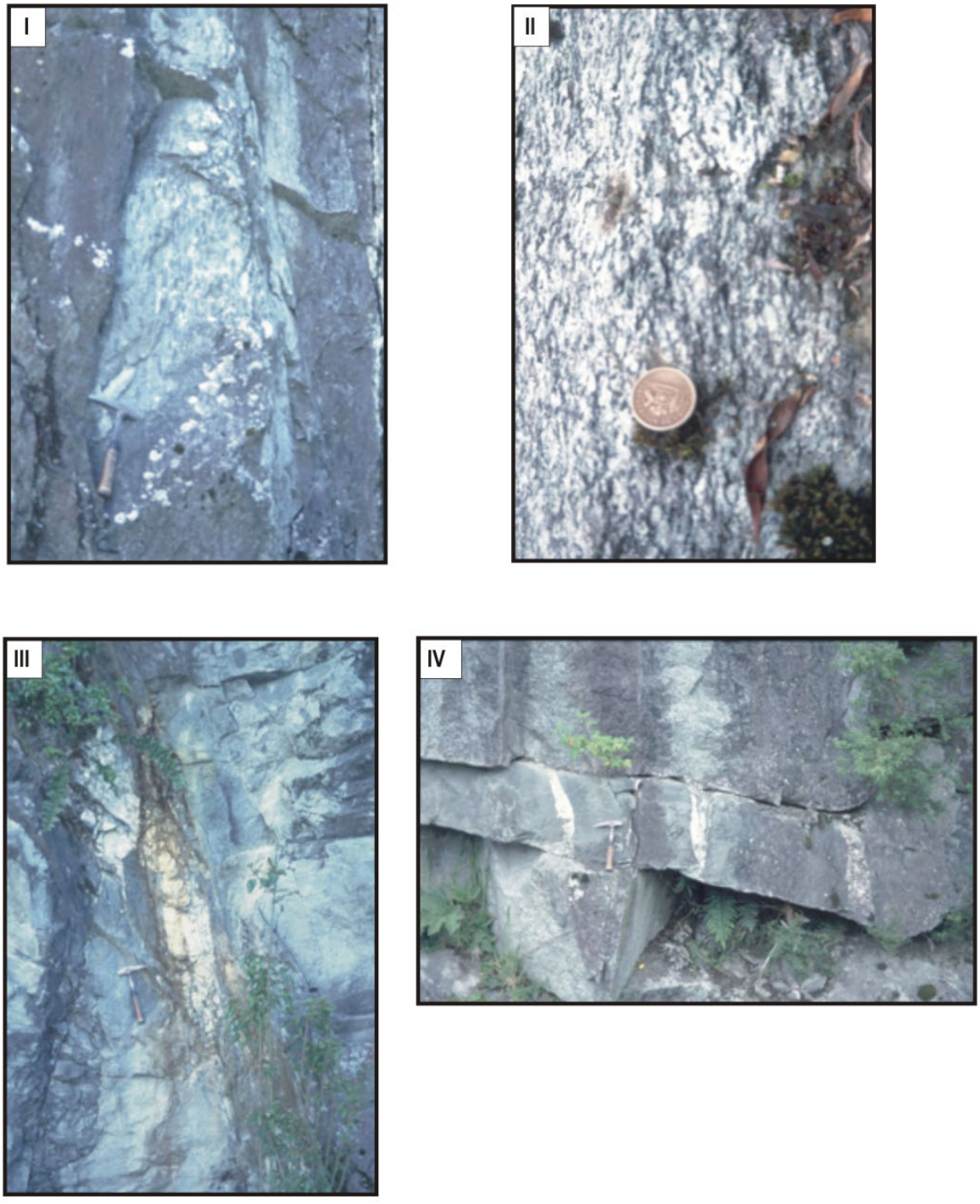

Figure 5.2c: Magmatic flow structures in the foliated tonalites from the Hornopirén area. Refer to discussion in section 5.2.2.

I) Lensoid microgranitoid enclaves, parallel to foliation, flattened by later solid-state deformation.
II) Coarse grained, Imbricate foliation of quartz-feldspar and mafic cumulates.
III) Aplitic segregations and schlieren layering, orientated parallel to the foliation.
IV) Synplutonic mafic dike with quartz segregations cutting through the magmatic foliation.

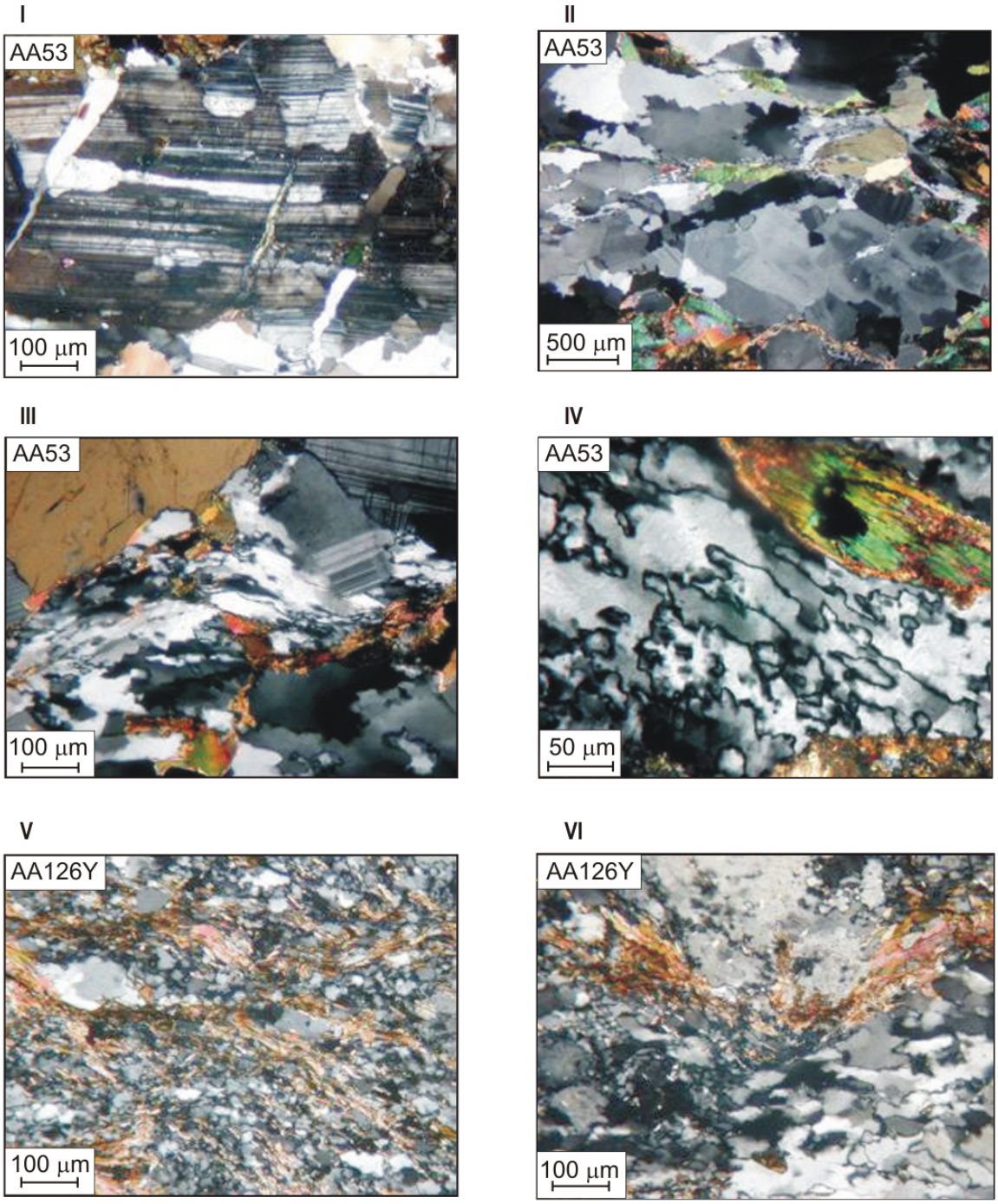

Figure 5.2d: Solid-state deformation in the foliated tonalites from the Hornopirén Area. Refer to discussion in section 5.2.3.

I) Fractured plagioclase sealed with quartz and biotite.
II) Magmatic aligned feldspar and quartz domains. Large biotites are kinked recrystallized with a fine size.
III) Quartz ribbons deflected around fractured feldspar and amphibole grains.
IV) Sutured grain boundaries, recrystallized grains, and subgrains in quartz.
V) Fine-grained, dynamically recrystallized quartz. Alignment of biotite flakes makes shear bands.
VI) Dynamically recrystallized quartz, biotite aggregate flowing around a rotated feldspar porphyroclast.

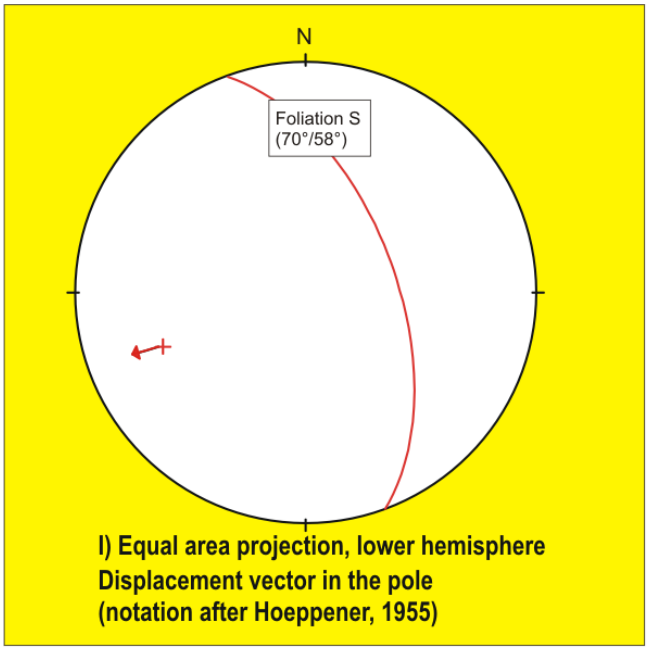

I) Equal area projection, lower hemisphere
Displacement vector in the pole
(notation after Hoeppener, 1955)

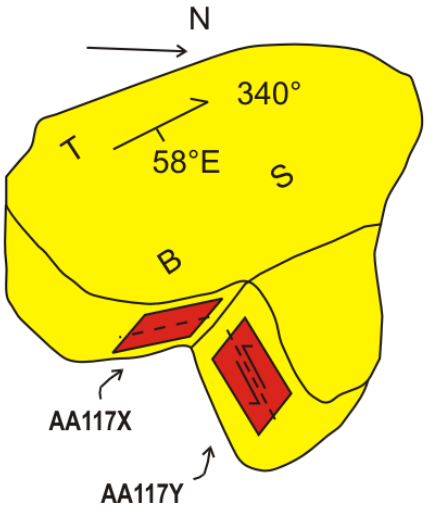

II) Sketch of the sample orientation.
T=top, B=bottom,
S=foliation plane

III)

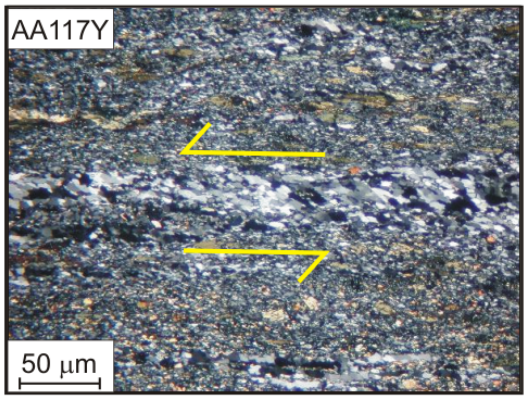

IV)

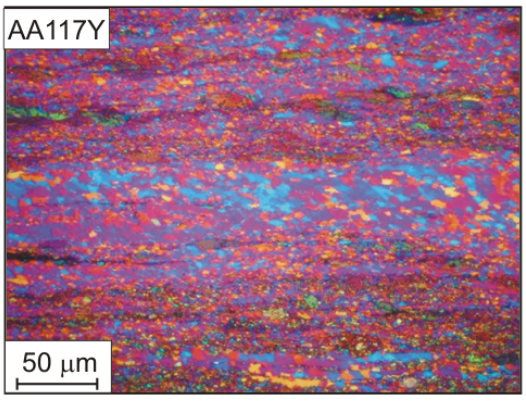

VI)

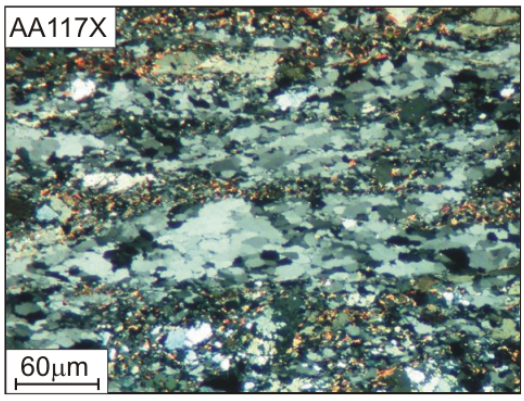

VI)

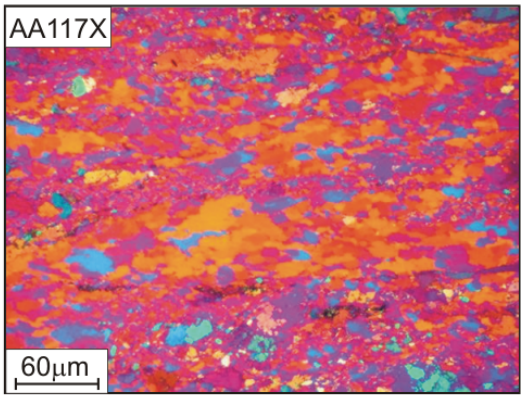

Figure 5.2e: Photomicrographs of SC-fabrics in sample AA117, at the eastern side of the LOFZ in the Hornopirén area. A marked obliquity in the quartz shape preferred orientation (SPO) is visualized by the arrows in image III. The images IV and VI, with the compensator red I inserted, reveal a pronounced CPO of quartz. Kinematic reconstruction indicates a reverse displacement, with the eastern block of the LOFZ uplifted. Refer to sections 5.2.2 and 5.2.5 for discussion.

5.2.4 Microfabrics in samples from the western block at Hornopirén

Towards the west of the LOFZ, the microstructures of the plutonic rocks indicate either deformation under low temperature conditions, or only very weak deformation (e.g. samples AA107-AA45 in figure 5.2b). In sample AA45, the feldspars show microfractures and widespread mechanical twins, also kink bands. Quartz fabrics are characterized by undulatory extinction and deformation lamellae; subgrains are also locally developed. Biotites are kinked and fractured. Other samples from different parts of the western block show less deformation, except for some plagioclase with deformation twins, quartz with undulatory extinction, and biotites slightly kinked. Such microstructures are indicative of weak deformation in the low-temperature plasticity field with subordinate recovery, generally observed at temperatures below 300° (e.g. Stöckhert et al., 1999).

Samples of the mica schists from Llancahué Island reveal quartz layers displaying an isometric polygonal grain shape, with straight or simply curved grain boundaries (e.g. samples AA119 and 109). The microstructure indicates boundary area reduction. In the absence of abundant water along the grain boundaries, these microfabrics suggest a stage of very low stress at high temperatures after deformation (e.g. Bons and Urai, 1992; Paschier and Trouw, 1996).

Muscovite and biotite Ar-Ar ages of 10 Ma and 7 Ma, respectively, have been reported for these outcrops by Cembrano et al. (2000), whereas similar and younger biotite ages have been obtained for the weakly deformed plutons at the islands west of the LOFZ (SERNAGEOMI, 1995, Cembrano et al., 2000). If the foliation of the southern outcrops of the metamorphic basement rocks is related to the LOFZ, then this data suggest post-tectonic magmatic activity along its western flank. If this is true, a renewed activity of the fault zone would be recorded by the younger, weakly deformed plutons exposed on the islands.

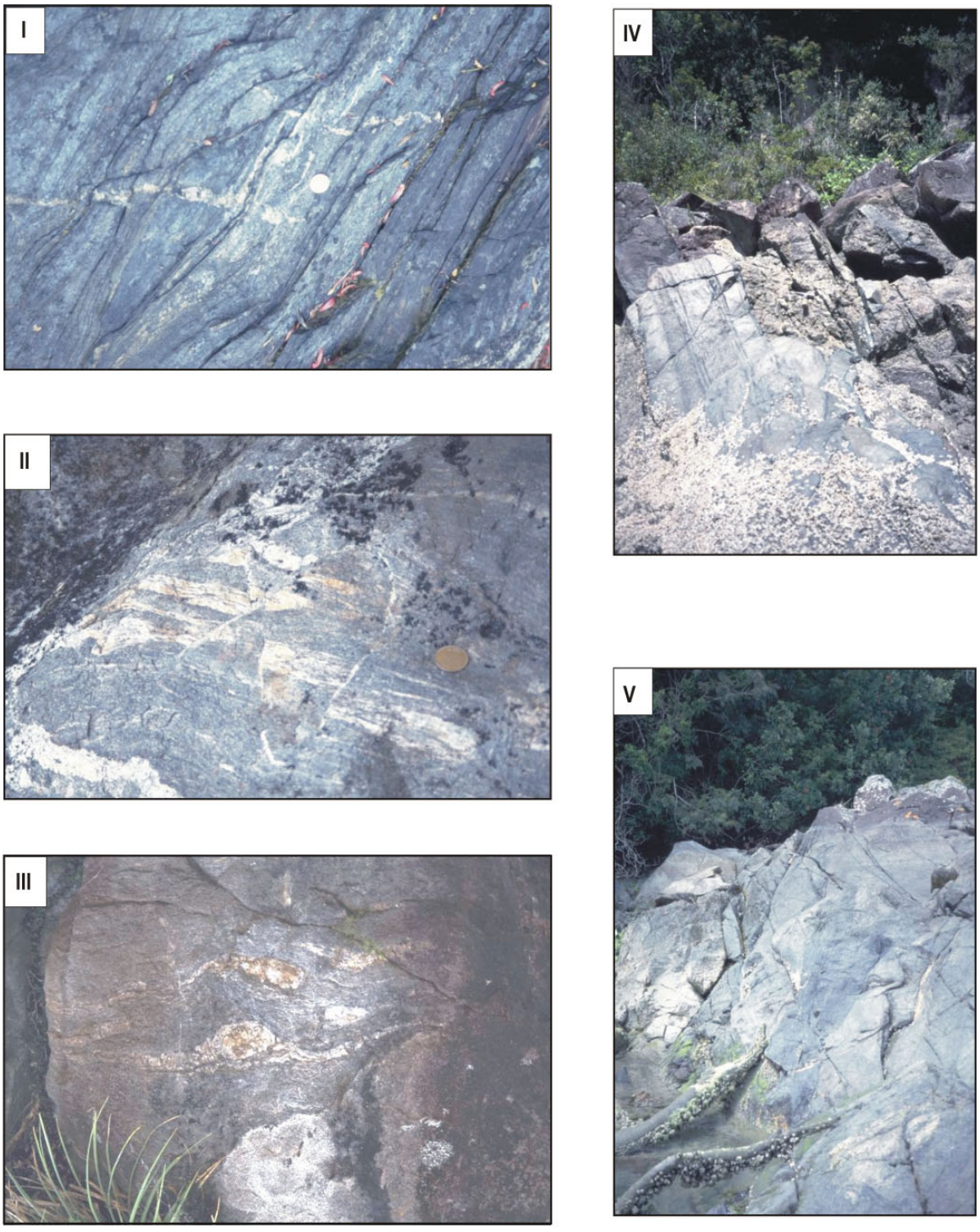

Figure 5.2f: **Field aspects of the metamorphic and plutonic rocks from the Llancahué and Pelada islands.**

I) Coarse-grained mica schists with transposed tectonic foliation and discordant quartz veins.
II) Conjugate shears displacing quartz layers, abundant discordant quartz veins.
III) Irregular transposed foliation, with relict quartz layers displaying tight isoclinal folds.
IV) Schlieren layering
V) Synplutonic mafic dikes within weakly deformed diorites and tonalites.

5.2.5 Evidence for vertical displacement in the Hornopirén Area

Al-in-hornblende crystallization depths of the plutonic rocks at the eastern side of the LOFZ yield ~15 km at Cholgo and ~8 km near río Mariquita (figure 5.2a, Hervé et al., 1996; Seifert et al., 2003). In contrast, on the western side of the fault zone, the metamorphic associations from contact aureoles suggest shallower levels of intrusion for the plutons on Llancahué Island (~6 km, Holdaway, 1971; Spear and Cheney, 1989). If the exposed plutonic rocks on both sides of the fault zone represent a single magma chamber, relative uplift of the eastern block is implied. This interpretation is supported by the contrast in deformation conditions observed across the fault zone, and by the kinematic indicators obtained at the eastern side (figure 5.2, section 5.2.2).

In the Hornopirén area, all thermochronologic data sets on both sides of the LOFZ indicate rapid cooling of the plutons between about 5Ma and 3Ma (see chapter 6). These patterns have been interpreted to correspond with cooling after shallow-level emplacement. Independent evidence for shallow level intrusion at the western block of the LOFZ is provided by the contact metamorphic associations on Llancahué Island. In addition, the data indicate the age of cessation of the fault activity.

For the eastern block two possible interpretations arise:

a) The sheared Miocene plutons from Río Mariquita and Cholgo correspond to deeper levels of the NPB, rapidly exhumed after emplacement. Significant denudation should have occurred in a single event in the Late Miocene-Pliocene.

b) The sheared plutons were syntectonically emplaced in an earlier stage and deformation took place during their post-magmatic cooling. Arguments favouring syntectonic intrusion (e.g. Paterson et al. 1989) are the continuity of the foliation of the wallrocks with the magmatic and solid-state foliation of the plutons, the S-C fabrics, and the elongated geometry of the plutons outlined in the map of the area.

5.3 Synthesis

An episodic history of intrusion and deformation along the LOFZ has been observed within the Reloncaví and Hornopirén Areas. Different styles of deformation in the plutonic rocks appear to be related to their cooling paths and by variable vertical components along the fault zone. A total dextral displacement of ca. 30 km is inferred from the geology of the region, with relative west block uplift along the Reloncaví estuary, and important relative east block uplift at Hornopirén. The deformation in the exhumed plutons with steady and moderate cooling rates during the Late Miocene was observed at temperatures below ~300°C. Instead, some Cretaceous samples display deformation at higher temperature conditions, indicating previous activity at depth along the fault zone. In the Hornopirén Area, significant eastward block uplift is indicated by the different grades of deformation across the fault zone, kinematic analysis on deformed tonalites, geobarometry, and contact metamorphic phases. Late Miocene-Pliocene syntectonic emplacement is proposed in the Hornorpirén area, overprinting earlier phases of deformation and intrusion along the LOFZ.

6. Cooling History of the North Patagonian Batholith and Regional Denudation: Discussion

It has been shown in the previous chapters that the North Patagonian Batholith is not a single homogeneous plutonic unit, but instead a composite of sequentially intruded plutons emplaced at different crustal levels of the Main Andean Range. This chapter addresses the different cooling histories of the plutons of the NPB in relation to the activity of the Liquiñe-Ofqui fault zone within the Chiloé and Los Lagos Regions (41°-42°S). Thermal constraints for the interpretation of magmatic cooling are first presented and discussed, followed by a classification, in terms of time-Temperature (t-T) histories, for different classes of plutons of the NPB, based on integrated thermochronologic and geobarometric data. The regional distribution of the cooling curves is observed in relation to the activity of the LOFZ, and the timing and nature of denudation along the fault zone are examined in relation to the migrating position of the CTJ. Following a discussion on the assumptions on the paleo-geotherm in the region, denudation rates along the LOFZ are finally estimated, supported with structural and geobarometric constraints. The chapter resumes with some important implications for the Late Cenozoic denudation history and landscape evolution of the southern Andes.

6.1. Thermal Considerations for the Construction of Time-Temperature (t-T) Paths

The interpretation of the thermochronologic data is generally based on the closure temperature concept (Dodson, 1973), that is, the temperature for a given system at the time represented by its apparent age. For normal isotopic systems this is the temperature at which atomic diffusion effectively ceases or becomes nil in a geologic time frame. For a given system, the closure temperature is a function of the cooling rate, mineral composition, defect structure, and other specific properties that are still not completely constrained (e.g. Harrison et al., 1985; Stöckhert et al., 1999). Nevertheless, closure temperatures have been established for most geochronologic systems, which appear to yield consistent results in most studies on natural systems (e.g. Hodges, 1991; Stöckhert et al., 1999).

A precondition to integrate fission track systems with normal isotopic systems in the low temperature part of cooling paths is that the studied samples have not undergone any complex thermal history at low temperature (ref. chap. 3.5). This is plausible in this study because all of the apatite FT samples investigated in the Main Range display track length distributions indicating normal to fast cooling histories (chapter 4). However, several zircon FT ages along the fault zone suggest some degree of thermal overprinting. Their interpretation for the t-T paths requires special consideration. Miocene zircon FT ages belong in most cases to samples being rapidly cooled from originally much higher temperatures, so they are included in the t-T paths. Samples of Cretaceous plutons with high age dispersions may indicate a history of reburial and exhumation, although this seems unlikely in the study area due to the few amount of Cenozoic overburden.

Numerical modelling on the thermomechanical properties of ascent and emplacement of granitic intrusives (Kukowski et al., 1989, Kukowski and Neugebauer, 1990; Kukowski, 1992) reveal that viscosity contrasts and absolute viscosity of magmas determine the splitting behaviour and differing emplacement levels of magma chambers, in concordance to what is observed in several plutonic complexes from different orogenies. While ascent and emplacement take place relatively rapidly (within ~0.8-1 Ma), the cooling of these bodies can persist over time scales several orders of magnitudes larger. At depths of ~20-10 km large plutons may retain heat flow density levels exceeding 170mW/m^2 over 10^5 years. At such emplacement levels, buoyancy alone is not sufficient to account for significant uplift in the crust, and conductive cooling processes take place over in a much larger geological time-scale, with heat flow density levels remaining between 80 and 100mW/m^2.

Within the upper ~15 km of the crust, thermal channels (with temperatures exceeding 900°C) in the magma tic systems define themselves for timescales of up to ~2Ma, allowing for splitting of magma chambers with contrasting densities and emplacement at different levels. At shallow levels in the upper crust (~5km), heat transfer within a magma chamber is more likely to occur through thermal convection and hydrothermal fluid advection. Depending on the permeability of the wallrocks, the anomalous heat flow distorts the shape and distribution of the geothermal gradients in their surroundings, lifting and flattening the isotherms above the chamber to the Earth's surface. Furthermore, if the base of the chamber is connected through channels with hotter magma, the thermal perturbations and fluid circulation may continue for several millions of years (Kukowski, 1992; Best, 2002).

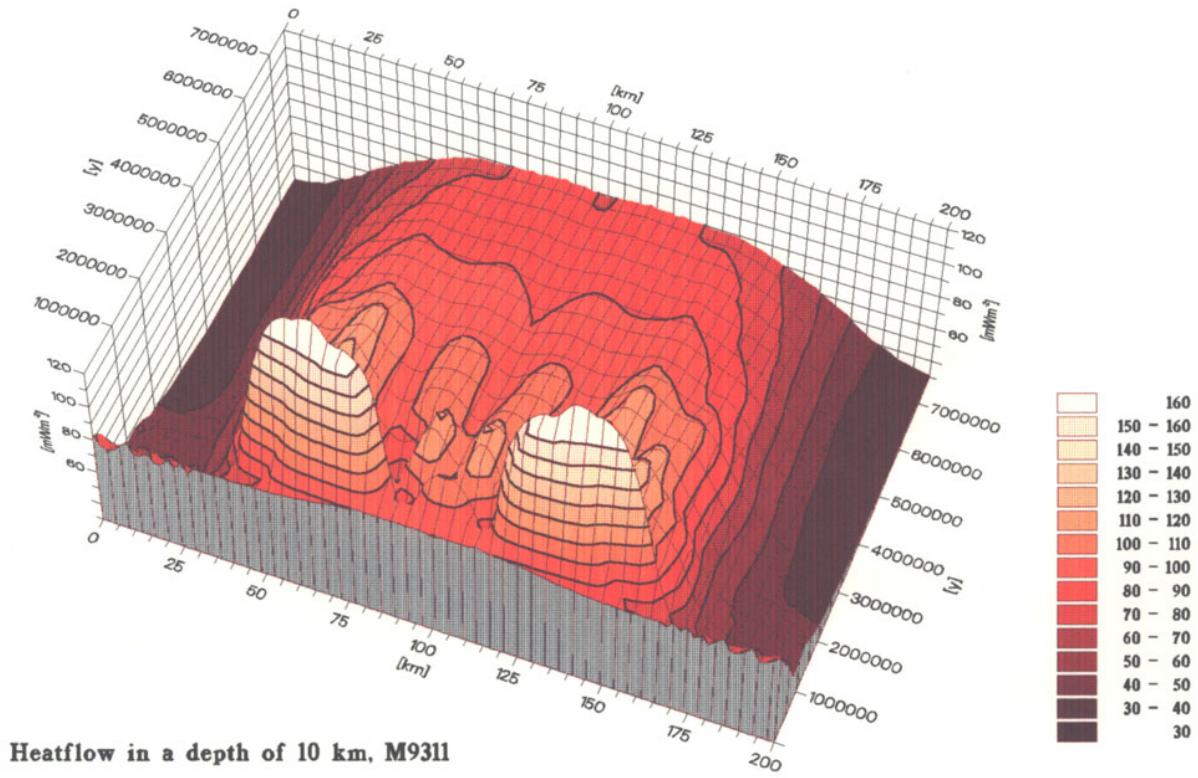

Figures 6.1a: Time-variation of the surface heat flow density (in mWm^{-2}) during the conductive cooling of an ideal magma chamber at a depth of 10 km in the upper crust, after finite element modelling by Kukowski (1992). In the figure, the vertical heat flow density is projected in coloured surfaces against the horizontal long axis of the modelled chamber (which has an ellipsoidal form), and time (in years). The figure describes the redistribution of heat through thermal channels in the chamber during the early stages of cooling after emplacement, resulting in the splitting of the chamber into two different portions.

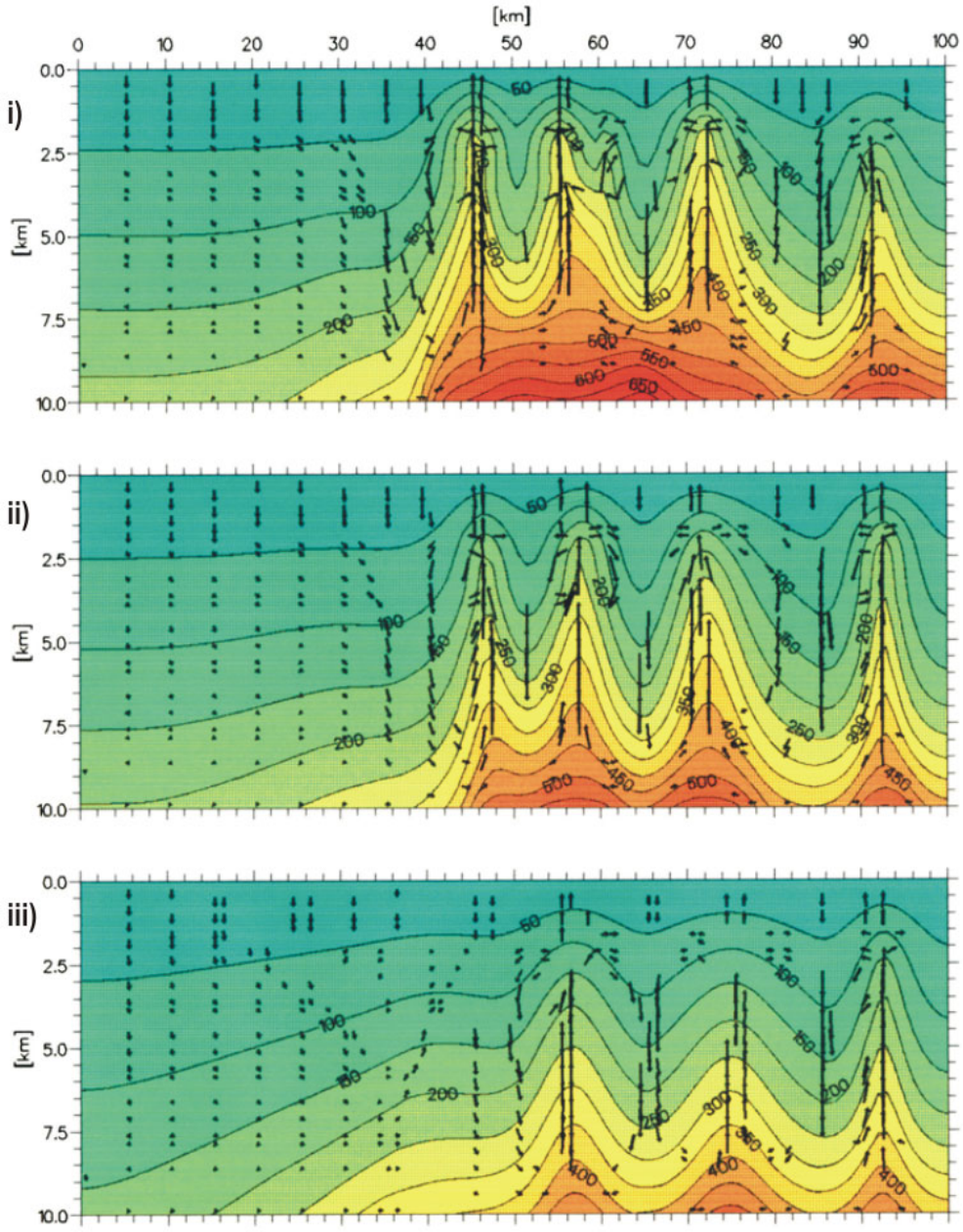

Figure 6.1b: Scheme of the time-evolution of the upper crustal isotherms (in °C) and fluid velocity vectors (represented with arrows) during a convective hydrothermal event (from Kukowski, 1992). Caption (i) shows the position of the isotherms after 0.7 Ma, (ii) by 1.6 Ma, and (iii) by 6.3 Ma.

6.2 Time-Temperature (t-T) plots from the North Patagonian Batholith

Time-temperature plots for the rocks of the NPB have been constructed based on the integration of zircon and apatite FT cooling ages with available thermochronologic data from related outcrops (chapters 2 and 4). The closure temperatures defining the t-T paths in this study are based on widely accepted values. Higher cooling rates may

be expected along active orogens (in particular within magmatic arc settings) than in anorogenic zones, thus the upper ranges of the partial annealing zones for the apatite and zircon FT system have been considered as a proxy for a closure temperature (e.g. Thomson, 2002; Stöckhert et al., 1999).

U-Pb zircon and whole-rock Rb-Sr ages have been assumed to give the time of magmatic intrusion (e.g. Faure, 1986). Amphibole K-Ar and Ar-Ar closure temperatures were set in a transition zone from "deep to shallow" cooling at 500°±50°C (Harrison, 1981). Generally accepted closure temperatures of 350°±50°C and 300°±50°C have been assumed for the low temperature magmatic and/or metamorphic cooling K-Ar and ^{40}Ar-^{39}Ar ages on muscovite and biotite (Purdy and Jäger, 1976; Stöckhert et al., 1999). Extrapolated closure temperatures for the zircon and apatite fission track system have been assumed by 280°±30°C and 100°±20°C respectively.

Where available, t-T paths for the apatite FT system were constructed using inverse modelling from Laslett et al. (1987), based on the well-known annealing characteristics of the Durango apatite (chapter 3.5.1). The modelling was assisted with the software AFTsolve© (Ketcham and Donelick, 2000), and set up with an initial track length of 15.7 μm. Nevertheless, the interpretation of the t-T paths applied in this study is focussed mainly on magmatic cooling processes, which can be better visualized at a larger temperature range than that of the apatite partial annealing zone. 51 cooling paths have been obtained from the main Andean range and are included in appendix 4. The shape of the derived t-T plots allowed classification of the cooling histories into three main types, shown in figures 6.2a-b:

Type-A paths describe very slow cooling rates (up to 2.5°C/Myr for temperatures below 310°C) following Cretaceous emplacement (occurred in a rapid event) at depths of ~7-10 km, followed by rapid cooling and exhumation in the late Miocene-Pliocene (~50°C/Myr below 150°C). These have been constructed based on the correlation of zircon and apatite FT ages with mid-Cretaceous biotite K-Ar and Ar-Ar cooling ages from the area (Carrasco, 1995; Sernageomin, 1995). The emplacement depths are supported with available Al-in-Hornblende geobarometry data from similar outcrops (Seifert et al., 2003).

The wide time-span in the t-T plots nevertheless allows the possibility that these have been reburied after previous denudation (figure 6.2b). This is difficult to constrain, since in the studied region no information of a denudation event prior Miocene times can be directly inferred from field or from the apatite track length distributions. The closure temperature of the apatite FT system may be reset by a thermal event along the fault zone, due to fluids or to the effect of heat advection and topography during denudation (see chapter 6.3).

Type-B paths characterize a history of steady cooling, with cooling rates ranging from 30° to 50°C/Myr after emplacement at moderate depths, since Cretaceous (?) to early Miocene times. The steady cooling rates suggest that these plutons were exhumed from an emplacement depth exceeding 10 km, which is in good agreement with Al-in-hornblende geobarometry from the area, although no intrusion dates are presently available for these plutons.

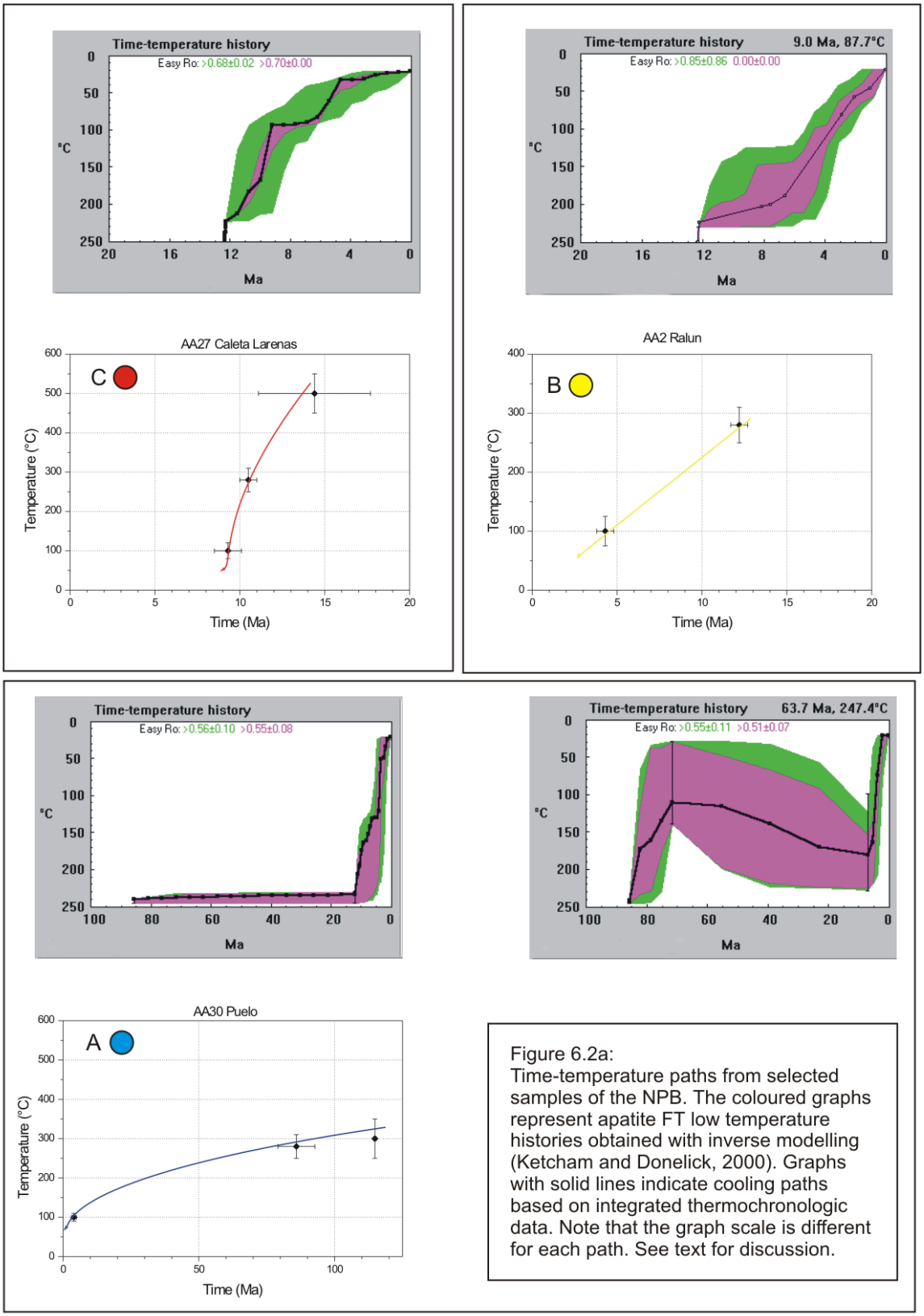

Figure 6.2a:
Time-temperature paths from selected samples of the NPB. The coloured graphs represent apatite FT low temperature histories obtained with inverse modelling (Ketcham and Donelick, 2000). Graphs with solid lines indicate cooling paths based on integrated thermochronologic data. Note that the graph scale is different for each path. See text for discussion.

Type-C paths indicate very rapid cooling after emplacement at a shallow levels in the upper crust, e.g. less than ~5 km. Cooling rates well-exceed values of 50°C/Myr, in some cases comparable to those described at deformation zones in core-complex settings (e.g. Johnson et al., 1997). However, here such rates indicate a shallow level of emplacement of the plutonic units, as discussed in the previous section.

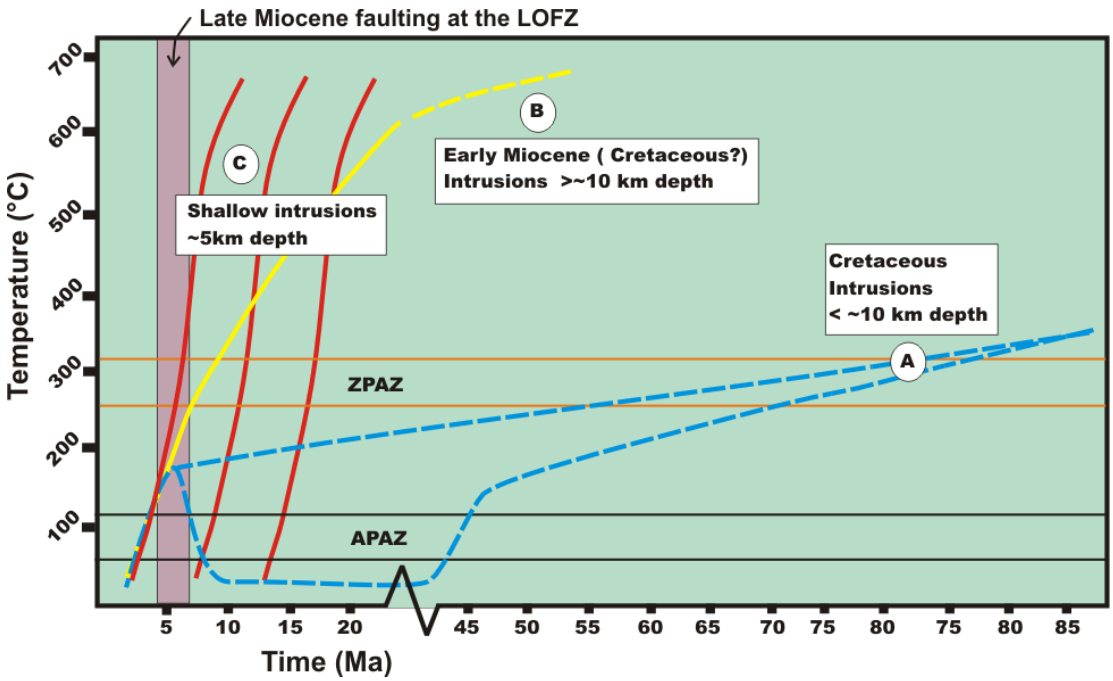

Figure 6.2b: Scheme of the Time-Temperature histories from the plutons of the NPB in the Chiloé and the Los Lagos regions along the LOFZ. The main denudation event related to the LOFZ in the study area is constrained by the zircon and apatite FT cooling ages along the fault zone (see section 6.3). Type-A curves indicate slow cooling followed by rapid cooling and exhumation in the Late Miocene-Pliocene (or Late Miocene-Pliocene thermal resetting after previously being denuded). Type-B curves describe steady cooling with moderate rates, followed by rapid cooling and exhumation in the Late Miocene-Pliocene. Type-C curves represent shallow-level intrusions, very rapidly cooled after emplacement. Three schematic shallow intrusion events are outlined in the study region. The youngest event coincides with the end of the proposed denudation event along the LOFZ. See text for discussion.

The regional distribution of the cooling path types within the rocks of the NPB is shown in figures 6.2c-d. In the Reloncaví area (figure 6.2c), type-A cooling paths are scattered mainly along the eastern border of the Reloncaví estuary, across the Todos los Santos Lake, and at the eastern side of the Main Range. Type-B paths are distributed mainly on the western side of the Reloncaví area, concentrated on the western border of the estuary, and as well at the eastern border of the Todos Los Santos Lake.

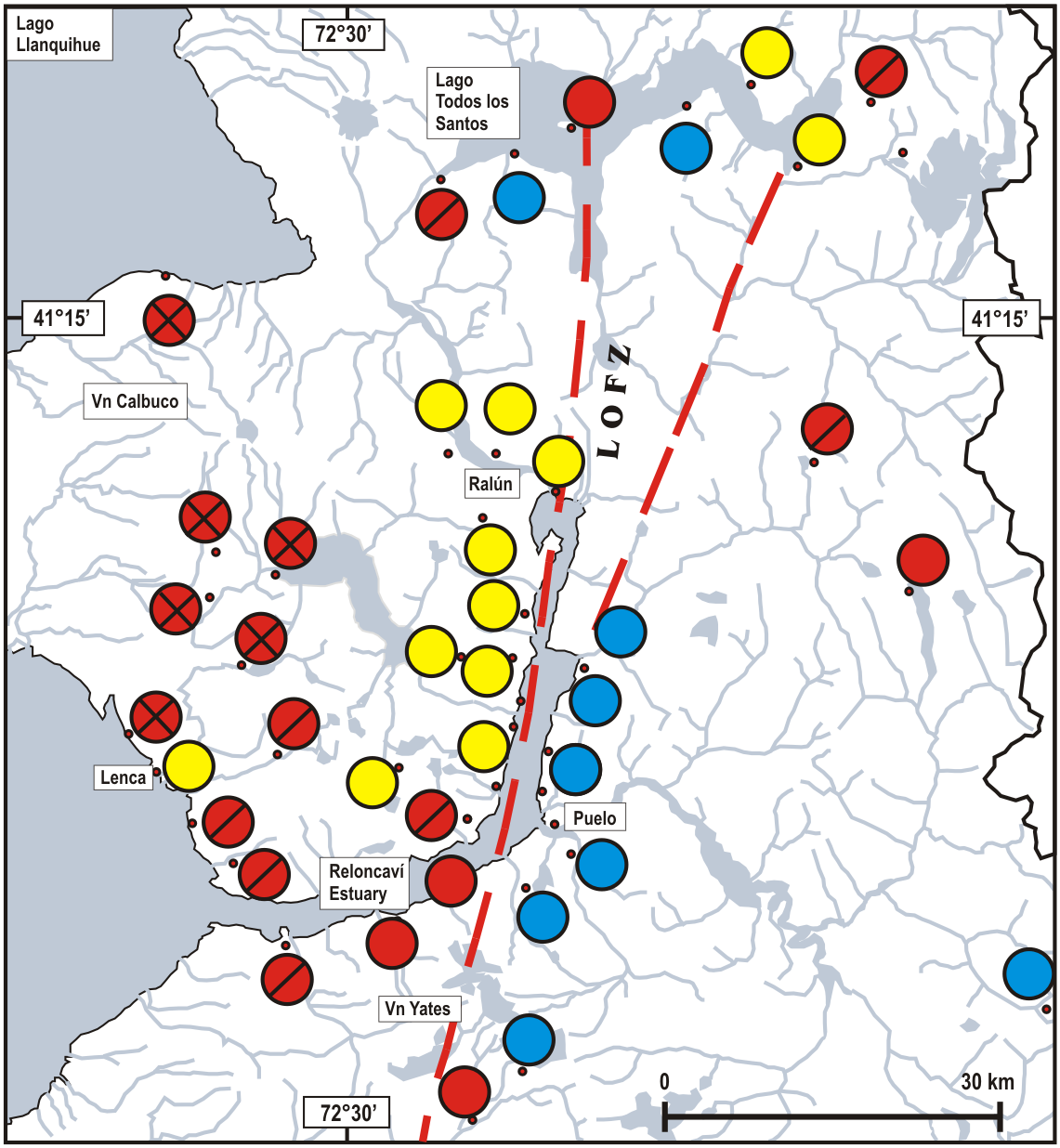

Figure 6.2c: Distribution of Cooling Paths from the North Patagonian Batholith in the Reloncaví Area

Thermal History

~5Ma ~10Ma ~15Ma

Young, shallow intrusion and rapid cooling in the upper crust < ~5 km

Uplift/erosion with moderate cooling rates (exhumation from > ~10km)

Cretaceous intrusions in the upper crust, exhumation from 3-7 km in the Late Miocene-Pliocene

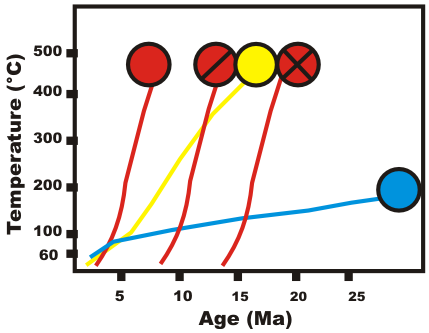

The relative alignment of the types- A and B cooling paths with respect to the position of the main fault strand of the LOFZ along the Reloncaví estuary indicates a western-side uplift between plutons emplaced at different levels and different times. The relative movements must have ended in the Pliocene (~5-3Ma), given by the similar apatite cooling histories on both sides of the fault zone. A similar comparison between the different t-T histories at the eastern border of the Todos Los Santos Lake indicates an eastern-side uplift across the NNE-trending fault segment of the LOFZ.

Type-C cooling paths appear to be distributed irregularly over the batholith, and are also found along the main trace of the LOFZ. The available data indicate that these bodies were emplaced since early Miocene times. For display on the maps, the ages were binned at intervals of 15Ma ± 2.5 Ma, 10Ma ± 2.5 Ma, 5Ma ± 2.5 Ma. This classification reveals a tendency of younger ages towards the LOFZ.

In the Hornopirén area (figure 6.2d), type-C t-T histories were obtained from samples on both sides of the LOFZ, indicating extreme cooling rates in the upper Miocene-Pliocene. These fast cooling rates imply that the intruded wallrocks must have been at low temperatures, as indicated as well by the contact aureoles from the basement rocks at the Llancahué and Pelada islands (chapter 5), and by one type-A cooling curve near río Blanco. Structural reconstruction of this area indicates that the eastern side of the LOFZ was uplifted, where ductile deformation of the plutons is more pronounced (chapter 5.2). The microstructures of the mylonites indicate that deformation occurred during the cooling of these plutons, at subsolidus temperatures, and the rapid cooling histories constrain this deformation to a very short event.

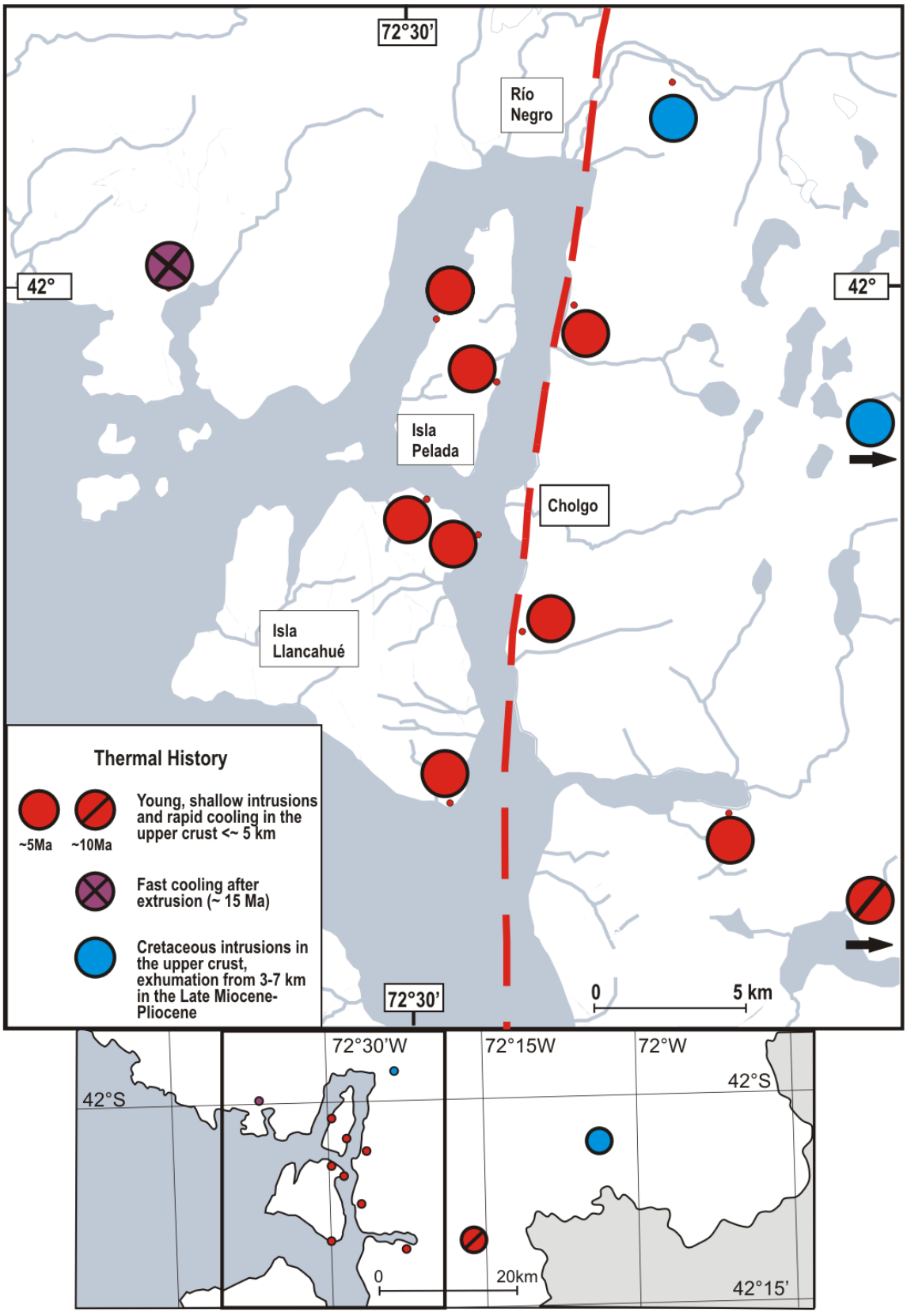

Figure 6.2d: Distribution of Cooling Paths from the North Patagonian Batholith in the Hornopirén Area

6.3 Timing, Nature of Denudation, and Denudation Rates along the LOFZ

If the episode of denudation is controlled by vertical displacement along the LOFZ, then the movement along its trace can be dated as late Miocene. Independent thermochronologic and structural data describe the structure as a right-lateral fault with important vertical offset (chap. 5; figure 6.3a). The timing of cessation of relative vertical displacement is constrained by the apatite FT data, which indicate uniform fast cooling since ~5-3 Ma on both sides of the LOFZ (figure 6.2b). Differential uplift must have come to rest at pre-Pliocene times.

Cooling following granitoid intrusion could only have played a very minor role in the cooling indicated by the apatite FT data if no accompanying denudation took place, and cannot explain fast cooling of over 60 degrees (i.e. through the apatite PAZ) within a few million years. The most likely cause to denudation is transpression, as suggested by the tectonic configuration of the southern Andes during the Late Miocene.

Plate tectonic reconstructions indicate that the subduction of the Chile Ridge beneath the southernmost part of the South American continent began at ~14-10 Ma (Cand and Leslie, 1987). Since this event, the CTJ has migrated northwards along the Perú-Chile trench more than 700 km until its present-day position near the Golfo de Penas. Several authors have interpreted this event as ridge collision (e.g. Murdie et al., 1993; Forsythe et al., 1986), although evidence is limited. Within the study area, the actual position of the volcanic arc is at a distance of ca. 200 km away from the Peru-Chile trench, implying that beneath the LOFZ the subducted Nazca plate should reach depths exceeding 150 km. The southernmost section of the LOFZ must have been reached by the northern portions of the subducted ridge in an episode between ~6-3 Ma (Murdie et al., 1993). Two interpretations for the activation of the fault have been considered: a) A jerky movement of a subducted transform fault of the Chile ridge may have enhanced displacement along the LOFZ. b) The diverging fracture portions of the ridge may have been trapped at depth during subduction, allowing additional heat input into the mantle wedge and magma generation, followed by ascent and emplacement of plutons at different crustal levels along the thermally weakened intra-arc fault zone.

Strain partitioning in the overriding plate is suggested from the different structural domains along the Andean orogen to the north and south of the Peninsula de Taitao (Ramos, 1989; Dewey and Lamb, 1992; Cembrano et al., 2002). North of the CTJ, an important amount of contraction must have been distributed within the arc zone by the LOFZ, since no extensive fold and thrust belt sequence is found in the back arc region. Evidences for transpression in the study region are nevertheless limited. This is probably caused by the long-lived history of the fault zone, at least active since Cretaceous times, and because episodic magmatism along its traces has overprinted previous deformation. It may be possible that continued fast exhumation of the Andean range on both sides of the LOFZ has occurred since late Miocene times (e.g. Thomson, 2002), but with no relative vertical displacement. This could be indirectly related with increased glacial erosion acting with equal vigour on both sides of the fault, although it would not be evidence for transpression, at least in the Chiloé and Los Lagos regions.

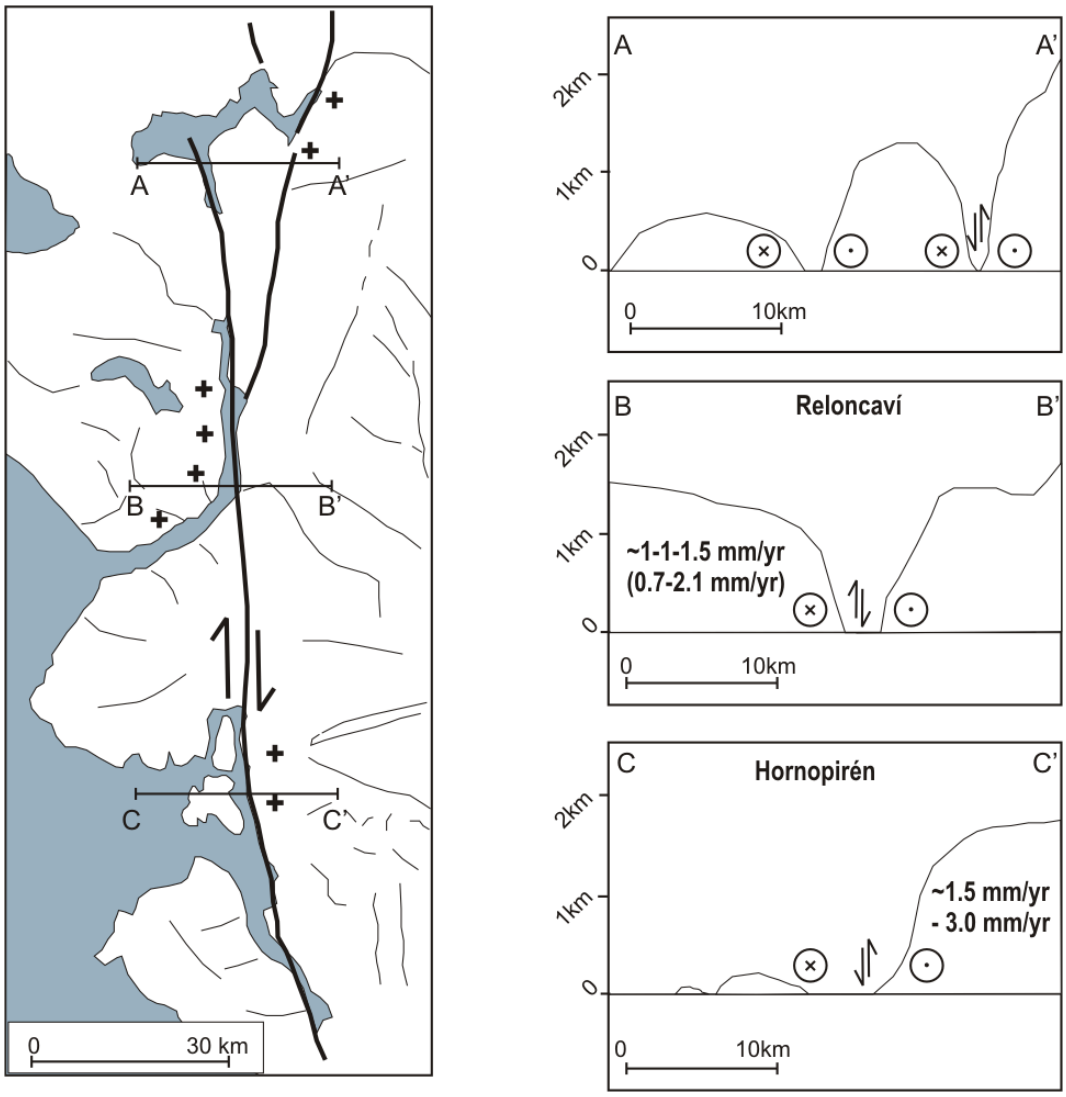

Figure 6.3a: Scheme of the Late Miocene denudation event along the LOFZ in the Los Lagos-Chiloé Regions. Plan view and cross sections along the LOFZ display the relative offsets (+ indicates uplifted areas) determined from structural analysis and integrated t-T histories of the plutons of the NPB. The timing of denudation coincides with plate tectonic reconstructions of the indention of the Chile Ridge beneath the LOFZ, in a transpressional regime, between ~7 and ~4 Ma (Ramos and Kay, 1992, Thomson et al. 2001). Present-day approximate topography is displayed. The marked relief in the area suggests a strong influence over the shape of the upper-crustal isotherms prior and during denudation. Compare with figure 6.3b. Estimates of denudation rates are discussed below.

Constrains on the amounts of denudation occurred along the LOFZ are more difficult to obtain. Aside from tectonic forcing, denudation, particularly erosion, may be driven by other processes, like local relief (rather than an increase in elevation), changing climate, and orography (e.g. Whipple et al, 1999; Fitzgerald et al., 1995; Small, 1999; Montgomery et al., 2001; Montgomery and Brandon, 2002; Willet, 1999).

The translation of cooling histories derived from thermochronologic data to denudation rates relies on the assumption on the geotherm of the upper crust, which varies as a function of time, topography, heat advection, inhomogeneously distributed rock conductivities, and convective fluid circulation in the upper crust (Mancktelow and Grasemann, 1997).

In a simple model, the local relief of a sinuous topography affects steady-state upper-crustal isotherms, in that the geotherm is higher under a valley than under a mountain peak or a ridge (figure 6.3b; Stüwe et al., 1994). Closure of the apatite FT system occurs at depths where isotherms can be perturbed by these effects. In active convergent orogens, heat advection during periods of rapid exhumation results in a progressive elevation of the isotherms, consequently increasing the near-surface geotherm (Stüwe et al., 1994; Mancktelow and Grasemann, 1997). Thus, both erosion and surface topography cause a time-dependent variation in the isotherm geometry that can result in significant errors on the estimation of denudation rates (figure 6.3b).

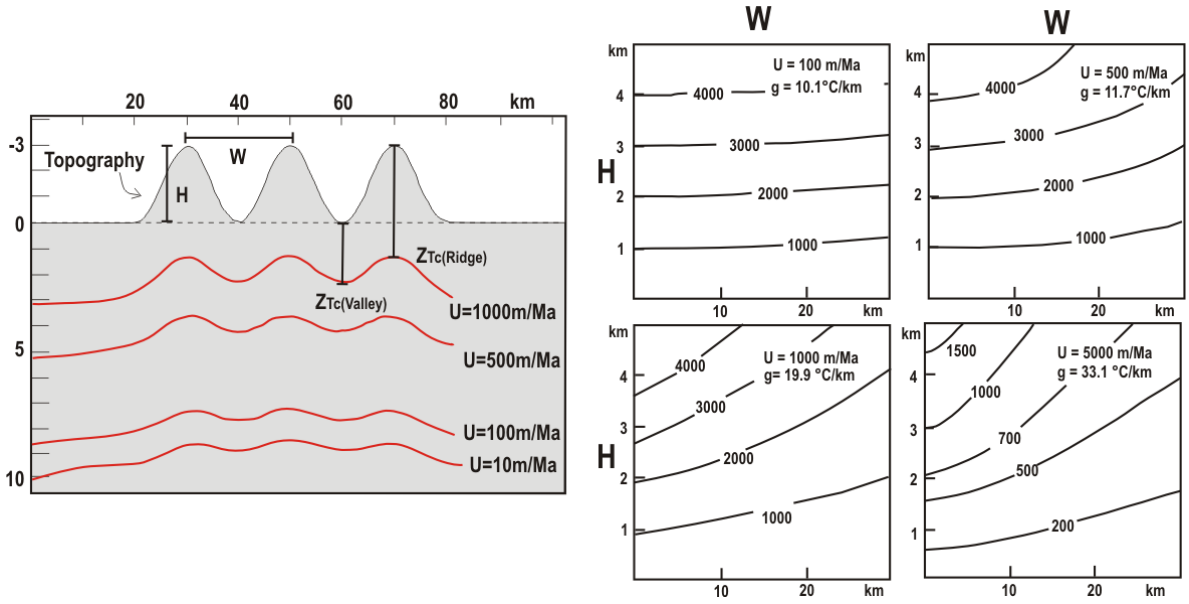

Figure 6.3b (from Stüwe et al., 1994) Example of the shape of the steady-state 100°C isotherm underneath a sine-shaped topography for different denuding rates of U =10, 100, 1000 m/Myr, calculated using an analytical solution for the diffusion-advection equation in two dimensions. Left: amplitude of topography H, against the wavelength W, for a sine-shaped topography contoured for steady-state $\Delta Z = \Delta Z_{Tc(ridge)} - \Delta Z_{Tc(valley)}$ in meters. The perturbation amplitude is given by H-ΔZ, and increases with increasing erosion rates.

According to Mancktelow and Grasemann, direct conversion of cooling rates to exhumation rates that assume a simple constant linear geotherm, especially when exhumation rates are rapid (>1 mm/yr), can markedly underestimate peak exhumation rates, and overestimate rates during periods of isotherm relaxation as exhumation wanes.

Therefore, a realistic estimate for denudation rates in this region requires at least combining different considerations, such as structural constraints, emplacement depths, and the cooling histories of the plutons.

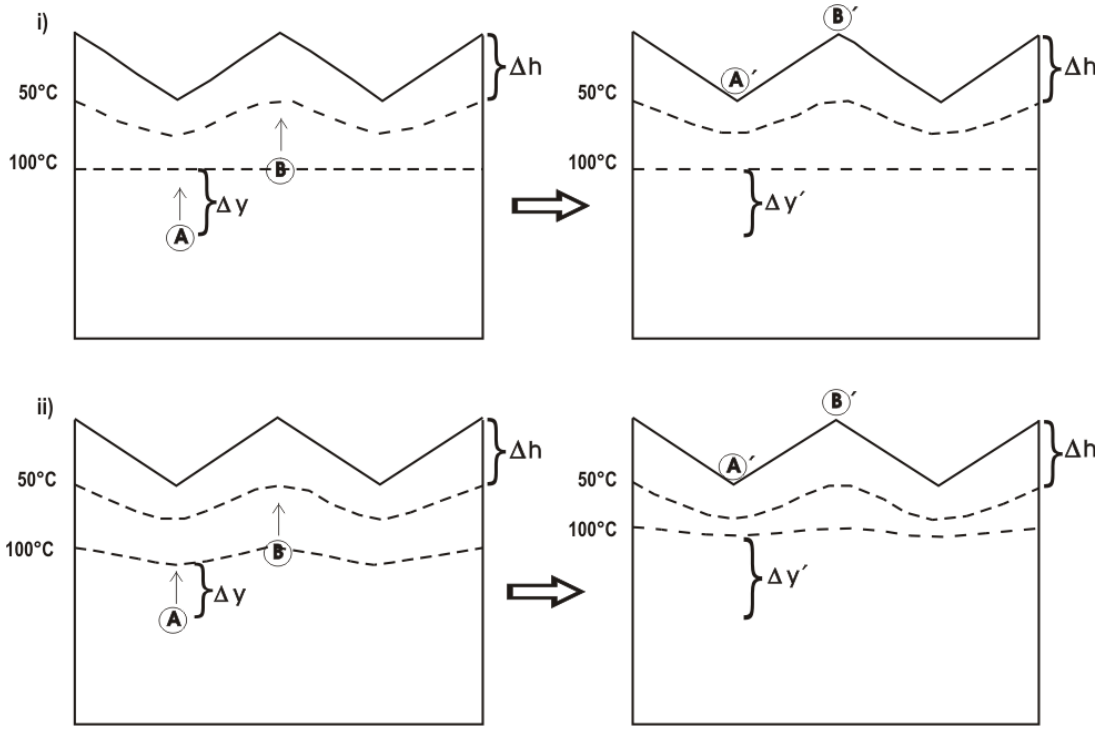

Figure 6.3c: Influence of heat advection during denudation on the calculation of exhumation rates, determined from two samples with an initial vertical separation Δh and blocking temperature of 100°C (from Mancktelow and Grasemann, 1997). In case (i) the topography has a certain influence over the temperature distribution, but does not disturb the 100°C isotherm. The distance between the initial location of sample A and the 100°C isotherm (Δy) is equal to the distance Δh. Because there is no advection of heat, the rocks exhume through a constant but not uniformly distributed isotherm pattern (due to lateral cooling), and after exhumation the distance between the initial location of sample A and the 100°C isotherm (Δy´) is equal to (Δy). In case ii) the 100°C isotherm is also affected by the topography, and in addition heat advection is included in the exhumation process. Due to the depressed 100°C isotherm, the distance Δy is smaller than Δh. During the exhumation process, heat advection elevates the isotherms to a shallower level and as a result the distance Δy' is larger than Δy, and sometimes (but not necessarily) larger than Δh.

Regional surface heat flow measurements in the Southern Andes yield current values of ~80-100 mW/m^2 (Hamza and Muñoz, 1996, Muñoz, 1999). Thermal conductivities for granitoid rocks in the upper crust vary between 2.5 and 3.5 W/(m·K) (Seypold, 1998). Thus, the present-day geothermal gradient near the surface may vary between 23 and 45°C/km (e.g. Thomson, 2002). A basic assumption is that the upper-crustal geotherm in the past is not significantly different from present day, at least during the late Cenonozoic history of this region. This is not valid within areas occupied by young, shallow-level intrusions.

A reasonable denudation estimate along the LOFZ can be obtained from the uplifted blocks (with type-B t-T histories) along the Reloncaví area with steady cooling rates of 30-50°C/Myr occurred during the late Miocene to Pliocene (figure 6.3a). Assuming a constant gradient of 30°C/km, this would imply moderate erosion rates of between ~1 and 1.5 mm/yr (for values ranging between 23° and 45°C/km, this would imply denudation rates of 0.7mm/yr to 2.1mm/yr). Available Al-in hornblende geobarometry data for these plutons indicate emplacement depths exceeding ~10 km along the fault zone. Nevertheless, no intrusion ages are available to constrain

independently average denudation rates from the time of emplacement to the surface. Assuming an early Miocene age of emplacement for the plutons, the average rates would reach ~0.5 mm/yr, one third of those obtained with FT thermochronology. These denudation estimates may be exaggerated by the effect of topography, as they are based on cooling rates from samples located at the bottom of a valley (figures 6.3a-b). For a sinuous topography defined by a wavelength of ~20 km, an amplitude of ~1.5 km, a geotherm of 20°C/km, and steady-state erosion rates of ~1mm/yr, Stüwe et al. (1994) determine a deviation effect of ca. 20%.

Estimates for denudation rates in the Hornopirén area are difficult to constrain because of the type-C cooling histories obtained along both sides of the LOFZ, which indicate the presence of shallow intrusions (figure 6.2d). Thermal convection and heat advection through hydrothermal fluids could have reset the isotopic systems of the plutons exposed along the fault zone. Structural reconstruction of this area nevertheless indicates relative eastside block uplift along the LOFZ (chapter 5.2). The correlation of one U-Pb intrusion age of 9.9±0.2 Ma (Cembrano et al., 2000) from a sample of a deformed tonalite located at Cholgo with Al-in-Hornblende geobarometry data indicating a maximum emplacement depth of ~15 km (Seifert et al., 2003; Hervé et al., 1996) imply an average exhumation rate of ~1.5 mm/yr for the uplifted eastern block. If the apatite FT ages along the eastern border of the fault zone are not reset ages from shallow intrusions, they could indicate as well the general denudation pattern from the study region (between 5 and 3 Ma). The denudation ages would imply a maximum exhumation rate of ca. 3 mm/yr after emplacement, which should have probably occurred during a short lapse of time. Such high denudation rates are expected for collisional mountain belts, and would imply important amounts of heat advection due to tectonic erosion (Mancktelow and Grasseman, 1997).

6.4 Implications for the Denudation History of the Southern Andes

An important tectonic event in the late Miocene is documented by relative vertical components of displacement along the right-lateral LOFZ implied by both thermochronologic and structural data. Differential exhumation rates of ~1 to 1.5 mm/yr, and possibly up to ~3 mm/yr, have been constrained by FT thermochronology, structural reconstructions, and geobarometry in the Reloncaví and Hornopirén areas of the Main Range (41°-42°S).

These relatively high erosion rates allow different styles of intrusions of the NPB to be exposed along the LOFZ, ranging from intermediate depths to shallow levels in the upper crust. The youngest shallow intrusions may have been emplaced along dilational zones produced during right-lateral movements along the fault zone. Similar emplacement mechanisms have been described along shear zones within magmatic arc settings (e.g. Paterson et al., 1991; Hutton and Reavy; 1992, Tikoff and Saint Blanquat, 1997).

Thus, the results from this study strongly support a coupling between Late Cenozoic tectonics and magmatism along the Southern Andes. The timing of denudation is coincident with the moment of the indention of the Chile ridge at the southern-most

section of the present LOFZ (6-3Ma). Further south of the study area, Thomson (2002) determined important amounts of cooling and denudation along the LOFZ occurred between ~7 and 2 Ma, suggesting that the effect of ridge indention and northwards migration of the CTJ in the deformation of the arc is more present south of ~42°S.

In addition, the fission track data from this study indicate that transpression-induced rock uplift and erosion was dominant between Late Miocene and Pliocene times, before the initiation of the widespread glaciation in the southern Andes (e.g. Mercer and Sutton, 1982; Heusser, 1990; Lliboutry 1999). Glacial erosion rates are more than sufficient to maintain a steady-state landscape, irrespective of any uplift rates in active orogens (e.g. Brozovic et al., 1997; Hallet et al., 1996; Thomson, 2002; chap. 2.3.4). The widespread distribution of the outcrops of the NPB along the Main Range, the poor preservation of Meso-Cenozoic overlying strata, and the low topography of the region evidence high amounts of glacial erosion. Although this present study is not conclusive about its influence, it suggests that climatically controlled uniform erosion and uplift have dominated the region starting from Pliocene times.

7. Summary and Conclusions

The southern Chilean Andes in the Chiloé-Los Lagos regions provide an ideal natural laboratory to understand processes of cooling and denudation in relation to regional tectonics, magmatism, and climate at active continental margins. Fission Track (FT) thermochronology of zircon and apatite was applied to study the low-temperature history of the Andean basement rocks in relation to the late Cenozoic activity of the mega-scale Liquiñe-Ofqui Fault Zone (LOFZ) and the migration of the Chile Triple Junction (CTJ).

Research was focused on three different sectors of the Chiloé and Los Lagos regions of Chile (figure 2.1): the Chiloé Island in the fore-arc (41°45'– 43°30'S, 73°30'-74°W; figure 2.3a), the Reloncaví and the Hornopirén areas at the Main Cordillera (41°-42°15'S, 72°-73°W, figures 2.3b-c). 63 zircon and 60 apatite FT ages, plus 38 track length measurements were determined from 69 samples (59 belonging to the Main Cordillera) in this study (table 4.2). The samples are from the Meso-Cenozoic North Patagonian Batholith (NPB), the surrounding Paleozoic-Early Triassic metamorphic basement, and from overlying Tertiary volcanic sequences.

Seven zircon and nine apatite FT ages were obtained in Chiloé Island (figure 4.3a). The cooling ages of the metamorphic basement rocks on the island range between Upper Jurassic and Eocene. Comparison between these dates and late Triassic K-Ar and ^{40}Ar-^{39}Ar post-metamorphic cooling ages reported from similar outcrops of the unit at the northern border of the island allows a wide time-span for the occurrence of any geologic processes, including thermal resetting by intrusions. A direct correlation between their different closure temperatures suggests slow cooling (<5º/Ma beween 220Ma and 60 Ma) and hence little erosion since pre-Late Triassic metamorphism, although evidence is limited. Late Cretaceous zircon FT ages with high age dispersions were obtained from two samples of the metamorphic unit at the central and southern parts of the island. The younger components found within their single grain age populations suggest thermal overprinting by Late Cretaceous to Eocene shallow intrusions (figure 4.3b). Late Eocene extrusion ages were obtained in two samples of volcanic rocks from the center of the island.

56 zircon and 51 apatite FT ages, plus 37 apatite track-length measurements were obtained from samples of plutonic and contact metamorphic rocks of the Main Range (Reloncaví and Hornopirén areas, figures 4.4a-b and 4.5a-b). The apatite samples yield FT central ages down to 3.3±1.2 Ma along the LOFZ, whereas older Miocene ages were obtained to the west and east of the fault zone. In all of the measured apatite samples, the track length distributions indicate normal-to-rapid cooling histories. Rapid cooling by ca. 5-3 Ma along both sides of the fault zone is implied by the young ages and uniform track length distributions with long tracks. The zircon FT ages range between Cretaceous and Pliocene, depending on the history of emplacement and cooling of the plutons of the NPB. A marked difference in the orographic distribution of the zircon FT ages was observed across the LOFZ at Reloncaví. At Hornopirén, the similar apatite and zircon FT central ages along the LOFZ imply very rapid cooling by ~5 to 3 Ma. 9 zircon and 4 apatite FT central ages from the Main Range reveal high age dispersions, suggesting partial resetting by heat input from from magma or hydrothermal fluids. These samples are predominantly located near the traces of the LOFZ.

To gain insight into the thermal structure of the composite intrusions that constitute the NPB, and to discriminate between postmagmatic cooling at different emplacement levels in the crust and cooling resulting from denudation in response to tectonic activity, the following concept was followed. The FT data from the plutonic and contact metamorphic rocks of the Main Range were combined with available Rb-Sr, U-Pb, K-Ar, and ^{40}Ar-^{39}Ar ages from nearby outcrops, to construct cooling paths based on widely accepted closure temperatures (e.g. Hurford, 1986). Three different classes of intrusions within the NPB have then been characterized by their cooling paths (shown in figures 6.2a-b), and their geographic distribution within the study region was specified (maps in figures 6.2c-d):

a) Cretaceous upper crustal intrusions. They are characterized by very slow cooling rates since Cretaceous emplacement in the upper ~10 km of the crust, followed by rapid cooling in the Late Miocene-Pliocene along the LOFZ.

b) Early Miocene to Cretaceous deep intrusions. They are characterized by moderate and steady cooling rates from emplacement depths exceeding ~10 km. The relative position of plutons with type-(a) and -(b) cooling paths observed in the Reloncaví area indicate a local uplift of the western block along the LOFZ during the Late Miocene- Pliocene.

c) Miocene shallow intrusions, with very rapid cooling rates after emplacement at a depth of a few km in the upper crust. The very fast cooling may result from heat transfer by convection of hydrothermal fluids. An E-W zonation of the age of the shallow-level intrusions was recognized, with the younger intrusions emplaced near the main traces of the LOFZ.

The structural and microstructural observations on outcrops and samples of plutons along the LOFZ indicate an episodic history of intrusion and deformation. Different styles of deformation were observed along the fault zone; to some extent these appear to be related to the differing cooling paths of the plutons, or to variable vertical components of displacement along the fault zone.

In the Reloncaví area, the microstructures of samples from plutons with type-(a) and -(b) cooling histories indicate generally weak deformation at temperatures below about 300°C. Some samples of Cretaceous plutons with type-(a) cooling histories show significant deformation of quartz by dislocation creep, which could have taken place related to the activity of LOFZ at the level of pluton emplacement. One sample with a Cretaceous zircon FT cooling age shows a marked deformation at higher temperatures, indicating earlier activity at depth along the LOFZ, or a precursor fault zone.

In the Hornopirén Area, significant uplift of the eastern block is indicated by the different grades of deformation observed across the fault zone and by the shear sense indicators in a deformed tonalite. The relative uplift of the eastern block is supported by Al-in-Hornblende geobarometry from the deformed tonalites and contact metamorphic phase assemblages in the wallrocks, both indicating a deeper level of emplacement of the plutons to the east of the LOFZ. The very fast cooling rates

obtained from the integrated thermochronologic data in the area indicate the presence of Late Miocene to Pliocene shallow-level intrusions.

If the episode of denudation is controlled by a vertical component of displacement along the LOFZ, the respective activity of the fault can be dated as Late Miocene. In addition, the timing of the activity is constrained to pre-Pliocene by the apatite FT data. The non-uniform denudation across the LOFZ is most probably caused by transpression, as suggested by the regional deformation pattern along the Andean orogen north of the CTJ. The timing of this event correlates with plate tectonic reconstructions that suggest contemporaneous arrival of the Chile Ridge beneath the southernmost section of the LOFZ. Thus, a coupling between magmatic and tectonic activity along the Liquiñe-Ofqui fault zone is strongly supported by the results of this study.

The translation of cooling rates derived from thermochronologic data into denudation rates is based on an assumed steady geotherm, which in the studied region is likely to vary in time as a function of magmatic heat input, topography, and convective fluid circulation in the upper crust. Estimates of denudation rates thus need to be supported with structural and geobarometric constraints. Assuming a pre-denudational regional gradient of 30°C/km (resembling present day values, Hamza and Muñoz, 1996), the steady cooling rates of 30-50°C/Myr of plutons emplaced at depths of > 10 km (obtained for the uplifted western block from the Reloncaví area) imply moderate exhumation rates of ~1-1.5 mm/yr during the late Miocene to Pliocene (~6 to 3 Ma). In the Hornopirén Area, direct estimates of denudation rate are complicated by the presence of shallow-level intrusions. An average denudation rate of ~1.5 mm/yr is suggested from geobarometry (~15 km, Hervé et al., 1996) and the emplacement age (9.9 Ma, Cembrano et al., 2000) of a deformed tonalite with type c-cooling history in the uplifted eastern block. If the apatite FT ages at the location reflect the general denudation pattern in the study region, a maximum exhumation rate of ca. 3 mm/yr can be inferred.

The low topography of the Andean region, the wide areas with exposed plutons of the NPB, and the locally preserved Meso-Cenozoic cover sequences, suggest that glacial erosion processes played an important role for the Neogene history of the orogenic belt. Although this present study does not allow definite conclusions in this aspect, it suggests that tectonically driven differential uplift and erosion have dominated the landscape development of the region in pre-Pliocene times, and that climatically controlled uniform erosion and uplift have levelled the Main Andean Range since the Pliocene and during the ice ages.

8 Acknowledgements

I am in deep gratitude for the guidance and patience of my teachers who helped me to carry out this work. I thank Professor Dr. Bernhard Stöckhert for his invitation to study and join the Endogene Geology Department at the Ruhr University of Bochum, and especially for his corrections, and invaluable comments and ideas for the thesis.

I thank Dr. Stuart Thomson and Dr. Manfred Brix for instructing me in fission track thermochronology, as well as for offering their support and friendship during research. I thank them as well for correcting earlier drafts of the manuscript, and for sharing with me gratifying experiences during field trips, at congresses, and in the laboratory.

I thank Professor Dr. Francisco Hervé, from the Universidad de Chile, for recommending me to come to Bochum and learn fission track thermochronology, and for his advice and comments during this investigation.

I thank the DAAD, the University of Bochum, and the Universidad de Chile for having sponsored this study.

I thank Frank Hansen, for his help, advice and support at the lab.

I thank Regina Zimmerman, Klaus Roller, Johannes Duyster, Matthias Wachmann, Dorothée, Jens Orzol, Jens Steffahn, Ralph, Miriam, María del Carmen, Annette, and many other friends that have helped me during my stay in Bochum.

I thank Yvonne for helping me to keep motivated during the hard part of the work.

9 References

Aguirre, L., F. Hervé, and E. Godoy, Distribution of metamorphic facies in Chile- an outline, *Krystalinikum*, *9*, 7-19, 1972.

Anderson, J.L., and S.R. Paterson, Emplacement of Cretaceous Mount Stuart Batholith, north Cascades, Washington, *GSA Abstracts with Programs*, *23*, A 387, 1991.

Anderson, J.L., and D.R. Smith, The effects of temperature and fO_2 on the Al-in hornblende geobarometer, *Am. Mineral.*, *80*, 549-559, 1995.

Araya, E., Estudio geológico preliminar del área ubicada entre los 42°30' y 43°20' L.S. y los 72°30' y 73° L.W. (comuna de Chaitén, Provincia de Chiloé, X region), Mem. de Titulo, Dpto.Geol. Univ. de Chile, Santiago, Chile, 1979.

Augustsson, C., and H. Bahlburg, Active or passive continental margin? Geochemical and Nd isotope constraints in the backstop of a pre-Andean accretionary wedge in southernmost Chile (46°30'- 48°30'S), in *Tracing Tectonic Deformation Using the Sedimentary Record*, edited by T. McCann and A. Saintot, pp. 253-268, Geol. Soc. London Spec. Pub., 208, 2003.

Baard, J.H., W.L. Zijp, and H.J. Nolthenius, *Nuclear Data Guide for Reactor Meterology,* Kluwer Acad. Press, Dordrecht, Netherlands, 1989.

Bangs, N., and S. Cande, Episodic development of a convergent margin inferred from structures and processes along the southern Chile margin, *Tectonics, 16(3)*, 489-503, 1997.

Barbarand J., M. Pagel, Ph. Blanc, J. Braun, M. Chaussidon, Ch. Vétil, F. Walgenwitz, Combined cathodoluminescence spectra, fission-track age and chemistry of detrital apatite grains: towards a better understanding of fission track annealing, in *Int. Conf. on Cathodoluminescence and related techniques in Geosciences and Geomaterials, Nancy, France, Abstracts,* pp.19-20, 1996.

Barrientos, S.E., and P. Acevedo, Seismological aspects of the 1988-1989 Lonquimay (Chile) volcanic eruption, *J. Volc. Geotherm. Res., 53*, 73-87, 1992

Beck, M.E., C. Rojas, and J. Cembrano, On the nature of buttressing in margin-parallel strike-slip fault systems, *Geology, 21*, 755-758, 1993.

Beck, M.E., R. Burmester, J. Cembrano, R. Drake, A. García, F. Hervé, and F. Munizaga, Paleomagnetism of the North Patagonian batholith, southern Chile. An exercise in shape analysis, *Tectonophysics, 326*, 185-202, 2000.

Bergmann, S.C., and J. Corrigan, Compositional variation of natural apatites subjected to fission track analysis, in *8th Int. Workshop Fission-Track Dating, Gent, Belgium, Abstracts,* 7, 1996.

Best, M.G., *Igneous and Metamorphic Petrology*, 2nd edition, 756 pp., Blackwell Science, United Kingdom, 2003.

Bhandari, N., S.G. Baht, D. Lal, G. Rjagopalan, A.S. Tamhane, and V.S. Venkatavaradan, Fission Tracks in apatite: recordable track lengths, *Earth Planet. Sci. Lett.*, *13*, 191-199, 1971.

Bigazzi, G., The problem of the decay constant λ_f of ^{238}U., *Nucl. Tracks, 5*, 35-44, 1981.

Blumenfeld, P., and J.L. Bouchez, Shear criteria in granite and migmatite deformed in the magmatic and solid states, *J. Struct. Geol.*, *10*, 361-372, 1988.

Bodu, R., H. Bouziges, N. Morin, and J.P. Pfiffelmann, On the existence of anomalous isotopic abundances in uranium from Gabon, *Compt., Rend. Acad. Sci. Paris, D 275*, 1731-1732, 1972.

Bons, P.D., and J.L. Urai, Syndeformational grain growth microstructures and kinetics, *J. Struct. Geol.*, *14*, 403-411, 1992.

Brandon, M.T., Decomposition of fission-track grain age distributions, *Am. J. Sci., 292*, 535-564, 1992.

Brandon, M.T., Probability density plots for fission-track grain age distributions, *Radiation Measurements*, *26*, 663-676, 1996.

Brandon. M.T., Decomposition of mixed grain age distributions using Binomfit, *On Track, 24*, 13-18, 2002.

Brandon, M.T., M.K. Roden-Tice, and J. Garver, Late Cenozoic exhumation of the Cascadia accretionary wedge in the Olympic Mountains, northwest Washington State, *Geol. Soc. Am. Bull. 110*, 985-1009, 1998.

Brandon, M.T., and J.A. Vance, Tectonic evolution of the Cenozoic Olympic subduction complex, Washington state, as deduced from fission track ages for detritical zircons, *Am. J. Sci., 292*, 565-636, 1992.

Brix, M.R., B. Stöckhert, E. Seidel, T. Theye, S.N. Thomson, and M. Küster, Thermobarometric data from a fossil zircon partial annealing zone in high pressure-low temperature rocks of eastern and central Crete, Greece, *Tectonophysics, 349*, 309-326, 2002.

Brown R.W., and M.A. Summerfield, Some uncertainties in the rates of derivation of rates of denudation from thermochronologic data, *Earth Surf. Process. Land., 22*, 239-248, 1997.

Brozovic, N., D.W. Burbank, and A.J. Meigs, Climatic limits on landscape development in the northwestern Himalaya, *Science, 276*, 571-574, 1997.

Bruce, R.M., E.N. Nelson, S.G. Weaver, and D.R. Lux, Temporal and spatial variations in the southern Patagonian batholith; constraints on magmatic arc development, *Spec. Pap. Geol. Soc. Am., 265*, 1-12, 1991.

Burchart, J., Evaluation of uncertainties in fission track dating: some statistical and geochemical problems, *Nucl. Tracks, 5*, 87-92, 1981.

Butler, R.F., F. Hervé, F. Munizaga, M.E. Beck, R.F. Burmester, and E. Oviedo, Paleomagnetism of the Patagonian plateau basalts, Southern Chile and Argentine, *J. Geophys. Res., 91*, 6023-6034, 1991.

Butner, R.L., A. Nigrini, and R.A. Donnelick, Thermochronology of Lower Cretaceous source rocks in the Idaho-Wyoming thrust belt, *AAPG Bull.*, *78*, 1613-1636, 1994.

Cande, S.C., and R.B. Leslie, Late Cenozoic tectonics of the southern Chile trench, *J. Geophys. Res., 91*, 471-496, 1986.

Carlson, W. D., Mechanisms and kinetics of apatite fission-track annealing, *Am. Mineral., 75*, 1120-1139, 1990.

Carlson, W.D., R.A. Donnelick, and R. Ketcham, Variability of apatite fission-track annealing kinetics: 1. Experimental results, *Am. Mineral., 84*, 1213-1223, 1999.

Carrasco, V., Geología y geoquímica del Batolito Norpatagónico y rocas volcánicas asociadas a la zona de falla Liquine-Ofqui (41°-05-41°40'L.S.), X región, Mem. de Titulo Depto. Geol. Univ. de Chile, Santiago, Chile, 1995.

Castillo, J.C., Geología del Sector Occidental de la Comuna de Futaleufú, Provincia de Palena, X. Región de los Lagos, Mem. de Titulo Depto. Geol. Univ. de Chile, Santiago, Chile, 1983.

Cembrano, J., Kinematics and timing of intra-arc deformation, southern chilean Andes, PhD thesis, Dalhousie Univ., Canada, 1998.

Cembrano, J., F. Hervé, and A. Lavenu, The Liquiñe Ofqui Fault Zone: a long lived intra arc fault system in southern Chile, *Tectonophysics*, 259, 55-66, 1996.

Cembrano, J., E. Schermer, A. Lavenu, and A. Sanhueza, Contrasting nature of deformation along an intra-arc shear zone, The Liquiñe Ofqui Fault Zone, Southern Chilean Andes, *Tectonophysics, 319*, 129-149, 2000.

Cembrano, J., A. Lavenu, P. Reynolds, G. Arancibia, G. Lopez, and A. Sanhueza, Late Cenozoic transpressional ductile deformation north of the Nazca-South America-Antrtica triple junction, *Tectonophysics, 354*, 289-314, 2002.

Chadderton, L.T., On the anatomy of a fission track, *Nucl. Tracks, 15,* 11-29, 1988.

Chester, F.M., and J.M. Logan, Composite planar fabric of gouge from the Punchbowl fault, California, *J. Struct. Geol., 9,* 621-634, 1987.

Chinn, D.S., and B.S. Isacks, Accurate source depths and focal mechanisms of shallow earthquakes in western South America and in the New Hebrides island arc, *Tectonics, 2,* 529-563.

Cifuentes, L.I., The 1960 Chilean earthquake, *J. Geophys. Res., 94*, 655-680, 1989.

Corrigan, J.D., Inversion of apatite fission track data for thermal history information, *J. Geophys. Res.*, *96*, 10347-10360, 1991.

Corrigan, J.D., Apatite fission track analysis of Oligocene strata in South Texas, U.S.A.: testing annealing models, *Chem. Geol.*, *104*, 227-249, 1993.

Cowan, G.A., and H.H. Adler, The variability of the natural abundance of ^{235}U, *Geochim. Cosmochim. Acta, 40*, 1487-1490, 1976.

Coyle, D.A., and G.A. Wagner, Fission-track dating of zircon and titanite from the 9101 m deep KTB: Observed fundamentals of track stability and thermal history reconstruction, in *International Workshop of Fission Track Dating, University of Gent, Belgium,* Abstracts Volume, 22, 1996.

Crowley, 1993, Lenmodel: a forward model for calculating length distributions and fission track ages in apatite, *Comp. Geosc., 19*, 619-626.

Crowley, K.D., M. Cameron, and R.L. Schaefer, Experimental studies of annealing of etched fission tracks in fluorapatite, *Geochim. Cosmochim. Acta, 55*, 1449-1465, 1991.

Dahl, P.S., A crystal-chemical basis for Pb retention and fission-track annealing systematics in U-bearing minerals, with implications for geochronology, *Earth Planet. Sci. Lett., 150*, 277-290, 1997.

Davidson, J., C. Mpodozis, E. Godoy, F. Hervé, R.J. Pankhurst, and M. Brook, Late Paleozoic accretionary complexes in the Gondwana Margin of Southern Chile: evidence from the Chonos Archipelago, in: *Gondwana Six: Structure, Tectonics and Geophysics,* Geophys. Monogr. Ser.,Vol. 42*,* edited by G. McKenzie, pp. 221-227, AGU, Washington D.C., 1987.

De la Cruz, R., M. Suárez, V. Covacevich, and D. Quiroz, Estratigrafía de la zona de Palena y Futaleufú (43°15'- 43°45' L. S.), X Region, Chile, *XIII Congreso Geológico Argentino y III Congreso de Exploración de Hidrocarburos, Actas, 1,* 417-424, 1996.

Dell'Angelo, L.N., and J. Tullis, Fabric development in experimentally sheared quartzites, *Tectonophysics, 169*, 1-21, 1989.

Dewey, J.F., and S.H. Lamb, Active tectonics of the Andes, *Tectonophysics, 205*, 79-95, 1992.

Diriason, M., P.R. Cobbold, E.A. Rosello, and A.J. Amos, Neogene dextral transpression due to oblique convergence across te Andes of northwestern Patagonia, Argentina, *J. South Am. Earth Sci.*, *11*, 519-532, 1998.

Dodson, M.H., Closure temperature in cooling geochronological and petrological systems, *Contrib. Mineral. Petrol., 40*, 259-274, 1973.

Dokka, R.K., M.J. Mahaffie, and A.W. Snoke, Thermochronologic evidence of a major tectonic denudation associated with detachment faulting, northern Ruby Mountains-East Humboldt Range, Nevada, *Tectonics, 5*, 995-1006, 1986.

Donelick, R.A., Crystallographic orientation dependance on mean etchable fission track length in apatite: an empirical model and experimental observations, *Am. Mineral., 76*, 86-91, 1991.

Donelick, R.A., M.K. Roden, J.D. Mooers, B.S. Carpenter, and D.S. Miller, Etchable length reduction of induced fission tracks in in apatite at room temperature (~23°C): crystallographic orientation effects and "initial" mean lengths, *Nucl. Tracks*, *17*, 261-265, 1990.

Duddy, I.R., P.F. Green, and G.M. Laslett, Thermal annealing of fission tracks in apatite, 3. Variable Temperature behaviour, *Chem. Geol., 73*, 25-38, 1988.

Duhart, P., G. Crignola, B.A. Ordoñez, and J. Muñoz, Franjas metalogénicas en Chiloé continental (41°-44°S), *IX Congreso Geológico Chileno, Puerto Varas, Chile, Actas, 1,* 201-205, 2000.

Duhart, P., M. McDonough, J. Muñoz, M. Martin, and M. Villeneuve, El Complejo Metamórfico Bahía Mansa en la Cordillera de la Costa del centro-sur de Chile (39°30'- 42°00'S): geocronología en K-Ar, $^{40}Ar/^{39}Ar$ y U-Pb e implicancias en la evolución del margen suroccidental de Gondwana, *Rev. Geol. Chile, 28(2)*, 179-208, 2001.

Duncan, R.A., and R.B. Hargraves, Plate tectonic evolution of the Caribbean region in the mantle reference frame, in: *The Caribbean–South American Plate Boundary and Regional Tectonics,* edited by W.E. Bonini, R.B. Hargaves, and R. Shagam, Geol. Soc. Am. Mem., 162 pp., 81-93, 1984.

Dunkl, I., Trackkey: A Windows program for calculation and graphical presentation of fission track data, *Computers and Geosciences*, *28(1)*, 3-12, 2002.

England, P.C., and P. Molnar, Surface uplift, uplift of rocks, and exhumation of rocks, *Geology, 18*, 1173-1177, 1990.

Evans, J.P., Deformation mechanisms in the granitic rocks at shallow crustal levels, *J. Struct. Geol., 10*, 437-444, 1988.

Fang, Z., A. Boucot, V. Covacevich, and F. Hervé, Discovery of Late Triassic fossils in the Chonos Metamorphic Complex, southern Chile, *Rev. Geol. Chile, 25*, 165-174, 1998.

Faure, G., *Principles on Isotopic Geology*, 589 pp., John Wiley, New York, 1986.

FitzGerald, J.D., and H. Stüniz, Deformation of granitoids at low metamorphic grade I: reactions and grain size reduction, *Tectonophysics, 221,* 299-324, 1993.

Fitzgerald, P.G., R.B. Sorkhabi, T.F. Redfield, and E. Stump, Uplift and denudation of the Central Alaska Range; a case study in the use of apatite fission track thermochronolgy to determine absolute uplift parameters, *J. Geophys. Res., 100*, 20175-20191, 1995.

Fleischer, R.L., and P.B. Price, Techniques for geological dating of minerals by chemical etching of fission fragment tracks, *Geochim. Cosmochim. Acta*, *28*, 755-766, 1964.

Fleischer, R.L., P.B. Price, and R.M. Walker, Effects of temperature, pressure, and ionization on the formation and stability of fission tracks in minerals and glasses, *J. Geophys. Res., 70,* 1491-1496, 1965a.

Fleischer, R.L., P.B. Price, R.M. Walker, and M. Maurette, Cosmic ray exposure ages of tektites by the fission-track technique, *J. Geophys. Res., 70,* 1491-1496, 1965b.

Fleischer, R.L., P.B. Price, and R.M. Walker, The ion explosion spike mechanism for formation of charged particle tracks, *J. Appl. Phys., 36,* 3645-3652, 1965c.

Fleischer, R.L., P.B. Price, R.M. Walker, M. Maurette, and M. Morgan, Tracks of heavy primary cosmic rays in meteorites, *J. Geophys. Res., 72,* 355-366, 1967.

Fleischer, R.L., G.M. Compstock, and H.R. Hart Jr., Dating of mechanical events by deformation-induced erasure of particle tracks, *J. Geophys. Res., 77*, 5050-5053, 1972.

Fleischer, R.L., and H.R. Hart Jr., Fission track dating: techniques and problems, in *Proc. Burg Wartenstein Conf. On Calibration of hominoid Evolution*, pp. 135-170, edited by W.W. Bishop, D.A. Miller, and S. Cole, Scott. Acad. Press, Edinburgh, 1972.

Fleischer, R.L., P.B. Price, and R.M. Walker, *Nuclear Tracks in Solids: Principles and Applications,* University of California Press, Berkeley, 1975.

Flerov, G.N., and K.A. Petrzakh, Spontaneous Fission of Uranium, *J. Phys., 3*, 275-280, 1940.

Forsythe, R.D., The Late Paleozoic to Early Mesozoic evolution of the Southern South meric: a plate tectonic interpretation, *J. Geol. Soc. London,* 139, 671-682, 1982.

Forsythe, R., and C. Mpodozis, Geologia del basamento pre-Jurásico Superior em el archipélago Madre de Dios, Magallanes, Chile, *Serv. Geol. Miner. Bol., 39,* 63 pp., 1983.

Forsythe, R., and E. Nelson, Geological manifestations of ridge collision: evidence from the Golfo de Penas-Taitao Basin, southern Chile, *Tectonics, 4*, 477-495, 1985.

Forsythe, R., E.P. Nelson, M.J. Carr, M.E. Kaeding, M. Hervé, C. Mpodozis, J.M. Soffia, and S. Harambour, Pliocene near-trench magmatism in southern Chile: A possible manifestation of ridge collision, *Geology, 14,* 23-27, 1986.

Fortey,, R.A., R.J. Pankhurst, and F. Hervé, Devonian trilobites at Buill, Chiloé (42°S), *Rev. Geol. Chile, 19*, 133-143, 1992.

Fuenzalida, J.L., Estudio Geológico preliminar de la península de Huequi, X región. Mem. de Titulo Depto. Geol. Univ. de Chile, Santiago, Chile, 1979.

Galbraith, R.F., On statistical models for fission track counts, *Math. Geol., 13*, 471-478, 1981a.

Galbraith, R.F., Statistical analysis of some fission-track counts and neutron-fluence measurements, *Nucl. Tracks, 6*, 99-107, 1981b.

Galbraith, R.F., Graphical display of estimates having different standard errors, *Technometrics, 30*, 271-281, 1988.

Galbraith, R.F., The radial plot: graphical assesment of spread in ages, *Nucl. Tracks, 17*, 207-214, 1990.

Galbraith, R.F., and P.F. Green, Estimating the component ages in a finite mixture, *Nucl. Tracks, 17,* 197-206, 1990.

Galbraith, R.F., and G.M. Laslett, Statistical models for mixed fission track ages, *Nucl. Tracks, 21*, 459-470, 1993.

Gallagher, K., Evolving temperature histories from apatite fission-track data, *Earth Planet. Sci. Lett., 126,* 421-435, 1995.

Gallager K., R. Brown, and C. Johnson, Fission Track Analysis and its applications to geologic problems, *Annu. Rev. Earth Planet. Sci., 26*, 519-72, 1998.

Galliker, D., E. Hugentobler, and B. Hahn, Spontane Kernspaltung von ^{235}U und ^{241}Am, *Helv. Phys., Acta, 43*, 593-606, 1970.

García, A., M.E. Beck, R.E. Burmester, F. Hervé, and F. Munizaga, Paleomagnetic reconaissance of the Región de los Lagos, southern Chile, and its tectonic implications, *Rev. Geol. Chile, 15*, 13-30, 1988.

Gleadow, A.J.W., Fission track dating methods: what are the real alternatives? *Nucl. Tracks, 5*, 3-14, 1981.

Gleadow, A.J.W., and J.F. Lovering, The effect of weathering on fission track dating, *Earth Planet. Sci. Lett., 22,* 173-168, 1974.

Gleadow, A.J.W., A.J. Hurford, and R.D. Quaife, Fission track dating on zircon: improved etching conditions, *Earth Planet. Sci. Lett., 33*, 273-276, 1976.

Gleadow, A.J.W., and J.F. Lovering, Geometry factor for external track detectors in fission track dating. *Nucl. Tracks, 1,* 99-106, 1977.

Gleadow, A.J.W., and I.R. Duddy, A natural long-term annealing experiment for apatite, *Nucl. Tracks, 5*, 3-14, 1981.

Gleadow, A.J.W., I.R. Duddy, and J.F. Lovering, Fission track analysis: A new tool for the evaluation of thermal histories and hydrocarbon potential, *Austral. Petrol. Expl. Ass. J., 23,* 93-102, 1983.

Gleadow, A.J.W., I.R. Duddy, P.F. Green, and J.F. Lovering, Confined fission track lengths in apatite: a diagnostic for thermal analysis, *Contrib. Mineral. Petrol., 94*, 405-415, 1986.

Gonzalez-Diaz, E., Chronological zonation of granitic plutonism in the northern Patagonian Andes of Argentina: the migration of intrusive cycles, *Earth Planet. Sci. Lett., 41,* 60-66, 1982.

Gorring, M.L., S.M. Kay, P.K. Zeitler, V.A. Ramos, D. Rubiolo, M.I. Fernandez, and J.L. Panza, Neogene Patagonian plateau lavas: Continental magmas associated with ridge collision at the Chile Triple Junction, *Tectonics, 16,* 1-17, 1997.

Grasemann, B., and N.S. Mancktelow, Two-dimensional thermal modelling of normal faulting: The Simplon Fault Zone, Central Alps, Switzerland, *Tectonophysics, 225,* 155-165, 1993.

Green, P.F., A new look at statistics in fission track dating, *Nucl. Tracks, 5,* 77-86, 1981.

Green, P.F., The relationship between track shortening and fission track age reduction in apatite: combined influences on inherent instability, annealing anisotropy, length bias and system calibration, *Earth Planet. Sci. Lett., 89*, 335-352, 1988.

Green, P.F., and S.A. Durrani, Annealing studies of tracks in crystals, *Nucl. Track Detection, 1*, 33-39, 1977.

Green, P.F., and S.A. Durrani, A quantitative assessment of geometry factors for use in fission track dating, *Nucl. Tracks, 2*, 207-213, 1978.

Green, P.F., and A.J. Hurford, Thermal neutron dosimetry for fission track dating, *Nucl. Tracks, 9*, 231-241, 1984.

Green, P.F., I.R. Duddy, A.J.W. Gleadow, P.R. Tingate, and G.M. Laslett, Thermal annealing of fission tracks in apatite: 1. a qualitative description, *Chem. Geol., 59,* 237-253, 1986.

Green, P.F., I.R. Duddy, G.M. Laslett, K.A.Hegarthy, A.J.W. Gleadow, and J.F. Lovering, Thermal annealing of fission tracks in apatite 4. Quantitative modelling techniques and extension to geological time scales, *Chem. Geol., 79,* 155-182, 1989.

Green, P.F., K.A. Hegarty, I.R. Duddy, S.S. Foland, and V. Gorbachev, Geological constraints on fission track annealing in zircon. in *8th International workshop on fission-track dating, Gent, abstract volume*, 44, 1996.

Grocott, J., M. Brown, R.D. Dallmeyer, G. Taylor, and P.J. Treloar, Mechanisms of continental growth in extensional arcs: An example from the Andean plate-boundary zone, *Geology, 22*, 391-394, 1994.

Hagesawa, K., K. Matsushita, T. Nishimura, F. Hervé, and Y. Akagi, Geological note at las Chivas District, Aysén Province, Chile, *Report of the Geol. Survey of Hokkaido, 44*, 25-29, 1971.

Hallet, B., L. Hunter, and J. Bogen, Rates of ersoion and sediment evacuation by glaciers: A review of field data and their implications, *Global Planet. Change, 12*, 213-235, 1996.

Hamza, V.M., and M. Muñoz, Heat flow map of South America, *Geothermics, 25*, 599-646, 1996.

Harrison, T.M., Diffusion in ^{40}Ar in Hornblende, *Contrib. Mineral. Petrol. 78,* 324-331, 1981.

Harrison, T.M., R.L. Armstrong, C.W. Naeser, and J.E. Harakal, Geochronology and thermal history of the Coastal Plutonic Complex, near Prince Rupert, British Columbia, *Can. J. Earth Sci., 16*, 400-410, 1979.

Harrison, T.M., I. Duncan, and I. McDougall, Diffusion of ^{40}Ar in Biotite: temperature, pressure and compositional effects, *Geochim. Cosmochim. Acta, 49*, 2461-2468, 1985.

Hein, R., Geología del valle California y de las areas mineralizadas de la región de Alto Palena, Chiloé Continental, 185 pp., Mem. de Titulo Depto. Geol. Univ. de Chile, Santiago, Chile, 1979.

Hervé, F., Rejuvenecimiento de edades radiométricas y el sistema de fallas Liquiñe-Ofqui, *Com. Dep. Geol. Univ. Chile, 35*, 107-116, 1984.

Hervé, F., Late Paleozoic subduction and accretion in southern Chile, *Episodes, 11,* 183-188, 1988.

Hervé, F., Paleozoic metamorphic complexes in the Andes of Aysén (west of ?Occidentalia), in *Proceedings of First Circum-Pacific and Circum-Atlantic Terrane Conference,* edited by F. Ortega Gutiérrez, P.J. Coney, E. Centeno-Garcia, and Gomez-Caballero, pp. 64-65, Guanajuato, Mexico, 1993.

Hervé, F., Late Triassic rocks in the subduction complex of Aysén, southern Chile, in *Special Abstract Volume, Gondwana 10: Event stratigraphy of Gondwana, J. African Earth Sci., 27,* 224, 1998.

Hervé, F., E. Araya, J. Fuenzalida, and A. Solano, Edades radiométricas y tectónica neógena en el sector costero de Chiloé Continental. X Región, *Segundo Congreso Geológico Chileno, Arica, Actas,* 1, F1-F18, 1979.

Hervé, F., E. Godoy, M.A. Parada, V. Ramos, C.W. Rapela, C. Mpodozis, and J. Davidson, A general view on the Chilean-Argentine Andes with emphasis on their early history. in: *Circum-Pacific Orogenic Belts and the Evolution of the Pacific Ocean Basin,* edited by J.W.H. Monger and J. Francheteau, AGU Geodynamic Series, 18, 97-114, 1987.

Hervé, F., and Y. Ota, Fast Holocene uplift rates at the Andes of Chiloé, southern Chile. *Rev. Geol. Chile*, *20(1), 15-23,* 1993.

Hervé, F., R.J. Pankhurst, R. Drake, M.E. Beck, and C. Mpodozis, Granite generation and rapid unroofing related to strike-slip faulting, Aysén, Southern Chile, *Earth Planet. Sci. Lett., 120*, 375-386, 1993.

Hervé, F., R.J. Pankhurst, R. Drake, and M.E. Beck, Pillow metabaslts in a mid-Tertiary extensionl basin adjcent to the Liquiñe Ofqui fault zone: the Isla Magdalena area, Aysén, Chile, *J. S. Am. Earth Sci, 8,* 33-46, 1995.

Hervé, F., R.J. Pankhurst, A. Demant, and E. Ramirez, Age and Al-in-hornblende geobarometry in the North Patagonian Batholith, Aysén, Chile, in *Third International Symposium on Andean Geodynamics (ISAG), St Malo, France, Abstracts*, pp. 17-19, ORSTROM, Paris, 1996.

Hervé, F., C.M. Fanning, J. Bradshaw, M. Bradshaw, and J.P. Lacassie, Late Permian SHRIMP U-Pb detrial zircon ages constrain the age of accretion of oceanic basalt to the Gondwana margin at the Madre de Dios Archipelago, southern Chile, in *Fourth ISAG, Göttingen, Germany, abstracts,* pp. 327-328, ORSTROM, Paris, 1999.

Hervé, F, A. Demant, V. Ramos, R.J. Pankhurst, and M. Suárez, The Southern Andes, in *Tectonic evolution of South America,* edited by U.G. Cordani, E.J. Milani, A. Thomaz Filho, and D.A. Campos*,* Rio de Janeiro, pp. 605-634, 2000.

Hervé, F., and C.M. Fanning, Late Triassic detrital zircons in metaturbidites of the Chonos Metamorphic Comlpex, southern Chile, *Rev. Geol. Chile, 28(1)*, 91-104, 2001.

Hervé, M., Estudio Geológico de la Falla Liquiñe-Reloncaví en el área de Liquiñe: antecedentes de un movimiento transcurrente, *Primer Congreso Geológico Chileno, Santiago, Actas, 1,* B39-B56, 1976.

Heusser, C. J., Chilotan piedmont glacier in the Southern Andes during the glacial maximum, *Rev. Geol. Chile, 15(1),* 13-30, 1990.

Hirth, G., and J. Tullis, Dislocation creep in quartz aggregates, *J. Struct. Geol., 14,* 145-159, 1992.

Hodges, K.V., Pressure-temperature-time paths, *Ann. Rev. Earth Planet. Sci., 19,* 207-236, 1991.

Hoeppener, R., Tektonik im Schiefergebirge, *Geol. Rund., 44,* 26-58, 1955.

Holdaway, M.J., Stability of Andalusite and the aluminosilicate phase diagrams, *Am. J. Sci., 271*, 97-131, 1971.

Holden, N.R., Total and spontaneous fission half-lives of uranium, plutonium, americium, and curium nuclides, *Pure Appl. Chem., 61*, 1989.

Huffman, L., and H. Massone, Ancient arc/back arc and N-Morb volcanics incorporated in the Late Paleozoic/Early Mesozoic metamorphic complex of the Coastal Cordillera of Chiloé, Southern Central Chile. in *IX Congreso Geológico Chileno, Puerto Varas, Actas, 2,* 738-741, 2000.

Hunziker, J.C., J. Desmons, and A.J. Hurford, Thirty-two years of geochronological work in the Central and Western Alps: a review on seven maps, *Mém. Geol. (Lausane), 13*, 59, 1992.

Hurford, A.J., Cooling and uplift patterns in the Lepontine Alps, South Central Switzerland and an age of vertical movement on the Insubric line, *Contrib. Mineral. Petrol., 92*, 413-427, 1986.

Hurford, A.J., Standarization of fission track dating calibration: recommendation by the Fission Track Working Group of the I.U.G.S. Subcommision on Geochronology, *Chem. Geol., 80,* 171-178, 1990a.

Hurford, A.J., International Union of Geological Sciences Subcommision on Geochronology recommendation for the standarization of fission track dating calibration and data reporting, *Nucl. Tracks, 17,* 233-236, 1990b.

Hurford, A.J., A.J.W. Gleadow, and C.W. Naeser, Fission track dating of pumice from the KBS tuff, East Rudolf, Kenya, *Nature, 263*, 738-740, 1976.

Hurford, A.J., and P.F. Green, Standards, dosimetry and uranium-238 λ_f decay constant: a discussion, *Nucl. Tracks, 5,* 73-75, 1981.

Hurford, A.J., and P.F. Green, A user's guide to fission track dating calibration, *Earth Planet. Sci. Lett., 59*, 343-354, 1982.

Hurford, A.J., and P.F. Green, The zeta age calibration of fission track dating, *Chem. Geol., 1*, 285-317, 1983.

Hurford, A.J., F.J. Fitch, and A. Clarke, Resolution of the age structure of the detrital zircon populations of two Lower Cretaceous sandstones from the Weald of England by fission track dating, *Geol. Mag., 121,* 269-277, 1984.

Hurford, A.J., J.C. Hunziker, and B. Stöckhert, Constraints on the thermotectonic evolution of the Western Alps: evidence for episodic rapid uplift, *Tectonics, 10*, 758-769, 1991a.

Hurford, A.J., and A. Carter, The role of fission track dating in discrimination of provenance. in *Developments in sedimentary provenance studies,* edited by A.C. Moreton, S.P. Todd, and P.D.W. Haughton, Spec. Pub. Geol. Soc. Lond., 57, 67-78, 1991b.

Hutton, D.H.W., and R.J. Reavy, Strike-slip tectonics and granite petrogenesis: *Tectonics, 11*, 960-967, 1992.

Jaffey A.H., K.F. Flynn, L.E. Glendenin, W.C. Bentley, and M. Essling, Presicion measurements of half-lives and specific activities of ^{235}U and ^{238}U, *Phys. Rev., 4,* 1889-1906, 1971.

Jaillard, E., P. Soler, G. Carlier, and T. Mourier, Geodynamic evolution of the northern and Central Andes during early to middle Mesozoic times; a Thetyan model, *J. South Am. Earth Sci.*, *8*, 33-46. 1990.

Johnson, C., N. Harbury, and A.J. Hurford, The role of extension in the Miocene denudation of the Nevado-Filábride Complex, Betic Cordillera (SE Spain), *Tectonics, 16,* 189-204, 1997.

Johnson, M.C., and M.J. Rutherford, Experimental calibration of Al in Hornblende geobarometer with application to Long Valley caldera (California), *Geology, 17,* 837-841, 1989.

Johnson, M.C., A.T., Anderson Jr., and M.J. Rutherford, Pre-eruptive volatile content of magmas. in *Volatiles in magmas,* edited by M.R. Carroll, and J.R. Holloway. Rev. Mineral. 30, 281-323, 1994.

Kato, C.T., Pre-Andean orogenesis in the Coastal Ranges of Chile, *Geol. Soc. Am. Bull., 96,* 918-924, 1985.

Kato, C.T., and E. Godoy, Petrogenesis and tectonic significances of Late Paleozoic caorse-crystalline blueschist and amphibolite boulders in the coastal range of Chile, *Int. Geol. Rev., 37*, 992-1006,1995.

Kasuya, M., and C.W. Naeser, The effect of a damage on fission track annealing in zircon, *Nucl. Tracks, 14,* 477-488, 1988.

Ketcham, R.A., R.A. Donnelick, and W.D. Carlson, Variability of apatite fission-track annealing kinetics: III Extrapolation to geological time scales, *Am. Mineral., 84,* 1235-1255, 1999.

Ketcham, R.A., R.A. Donelick, and M.B. Donelick, AFTSolve: A program for multi-kinetic modeling of apatite fission-track data, *Geological Materials Res.*, *2*, no. 1 (electronic), 2000.

Krishnaswami, S., D. Lal, N. Prahbu, and D. MacDougall, Characteristics of fission tracks in zircon: applications to geochronology and cosmology, *Earth Planet. Sci. Lett., 22,* 51-59, 1974.

Kukowsi, N., Plutonische hydrothermale Systeme in der kontinentalen Kruste: Numerische Modellrechungen zu räumlichen Dimensionen und zeitlichen Variationen von Quelle und Umfeld, Ph.D. Thesis, 118 pp., Math. Nat. Fak. Univ. Bonn, Germany, 1992.

Kukowski, N., G. Morteani, and H.J. Neugebauer, Structural development, thermal history, and dating of granitoid complexes, *Terra Abstracts 1, 280,* 1989.

Kukowski, N., and H.J. Neugebauer, On the ascent and emplacement of granitoid magma bodies- dynamic-thermal numerical models, *Geol. Rundschau, 79*, 227-239, 1990.

Lakatos, S., and D.S. Miller, Evidence for the water content on fission track annealing in volcanic glass, *Earth Planet. Sci. Lett., 14,* 128-130, 1972.

Lara, L., C. Rodríguez, H. Moreno, and C.P. Perez de Arce, Geocronología K-Ar y geoquímica del volcanismo plioceno superior-pleistoceno de los Andes del sur (39-42°S), *Rev. Geol. Chile, 28(1),* 67-90, 2001.

Laslett, G.M., W.S. Kendall, A.J.W Gleadow, and I.R. Duddy, Bias in measurement of fission track length distributions, *Nucl. Tracks, 6,* 79-85, 1982.

Laslett, G.M., P.F. Green, I.R. Duddy, and A.J.W. Gleadow, Thermal annealing of fission tracks in apatite: 2. A quantitative analysis, *Chem. Geol., 65,1-13,* 1987.

Laslett, G.M., and R.F. Galbraith, Statistical modelling of thermal annealing of fission tracks in apatite, *Geochim. Cosmochim. Acta, 60,* 5117-5131, 1996.

Lavenu A., and J. Cembrano, Compressional- and transpressional-stress for Pliocene and Quarternary brittle deformation in fore arc and intra-arc zones (Andes of Central and Southern Chile), *J. Struct. Geol., 2,* 1669-1691, 1999.

Levi, B., A. Aguilar, and R. Fuenzalida, Reconocimiento geológico en las provincias de Llanquihue y Chiloé, 45 pp**.,** Boletín Instituto de Investigaciones Geológicas, Santiago, Chile, 19, 1966.

Lister, G.S., and A.W. Snoke, S-C Mylonites, *J. Struct. Geol., 6,* 617-638, 1984.

Llitboury, L., Glaciers of the Wet Andes, in *Satellite image atlas of the glaciers of the World, South America,* edited by R.S. Williams, and J.G. Ferrigno, USGS professional paper 1386-I, http://pubs.usgs.gov.prof/p1386i/index.html, 1999.

López-Escobar, L., M.A. Parada, H. Moreno, F.A. Frey, and R.A. Hickey-Vargas, Contribution to the petrogenesis of Osorno and Calbuco volcanoes, Southern Andes (41°- 41°30'S): a comparative study, *Rev. Geol. Chile, 19(2)*, 11-226, 1992.

López-Escobar, L., J. Cembrano, and H. Moreno, Geochemistry and tectonics of the Chilean Southern Andes basaltic Quaternary volcanism (37 - 46°S), *Rev. Geol. Chile, 22(2),* 219-234, 1995.

Lutz, T.M., and G.I. Otmar, An inverse method of modelling thermal histories from apatite fission track data, *Earth Planet. Sci. Lett., 104*, 383-393, 1991.

Mancktelow, N.Z., and B. Grasemann, Time-dependent effects of heat advection and topography in cooling histories during erosion, *Tectonophysics, 270,* 167-195, 1997.

Martin, M.W., C.T. Kato, C. Rodriguez, E., Godoy, P. Duhaart, M. McDonough, and A. Campos, Evolution of the Late Paleozoic Accretionary Complex and overlying fore-arc magmatic arc, south-central Chile (38°- 41°S), Constraints for the tectonic setting along the southwestern margin of Gondwana, *Tectonics, 18, 4*, 582-605, 1999.

Massone, H.J., F. Hervé, O. Medembach, V. Muñoz, and A.P. Willner, New petrological results on high-pressure, low-temperature metamorphism of the Upper Paleozoic basment of central Chile, Third Int. Symp. On Andean Geodynamics (St. Malo), Abstracts, 783-785, 1996.

Massone, H.J., F. Hervé, O. Medembach, V. Muñoz, and A.P. Willner, Zussmanite in ferrugineous metasediments from southern central Chile, *Mineral. Mag., 62*, 869-876, 1998.

Massonne, H.J., L. Huffmann, P. Duhart, F. Hervé, and A.P. Willner, New insights into the structure of the upper Paleozoic/Mesozoic accretionary wedge complex of the Coastal Cordillera of central and southern Chile. in *Fourth ISAG*, *Göttingen*; *Germany, abstracts*, pp. 492-495, ORSTROM, Paris, 1999.

McDougall, I., and T.M. Harrison (Eds.), *Geochronology and thermochronology by the $^{40}Ar/^{39}Ar$ method*, 2nd ed., 269 pp., Oxford Univ. Press, New York, 1999.

Mercer, J.H., Glacial history of southernmost south America, *Quat. Res., 6(*2), 125-166, 1976.

Mercer, J.H., and J.F. Sutter, Late Miocene-earliest Pliocene glaciation in southern Argentina: Implications for global ice-sheet history, *Paleogeograph., Paleoclimatol., Paleoecol., 38*, 185-206, 1982.

Montgomery, D.R., G. Balco, and S.D. Willet, Climate, tectonics, and the morphology of the Andes, *Geology, 29*, 579-582, 2001.

Montgomery, D.R., and M.T. Brandon, Topographic controls on erosion rates in tectonically active mountain ranges, *Earth Planet. Sci. Lett., 1*, 481-489, 2002.

Moreno, H., Airplane flight over active volcanoes of central-south Chile. IAVCEI Symp. on Andean and Antarctic Volcanology Problems. Guide Book D-3, Dep. Geol. Univ. Chile, Santiago, Chile, 1974.

Moreno, H., and J. Varela, Mapa geológico del Volcán Calbuco a escala 1:50000. in: Geología y riesgo volcánico del volcán Calbuco y centros eruptivos menores. Proy. Canutillar, ENDESA-Universidad de Chile, technical report, edited by A. Lahsen, H. Moreno, J. Varela, F. Munizaga, and L. Lopez-Escobar, 138, 1985.

Munizaga, F., F. Hervé, R. Drake, R.J. Pankhurst, M. Brook, and N. Snelling, Geochronology of the Lake Region of South Central Chile (39°- 42°S): Preliminary results, *J. South Am. Earth Sci., 1(3),* 309-318, 1988.

Muñoz, M., Tectonophysics of the Andes region: Relationships with heat flow and the thermal structure, *Fourth International Symposium on Andean Geodynamics, Göttingen, Extended Abstracts*, pp. 532-534, ORSTROM; Paris, 1999.

Muñoz, V., and F. Herve, Consideraciones de la alta presion-baja tempreatura para la serie oeste del basamento metamorfico paleozoico, en base a clorita, cimrita y mica blanca en sulfuros masivos de Piren Alto; *Actas IX Congreso Chileno de Geología, Resmunenes Expandidos, 1*, 654-658, 2000.

Muñoz, N., R. Troncoso, P. Duhart, P. Crignola, L. Farmer, and C. Stern, The relation of the mid-Tertiary coastal magmatic belt in south-central Chile to the late Oligocene increase in plate convergence rate, *Rev. Geol. Chile, 27(2)*, 177-203, 2000.

Murdie, R.E., D.J. Prior, P. Styles, S.S. Flint, R.G. Pearce, and S.M. Agar, Seismic responses to ridge transform subduction: Chile Triple Junction, *Geology, 21,* 1095-1098, 1993.

Naeser, C.W., The use of apatite and sphene for fission track age determinations, *Bull. Geol. Soc. Am., 78*, 1523-1526, 1967.

Naeser, C.W., Fission track dating and geologic annealing of fission tracks, in *Lectures in Isotopic Geology*, edited by E. Jäger, and J.C. Hunziker, pp. 154-169, Springer-Verlag, Berlin, 1979.

Naeser, C.W., The fading of fission tracks in the geological environment- data from deep drill holes, *Nucl. Tracks, 5,* 248-250, 1981.

Naeser, C.W., and H. Faul, Fission track annealing in apatite and sphene, *J. Geophys. Res., 74*, 705-710, 1969.

Naeser, C.W., G.A. Izett, and J.D. Obradovich, Fission track and K/Ar ages of natural glasses, *U.S.G.S. Bull., 1489*, 31, 1980.

Nelson, E., Forsythe, R., and I. Arit, Ridge Collision tectonics in terrane development, *J. South Am. Earth Sci., 7,* 271-278, 1994.

O'Sullivan, P.B., and R.R. Parrish, The importance of apatite composition and single-grain ages when interpreting fission track data from plutonic rocks: a case study from the Coast Ranges, British Columbia, *Earth Planet. Sci. Lett., 132,* 213-224, 1995.

Pankhurst, R.J., F. Hervé, F.L. Rojas, and J. Cembrano, Magmatism and tectonics in continental Chiloé, Chile (42°- 42°30'S), *Tectonophysics, 205*, 673-694, 1992.

Pankhurst, R.J., P.T. Leat, P. Sruoga, C.W. Rapela, M. Márquez, B.C. Storey, and T.R. Riley, The Chon-Aike silicic igneous province of Patagonia and related rocks in West Antarctica: a silicic LIP, *J. Volcano. Geotherm. Res., 81,* 113-136, 1998.

Pankhurst, R.J., S.D. Weaver, F. Hervé, and P. Larrondo, Mesozoic-Cenozoic evolution of the North Patagonian Batholith in Aysén, southern Chile, *J. Geol. Soc. London, 156,* 673-694, 1999.

Pankhurst, R.J., T.R. Riley, C.M. Fanning, and S.P. Kelley, Episodic silicic volcanism in Patagonia and the Antarctic Peninsula: chronology of magmatism associated with the break-up of Gondwana, *J. Petrol., 41*, 605-625, 2000.

Parada, M., E. Godoy, F. Hervé, and R. Thiele, Miocene calkalcaline plutonism in the Chilean Southern Andes, *Rev. Bras. Geosciências, 17(4)*, 450-455, 1987.

Pardo-Casas, F., and P. Molnar, Relative motion of the Nazca (Farallon) and South American plates since Late Cretaceous times, *Tectonics, 6,* 233-248, 1987.

Paschier,C.W., and R.A.J. Trouw (Eds.) *Microtectonics,* Springer-Verlag, New York, 1996.

Paterson, S.R., R.H. Vernon, and O.T. Tobisch, A review of criteria for the identifictction of magmatic and tectonic folition in granitoids, *J. Struc. Geol.*, *11*, 349-363, 1989.

Paterson, S.R., R.H. Vernon, and T.K. Fowler Jr., Aureole Tectonics, in *Contact Metamorphism*, edited by D. Kerick, Rev. Mineral., 26, pp. 673-722, 1991.

Petrov, Yu.V., The Oklo natural reactor, *Soviet Phys. Uspekhi., 20 (11),* 937-944, 1977.

Poirier, J.P., *Creep of crystals: high temperature deformation of metals, ceramics and minerals,* Cambridge Univ. Press, Cambridge, 1985.

Purdy, J.W., and E. Jäger, K-Ar ages on rock-forming minerals from the Central Alps, *Mem. Inst. Geol. Mineral. Univ. Padova*, *30*, 1-34, 1976.

Price, P.B., and R.M. Walker, Observation of fossil particle tracks in natural micas, *Nature, 196*, 732, 1962.

Rabassa, J., and C.M. Clapperton, Quaternary glaciations of the southern Andes, *Quat. Sci. Rev., 9,* 153-174, 1990.

Rahn, M.K., M.T. Brandon, G.E. Batt, and J.I. Garver, Fission-track annealing in 'zero-damage' zircons: field constraints and an empirical model, in *9th International Conference of Fission Track Dating and Thermochronology, Lorne, Australia*, *Abstracts*, 271, 2000.

Ramos, V., Anden foothills structures in Northern Magallanes basin, Argentina, *AAPG Bull., 73*, 887-903, 1989.

Ramos, V., and S. Kay, Southern Patagonian plateau basalts and deformation: Backarc testimony of ridge collisions, *Tectonophysics, 205*, 261-282, 1992.

Rojas, C., M.E. Beck, R.F. Burmeser, J. Cembrano, and F. Hervé, Paleomagnetism of the mid-Tertiary Ayacara Formation, southern Chile: Counterclockwise rotation in a dextral shear zone, *J. South Am. Earth Sci., 7*, 45-56, 1994.

Romero, G., Geología del Sector Alto Palena-Puerto Ramírez. Chiloé Continental. Mem. de Titulo Depto. Geol. Univ. de Chile, Santiago, Chile, 1983.

Saint Blanquat, M., B. Tikoff, B. Teyssier, and J.L. Vignesse, Transpressional kinematics of magmatic arcs. in *Continental Transpressional and Transtensional Tectonics,* edited by R.E. Holdsworth, R. Strachan, and J.F. Dewey, pp. 327-340. Geol. Soc. London Spec. Pub. 135, 1998.

Saliot, P., Ètude gèologique dans l'île de Chiloé (Chili), *Bull. Soc. Géol. France, 7(11)*, 388-399,1969.

Sambridge, M.S., and W. Compston, Mixture modelling of multi-component data sets with application to ion-probe zircon ages, *Earth Planet. Sci. Lett., 128,* 373-390, 1994.

Segré, E., Spontaneous Fission, *Phys. Rev. 86*, 21-28, 1952.

Seifert, W., M. Rosenau, and H. Echtler, The evolution of the South Central Chile magmatic arcs: Crystallization depths of granitoids estimated by hornblende geothermobarometry – implications for mass transfer processes along the active continental margin, *Neues Jahrbuch für Geologie und Paläontologie*, in press, 2003.

Seipold, U., Temperature dependance of thermal transport properties of crystalline rocks- A general law, *Tectonophysics, 291,* 161-171, 1998.

SERNAGEOMIN, Mapa geológico de Chile, escala 1:1.000.000, Servicio Nacional de Geología y Minería, Santiago, Chile, 1980.

SERNAGEOMIN-BRGM, Mapas geológicos y metalogénicos Puerto Montt, Castro y Palena, entre los 41° y 44°LS, Internal Report, Servicio Nacional de Geología y Minería, Santiago, Chile, 1995.

Seward, D., and D.A. Rhoades, Clustering technique for fission-track dating of fully to partially annealed minerals and other non-unique populations, *Nucl. Tracks, 11,* 259-268, 1986.

Silk, E.C., and R.S. Barnes, Examination of fission fragment tracks with an electron microscope, *Philos. Mag., 4*, 970-972, 1959.

Simpson, C., Deformation of granitic rocks across the brittle-ductile transition, *J. Struct. Geol.*, 7, 503-511, 1985.

Small, E., Does global cooling reduce relief? *Nature, 401,* 31-33, 1999.

Solano, A., Geología del sector costero de Chiloé continental entre los 41°50' y 42°10' L.S., Mem. de Titulo Depto. Geol. Univ. de Chile, Santiago, Chile, 1978.

Somoza, R., Updated Nazca (Farallon)-South America relative motions during the last 40 Ma: Implications for mountain building in the central Andean region, *J. South Am. Sci., 11,* 211-215, 1998.

Spear, F.S., *Metamorphic phase equilibrium and pressure-temperature-time paths,* Min. Soc. Am. Monograph, Washington DC, 1993.

Spear, F.S. and Cheney, J.T., A petrogenetic grid for pelitic schists in the system SiO_2-Al2O_3-FeO-MgO-K_2O-H_2O, *Contrib. Mineral. Petrol., 83*, 348-357, 1989.

St-Onge, M.R., The muscovite-melt bathograd and low P isograd suites in north-central Wopmay Orogen, Northwest Territories, Canada*, J. Metam. Geol., 2,* 315-326, 1984.

Steiger, R.H., and E. Jäger, Subcommision on geochronology: convention on the use of decay constants in geo- and cosmochronology, *Earth Planet. Sci. Lett., 36*, 359-362, 1977.

Stern, C., and M. Vergara, New age for the vitrophyric rhyolite-dacite from Ancud (42°S) Chiloé, Chile, *Rev. Geol. Chile, 19(2*), 249-251, 1992.

Stöckhert B., M.R. Brix, R. Kleinschrodt, A.J. Hurford A.J., and R. Wirth, Thermo-chronometry and microstructures of quartz- a comparison with experimental flow laws and predictions on the temperature of the brittle-plastic transition, *J. Struct. Geol., 21*, 351-369, 1999.

Stüwe, K., L. White, and R. Brown, The influence of eroding topography on steady-state isotherms. Application to fission-track analysis, *Earth Planet. Sci. Lett.*, *124*, 63-74, 1994.

Suarez, M., and R. De la Cruz, Tectonics in the eastern central Patagonian Cordillera (45°30'- 47°30'S), *J. Geol. Soc. London, 157,* 995-1001, 2000.

Székely, B., A possible comparative technique for fission track measurements- a proposal, in *10th International Workshop on Fission Track Analysis: Theory and Applications, Geotemas, 4, Extended Abstracts*, pp.155-156, 2002.

Tagami, T., and C. Shimada, Natural long-term annealing of the zircon fission track system around a granitic pluton, *J. Geophys. Res., 101*, 8245-8255, 1996.

Tagami, T., Carter A., and A.J. Hurford, Natural long-term annealing of the zircon fission track system in Vienna basin deep borehole samples: Constraints upon the partial annealing zone and closure temperature, *Chem. Geol.*, *130*, 147-157, 1996.

Tagami, T., R.F. Galbraith, R. Yamada, and G.M. Laslett, Revised annealing kinetics of fission tracks in zircon and geological implictions. in *Advances in fission track geochronolgy*, edited by P. Van den haute, and F. de Corte, Kluwer Academic Publishers, Dordrecht, Netherlands, pp. 99-102, 1998.

Tebbens, S.F., and S.C. Cande, Southeast Pacific tectonic evolution from early Oligocene to Present, *J. Geophys. Res., 102B,* 12061-12084, 1997.

Thiel, K., and W. Herr, The ^{238}U spontaneous fission decay constant re-determined by fission tracks, *Earth Planet. Sci. Lett., 30,* 50-56, 1976.

Thiele, R., J. Castillo, R. Hein, and M. Ulloa, Geología del sector fronterizo de Chiloé Continental entre los 43° y 43°45' L.S., Chile, *VII Congreso Geol. Argentino, Neuquén, Actas, 1,* 577-592, 1978.

Thiele, R., F. Hervé, M.A. Parada, and E. Godoy, The Liquine-Ofqui megafault at the Reloncaví Fiord (41°30'S), Chile, *Com. Dep. Univ. Chile, 46*, 3-15, 1986.

Thomson, S.N., Thermo-tectonics of the Calabrian Arc, southern Italy, constraints from fission track analysis, Thesis Dept. Geol. Sci., Univ. College London, 271pp., 1992.

Thomson, S.N., Late Cenozoic geomorphic and tectonic evolution of the Patagonian Andes between latitudes 42°S and 46°S: an appraisal based on fission track results from the transpressional intra-arc Liquine Ofqui fault zone, *GSA Bull., 114(9),* 1159-1173, 2002.

Thomson, S.N., F. Hervé, and C.M. Fanning, Combining fission-track and U-Pb SHRIMP zircon ages to establish stratigraphic and metamorphic ages in basement sedimentary rocks in southern Chile, *IX Congreso Geológico Chileno, Puerto Varas, Chile, Resumenes Expandidos, IX,* 769-773, 2000.

Thomson, S.N., F. Hervé, and B. Stöckhert, The Mesozoic-Cenozoic denudation history of the Patagonian Andes (southern Chile) and its correlation to different subduction processes, *Tectonics, 20,* 693-711, 2001.

Thomson, S.N., and F. Hervé, New time constraints for the age of metamorphism at the ancestral Pacific Gondwana margin of southern Chile (42°- 52°S), *Rev. Geol. Chile, 29(2),* 255-271, 2002.

Tikoff, B., and M. Saint-Blanquat, Transpressional shearing and strike-slip partitioning in the Late Cretaceous Sierra Nevada magmatic arc, California, *Tectonics, 16*, 442-459,1997.

Ulloa, M., Geología del sector suroriental de la Comuna de Futaleufú, X Región, 126 pp., Mem. de Titulo Depto. Geol. Univ. de Chile, Santiago, Chile 1980.

Valdivia S., and E. Valenzuela, Volcanitas riodaciticas de Gambo, Isla de Chiloé, X Región, Chile, *V Congreso Geologico Chileno, Santiago, Actas, 3*, 261-273, 1988.

Vargas, G., and F. and F. Hervé, Emplazamiento hipabisal Mioceneo tardío del stock paso de las Llaves en la región de Tras Arco, Aysén, *Com. Dep. Geol. Univ. de Chile*, *46*, 3-15 1995.

Vergara, M., and F. Munizaga, Age and evolution of the Upper Cenozoic Andesitic Volcanism in Central-South Chile, *GSA Bull., 85*, 603-606, 1974.

Vernon, R.H., *Metamorphic processes*, 247 pp., Allen and Unwin (Eds.), London, 1976.

Wagner, G.A., and G.M. Reimer, Fission track tectonics: the tectonic interpretation of fission track apatite ages, *Earth Planet. Sci. Lett., 14*, 263-268, 1972.

Wagner, G.A., G.M. Reimer, G.S. Carpenter, H. Faul, R. Van der Linden, and R. Gijbels, The spontaneous fission rate of ^{238}U and fission track dating, *Geochim. Cosmochim. Acta, 39*, 1279-1286, 1975.

Wagner, G.A., G.M. Reimer, and E. Jäger, Cooling ages by apatite fission track, mica Rb-Sr, and K-Ar dating: the uplift of the central Alps, *Mem. Inst. Geol. Mineral. Univ. Padova, 30*, 1-27, 1977

Wagner, G.A., D.S. Miller, and E. Jäger, Fission track ages on apatite of Bergell rocks from Central Alps and Bergell boulders in Oligocene sediments, *Earth Planet. Sci. Lett., 45*, 355-360, 1979

Wagner, G.A., and P. Van den haute, *Fission track dating,* 285 pp., Enke-Verlag, Stuttgart, 1992.

Wagner, G.A., R. Altherr, and P. Van den haute, Apatite fission track analysis of Kenyan basement rocks: constraints on the thermotectonic evolution of the Kenya dome. A reconnaissance study, *Tectonophysics, 204,* 93-110, 1992.

Wagner, G.A., D.A. Coyle, J. Duyster, F. Henjes-Kunst, A. Peterek, B. Schröder, B. Stöckhert, K. Wemmer, G. Zulauf, H. Ahrendt, R. Bischoff, E. Hejl, E. Jacobs, J. Menzel, Nand Lal, P. Van den haute, C. Vercoutere, and C. Welzel, Post-Variscan thermal and tectonic evolution of the KTB site and its surroundings, *J. Geophys. Res. 102 B8)*, 18221-18232, 1997.

Weaver, S.G., R. Bruce, E.P. Nelson, H.K. Brueckner, and A.P. LeHuray, The Patagonian batholith at 48° latitude, Chile. Geochemical and isotopic variations, *Spec. Pap. Geol. Soc. Am., 241,* 33-50, 1990.

Whipple, K., E. Kerby, and S.H. Brocklehurst, Geomorphic limits to climate-induced increases in topographic relief, *Nature, 401,* 39-43, 1999.

Willet, S.D., Modelling thermal annealing of fission track in apatite, in *Short Course Handbook on Low Temperature Thermochronology,* edited by M. Zentilli, and P.H. Reynolds, Min. Soc. Can., Toronto, Canada, pp. 43-72, 1992.

Willet, S.D., Inverse modelling of annealing of fission tracks in apatite,1. A controlled random search model, *Am. J. Sci., 297(10),* 939-969, 1997.

Willet, S.D., Orogeny and Orography: The effects of erosion on the structure of mountain belts, *J. Geophys. Res.*, *104*, 28957-28981, 1999.

Willner, A.P., F. Hervé, and H.J. Massone, Mineral chemistry and pressure-temperature evolution of two contrasting high-pressure-low-temperature belts in the Chonos Archipelago, southern Chile, *J. Petrol., 41,* 309-330, 2000.

Willner, A.P., S. Paulig, H.J. Massone, and F.Hervé, Metamorphic evolution of spessartine quartzites (coticules) in the high-pressure, low-temperature complex at bahía Mansa, Coastal Cordillera of South-Central Chile, *Canad. Mineral., 39*,1547-1569, 2001.

Yamada, R., T. Tagami, S. Nishimura, and H. Ito, Annealing kinetics of fission track in zircon: an experimental study, *Chem. Geol., 122,* 249-258, 1995.

Yamada R., T. Tagami, S. Nishimura, and H. Ito, Annealing kinetics of fission tracks in zircon: an experimental study, in *Internaitonal workshop on fission track dating, Gent, Abstracts Volume*, 131 pp., 1996.

Yund, R.A., and J. Tullis, Compositional changes of minerals associated with dynamic recrystallization, *Contrib. Mineral. Petrol., 108*, 346-355, 1991.

Zeitler, P.K., N.M. Johnson, C.W. Naeser, and R.A.K. Tahirkehli, Fission track evidence for Quaternary uplift of the Nanga Parbat region, Pakistan, *Nature*, *298,* 255-257, 1982.

Appendix

Appendix 1. Sample Handling Procedures for Fission Track Analysis

I) Separation of Apatite and Zircon

Samples are first washed and dried, then split and crushed using an automatic jaw crusher. The resultant fragments are then put through a standard Bico® disc mill reducing the sample to fine-grain sized fragments. The heavy mineral fraction of the sample that includes both zircon and apatite grains, is then separated using a Whifley® table. The heavy mineral concentrate is dried, and the larger grains that remain removed using a 500 μm sieve. The heavy minerals that have magnetic characteristics, including biotite, magnetite, muscovite, ore minerals, and amphiboles are removed using a Franz® magnetic separator. To separate the remaining quartz and feldspar grains, the <500 μm sieve is passed through the heavy liquid bromoform (s.g. = 2.88-2.91 g/cm^2). The remaining heavy minerals are washed with acetone and dried. Apatite (s.g. = 3.1-3.35 g/cm^2) is separated from zircon (s.g. = 4.6-4.7 g/cm^2) using the heavy liquid di-odomethane (s.g.= 3.35 g/cm^2).

II) Mounting of Apatite Grains

Apatite crystals are mounted in Araldite® epoxy resin. First, a 2:1 microscope slide is degreased using acetone, and the relevant sample number is marked using a diamond pen. This is then placed on a hot-plate at temperature of 70°C. Araldite® is then thoroughly mixed using 5 parts resin to 1 part hardener by volume in a plastic container. Then, in a fume cabinet, a few drops of Araldite® are placed on to the microscopic slide, with the number side down, and stirred gently to release any air bubbles. A portion of the apatite fraction of the sample is then poured onto the Araldite®. Using a clean needle, the crystals are stirred in to spread out the individual grains. The Araldite® is then allowed to harden and cure.

III) Mounting of Zircon Grains

Zircon crystals are mounted in melted FEP Teflon plastic. First a hot plate is heated to 290 ± 5°C in a fume cabinet (molten FEP Teflon produces the toxic gas perfluorobutadiene). Two microscope slides are then degreased using acetone. On one slide a portion of the zircon crystals are placed and arranged using a needle. The slide is then tapped to allow the zircon crystals to settle on their prismatic faces, and then placed on the hot plate for 2 min. Using tweezers, a 1.5cm square of 0.5mm thick translucent FEP Teflon is placed on top of the zircon crystals. The second preheated slide is then placed on top of the FEP Teflon. This is then pressed down firmly using tweezers until the FEP Teflon is observed to melt (by going water clear and flowing slightly at the edges). After 20 seconds, the sandwich of slides and FEP Teflon can be removed from the hot plate. After 2 minutes the top slide should separate easily from the FEP Teflon using a needle, and the FEP Teflon square with mounted zircon crystals can be removed.

IV) Polishing Apatite Mounts

The Araldite® apatite mounts are first hand-ground using wet 180/320 grade grinding paper. Then using a Streuers® polishing machine, the mounts are polished using 1μm alumina slurry on a nylon polishing cloth for ~5 min. at 200 r.p.m. The mounts should then be inspected, and the process repeated until sufficient internal cross-sections of the apatite crystals are achieved. The mounts and polishing machine are then thorouhgly cleaned. To remove any remainig polishing scratches the mounts are polished using 0.3μm alumina slurry (or 0.25 μm diamond slurry) on a Nylon polishing cloth (or DUR cloth) for ~5 min. or until a satisfactory finish is accomplished.

V) Polishing of Zircon Mounts

The FEP Teflon zircons are attached to aluminium blocks using a double-sided adhesive tape. They are first lightly hand-ground using 1000 grade grinding paper. Then using a Streuers® polishing machine, the mounts are polished with ~2-3 cm of 1μm diamond paste on a DUR polishing cloth. The lap is first wetted with DP Blue lubricant, then the mounts are polished for ~30 min. at 125 r.p.m., with a lubricant drop rate of 1-2 drops/sec. After this time the mount surface should be perfectly flat, with any polishing scratches just visible. To apply a final wash and remove any remaining polishing scratches, the zircons mounts are re-polished as above, but with a 0.25 μm diamond paste. Care should be taken during zircon polishing to avoid removing the thin lip of FEP Teflon that holds the zircon crystal in place, as there is no adhesion between the crystal and the mount.

VI) Etching the Apatite and Zircon Mounts

The basic fundamentals of etching to reveal fission tracks are explained in chapter 3, section 3.3.2. The apatite mounts were etched for 20-25 seconds in 5M HNO_3. The zircon mounts are etched in a molten 1:1 Molare, binary eutectic of KOH and NaOH at 220±5°C, in a platinum crucible. Etch times can vary from 2 hours to 72 hours. Therfore, a step etching procedure was used for all samples, until the desired amount of etching is achieved. Finally, all etched zircon mounts are thoroughly soaked and washed to remove all traces of alkali.

VII) Thermal Neutron Irradiation

The external detector method (chapter 3.3) requires each mineral mount to be attached against a mica detector. The polished apatite mounts should be ground using a coarse grinding cloth until they measure 14×20 mm. The FEP Teflon mounts can be cut to a similar size using scissors. A small piece of unscratched mica should be cut using sharp scissors or a scalpel blade to the same size of the sample mount and numbered using a needle. For each sample a corner should be cut off, to enable the correct orientation of the mica to be determined when it is removed after irradiation. The

mica is attached firmly to the sample mount using Scotch® adhesive tape. The samples with attached mica detectors are then placed in a purpose built Poly-Carbonate (PC) holder (figure Ia), along with the relevant dosimeter glasses, with a careful note taken of the positions of each sample. Spacers are then added at either end of the stack, and the PC holder screwed until finger tight. The PC holder is added at either end of the stack into an alumium holder. For each batch the thermal neutron fluence dose required must be clearly stated: for apatite 1.2×10^{16} n·cm^{-2} and for zircon a fluence of 1.0×10^{15} n·cm^{-2}. After the sample batches return from irradiation, the mounts must be very carefully removed. The micas are separated from the zircon or apatites mounts and are then ready for etching. To aid the location of the induced mica image detector, of an apatite or zircon crystal, a sharp needle should be used before removal of the mica to punch a hole in the mica and an impression in the sample mount (figure Ib).

VIII) Etching External Mica Detectors

The tracks recorded in the mica detectors are revealed by etching in 40% HF, which is an extremely dangerous chemical and should be handled with great care in a fume cabinet. HF is poured into a PVC dish (HF will attack glass), until a depth of ~5mm. Then, using tweezers, the mica detectors are placed into the acid. They are then left for 45 min. at a room temperature of ~20°C. For the micas attached to the dosimeters, 60 min. etching time is required. Note: higher ambient temperatures accelerate the etching rates of the micas. After etching, the micas are removed, rinsed in distilled water, and allowed to soak, preferably overnight. After soaking, excess water and HF can be driven off by placing the micas under an infrared lamp. The mica detectors should be handled very carefully, as they are easily cleaved. A damaged mica detector can result in the loss of any recorded tracks, thus rendering the mount useless.

(Reference: Thomson, 1992)

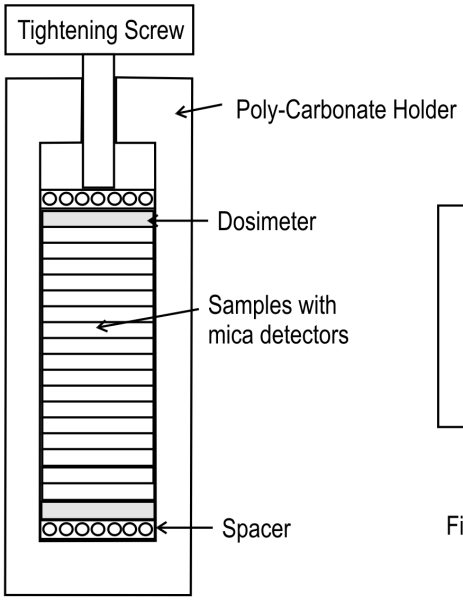

Figure Ia: Sample Package for Thermal Neutron Irradiation

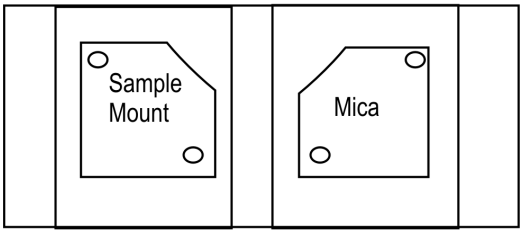

Figure Ib: Slide Mount for EDM analysis

Appendix II. Field Descriptions of the Samples

Sample Number	Location GPS coordinates	Date	Rock type	Field description
AA1	Lago Llanquihue 41°12'58''S; 72°40'13''W	10-3-99	Tonalite	Los Riscos, ~100 m^2 outcrop of biotite tonalites with mafic enclaves. Phaneritic feldspar phenochrystals, mafic minerals with cumulate growth textures. Enclaves of up to 30 cm. Subhedral-anhedral quartz.
AA2	Ralun 41°22'55''S; 72°18'11''W	10-3-99	Tonalite	Bahía Ralún, Petrohué bridge. ~400m^2 outcrop of granodiorites, with abundant enclaves, and some foliation defined by the alignment of feldspars. Rough orientation N60°E/subvertical.
AA3	E. Reloncaví 41°32'10''S; 72°20'06''W	11-3-99	Tonalite	E. Reloncaví, Popehuén Bajo (~1 km S of Canutillar). Small outcrop of fine-grained tonalite-diorites, with scarce mafic xenoliths.
AA4	E. Reloncaví 41°36'24''S; 72°23'08''W	11-3-99	Tonalite	E. Reloncaví, western border across Puelo river. 100 m^2 outcrop of coarse-grained tonalites, intruded by N-NE trending dioritic dikes. Quartz veins near the contact zones. Banded xenoliths, or schlieren (?).
AA5	E. Reloncaví 41°36'06''S; 72°21'42''W	11-3-99	Quartz-diorite	Baños de Sotomó. Small outcrop of quartz-diorites with porphyric aspect, Clay minerals replacing plagioclase phenochrysts. Anhedral quartz.
AA6	E. Reloncaví 41°34'14''S; 72°20'45''W	11-3-99	Quartz-diorite	Western border of Reloncaví estuary, ~3 km south of Canutillar. Small outcrop of coarse-grained quartz-diorites.
AA8	E. Reloncaví 41°36'59''S; 72°18'40''W	12-3-99	Granodiorite	E border of E. Reloncaví, ca. 4 km N of Balseo. ~1000m^2 outcrop of coarse-grained granodiorites, intruded by dioritic dykes, orientation ~N72°E/35°S.
AA9	E. Reloncavi 41°34'02''S; 72°18'32''W	12-3-99	Granite	E border of E. Reloncaví, 8 km N of Balseo, along the road to Puelo. Small outcrop of hornblende-biotite granodiorites-granites. K-feldspar with red clay at the weathered surfaces.
AA10	Cochamo 41°30'33''S; 72°16'35''W	12-3-99	Granodioritess	Small outcrop (~100m^2) of coarse-grained granodiorites-granites. Biotite-amphibole cumulates. Sample near contact zone to diorite (gabro?) plutonic unit.
AA11	E. Reloncaví 41°26'55''S; 72°19'57''W	12-3-99	Granodiorite	10 km S from Ralun. Coarse grained, biotite granites and granodiorites. Pink surfaces of feldspar phenocrysts reflect possible clay-alteration.
AA12	Canutillar 41°30'16''S; 72°20'35''W	12-3-99	Tonalite	Western border of Reloncaví estuary, Canutillar. Hornblende and biotite ganodiorites, with mafic inclusions of up to 30 cm. Magmatic alignement defined along orientation of feldspar and mafic minerals.
AA13	L.Chapo 41°30'00''S;72°22'39''W	12-3-99	Tonalite	Ca. 1 km to the E of Lago Chapo, fine-grained granodiorites, small veins with chlorite in fractures.
AA14	Chiloe Guabun 41°47'45''S; 74°02'14"W	13-3-99	Micaschist	Guabún beach, northern border. Large (~2000m^2) outcrop of quartz-muscovite schists. Intense folding, mesoscopic crenulation cleavege, and quartz boudins. General trend of foliation N60°W/30°E. Fine-grained layers are more tightly folded.
AA17	Chiloe Gamboa Alto 42°51'51"S; 73°51'51"W	15-3-99	Dacite	Summit of Cerro Gamboa Bajo. Small (~20m^2) outcrop of brown-coloured crystalline dacitic tuffs. Weathered surface of the sample with red tones.
AA18	Chiloe Gamboa Bajo 42°27'21"S; 73°50'30"W	15-3-99	Dacitic porphiry	Cantera Gamboa Bajo. 200 m away from sample AA17. Porphyric dacites, with columnar joints gently dipping southwards, define subvertical pentagonal and hexagonal rhombs of up to ca 1 m diameter. Fresh, unlatered exposed surfaces in the rocks.
AA19	Chiloe Gamboa alto 42°27'33"S; 73°53'45"W	15-3-99	Micaschist	Gamboa Alto, near Endesa electric station. Small outcrop on a road curve, defined by quartz-phylites with fine veins of quartz. Mica foliation (S2?) trends ~N50°W/31°E.
AA20	Correntoso 41°27'42"S; 72°37'40"W	16-3-99	Granodiorite	Rio Correntoso, large (~500m^2) outcrop of granodiorites with cm-large quartz and phenocrysts (microclines) and biotite cumulates. Some weathered feldspar (seritized?). Large dark enclaves (up to ~50cm) with anhedral feldspar grains. Isotropic texture.
AA21	L. Chapo	16-3-99	Granite	5 km away from sample 20, along road to Lago Chapo. Small quarry (~20m×50m) with coarse-grained biotite

	41°25'41"S; 72°37'20"W			granites. Pan-idiomorphic texture, with large feldspar and quartz grains.
AA22	L. Chapo 41°26'41"S; 72°33'49"W	16-3-99	Granodiorite	Lago Chapo, near tunel towards Zargazo lagoon. Small outcrop of granodiorites-tonalites with abundant xenoliths from the metamorphic basement. Some magmatic foliation defined by schlieren and mafics alignement.
AA23	L. Chaiquenes 41°30'38"S; 72°35'44"W	17-3-99	Gneiss	Rio Chaica, 1 km along CONAF's park Alerce Andino. Small outcrop of fine-grained quartz-biotite gneiss. Foliation trends ~N33E/20W, sinuous. Thick quartz lenses within mica layers.
AA24	Punta Metri 41°35'20"S; 72°40'32"W	17-3-99	Granodiorite	Punta Metri, 4 km S from the rio Chaica delta. Coarse-grained tonalites crop out continuously along the beach down to punta Metri. Large amphiboles and biotites with "book" textures. Anhedral quartz, less than 30%. Mafic inclusions of centimetre to decimetre size.
AA25	Punta Metri 41°33'33"S; 72°42'27"W	17-3-99	Tonalite	5 km north of sample AA24, rock hang outcrop of coarse-grained tonalites, with mafic inclusions of up to 5 cm large. Panidiomorphic texture, with large feldspar, amphiboles and biotites.
AA26	Caleta Larenas 41°37'38"S; 72°38'38"W	18-3-99	Tonalite	50m outcrop of fine-grained tonalites with aboundant mafic inclusions. Dioritic dike swarms present, "mingled" within the pluton.
AA27	Caleta Larenas 41°39'24"S; 72°36'23"W	18-3-99	Tonalite	La Cascada, near Caleta Larenas. 100m×50m outcrop of hornfels, with a foliation trending ~ N35E/70E. Aplitic veins cut this sequence. Sample AA28 for microstructure analysis.
AA29	Rio Cochamo 41°28'44"S; 72°15'38"W	19-3-99	Granite	Northern border of Cochamó river. 200m×50m outcrop of hornblende-biotite granites. Coarse grained, panidiomorphic textures, some anhedral quartz. Argilized aplitic veins cutting the rocks.
AA30	Balseo 41°37'38"S; 72°18'11"W	19-3-99	Granodiorite	Balseo town, at the border of Puelo river. Large (400m×50m) rock quarry, coarse grained hornblende and biotite granodiorites, with mafic enclaves of up to 30 cm.
AA31	Puelo Chico 41°39'02"S; 72°17'14"W	19-3-99	Granite	Río Puelo Chico, at the entrance of Puelo town, small outcrop of biotite granites. Coarse-grained and similar aspect to outcrops across the river (sample AA30).
AA32	Puelo 42°40'23"S; 72°19'47"W	19-3-99	Granodioirte	Puente Río Blanco, 100m×50m outcrop of coarse-grained hornblende-biotite granodiorites. Subhedral quartz, argilized feldspar, some epidote. Abundant mafic inclusions.
AA33	Volcan Yates 41°41'57"S; 72°27'08"W	20-3-99	Granodiorite	NW flank of Yates volcano. ~1 km outcrop of coarse-grained tonalites at the base of the volcano. Abundant mafic inclusions, ranging up to 10 cm. Fresh, unaltered aspect of the sample.
AA34	Volcan Yates 41°40'41"S; 72°23'56"W	20-3-99	Tonalite	5 km further W from sample AA33, basement of volcán Yates. Coarse-grained hornblende-biotite tonalites, with mafic inclusions of up to 30 cm.
AA35	Termas de Ralún 41°21'06"S; 72°21'32"W	20-3-99	Quartz-monzonite	Ralun springs, northern border of the Petrohué river. Over 100 m high rock hang consisting of medium- to coarse grained quartz-monzonites and tonalites.
AA36	Parque Alerce Andino 41°34'37"S; 72°32'16"W	21-3-99	Gneiss	Alerce Andino Park, SW border of Chaiquenes lake, in conjunction with Chaica river. Outcrop of coarse-grained gneisses with irregular foliation domains defined by orientation of quartz-mica, and quartz-feldspar (cordierite?)-biotite. Rough foliation trends ~N310°E/70°W. Some fine quartz-vines cutting through foliation. Sample AA36 for thin section study.
AA37	Parque Alerce Andino 41°34'34"S; 72°33'08"W	22-3-99	Granite	1 km south of Caleta Chaparrano. 500 m outcrop of coarse-grained biotite granites with quartz fenochrysts of up to 2 cm. Mafic inclusions of up to 30 cm.
AA39	Chaparrano 41°43'43"S; 72°33'21"W	22-3-99	Tonalite, foliated	Cuesta Farellon. 500×50m outcrop of coarse-grained tonalites, with abundant mafic inclusions of up to 20 cm length. Mineral alignement defines a steeply dipping magmatic foliation, roughly in the NNW direction.
AA40	Rio Mariquita 42°01'20"S; 72°26'47"W	23-3-99	Granodiorite	~5 km south from Cholgo, 200m×50m outcrop of fine-to medium grained biotite bearing granodiorites.
AA42	Pichanco 42°06'46"S; 72°27'37"W	23-3-99	Granodiorite	~3 km N of the entrance to Hornopirén national park. Small outcrop at the base of a steep slope of a rock hang, consisting in coarse-grained hornblende granodiorites and diorites. Feldspar slightly altered (clay and epidote). Thick vegetation obstructs visibility in the area.
AA43	Rio Negro 41°50'51"S; 72°22'39"W	24-3-99	Dacite	2-3 km W of Pichicolo town. Small outcrop of porphyric dacitic tuffs, with feldspar and biotite phenocrysts of up to 1 cm. Gray glassy matrix.
AA44	Pichicolo 41°59'36"S; 72°36'20"W	24-3-99	Tonalite	~2 km towards the eastern end of the Quintupeu fjord, massive subvertical hangwall of granitods. Coarse-grained hornblende-biotite tonalite. Amphiboles form cumulates of centimetric scale.

AA45	F. Quintupeu 42°09'40"S; 72°27'30"W	25-3-99	Micaschist	Isla Llancahué, NE border. Small outcrop of quartz-mica schists interlayered with coarse graine gneisses. Foliation obliterated by contact with aplitic dike or horn.
AA46	I. Llancahué 42°04'17"S; 72°28'40"W	25-3-99	Tonalite	Isla Llancahué, N border of the Island. Small outcrop of tonalites and diorites, with subhorizontal magmatic layering, alternating to fine mafic bands and aplitic segregations surrounding mafic inclusions.
AA102	I. Llancahué 42°03'53"S; 72°29'50"W	3-12-00	Tonalite	Park Saltos del Petrohué, at the eastern shore of the river. Large outcrops of fine-grained hornblene and biotite tonalites. Outcrops are partly covered by lava flows from the Osorno volcano.
AA106	Petrohué 41°08'38"S; 72°24'44"W	6-12-00	Tonalite	Southern border of the Pelada Island, small outcrop along the shoreline of the island. Unfoliated, fined-grained tonalites.
AA111	Isla Pelada 42°00'59"S; 72°27'18"W	6-12-00	Aplite	Western border of the Pelada Island, small outcrop along shoreline of granites with mafic enclaves, cut by several aplitic veins, or as segregation features. Weak "magmatic" foliation N70°E/75°S.
AA119	Isla Pelada 42°01'50"S; 72°29'43"W	7-12-00	Tonalite	SE border of the Llancahué Island. Outcrop in beach, quartz-mica schists. Orientation N325°E/85E. Metric-scaled quartz veins cut the schists, discordant to the foliation.
AA125	I. Llancahué 42°10'15"S; 72°29'16"W	9-12-00	Granite	~3 km eastwards along the Blanco river (upflow), southern side, steep-dipping hangwall of plutonic rocks. Fine-grained tonalite with mafic inclusions, unfoliated.
AA128	Rio Blanco 41°56'55"S; 72°23'05"W	11-12-00	Granite	SW shore of the Todos Los Santos lake, ~500 m westward of Las Cabras isle. Small outcrop of coarse grained, unfoliated granites. Dense vegetation.
AA129	Lago Todos Los Santos 41°07'44"S; 72°20'25"W	11-12-00	Granite	Isla Las Cabras, western side, direct on the LOFZ. Coarse grained, biotite granites and granodiorites. Some magmatic flow structures observed in rocks of the island, no strong foliation was observed.
AA130	Lago Todos Los Santos 41°06'44"S; 72°17'14"W	11-12-00	Granite	Northern border of the Todos los Santos lake. Steep hangwall with water spring, large (~50×100m) outcrop of coarse-grained granites.
AA131	Lago Todos Los Santos 41°04'34"S; 72°07'10"W	11-12-00	Granite	Eastern border of the Todos Los Santos lake, direction to Peulla. Large (100×100m) outcrop of coarse-grained granites with many mafic inclusions. Steep hangwall oriented in the NNE direction, unfoliated rocks.
AA132	Lago Todos Los Santos 41°05'30"S; 72°10'51"W	11-12-00	Tonalite	Eastern border of the Todos Los Santos lake, small outcrop of coarse-grained tonalites with enclaves. Thick vegetation.
BR409	Pte Las Trancas (Ralún) 41°25'04"S; 72°26'57"W	24.2.98	Granitic bands	Waterfall near Las Trancas bridge, on the highway from Ralún to Cochamó, NE side of the Reloncaví sound. Beige-coloured granitic layers interfingering with darker plutonic bands. The plutonic rocks are in contact to the west with quaternary volcanic strata, along the main trace of the LOFZ. Fine grained foliated NS trending green coloured rocks were observed at the base of the waterfall.
BR410	Laguna Patas, Ralún 41°17'17"S; 72°26'57"W	24.2.98	Diorite	Rockhang on parking place at the southernmost part of the Llanquihue lake, halfway towards Ensenada. Medium grained dark gray tonalite-diorite.
BR411	L. Llanquihue-Ensenada 41°13'00"S; 72°40'30"W	24-2-98	Granite	Granite from the front range, 30 km along the Puerto Varas- Ensenada highway.

Appendix 3. Zircon CN-2 Zeta Values and Weighted Mean Zeta

Irradiation	Date	Standard	Position	No. of Crystals	Spontaneous ρs (Ns)	Induced ρi (Ni)	ρs/ρi	Age Dispersion (Pχ2)	Dosimeter ρd (Nd)	Central Zeta
RU-4	12/10/01	Mt. Dromedary	36	20	1.618E+07 (3239)	4.719E+06 (945)	3.4275±0.134	0.3% (82.7%)	4.510E+05 (6228)	**127.7±5.05**
RU-4	26/9/01	Fish Canyon	3	20	4.695E+06 (2250)	5.127E+06 (2457)	0.9158±0.029	0.08% (89.58%)	4.59E+05 (6334)	**132.39±5.37**
RU-4	7/10/01	Tardree	35	20	6.808E+06 (857)	3.672E+06 (857)	1.8541±0.082	16.72% (35.14%)	4.054E+05 (6232)	**142.34±10.42**
RU-4	1/10/01	Buluk	4	20	9.825E+05 (867)	1.626E+06 (1435)	0.6042±0.027	12.88% (11.59%)	4.854E+05 (6330)	**116.986±5.44**
RU-5	7/10/01	Fish Canyon	3	20	6.567E+06 (1705)	6.051E+06 (1571)	1.0853±0.041	1.5% (76.81%)	3.755E+05 (5185)	**136.43±6.18**
RU-5	9/10/01	Mt. Dromedary	36	20	1.643E+07 (2745)	4.446E+06 (743)	3.6945±0.161	3.28% (71.47%)	3.827E+05 (5285)	**139.88±6.26**
RU-21	21/5/02	Fish Canyon	64	20	5.014E+06 (4300)	4.500E+06 (3859)	1.1143±0.029	5.56% (9.93%)	3.745E+05 (5172)	**133.67±5.19**
RU-22	23/5/02	Fish Canyon	3	20	6.174E+06 (2285)	5.436E+06 (2012)	1.1357±0.038	0.00% (97.10%)	3.912E+05 (5403)	**125.15±5.24**
RU-24	28/1/03	Fish Canyon	3	20	4.213E+06 (3404)	3.601E+06 (2909)	1.1702±0.033	6.23% (9.37%)	4.28E+05 (5905)	**111.41±4.55**
RU-24	28/1/03	Fish Canyon	4	20	1.212E+07 (4753)	3.863E+06 (1515)	3.1373±0.101	0.97% (64.59%)	4.26E+05 (5885)	**147.67±4.86**
					Weigthed Mean Zeta	**129.97±1.64**				

Notes:

(i) track densities (ρ) are as measured (x 10^6 tr cm^{-2}); number of tracks counted (N) shown in brackets;

(ii) analyses by external detector method using 0.5 for the $4\pi/2\pi$ geometry correction factor.

Appendix 3. Apatite CN-5 Zeta Values and Weighted Mean Zeta

Irradiation	Date	Standard Type	Position	No. of Crystals	Spontaneous ρ_s (N_s)	Induced ρ_i (N_i)	Dosimeter ρ_d (N_d)	Pooled Ratio ρ_s/ρ_i	Age Dispersion ($P\chi^2$)	Central Zeta
RU-A1	30.3.01	Fish Canyon	#3	20	2.131E+05 (156)	1.824E+06 (1348)	1.470E+06 (10153)	0.1157±0.009	0.00% (98.9%)	**326.83±29.02**
RU-A1	16.04.01	Durango	#2	20	1.525E+05 (242)	1.238E+06 (1965)	1.471E+06 (10156)	0.1232±0.008	0.00% (99%)	**346.65±24.50**
RU-A1	30.03.01	Durango	#24	20	1.888E+05 (232)	1.168E+06 (1436)	1.463E+06 (10115)	0.1616±0.016	0.00% (99%)	**265.69±19.45**
RU-A1	7.05.01	Fish Canyon	#2	20	2.768E+05 (372)	2.207E+06 (2965)	1.16E+06 (7996)	0.1255±0.007	1.26% (81%)	**382.51±23.58**
RU-A2	7.05.01	Durango	#20	20	1.520E+05 (320)	1.068E+06 (2248)	1.16E+06 (8023)	0.1423±0.009	0.00% (98%)	**379.66±23.86**
RU-A4	7.05.01	Mt. Dromedary	#2	20	8.448E+05 (350)	2.670E+06 (1106)	1.612E+06 (11136)	0.3165±0.020	0.00% (99.9%)	**386.96±24.13**
RU-A4	10.5.01	Mt. Dromedary	#25	20	1.070E+06 (421)	2.759E+06 (1086)	1.621E+06 (11193)	0.3877±0.023	13.95% (21.99%)	**318.05±21.58**
RU-A20	19.12.02	Durango	#2	20	1.765E+05(135)	1.370E+06 (1048)	1.620+E6 (11185)	0.1288±0.018	2.63% (41.9%)	**300.98±28.16**
RU-A21	2.01.03	Durango	#2	20	1.473E+05(142)	1.348E+06 (1299)	1.669+E6 (11523)	0.1093±0.097	0.01% (87.31%)	**344.21±31.08**

Weighted Mean Zeta	**333.92**
Error	**7.30**

Notes:

(i) track densities (ρ) are as measured (x 10^6 tr cm^{-2}); number of tracks counted (N) shown in brackets;

(ii) analyses by external detector method using 0.5 for the $4\pi/2\pi$ geometry correction factor

Appendix 4. Time-Temperature Histories for the Noth Patagonian Batholith in the Areas of Reloncaví and Hornopirén.

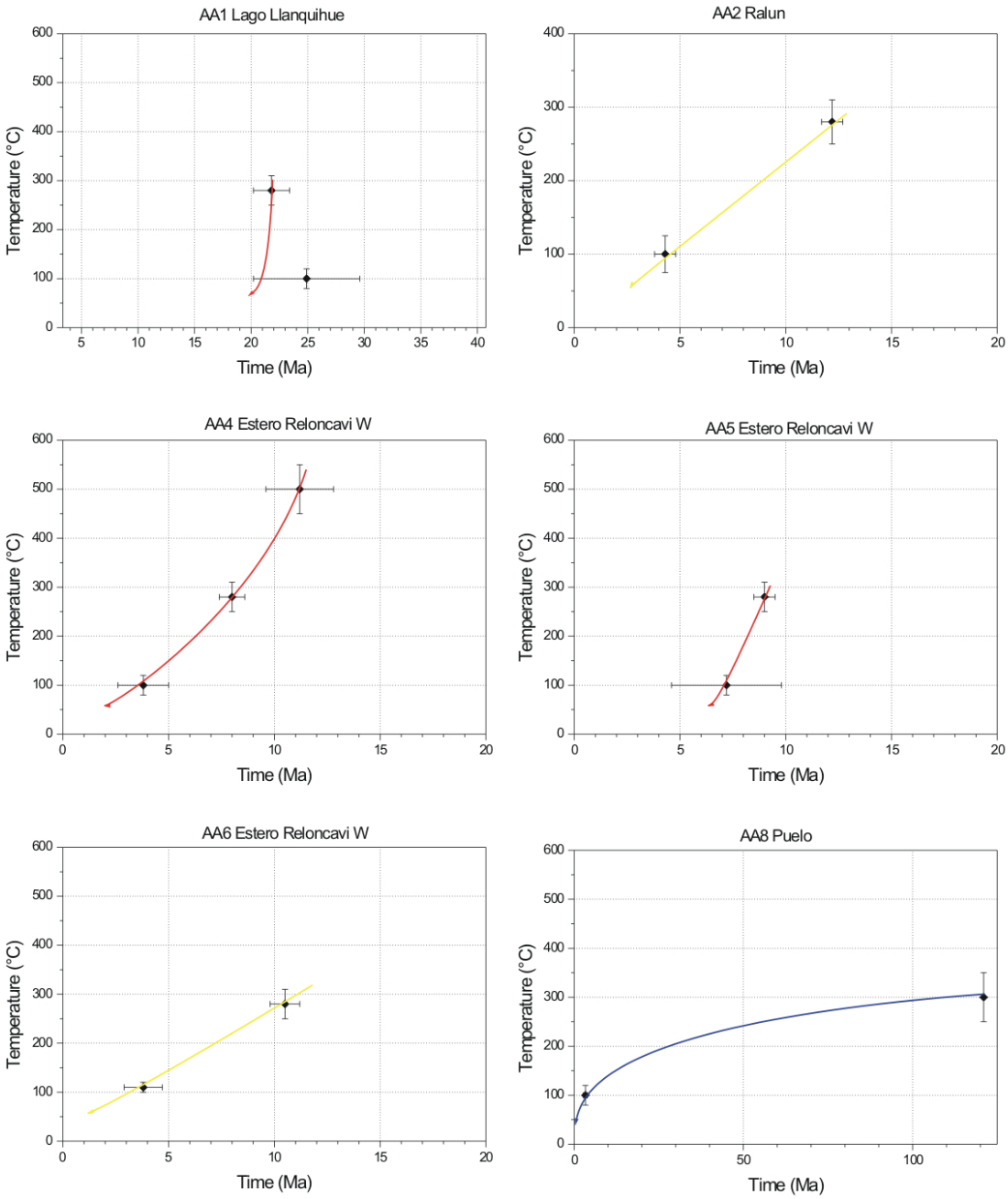

Note on the classification of the t-T histories:

The correlations are based on different thermochronometers from outcrops located nearby the FT sampling area. In some cases, the approximations are broad (e.g. AA25), especially for rapidly cooled samples. This can be related to uncertainties in each dating method, the different locations of the dated samples, or to alteration in the isotopic systems due to heat advection during the cooling history of the sample. Refer to chapter 6.2.

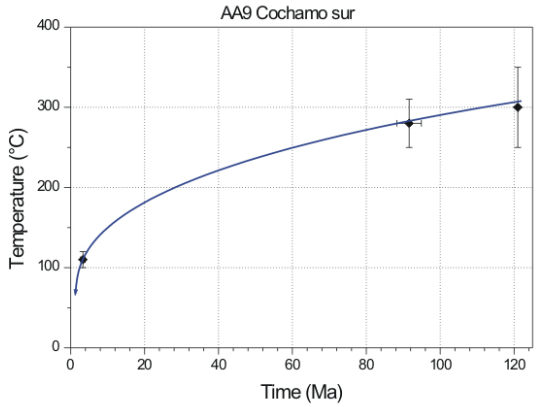
AA9 Cochamo sur
Temperature (°C)
Time (Ma)
0
100
200
300
400
0
20
40
60
80
100
120

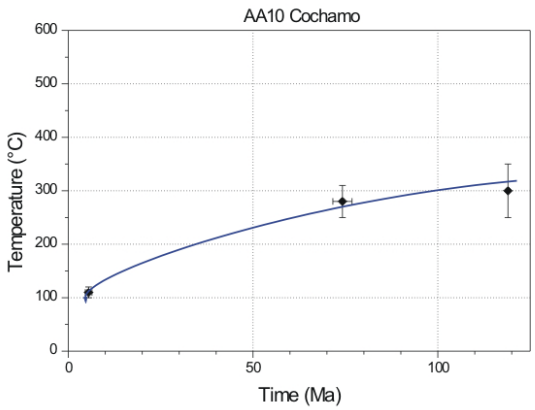
AA10 Cochamo
Temperature (°C)
Time (Ma)
0
100
200
300
400
500
600
0
50
100

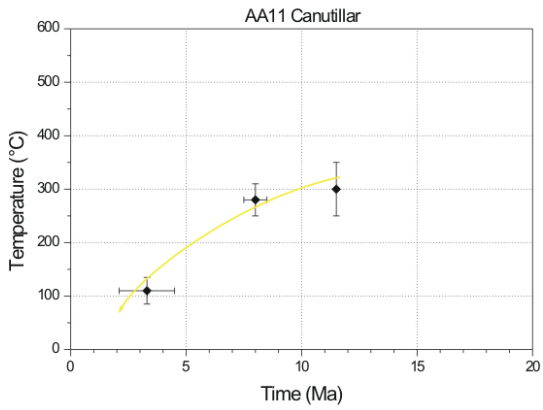
AA11 Canutillar
Temperature (°C)
Time (Ma)
0
100
200
300
400
500
600
0
5
10
15
20

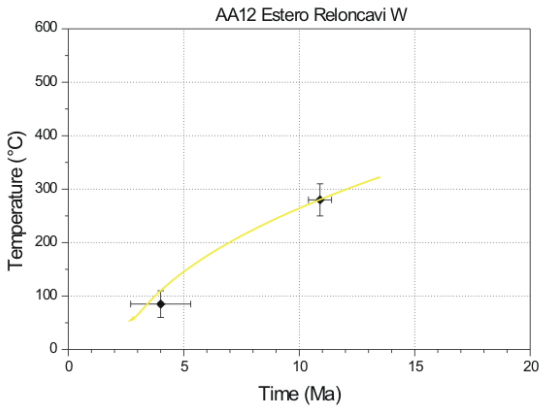
AA12 Estero Reloncavi W
Temperature (°C)
Time (Ma)
0
100
200
300
400
500
600
0
5
10
15
20

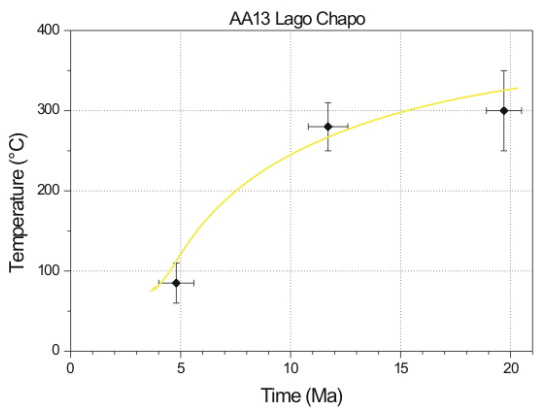
AA13 Lago Chapo
Temperature (°C)
Time (Ma)
0
100
200
300
400
0
5
10
15
20

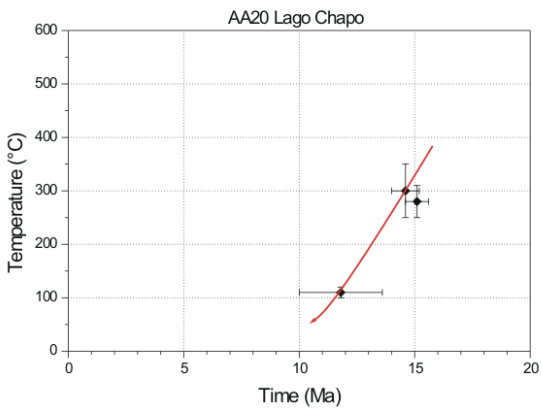
AA20 Lago Chapo
Temperature (°C)
Time (Ma)
0
100
200
300
400
500
600
0
5
10
15
20

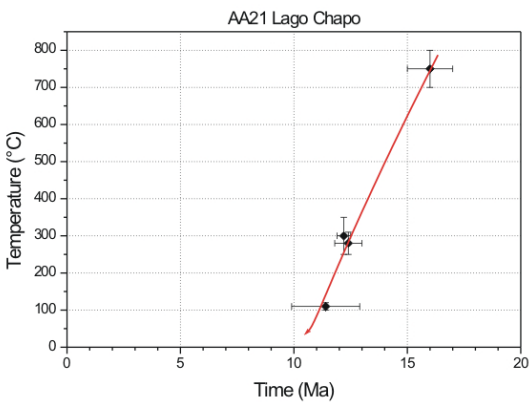
AA21 Lago Chapo
Temperature (°C)
Time (Ma)
0
100
200
300
400
500
600
700
800
0
5
10
15
20

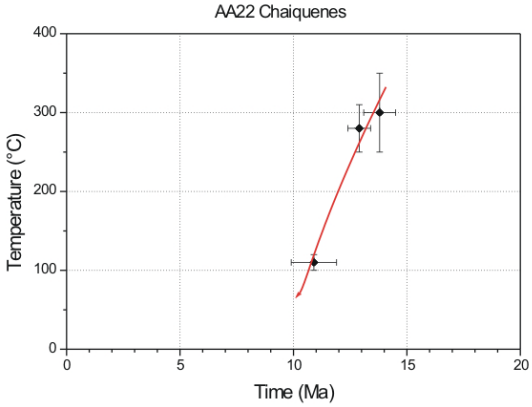
AA22 Chaiquenes
Temperature (°C)
Time (Ma)
0
100
200
300
400
0
5
10
15
20

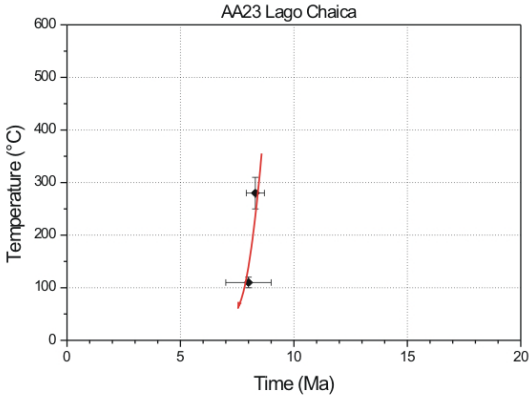
AA23 Lago Chaica
Temperature (°C)
Time (Ma)
0
100
200
300
400
500
600
0
5
10
15
20

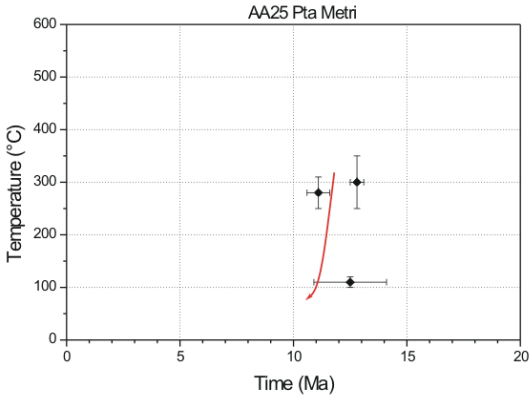
AA25 Pta Metri
Temperature (°C)
Time (Ma)
0
100
200
300
400
500
600
0
5
10
15
20

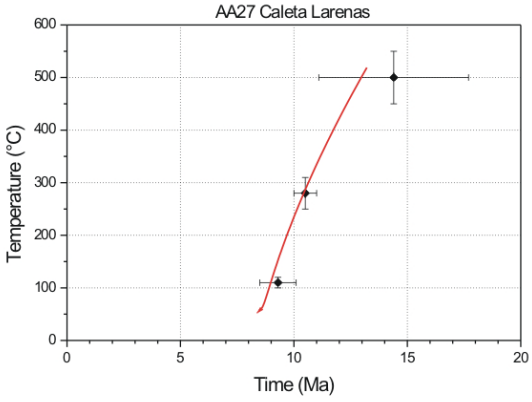
AA27 Caleta Larenas
Temperature (°C)
Time (Ma)
0
100
200
300
400
500
600
0
5
10
15
20

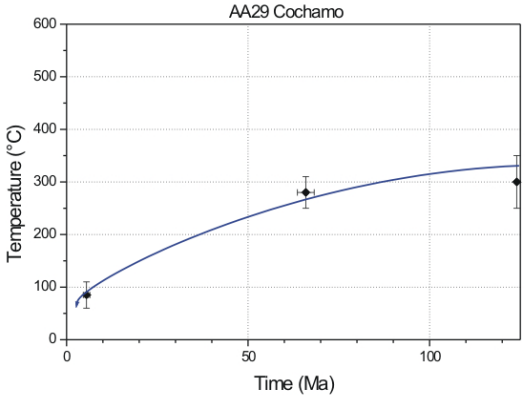
AA29 Cochamo
Temperature (°C)
Time (Ma)
0
100
200
300
400
500
600
0
50
100

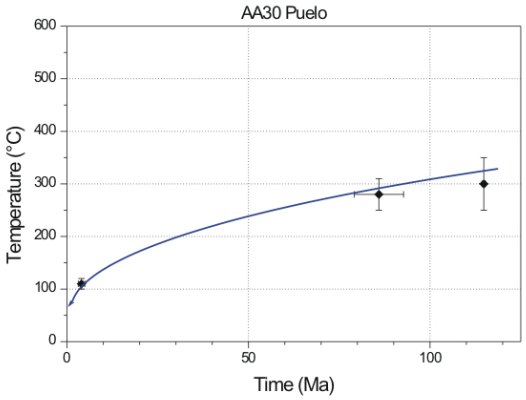
AA30 Puelo
Temperature (°C)
Time (Ma)
0
100
200
300
400
500
600
0
50
100

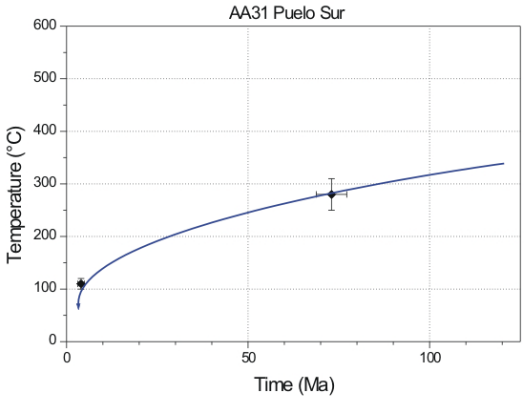
AA31 Puelo Sur
Temperature (°C)
Time (Ma)
0
100
200
300
400
500
600
0
50
100

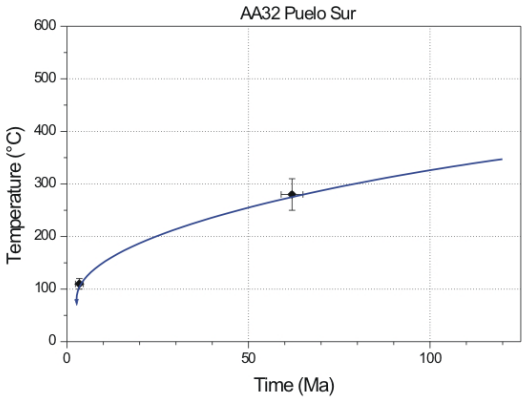
AA32 Puelo Sur
Temperature (°C)
Time (Ma)
0
100
200
300
400
500
600
0
50
100

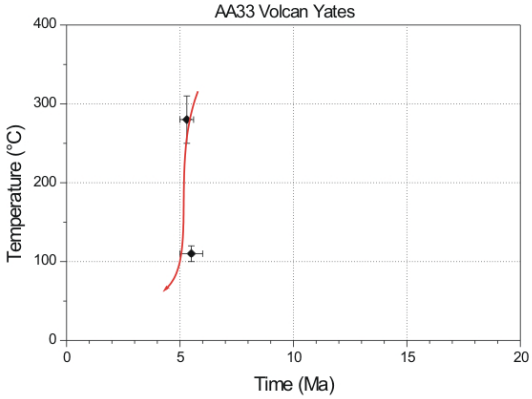
AA33 Volcan Yates
Temperature (°C)
Time (Ma)
0
100
200
300
400
0
5
10
15
20

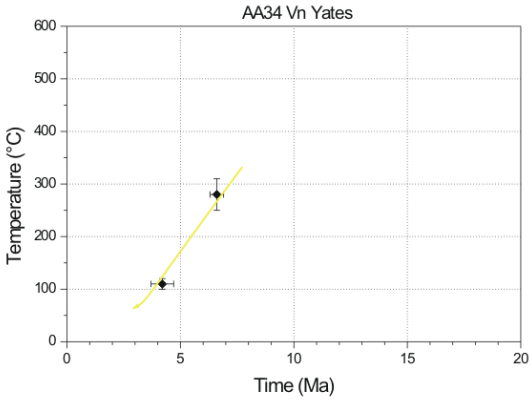
AA34 Vn Yates
Temperature (°C)
Time (Ma)
0
100
200
300
400
500
600
0
5
10
15
20

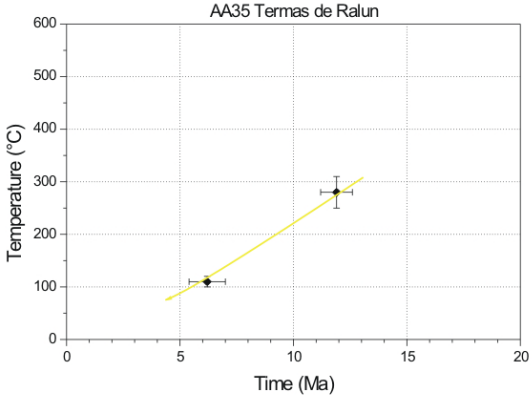
AA35 Termas de Ralun
Temperature (°C)
Time (Ma)
0
100
200
300
400
500
600
0
5
10
15
20

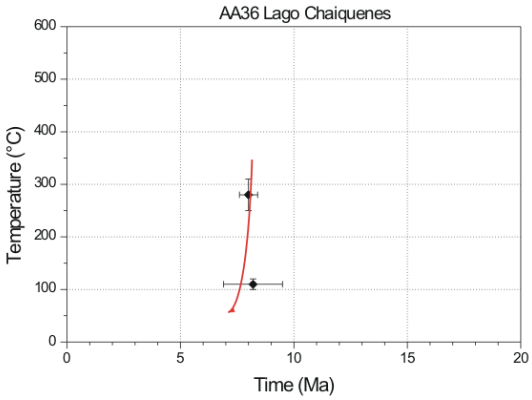
AA36 Lago Chaiquenes
Temperature (°C)
Time (Ma)

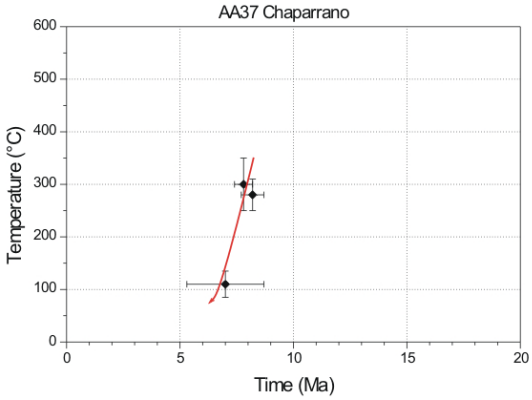
AA37 Chaparrano
Temperature (°C)
Time (Ma)

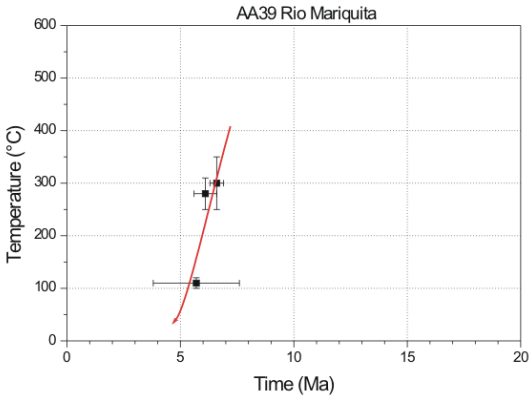
AA39 Rio Mariquita
Temperature (°C)
Time (Ma)

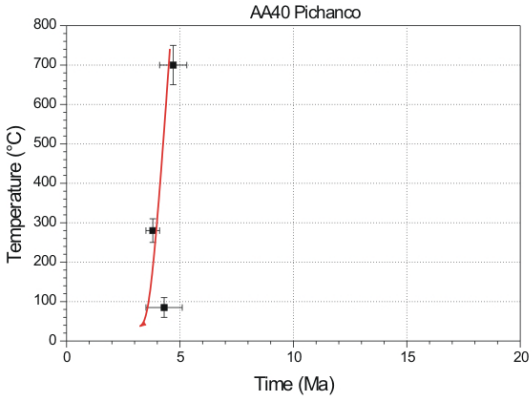
AA40 Pichanco
Temperature (°C)
Time (Ma)

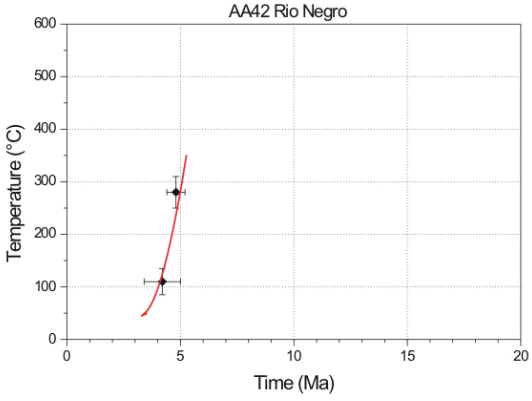
AA42 Rio Negro
Temperature (°C)
Time (Ma)

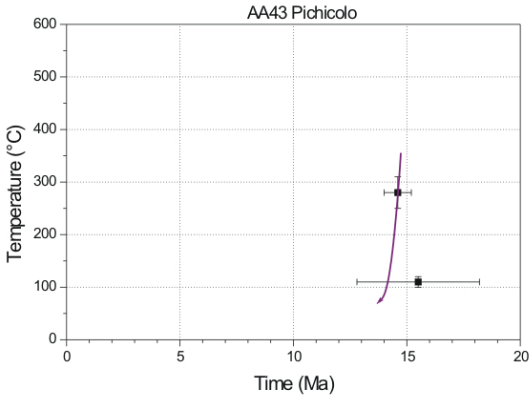
AA43 Pichicolo
Temperature (°C)
Time (Ma)

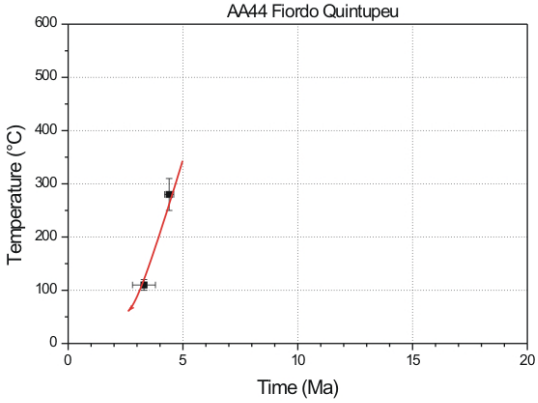
AA44 Fiordo Quintupeu
Temperature (°C)
Time (Ma)
0
100
200
300
400
500
600
0
5
10
15
20

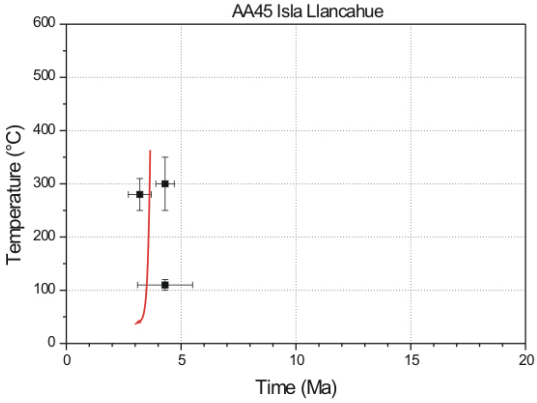
AA45 Isla Llancahue
Temperature (°C)
Time (Ma)
0
100
200
300
400
500
600
0
5
10
15
20

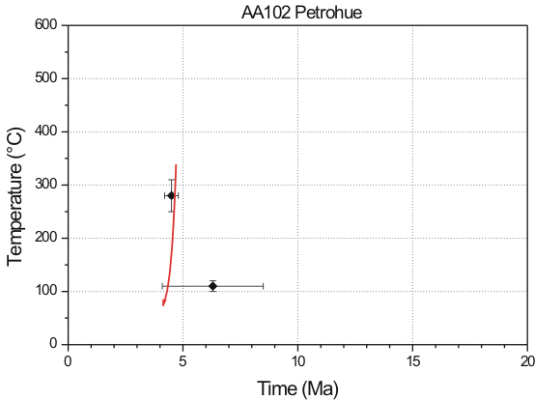
AA102 Petrohue
Temperature (°C)
Time (Ma)
0
100
200
300
400
500
600
0
5
10
15
20

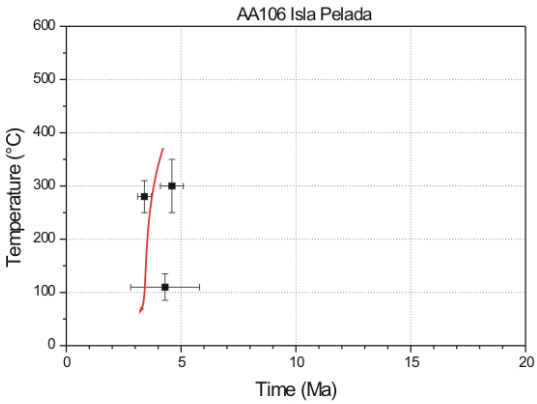
AA106 Isla Pelada
Temperature (°C)
Time (Ma)
0
100
200
300
400
500
600
0
5
10
15
20

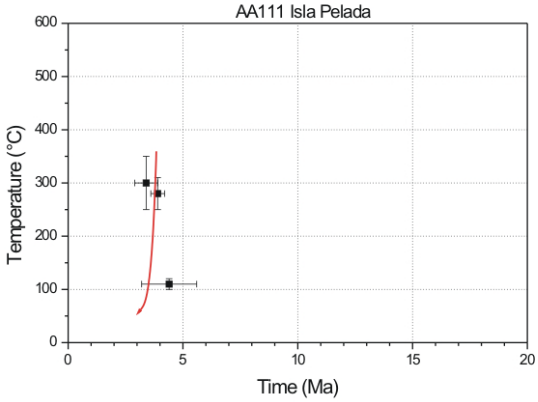
AA111 Isla Pelada
Temperature (°C)
Time (Ma)
0
100
200
300
400
500
600
0
5
10
15
20

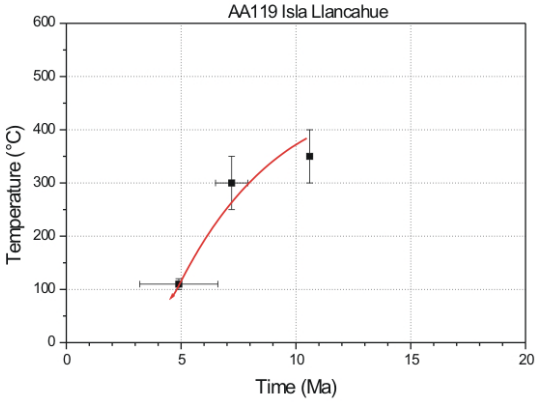
AA119 Isla Llancahue
Temperature (°C)
Time (Ma)
0
100
200
300
400
500
600
0
5
10
15
20

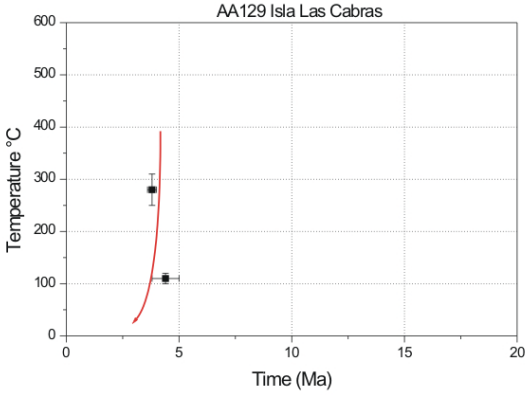
AA129 Isla Las Cabras
Temperature °C
Time (Ma)

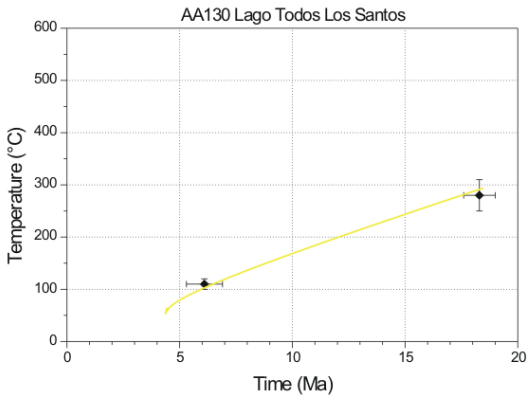
AA130 Lago Todos Los Santos
Temperature (°C)
Time (Ma)

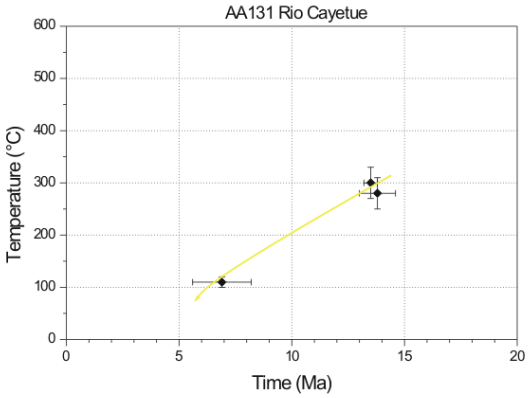
AA131 Rio Cayetue
Temperature (°C)
Time (Ma)

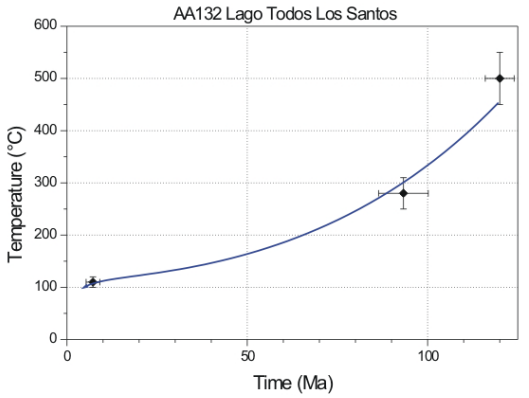
AA132 Lago Todos Los Santos
Temperature (°C)
Time (Ma)

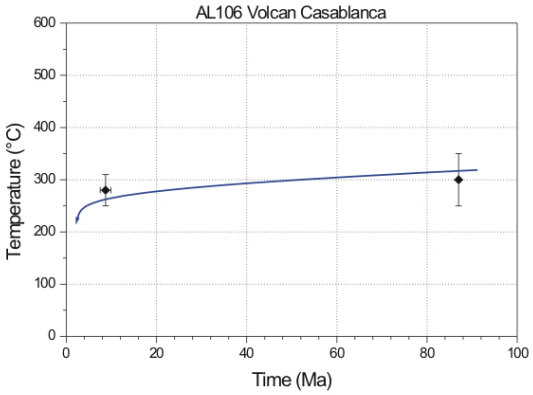
AL106 Volcan Casablanca
Temperature (°C)
Time (Ma)

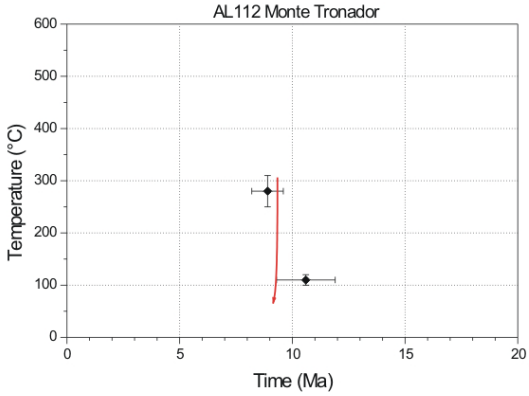
AL112 Monte Tronador
Temperature (°C)
Time (Ma)

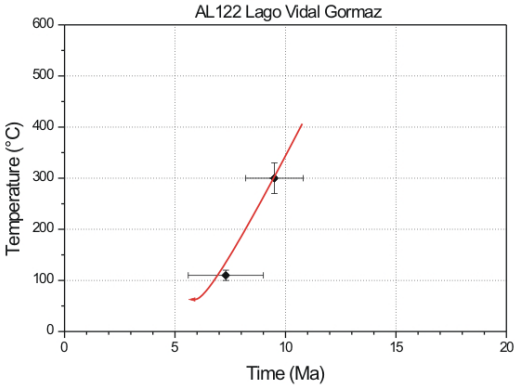
AL122 Lago Vidal Gormaz
Temperature (°C)
Time (Ma)
0
100
200
300
400
500
600
0
5
10
15
20

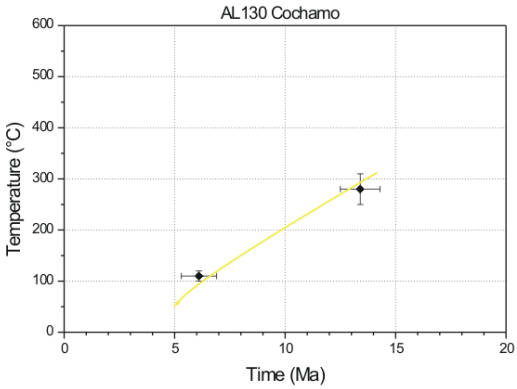
AL130 Cochamo
Temperature (°C)
Time (Ma)
0
100
200
300
400
500
600
0
5
10
15
20

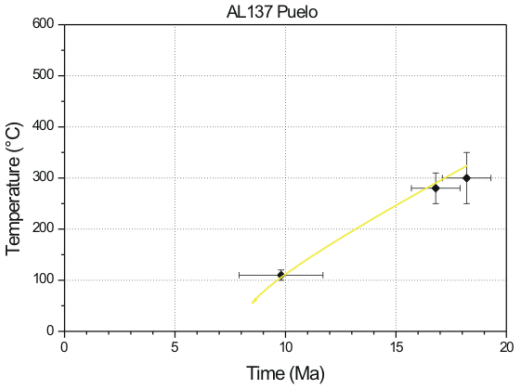
AL137 Puelo
Temperature (°C)
Time (Ma)
0
100
200
300
400
500
600
0
5
10
15
20

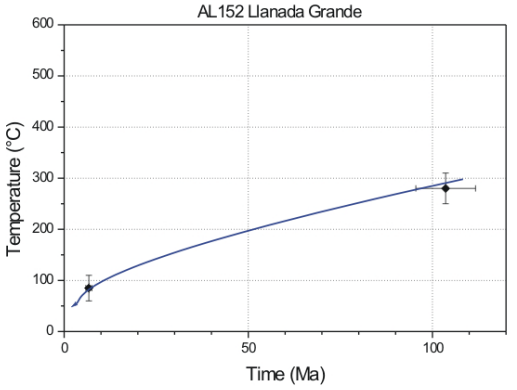
AL152 Llanada Grande
Temperature (°C)
Time (Ma)
0
100
200
300
400
500
600
0
50
100

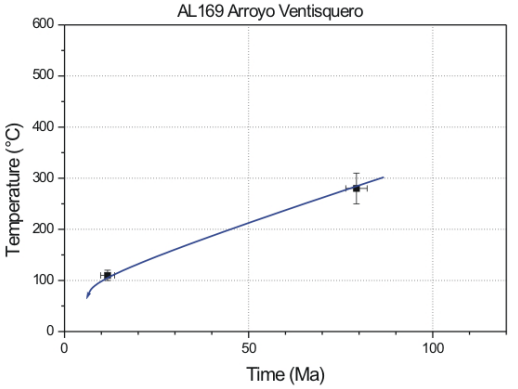
AL169 Arroyo Ventisquero
Temperature (°C)
Time (Ma)
0
100
200
300
400
500
600
0
50
100

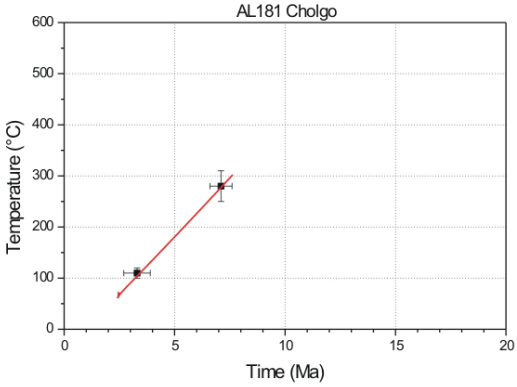
AL181 Cholgo
Temperature (°C)
Time (Ma)
0
100
200
300
400
500
600
0
5
10
15
20

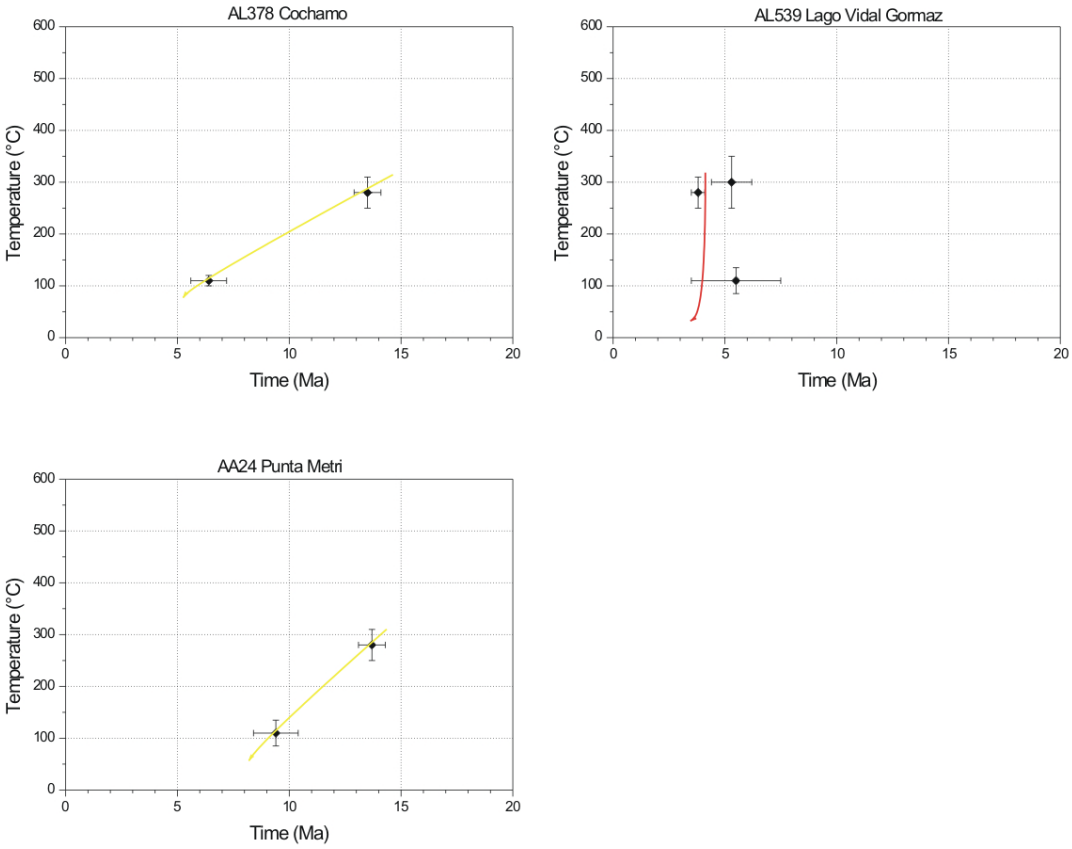

Appendix4b. Time-Temperature Histories for the Apatite FT System Determined with Aftsolve© (Ketcham and Donelick, 2000)

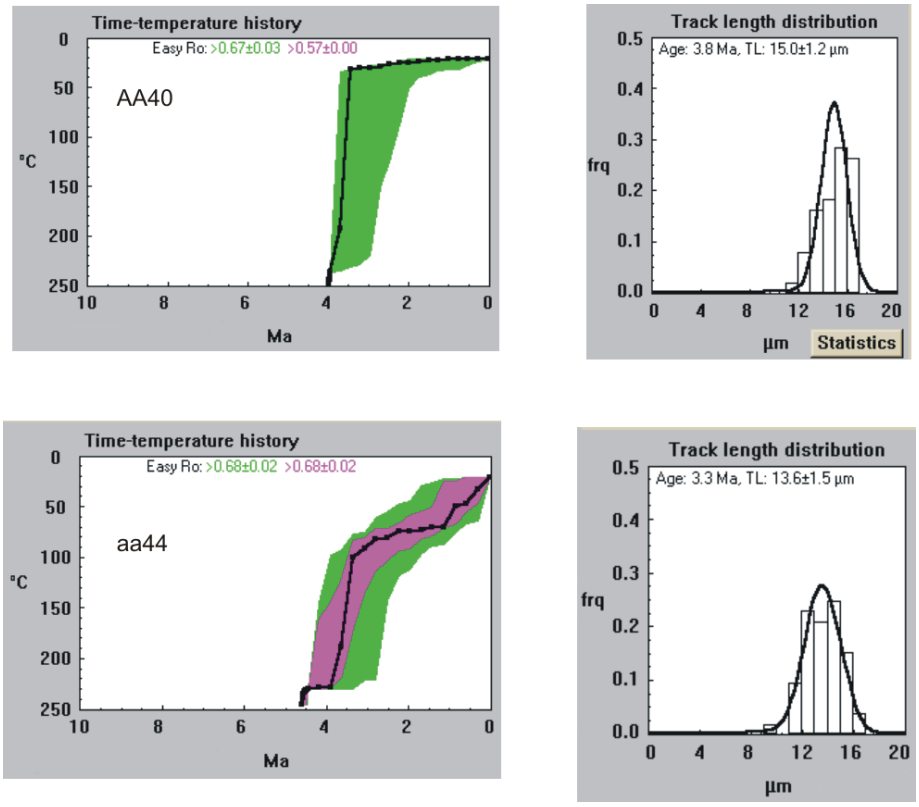

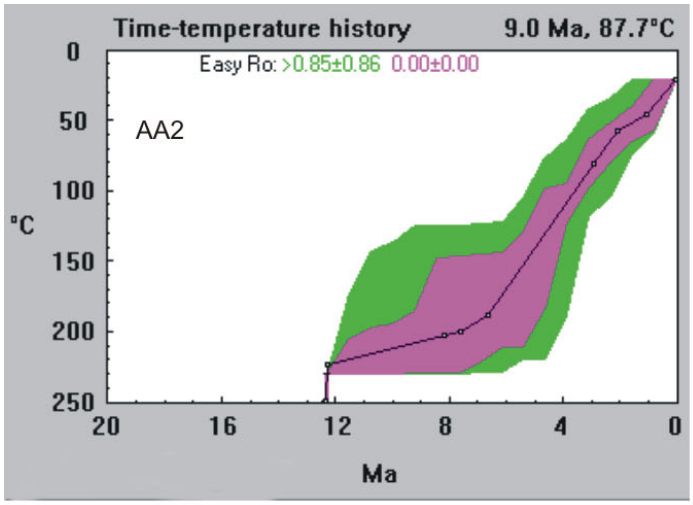
Time-temperature history
9.0 Ma, 87.7°C
Easy Ro: >0.85±0.86 0.00±0.00
AA2
°C
0
50
100
150
200
250
20
16
12
8
4
0
Ma

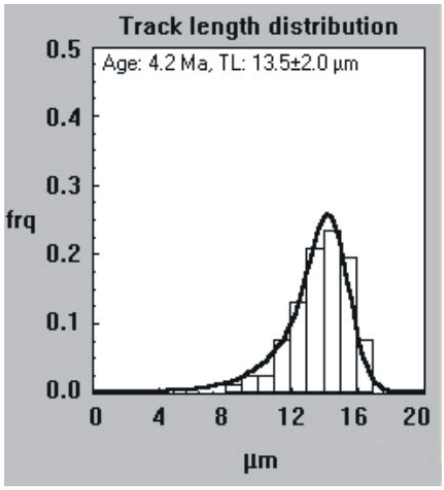
Track length distribution
Age: 4.2 Ma, TL: 13.5±2.0 µm
frq
0.5
0.4
0.3
0.2
0.1
0.0
0
4
8
12
16
20
µm

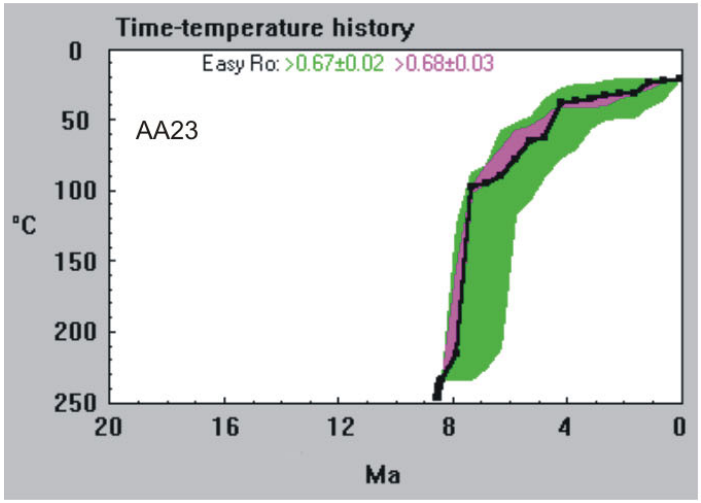
Time-temperature history
Easy Ro: >0.67±0.02 >0.68±0.03
AA23
°C
0
50
100
150
200
250
20
16
12
8
4
0
Ma

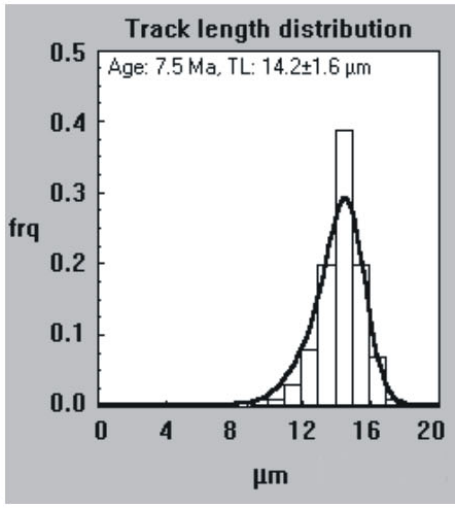
Track length distribution
Age: 7.5 Ma, TL: 14.2±1.6 µm
frq
0.5
0.4
0.3
0.2
0.1
0.0
0
4
8
12
16
20
µm

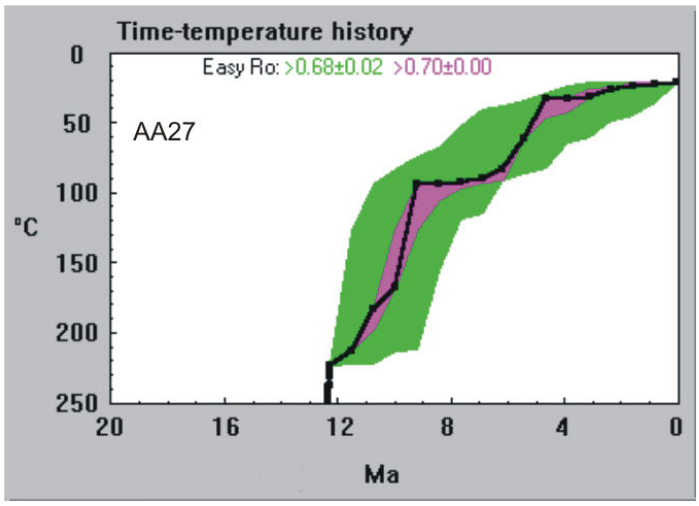
Time-temperature history
Easy Ro: >0.68±0.02 >0.70±0.00
AA27
°C
0
50
100
150
200
250
20
16
12
8
4
0
Ma

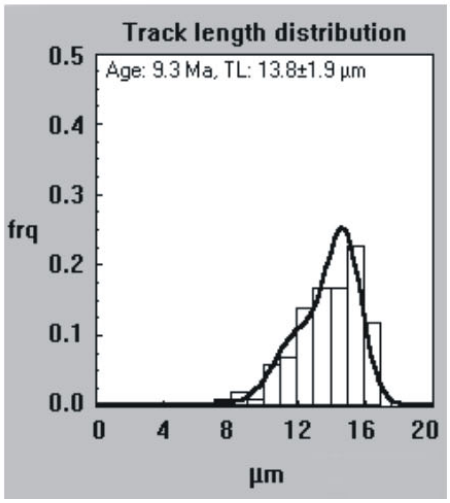
Track length distribution
Age: 9.3 Ma, TL: 13.8±1.9 µm
frq
0.5
0.4
0.3
0.2
0.1
0.0
0
4
8
12
16
20
µm

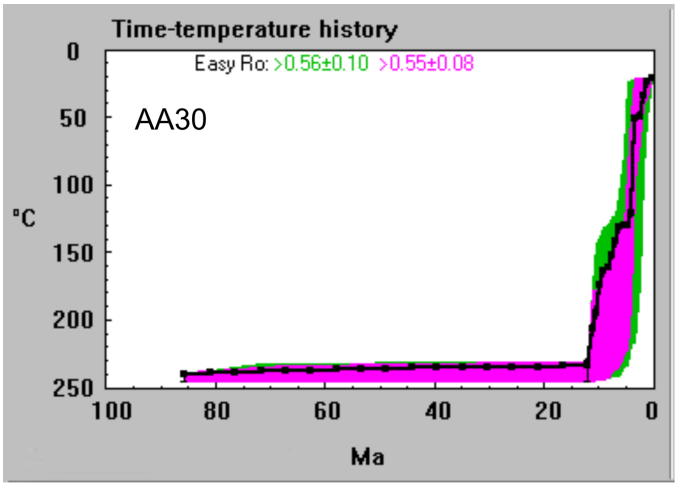

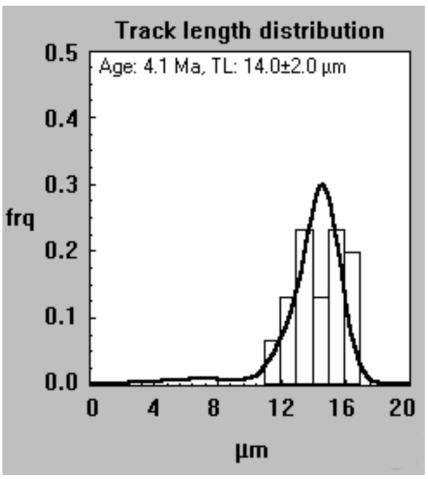

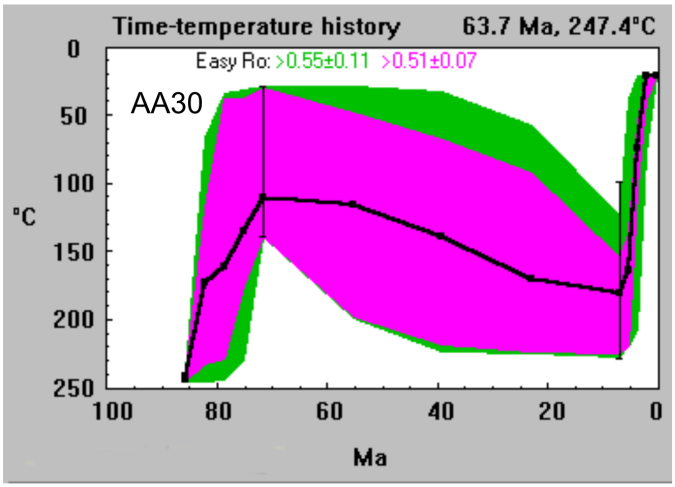

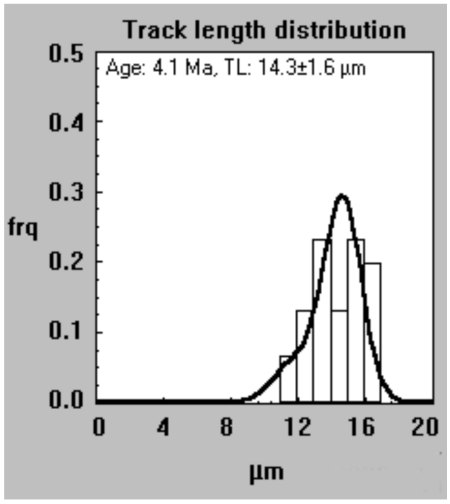

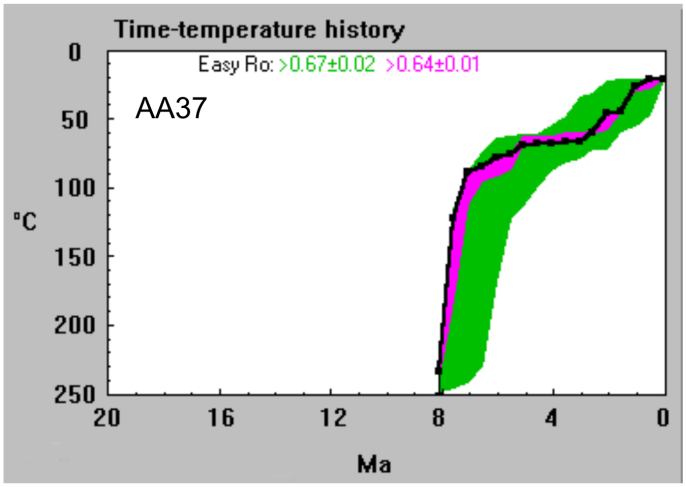

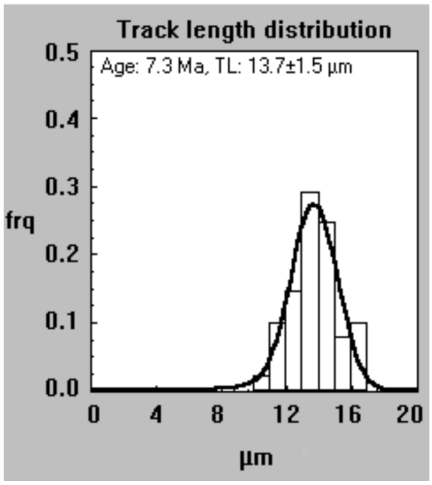

Parameters used in the thermal modelling of Aftsolve© 1.3 (Ketcham and Donelick, 2001): Inverse Modelling Algorithm: Laslett et al. (1987) Durango apatite. Length reduction in age standard: 0.893, initial track length: 15.7µm.
Pooled ages used for data modelling. Three different reliability levels describe the modeled results, green envelopes represent acceptable fits, magenta the good fits, and the central curve the best fits for the data. At the right, frequency distributions of measured confined track length data are overlain by the calculated probability density function with the best fit.

Appendix V. Location of Samples in the Reloncaví and Hornopirén Areas of the Main Range

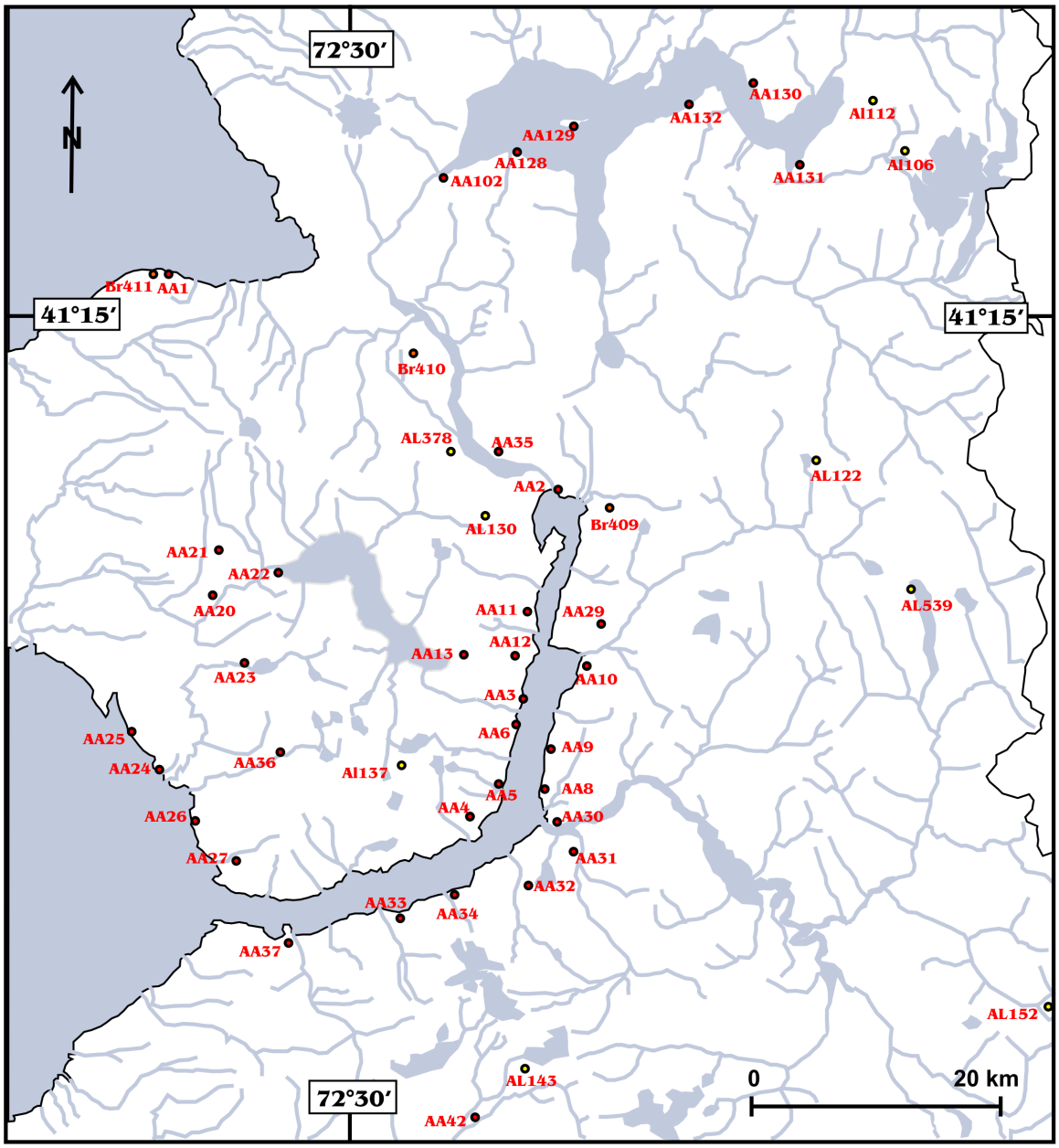

Reloncaví Area
Location of Samples for FT Dating

- Samples collected by A.A.
- Samples obtained from SERNAGEOMIN
- Samples collected by M.R.B.

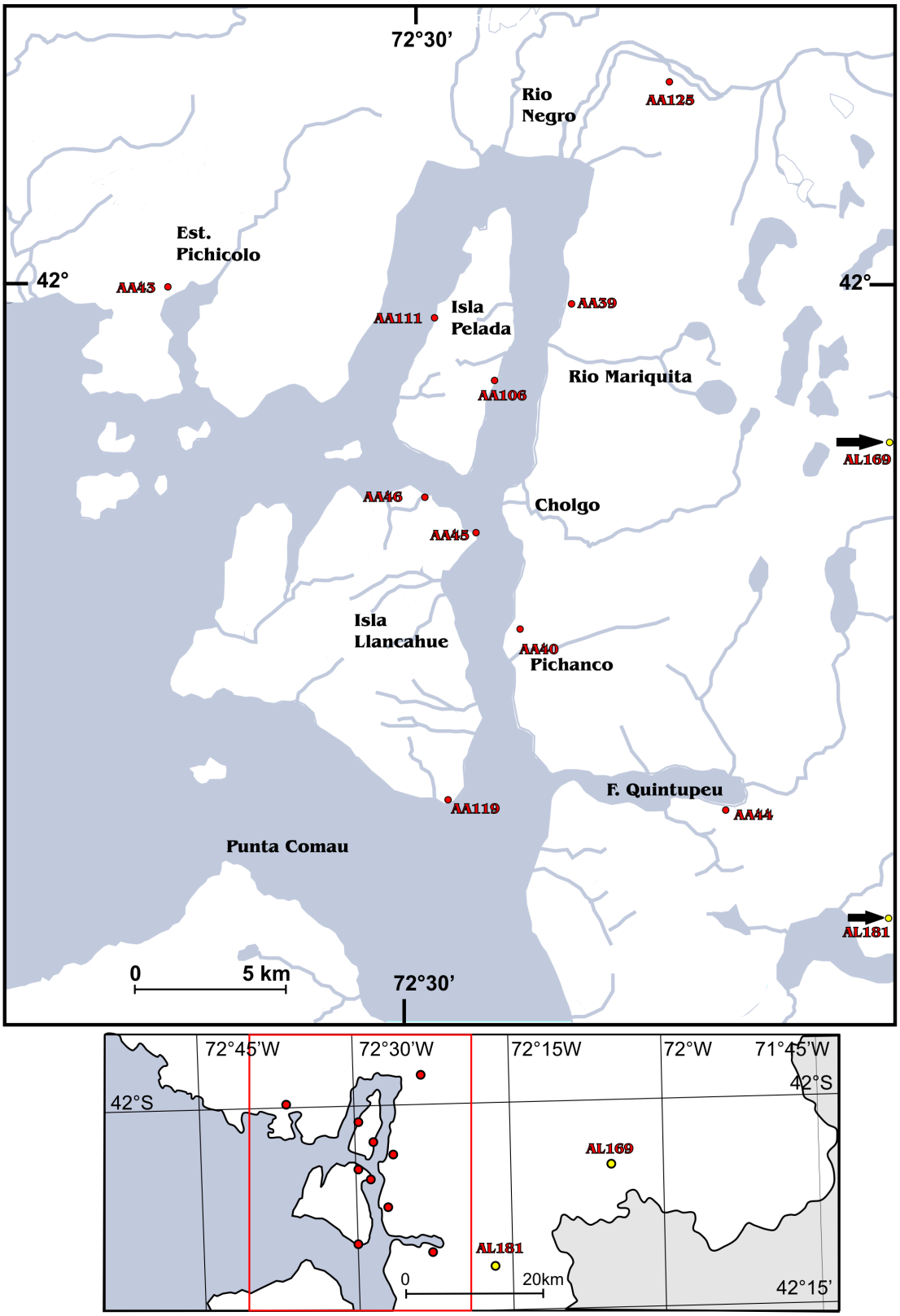

Sector Hornopirén- Location of Samples for FT Analysis

- Samples collected by A.A.
- Samples provided by SERNAGEOMIN